Magnetotransport in novel Dirac systems

Zur Erlangung des akademischen Grades eines

Doktor der Naturwissenschaften

der Fakultät für Physik
des Karlsruher Instituts für Technologie

genehmigte

Dissertation

von

Janina Klier, M. Sc.
aus Neustadt an der Weinstraße

Tag der mündlichen Prüfung: 20.07.2018
Referent: PD Dr. Igor Gornyi
Korreferent: Prof. Dr. Alexander Mirlin

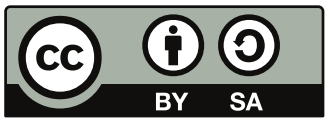

Acknowledgements

First, I want to express my sincere gratitude to Prof. Dr. Alexander Mirlin for giving me the opportunity to work in his research group, his support during this time, and for being co-referee of the thesis. Equally, I am indebted to thank PD Dr. Igor Gornyi for supervising me during my PhD, his support, and patience in these years. I want to thank both Igor Gornyi and Alexander Mirlin for many interesting discussion, the opportunities they offered me, and their advice on scientific matters and beyond.

Special thanks go to my collaborators Igor Krainov, Alexander Dmitriev, Svetlana Klyatskaya, Mario Ruben, Wolfgang Wernsdorfer. I really enjoyed or discussion and learned a lot in our joint projects.

I am obliged to thank the Carl-Zeiss-Stiftung for financial support during two years of my PhD thesis.

Furthermore, I want thank the people who proofread part of the manuscript and thus helped to improve it: Matthias Bard, Egor Kiselev, Julia Link, Tim Ludwig, Stefan Rex.

I also want to thank all members of the TKM for the pleasant atmosphere, the stimulating discussions, and the willingness to help. In particular, this applies to my roommates at the TKM and at the INT: Matthias Bard, Ulf Briskot, Nikolaos Kainaris, and Julia Link. I really enjoyed my time in both institutes.

Finally, I want to thank my family and my friends for the joyful time which always motivates me a lot. Especially, I want thank my parents for their unconditional support, their help and their valuable advice. I am grateful to my husband Sven for his support and his understanding when I spend my time on physics.

Introduction

I think it is a peculiarity of myself that I like to play about with equations, just looking for beautiful mathematical relations which maybe don't have any physical meaning at all. Sometimes they do.

— Paul A.M. Dirac (1902–1984) as quoted in Ref. [1]

The famous Dirac equation as published in 1928 has certainly a physical meaning, but still the above statement of Paul A. M. Dirac applies to the formula due to its beautiful mathematical relations. Moreover, at that time, it was surely not foreseen that the Dirac equation would become of such a high importance in condensed matter physics and thus get a physical meaning in less than three dimensions. The massless limit of the Dirac equation, the Weyl equation, proposed in 1929 to describe neutrinos [2], had no physical realization until the discovery of the three dimensional (3D) Weyl semimetal about 85 years later (since it was found that neutrinos have a mass) and still its nice mathematical relations have been studied long before. Nowadays, Weyl and Dirac materials are studied due to their extraordinary physical properties that offer a great potential for applications. Particular examples for those applications will be discussed in this thesis. The present thesis is devoted to the analysis of the properties of two Dirac systems hosting a huge magnetoresistance, 3D Weyl semimetals and carbon nanotubes with side-attached single-molecule magnets (both systems are defined below). These systems offer novel designs for magnetoresistance devices. Therefore, we demonstrate that equations without a physical realization might play an important role in future and hence are worth to be studied.

Physical systems showing a magnetoresistance (MR) of a giant magnitude have a great potential for different applications, for example, in sensors and magnetic memory. The MR is defined by the ratio $[\mathcal{G}(B) - \mathcal{G}(0)]/\mathcal{G}(0)$, where $\mathcal{G}(B)$ and $\mathcal{G}(0)$ denote the conductance with and without magnetic field, respectively. Apart from the magnitude of the MR, the size of the structure is another important quantity to characterize its potential for applications since one aim in building modern technological products is the device miniaturization.

A very prominent and recent experimental finding is the observation of the MR in transversal magnetic fields of three dimensional Weyl and Dirac semimetals [3–9]. With an extremely large magnitude of $10^4 - 10^6\%$, the transversal magnetoresistance (TMR) of Weyl semimetals is the first observation of a giant magnetoresistance in a homogeneous structure. Previously, such magnitudes were only observed in complex structures. Furthermore, the non-saturating linear behavior of the TMR is extraordinary. As it is clearly seen in Ref. [5], the TMR shows a linear behavior in both low but quantizing magnetic fields and highest magnetic fields where only the lowest Landau level contributes, the so-called quantum limit. In low magnetic fields, the TMR of Weyl and Dirac semimetals is superimposed by strong Shubnikov-de Haas oscillations.

Weyl and Dirac semimetals have, however, much more spectacular properties than the TMR. In order to discuss those properties, we first introduce both materials. The low energy quasiparticle spectrum of Dirac semimetals is characterized by the 4×4 Dirac Hamiltonian which describes the crossing of two twofold degenerate bands with linear dispersion. Known material realizations are Cd_3As_2 [10]

and Na_3Bi [11]. For broken inversion or time-reversal symmetry, the four component Dirac equation splits into two independent two component Weyl fermions of opposite chirality. The crossing points of the resulting non-degenerates bands, the so-called Weyl nodes, are located at distinct momenta. For example, the materials TaAs [12, 13], NbAs [14], TaP [15], and NbP [5] are classified as Weyl semimetals.

Close to the charge neutrality point, the transport properties of Weyl semimetals are highly peculiar. One central aspect of this peculiarity is the appearance of a disorder critical point. This was first pointed out within a mean field approach in Refs. [16, 17], later the fact was confirmed by a renormalization group (RG) analysis in $2 - \epsilon$ dimensions [18–20], an effective field theory [21], and in a numerical analysis [22]. For sufficiently weak disorder, meaning below the disorder critical point, the density of states vanishes quadratically in energy around the Weyl point within the perturbation theory. The effect of non-perturbative processes are currently under discussion. In several numerical studies [23–26] and in analytical calculations [27, 28], it was concluded that rare-region effects would produce an exponentially small density of states. However, most recent calculations claim that rare regions do not provide a finite density of states [29]. In the strong disorder regime, the density of states is finite at the Weyl point already without invoking exponentially small contributions.

The vanishing density of states for weak disorder manifests itself in a vanishing ac conductivity ($\propto |\omega|$ with external frequency ω) in the zero temperature limit while the dc conductivity remains finite for temperature going to zero [30]. In the strong disorder limit, the finite density of states ensures that both dc and ac conductivity remain finite in the zero frequency and temperature limit.

In an external magnetic field, transport in Weyl semimetals reveals an interesting physics besides the linear TMR. One reason for this is the unconventional Landau level quantization of Dirac fermions. Further, a single species of Weyl fermions displays the chiral anomaly that gives rise to a possibility of controlling the valley polarization. A strong anomalous Hall effect [1, 31, 32] and the negative longitudinal magnetoresistivity [5, 33–41] in Weyl semimetals have been predicted to originate from the chiral anomaly. Further properties as thermoelectrical effects [42] and induced superconductivity [43] have been studied recently, both theoretically and experimentally. Moreover, Josephson currents in different systems involving Weyl semimetals are recently studied theoretically where the chirality of the system leads to interesting features [44–47].

Recently, a new class of Weyl semimetals, the so-called type II Weyl semimetals, was discovered in the materials WP_2 and MoP_2 [48]. Those materials are characterized by a tilt in the dispersion relation. This type of Weyl semimetals shows an even larger transversal MR (magnitude of $10^7\%$) compared the Weyl semimetals described previously. Moreover, the dependence with respect to magnetic field of the TMR in type II Weyl semimetals is quadratic. This emphasizes the great potential of the whole class of Weyl semimetals for significantly easier designs for MR devices.

In order to further miniaturize the MR devices, "spin-valve" effects on a single-molecule level play an important role [49]. The field of molecular spintronics [50–55] provides a way to built such devices with the abilities to characterize, manipulate, and read out the molecular spin states of nanostructures down to the single-molecule level. Not only size miniaturization is driving this field but also the need to effectively interface organic and inorganic materials for biomedical and nanoelectronic applications [49]. By applying state-of-the-art optical and electronic techniques, single-molecule functionality on short time scales can be realized [56–64].

Such nanometer-scale structures with a stable spin orientation find a promising realization in single-molecule magnets (SMM) [54]. In general, SMMs consist of an inner magnetic core surrounded by a shell of organic ligands [65, 66]. The structure of organic ligands can be designed to bind the molecular magnets on surfaces or into molecular junctions [67–72]. To strengthen the magnetic interaction of the

core ions, delocalized bonds in SMMs are utilized and can further enhance the conducting properties of the molecule. The possibility of selective substitution of the ligands together with the variety of shapes and sizes of the existing SMMs provide the possibility to adjust the SMMs for an ideal coupling to the environment [73]. By exchanging the magnetic ions in the SMMs, the magnetic properties can be varied without modifying the structure [74]. Although the deposition of SMMs on surfaces or between leads may affect their magnetic properties [73, 75], SMMs with their low structural versatility prevail over non-molecular nanosystems which typically show large size and anisotropy distributions. The essential advantage of SMMs compared to magnetic nanoparticles is that they are extremely monodisperse and can be investigated in molecular crystals.

In particular, the unification of the macroscale properties of a magnet with the quantum features of a nanoscale object leads to an observation of an impressive variety of quantum effects in SMMs. Ranging from Berry-phase interference and quantum coherence to quantum tunneling of magnetization, the quantum effects are observable up to very high temperatures due to the progress in molecular designs. The study of SMMs has already caused a strong impact on spintronics [52]. However, further development of designs for devices based on individual SMMs promise even more striking results.

Transport in nanostructures is strongly modified by SMMs. Building blocks for such nanostructures are, for example, graphene or carbon nanotubes (CNT). The ligands of the SMMs can be designed such that they couple via supramolecular $\pi - \pi$ interaction with the π electrons of graphene or of the CNTs. Both graphene and CNTs are Dirac materials. Carbon nanotubes, as a rolled up sheet of graphene, have either a gapped Dirac spectrum which provides a semiconducting system or a linear spectrum with two crossing one dimensional modes which is a metallic system. If the system is metallic or semiconducting as well as the size of the gap in the semiconducting system is dependent on the diameter of the CNT and chiral angle defining the lattice sites of graphene which superpose in the rolled up CNT [76]. Due to their spectrum, CNT represent an one dimensional Dirac system.

In a CNT with the side-attached $TbPc_2$ SMMs, a remarkable giant magnetoresistance (GMR) and "spin-valve" effect is observed [58, 77, 78]. With its possible applications to senors or magnetic memory, the system of SMMs attached to CNTs marks the smallest realized "spin-valve" system. The GMR manifests itself in the observation of reproducible sharp jumps of the conductance of the CNT tunnel-coupled to the leads with a slow variation of magnetic field aligning the magnetic moments of the molecules parallel to each other. By a variation of gate voltage, the GMR effect in nanotubes can reach a magnitude of $10^3\%$. This spin-valve effect is by its manifestation similar to the prominent phenomenon of GMR in thin metallic films with magnetic contacts which is one of the most widely implemented phenomena in the field of spintronics. A similar spin-valve effect can be found in thin graphene strips with SMMs [79] and in CNTs with permalloy contacts [80].

This thesis will be concerned with the following aspects of magnetotransport in Dirac systems. One central aspect is the analysis of the TMR in Weyl semimetals involving the calculation of the effects of disorder in presence of magnetic field. Certainly, disorder in Weyl semimetals in the absence of a magnetic field is also quite peculiar and thus deserves a consideration in this thesis. Moreover, this thesis aims to describe the GMR in the system of CNTs with side-attached SMMs of $TbPc_2$. Since a main ingredient of this model is the resonant scattering off Fano-resonances, a more detailed analysis of transport with Fano-resonances is studied.

The appearance of a critical disorder strength in Weyl semimetals at the charge neutrality point was discussed in several works [16–22]. However, the analysis of disorder away from the charge neutrality includes the appearance of a "phase" of critical disorder. The behavior in this critical phase is however not fully understood since the mean field approach [16, 17] provides strongly different result from the RG in $2 - \epsilon$ dimensions[18–20]. The consideration of the critical phase within self-consistent Born

approximation performed in this thesis should provide a deeper understanding of the physics in the phase of critical disorder. Moreover, it was shown for the dc conductivity in weak disorder that vertex corrections to the conductivity are relevant already in the simplest disorder configuration [81]. With the full incorporation of vertex corrections in the strong disorder regime, we uncover the interesting effect of a saturating conductivity in dependence of an increasing disorder strength. The consideration of disorder in Weyl semimetals will be completed by establishing a model for impurity scattering in presence of magnetic field which is relevant to address the TMR.

One of the main goals of this thesis is to find a theoretical explanation for the huge linear TMR in Weyl semimetals as observed in experiment. Theoretically, the TMR in the ultra quantum limit, where only the zeroth Landau level contributes to transport, was considered in a model of strongly screened Coulomb impurities in a seminal paper by Abrikosov [82]. Naturally, this theoretical analysis provokes the following questions: (i) Does this model of the TMR provide a linear resistivity with respect to magnetic field when the model is applied higher Landau levels where the experimentally observed Shubnikov-de Haas oscillations can be studied? (ii) Does the theoretically obtained linear TMR in the ultra quantum limit crucially depend on the model of screened Coulomb impurities? Moreover, Ref. [82] addresses the TMR for finite chemical potential leading to a finite Hall conductivity. Thus, another important question will be how the Hall conductivity affects the TMR away from the quantum limit. These questions will be issued in the following thesis based on the works of Refs. [83] and [84]. In order to demonstrate the importance of this work, let us briefly comment on related works. The TMR in a different regime of Coulomb impurities compared to our works was performed in Ref. [85]. A quite similar consideration of the TMR was performed in Ref. [86], however, in a less elaborated model within simple Born approximation. A numerical confirmation of the results in the quantum limit was recently performed in Ref. [87]. Moreover, a different approach involving classical memory effects proposed a linear TMR in a smooth disorder potential [88].

Besides the investigation of Weyl semimetals, this thesis is further devoted to the magnetotransport in nanostructures with SMMs. Specifically, we propose a theoretical model for a CNT with side-attached $TbPc_2$ molecules. Theoretically, molecular quantum dots coupled to metallic leads were analyzed in a number of works. In particular, works devoted to a possible read-out for the local spin orientation via the measurement of the spin current [89], asymmetries in the Coulomb diamonds and Kondo peaks [90], and the spin-blockade effect associated with a change of magnetic anisotropy [91] were addressed. For a single-wall CNT with a single side-attached molecule, a mechanism of the spin-valve effect for (effectively infinite) CNTs with SMMs was proposed in Ref. [92]. Moreover, it has been argued that the tunnel magnetoresistance may depend on the exchange interaction between the CNT and the SMM [93]. However, the GMR and peculiar nonlinear transport observed experimentally in tunnel-coupled CNTs with several SMMs is not comprehensively explained in those theoretical descriptions. With the theoretical model presented in this thesis, we fill in this lack and provide a comprehensive explanation for the GMR and spin-valve effect for CNTs with side-attached SMMs. The model is based on our recent publication [94].

This thesis is structured as follows: **Chapter 1** introduces the physics of Dirac materials with a focus on the materials relevant to this thesis. Furthermore, we discuss the spectacular experimental findings which we model theoretically in this thesis. In **Chapter 2**, we discuss the methods of transport theory which are applied to the novel Dirac systems considered in this thesis. After those introductory chapters, we start in **Chapter 3** with the analysis of disorder in Weyl semimetals. In this part, we discuss first the behavior in absence of magnetic field where we provide a fully self-consistent description in the different regimes of disorder. The chapter continues with the analysis in the presence of magnetic field, where we focus on the broadening of Landau levels with respect to disorder and magnetic field. In

Chapter 4, we calculate the transversal magnetoresistance in presence of disorder for both pointlike and Coulomb impurities. In particular, we analyze the magnetoresistance in different regimes of temperature and chemical potential. Furthermore, we consider a model of Weyl nodes shifted in energy with respect to each other as it is most relevant to experiment. In **Chapter 5**, we turn to the system of a carbon nanotube with side-attached single-molecule magnets. In order to describe this system, we first analyze Fano-resonances in a confined geometry and then apply these results to a minimal model with two molecules attached to the nanotube to describe the magnetoresistance and spin-valve effect. The model of Ch. 5 is enhanced in **Chapter 6** by including Coulomb interaction. The inclusion of Coulomb interaction provides then a giant magnetoresistance and explains the features of the Coulomb map as obtained in experiment. **Chapter 7** summarizes the main results of this thesis and gives a prospect to further related research projects. Mathematical details of this thesis can be found in the appendices. For convenience, a summary of used Notations and Conventions and a list of Acronyms is provided on pages 161 and 163, respectively.

Contents

Chapter 1

1 Dirac systems

This thesis is mainly devoted to magnetotransport studied in two different Dirac systems, Weyl semimetals and a system of carbon nanotubes with side-attached single-molecule magnets. In this chapter, we will present the historical journey of the research on Dirac systems which became a central aspect of study in condensed matter physics in the last years.

There is a wide range of materials like graphene, topological insulators, d-wave superconductors, and 3D Weyl and Dirac semimetals sharing a fundamental property: the low energy spectrum is described by the Dirac Hamiltonian[1]. This behavior defines the class of Dirac materials. The most prominent Dirac material might be graphene [95], a two-dimensional material consisting of carbon atoms arranged in a honeycomb lattice first synthesized in 2004. Graphene shows many remarkable properties. Among those are the observation of a quantum Hall effect at nearly room-temperature [96] or the conductivity close to quantum conductance e^2/h at the Dirac point [97, 98]. In the last recent years however, the center of attention shifted more to topological insulators and 3D Weyl semimetals. Weyl semimetals, first discovered in the year 2015 [12], are the three-dimensional analogue of graphene and show also highly peculiar properties such as chiral anomaly [99], strong transversal magnetoresistance [5], etc. Material realizations are, for example, TaAs [12, 13], NbAs [14], TaP [15], and NbP [5]. Closely related to Weyl semimetals are the 3D Dirac semimetals with the material realizations of Cd_3As_2 [10] and Na_3Bi [11]. There exist also examples where modes in one dimension disperse linearly in condensed matter systems. Under certain conditions, single walled carbon nanotubes represent such systems. Even before the synthesis of graphene, single walled carbon nanotubes being one rolled up sheet of graphene, could be discovered in 1993 [100, 101]. Strictly speaking, carbon nanotubes are not a Dirac material. In fact, the spectrum of low energy excitation depends on how the graphene sheet is rolled up as discussed in detail later in this chapter. As in this thesis, carbon nanotubes are nowadays widely used as building blocks of nanostructures.

In this chapter, we present a brief overview on Dirac systems, Sec. 1.1, to classify these materials in general and motivate their realization in condensed matter systems. Then, we proceed with an introduction into the physics of Weyl semimetals, Sec. 1.2 including a review of the most peculiar properties as relevant to this thesis. Furthermore, we discuss the properties of 3D Dirac semimetals to demarcate them from Weyl semimetals for certain signatures. In Section 1.3, we establish the connection of Dirac materials with carbon nanotubes by calculating the band structure. Finally, the considered model of the carbon nanotube system with single molecule magnets attached, Sec. 1.4 is

[1] In the case of topological insulators, only the surface states are described by Dirac Hamiltonian while the bulk has a gapped spectrum

introduced including a review of the properties in the single molecule magnets and a discussion of the experimental results.

1.1 From Graphene to novel Dirac systems

In 1928, Paul Dirac published an equation to formulate a quantum theory which is compatible with special relativity. The Dirac equation for a free particle is

$$i\hbar\frac{\partial}{\partial t}\psi = \left(c\boldsymbol{\alpha}\cdot\mathbf{p} + \beta mc^2\right)\psi, \tag{1.1}$$

where $\boldsymbol{\alpha}$ and β form an algebra of anti-commuting 4×4 matrices and ψ is a four component spinor. There are several ways to express the parameters $\boldsymbol{\alpha}$ and β, for example $\boldsymbol{\alpha} = (\tau_z\otimes\sigma_x, \tau_z\otimes\sigma_y, \tau_z\otimes\sigma_z)$ and $\beta = -\tau_x\otimes\mathbb{1}$ as described in Ref. [1]. The equation was originally intended to describe an electron in three spatial dimension, which is of course a massive particle with spin 1/2. In one or two spatial dimensions, the right-hand-side of Eq. (1.1) reduces to a 2×2 Hamiltonian. As an example, in 2D the Hamiltonian reads

$$\mathcal{H} = c(\sigma_x p_x + \sigma_y p_y) + mc^2\sigma_z. \tag{1.2}$$

In three spacial dimensions, the decoupling can only be achieved in the massless limit, reading

$$i\hbar\frac{\partial}{\partial t}\chi_\pm = \pm c\boldsymbol{\sigma}\cdot\mathbf{p}\chi_\pm. \tag{1.3}$$

The massless simplification of the Dirac equation was proposed by Hermann Weyl in 1929 [2] originally to describe neutrinos. After a finite mass of neutrinos has been discovered, the condensed matter realization was the first application of this Hamiltonian.

In the following, we will show that an emergence of a Dirac-like Hamiltonian can in general be achieved in condensed matter systems and we will illustrate this statement by an particular example in the proceeding section.

According to Bloch's theorem, the eigenenergies $\varepsilon_n(\mathbf{p})$ and the eigenstates $|\psi_{n,\mathbf{p}}\rangle$ of a single band Hamiltonian $\mathcal{H}_0$ in a crystal can be described by a discrete band index n and the continuous crystal momentum $\mathbf{k}$ which can be constructed to the first Brillouin zone. We consider now two adjacent energy bands $\varepsilon_{n,+}(\mathbf{p})$ and $\varepsilon_{n,-}(\mathbf{p})$ which approach each other for some momentum $\mathbf{p}$ and are well separated from other bands. An effective Hamiltonian can be derived by considering two orthogonal Bloch states $|u_\mathbf{p}\rangle$ and $|v_\mathbf{p}\rangle$ consistent with the symmetries of the Hamiltonian $\mathcal{H}_0$. The effective Hamiltonian is given by

$$\mathcal{H}_{\text{eff}} = \sum_\mathbf{p}\psi_\mathbf{p}^\dagger\mathcal{H}(\mathbf{p})\psi_\mathbf{p} \tag{1.4}$$

where

$$\mathcal{H}(\mathbf{p}) = \begin{pmatrix}\langle u_\mathbf{p}|H_0|u_\mathbf{p}\rangle & \langle u_\mathbf{p}|H_0|v_\mathbf{p}\rangle \\ \langle v_\mathbf{p}|H_0|u_\mathbf{p}\rangle & \langle v_\mathbf{p}|H_0|v_\mathbf{p}\rangle\end{pmatrix} = f(\mathbf{p})\mathbb{1} + \sum_{j=1}^{3} g_j(\mathbf{p})\sigma_j, \tag{1.5}$$

with the unit matrix $\mathbb{1}$ and the Pauli matrices σ_j. Correspondingly, the one-particle spectrum of the effective Hamiltonian is

$$\varepsilon_\pm = f(\mathbf{p}) \pm \sqrt{\sum_{j=1}^{3} g_j^2(\mathbf{p})}. \tag{1.6}$$

The expression shows that the energy bands touch for $g_j(\mathbf{p}_0) = 0$ for each j at some point $\mathbf{p}_0$, called Dirac point. The Hamiltonian can be expanded near those Dirac points $\mathbf{p}_0$ as

$$\mathcal{H}(\mathbf{p}) = \varepsilon_{\mathbf{p}_0} + \mathbf{v}_0 \cdot (\mathbf{p} - \mathbf{p}_0)\mathbb{1} + \sum_{k=1}^{3} \mathbf{v}_k \cdot (\mathbf{p} - \mathbf{p}_0)\sigma_k. \tag{1.7}$$

The effective Hamiltonian $\mathcal{H}(\mathbf{p})$ has the form of an anisotropic Weyl Hamiltonian for $\mathbf{v}_0 = 0$ and mutually orthogonal vectors $\mathbf{v}_k$.

To show that the Dirac Hamiltonian can appear in real condensed matter systems, we discuss the presumably most prominent example of a simple band structure resulting in the low energy Hamiltonian of Eq. (1.7): the 2D Dirac semimetal graphene. Graphene consists of carbon atoms arranged in a two dimensional honeycomb lattice as shown in Fig. 1.1, first synthesized in 2004 [95] and is a single layer of graphite. The honeycomb lattice can be viewed as a triangular lattice in a basis that consists of two atoms in each unit cell where the corresponding lattice vectors are

$$\mathbf{a}_1 = \frac{a}{2}\left(3, \quad \sqrt{3}\right), \qquad \mathbf{a}_2 = \frac{a}{2}\left(3, \quad -\sqrt{3}\right). \tag{1.8}$$

The parameter a is the distance between the carbon atoms. To calculate the band structure of this lattice, we consider a tight-binding model as in Ref. [102], leading the the Hamiltonian

$$\mathcal{H} = -t \sum_{\langle i,j\rangle,\sigma} (a_{i\sigma}^\dagger b_{j,\sigma} + a_{i\sigma} b_{j,\sigma}^\dagger). \tag{1.9}$$

Here, the operator $a_{i,\sigma}$ ($a_{i,\sigma}^\dagger$) annihilates (creates) an electron with spin σ at the position $\mathbf{R}_i$ on sublattice A, with the corresponding definition for sublattice B with $b_{i,\sigma}$ ($b_{i,\sigma}^\dagger$). The sum $\langle i, j\rangle$ means a summation over pairs of nearest neighbors. Exploiting of the symmetries of the lattice the spectrum can be found as

$$\varepsilon_\pm = \pm t\sqrt{3 + 2\cos(\sqrt{3}k_y a) + 4\cos(\sqrt{3}k_y a/2)\cos(3k_x a/2)}, \tag{1.10}$$

with the "+" sign corresponding to the upper and the "−" sign to the lower band. Close inspection reveals that the spectrum is linear close the points $\mathbf{K}$ and $\mathbf{K}'$ in the reciprocal lattice, cf. Fig. 1.1. The points are given by

$$\mathbf{K} = \left(\frac{2\pi}{3a}, \frac{2\pi}{3\sqrt{3}a}\right), \qquad \mathbf{K}' = \left(\frac{2\pi}{3a}, -\frac{2\pi}{3\sqrt{3}a}\right). \tag{1.11}$$

Around those points the spectrum can be expanded as

$$\varepsilon_\pm = \pm v_F |\mathbf{p}|, \tag{1.12}$$

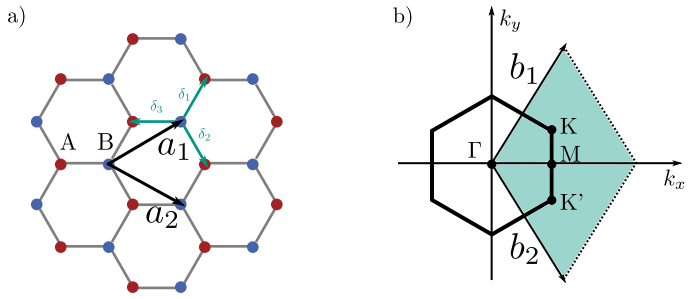

Figure 1.1: Honeycomb lattice and corresponding first Brillouin. The lattice vectors $\mathbf{a}_1$ and $\mathbf{a}_2$ are shown as well as the distances to the next nearest neighbors δ_1, δ_2, and δ_3. Moreover, the points $\mathbf{K}$ and $\mathbf{K}'$ are depicted in the first Brillouin zone (green region on the right-hand-side). The figure shows further the basis vectors of the reciprocal lattice $\mathbf{b}_1$ and $\mathbf{b}_2$.

where $\mathbf{p}$ is the momentum relative the Dirac point. The Fermi velocity is in this model given by $v_F = 3ta/2$. Thus, close to the points $\mathbf{K}$ and $\mathbf{K}'$, the Hamiltonian can be written in the form of the 2D Dirac Hamiltonian, reading

$$\mathcal{H} = v_F(\tau p_x \sigma_x + p_y \sigma_y), \tag{1.13}$$

with τ being the valley index. This example shows that relativistic physics can be studied in the energy regime of a condensed matter system.

With similar considerations, one can derive the band structure of other Dirac materials, for example topological insulators or d-wave superconductors. In the following chapter, we will show that tight-binding models can also be applied to derive a Weyl Hamiltonian in 3D, Sec. 1.2. Furthermore, we discuss the changes of the spectrum of graphene, when it is rolled up into a carbon nanotube, Sec. 1.3.

Let us further note, that recently materials with more exotic expansions of the Hamiltonian (1.7) have been received more and more attention. For example, materials with finite velocity $\mathbf{v}_0$ in the Hamiltonian (1.7) have became a subject of consideration called type II Weyl semimetals. The additional term in the anisotropic Weyl Hamiltonian leads to a 'tilt' in the energy spectrum as theoretically addressed in Ref. [104]. Material realizations are, for example, $Mo_xW_{1x}Te_2$ [105], MoP_2, and WP_2, receiving much attention due to their high quadratic transversal magnetoresistance (up to $10^7\%$) [48] and due to signatures of hydrodynamic transport in experiments[106]. However, the term Weyl semimetal as used in the following thesis stands only for the untilted Weyl cone, the so-called type I Weyl semimetal. Moreover, higher order expansions in the momentum in the effective Dirac Hamiltonian (1.7) are studied. They are called anisotropic Weyl semimetals or multiple Weyl semimetals and show also highly peculiar properties as high viscosity [107]. Possible realizations for anisotropic Weyl semimetals are proposed to emerge under pressure in $\alpha-(\text{BEDT-TTF})_2\text{I}_3$ [108]. The band structure calculations of $HgCr_2Se_4$ show the signatures for multiple Weyl semimetals.

1.2 3D Weyl and Dirac semimetals

In the previous section, we outlined an example for the appearance of an Dirac-like dispersion in a two-dimensional Dirac material. However, as has been known for a long time, band crossings are also stable in three dimensions [109, 110]. Around those crossing points, the bands in first order disperse

linearly. In order to get a three-dimensional Dirac-like crossing point, one needs to be able to tune the chemical potential to or close to the crossing point. Furthermore, additional bands at this energy need to be absent. If just two single bands without any additional degeneracy cross, the low energy dispersion of the crossing point is mathematically described by the Weyl equation. Materials with no degeneracy in the crossing points are thus referred to as Weyl semimetals with realizations like TaAs [12, 13], NbAs [14], TaP [15], and NbP [5]. Individually non-degenerate bands require that either time-reversal or inversion symmetry is broken. The current realizations of Weyl semimetals are all determined by broken inversion symmetry. For both time-reversal and inversion symmetry, the bands are two-fold degenerate and are described by the massless Dirac equation. The corresponding Dirac semimetal is realized in the materials Cd_3As_2 [10] and Na_3Bi [11]. Under the application of a finite magnetic field, these materials resemble a Weyl semimetal with broken time-reversal symmetry.

The difference between 3D Weyl and Dirac semimetals as well as the difference between a Weyl semimetal with broken time-reversal symmetry or broken inversion symmetry is manifested by the fermion doubling theorem which states that two nodal points of opposite chirality are required in the Brillouin zone (discussed in the following). The non-degeneracy of the bands in Weyl semimetals only exists for broken time-reversal or broken inversion symmetry. If both symmetries are present as for Dirac semimetals, the bands are degenerate. This is explained by the following argument: For a Weyl point with chirality "+1" at point $\mathbf{k}$, time-reversal symmetry requires another Weyl point with the same chirality at point $-\mathbf{k}$. Due to the fact that the net chirality is zero in the system, Weyl point with opposite chirality are present at the points $\mathbf{k}'$ and $-\mathbf{k}'$. This system with a minimal model of four Weyl nodes is the Weyl semimetal with broken inversion symmetry, [111]. However, inversion symmetry requires that the Weyl points at $\mathbf{k}$ and $-\mathbf{k}$ have opposite chirality leading to a minimal model of two Weyl nodes with opposite chirality for broken time-reversal symmetry [112]. If now both time-reversal and inversion symmetry are present, it is dictated that $\mathbf{k} = \mathbf{k}'$. This means that the minimal model for a Dirac semimetal has two nodal points where the doubly degenerate bands cross. In the following, we will discuss the topological features of these two model and analyze the stability of such materials related to their topological properties.

1.2.1 Weyl semimetals

Let us now review the properties of a Weyl semimetal. Similar to graphene, one can consider a tight-binding model to obtain a 3D Weyl Hamiltonian. In particular, we will discuss a cubic lattice hosting Weyl nodes under certain conditions as it is discussed in Ref. [1, 113, 114]. Considering a half-filled two band model leads to the following tight-binding Hamiltonian

$$\mathcal{H}(\mathbf{k}) = \frac{v_F}{a}\left[\left(\cos(k_x a) + m\left(2 - \cos(k_y a) - \cos(k_z a)\right)\right)\sigma_x + \sin(k_y a)\sigma_y + \sin(k_z)\sigma_z\right]. \tag{1.14}$$

This model breaks time reversal symmetry. The Weyl nodes of this Hamiltonian are located at $k_\pm = (\pm\pi/(2a), 0, 0)$. Expanding the Hamiltonian around those points leads to a simple low-energy Hamiltonian consisting of two bands, yielding

$$\mathcal{H}_\pm = \pm\hbar v_F(p_x\sigma_x + p_y\sigma_y + p_z\sigma_z). \tag{1.15}$$

Here, the Pauli matrices σ_i act in the space of the two energy bands. The two band touching points are called Weyl nodes with the expansion $p = (k - k_\pm)$. As expected for Dirac materials, the energy spectrum for both nodes is $\varepsilon = \pm v_F|\mathbf{p}|$. As a general property of Weyl fermions, each node is associated

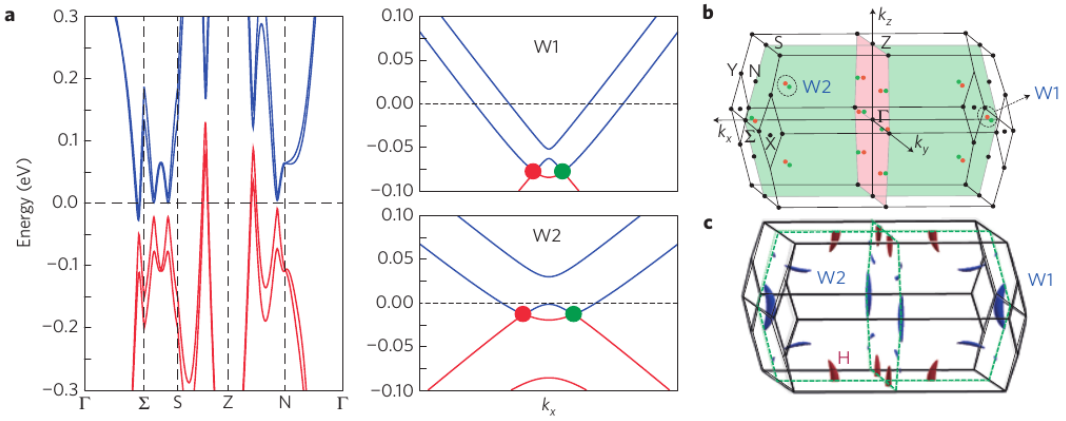

[Reprinted with permission from Springer Nature: Nature Physics **11** (8), 645649, Extremely large magnetoresistance and ultrahigh mobility in the topological Weyl semimetal candidate NbP, Chandra Shekhar, Ajaya K. Nayak, Yan Sun, Marcus Schmidt, Michael Nicklas et al., copyright 2015]

Figure 1.2: Band structure and first Brillouin zone of the Weyl semimetal NbP extracted from Ref. [5]. Panel a) presents the band structure obtained in an *ab initio* calculation showing the Weyl points close to the Σ and N points of the Brillouin zone. In the right of panel a), the band structures of around the two pairs of Weyl points are depicted along the k_y direction. In panel b), the first Brillouin zone is shown with the twelve pairs of Weyl points W1 and W2 indicated. Panel c) illustrates the Fermi surfaces where the blue parts correspond to the electron pockets of the Weyl point and the red part to hole pockets.

with a chirality ± 1 for the Hamiltonian $\mathcal{H}_{\pm}$. As discussed below, in band structures, the total chirality of the system must vanish. Furthermore, it should be noted that the considered Hamiltonian is a simplification of the general anisotropic Weyl Hamiltonian where the three velocities can be different (but still mutually orthogonal). The anisotropic Weyl semimetal should be contrasted to the type II Weyl semimetal where the cones are tilted as briefly discussed in Sec. 1.1.

As an example, the band structure of the Weyl semimetal NbP obtained by *ab initio* calculations in Ref. [5] is presented in Fig. 1.2. The lattice structure of NbP is body-centered tetragonal with the non-symmorphic space group $I4_1md$. The lack of inversion symmetry lifts the spin degeneracy in the band structure. Thus, twelve non-degenerate pairs of Weyl points appear close to the Fermi energy in the first Brillouin zone. The twelve pairs of Weyl points can be classified in two groups $W1$ and $W2$ where the four pairs of $W1$ point lie lower in energy than the eight pairs of $W2$ Weyl points.

An important property of Weyl fermions is that the nodal points are topological objects in momentum space. The Weyl points are monopoles of the Berry curvature or Berry flux $\boldsymbol{\mathcal{B}}(\mathbf{p})$ with the orientation depending on the chirality. Mathematically, the Berry curvature is defined via an effective vector potential $\boldsymbol{\mathcal{A}}(\mathbf{p})$, reading

$$\boldsymbol{\mathcal{A}}(\mathbf{p}) = -i \sum_{n,occ} \langle u_{n,\mathbf{p}} | \nabla_{\mathbf{p}} | u_{n,\mathbf{p}} \rangle, \tag{1.16}$$

$$\boldsymbol{\mathcal{B}}(\mathbf{p}) = \nabla_{\mathbf{p}} \times \boldsymbol{\mathcal{A}}(\mathbf{p}), \tag{1.17}$$

where the summation is carried out over occupied bands for the Bloch states $|u_{n,\mathbf{p}}\rangle$. The integration of the Berry curvature through a small surface enclosing a Weyl node results in $\pm 2\pi$ with the sign

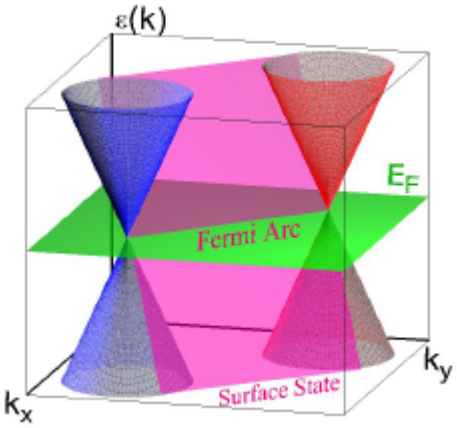

Figure 1.3: Reprinted figure from [112] illustrating surface states of a Weyl semimetal forming a Fermi arc. Fermi arcs connect two Weyl points (shown in blue and red) with the bulk dispersion depicted in red and blue. Surface states (pink plane) cross the Fermi level (green, horizontal plane) forming a Fermi arc.

determined by the chirality of the node. According to Gauss' law, the Weyl point is thus a monopole of the Berry flux. To obtain a net zero flux, the surface needs to enclose two Weyl nodes of opposite chirality known as fermion doubling theorem [115] explaining why the Weyl points always appear in pairs in the Brillouin zone.

Another interesting feature of Weyl semimetals is related to their surface states which form Fermi arcs [112]. Fermi arcs are disconnected or disjoint segments of the 2D surface states terminating at the nodal points. This is quite peculiar since Fermi surfaces are expected to form closed loops. The appearance of Fermi arcs in Weyl semimetals can be understood as follows. We consider a thick film of a Weyl semimetal in the minimal model of two Weyl cones with surfaces in the xy-plane. In the clean case, we can use translation invariance to label the single electron states by the crystal momentum in the plane. Away from the Weyl points, the surface states are well defined. However, at the nodal points, bulk and surface states coincide leading to ill-defined surface state. Thus, the surface states terminate and form an arc between the two Weyl points as illustrated in Fig. 1.3 when the pink plane is cutting the green plane of the Fermi level. Considering both the top and the bottom surface arcs of a Weyl semimetal in a thin slab, both arcs can be viewed to form a closed 2D Fermi surface. Increasing the thickness of the film, the two halves of the Fermi surface get spatially separated.

In presence of finite magnetic field, Weyl semimetals also have highly peculiar properties. Let as consider the Weyl Hamiltonian for chirality of $+1$ in the presence of a quantizing magnetic field in z direction

$$\mathcal{H}\left(\mathbf{p}\right) = \int d^3\mathbf{r}\Psi^\dagger(\mathbf{r})v\boldsymbol{\sigma}\left(\mathbf{p} - \frac{e}{c}\mathbf{A}\right)\Psi(\mathbf{r}), \tag{1.18}$$

with the vector potential in Landau gauge $\mathbf{A}(\mathbf{r}) = (0, Hx, 0)$. The eigenstates of the system are split

into zeroth and higher Landau levels, reading

$$\varepsilon_0 = v p_z, \tag{1.19}$$

$$\varepsilon_n^{(\pm)} = \pm \sqrt{(v p_z)^2 + \Omega^2 n}, \tag{1.20}$$

where $\Omega = v\sqrt{2eH/c}$ is the distance between the zeroth and first Landau level. The zeroth Landau level is a chiral mode dispersing in the direction set by chirality.

Related to the chiral mode of the zeroth Landau level is the important property that Weyl semimetals display chiral anomaly. Formally, the Hamiltonian (1.15) commutes with both the charge and the chiral charge. Thus, due to the Heisenberg equation of motion, charge and chiral charge need to be constant. Close inspection however reveals [99, 116] that an ultraviolet regularization is needed to obtain finite results. As physically desirable, this regularization is chosen to maintain the conservation of charge leading, however, to a non-conserved chiral charge in some configurations of the electromagnetic field. Thus, the continuity equation for the chiral charge transforms to

$$\frac{\partial N_5}{\partial t} + \nabla \cdot \mathbf{j}_5 = \pm \frac{e^2}{4\pi^2 c} \mathbf{E} \cdot \mathbf{H}, \tag{1.21}$$

where N_5 and $\mathbf{j}_5$ denote the chiral charge and the chiral current, respectively. The sign $\pm$ is determined by the chirality of the node. The non-conservation of charged particles for the chiral mode is known as chiral anomaly or Adler-Bell-Jackiw anomaly [99, 116]. Since the overall charge of a physical system needs to be conserved, the chiral anomaly provides an additional explanation for Weyl points appearing in pairs with opposite chirality. Physically, the chiral anomaly can be understood as follows: We consider low temperatures such that only the zeroth Landau level is relevant. This case is usually referred to as the ultra quantum limit. Furthermore, we apply an electric field $\mathbf{E}$ in the same direction as the magnetic field $\mathbf{H}$. Due to the semiclassical equations of motion, $\dot{\mathbf{k}} = -e\mathbf{E}$, the states will move along the electric field meaning that electrons appear or disappear at the Weyl point depending on the chirality.

Despite the total charge conservation, the chiral anomaly gives rise to several interesting effects. As a direct consequence of the transformed continuity equation (1.21), the chiral anomaly leads to a charge imbalance or valley polarization between the two nodal points, yielding

$$\frac{\partial (n_+ - n_-)}{\partial t} = \frac{e^2}{2\pi^2 c} \mathbf{E} \cdot \mathbf{H}. \tag{1.22}$$

Another direct consequence of the chiral anomaly is the decreasing longitudinal magnetoresistance [5, 40]. Furthermore, as reported in Ref. [117], the chiral anomaly provides a non-local dc current in a finite slab geometry.

Since the Weyl points are topologically protected, Weyl semimetals are very stable. As (pseudo)-magnetic monopoles, the 3D Weyl points cannot disappear by perturbations introducing a gap in the spectrum. By studying the Hamiltonian (1.15), it can be directly noticed that there is no Pauli matrix left to introduce a mass generating perturbation. Therefore, the nodal points can only be destroyed (beyond superconductivity) by the annihilation of Dirac cones. Moreover, the topological features require Weyl nodes separated in crystal momentum. Breaking translation symmetry by scattering between the two nodes might break the separation in crystal momentum and thus the topological properties. In fact, two Weyl nodes of opposite chirality moved together and merged in momentum space annihilate each other resulting in a fully gapped insulator. However, perturbations like disorder are normally not strong enough to merge or destroy two separated Weyl nodes.

1.2.2 Dirac semimetals

Dirac semimetals are described by the 4×4 Dirac Hamiltonian

$$\mathcal{H} = v_F \tau_z \boldsymbol{\sigma} \cdot \mathbf{k}, \tag{1.23}$$

which can be seen as two copies of the 2×2 Weyl Hamiltonian with opposite chiralities at the same point in momentum space. As discussed for Weyl semimetals, two Weyl nodes annihilate each other when they are moved together and merged in momentum space. Therefore, additional symmetries are required to protect the Dirac point. In general, distinct two-dimensional representations for the doubly degenerate bands lead to potential materials for Dirac semimetals [118]. As an example, the material Cd_3As_2 [10] is protected by an additional fourfold rotational symmetry [118]. In the material Na_3Bi the two touching bands belong to different irreducible representations due to threefold rotational symmetry [119].

While the single Weyl point cannot be gapped out perturbatively, Dirac semimetals are less robust against perturbations since there are several 4×4 matrices which can produce a gap in the spectrum Eq. (1.23).

Since the Weyl and Dirac semimetals share the 3D Dirac-like dispersion, they host naturally many of the same characteristics. On surfaces, Dirac semimetals have Fermi arcs touching each other at the Dirac points [118, 119] which is in contrast to the disconnected Fermi arcs in Weyl semimetals. Specifically, the very peculiar features of Weyl semimetals in finite magnetic fields of course apply all to Dirac semimetals due to the breaking of time-reversal symmetry. Therefore, the scaling of the transversal magnetoresistance, as theoretically discussed in Ch. 4, hold also for Dirac semimetals meaning that the term Weyl semimetal is used in a broader sense including also the degenerate case of Dirac semimetals.

1.2.3 Experimentally observed transversal magnetoresistance

In this section, we report on the experimental findings of a huge positive linear transversal magnetoresistance (TMR) in Dirac and Weyl semimetals as found in several experiments [3–9]. The term transversal magnetoresistance in this context means that the magnetic field is applied perpendicular to the applied electrical field. The linear and non-saturating TMR is one of the most spectacular findings in Weyl and Dirac semimetals. With a magnitude of $10^4 - 10^6\%$, the TMR in Weyl and Dirac semimetals offers a new possibility to build magnetoresistance devices. A magnetoresistance of comparable magnitudes was previously only observed in complex structures.[2] The experimental finding of the TMR in the Weyl semimetal NbP [5] is shown in Fig. 1.4. In this figure, the non-saturating, strong, and linear TMR is clearly seen. The figure highlights the appearance of Shubnikov-de Haas oscillations in the limit of intermediate magnetic fields while above a magnetic field of around 30T, the oscillations stop. Thus, this figure provides a nice read-out for the starting point of the ultra quantum limit, which is present in strongest magnetic fields where only the zeroth Landau level contributes to transport. Moreover, Fig. 1.4 illustrates the temperature dependence of the magnetoresistance showing the expected decrease of the magnitude of the TMR with increasing temperature.

Another example for the strong linear magnetoresistance is given in Fig. 1.5 where the resistivity in the Dirac semimetal Cd_3As_2 in transversal magnetic fields obtained in Ref. [3] is depicted. The figure

[2] An example for such a complex structure with an observed magnetoresistance of the order of $10^3\%$ is also part of the thesis (discussed in Sec. 1.4 and Chs. 5 and 6). The structure consists of a CNT with side-attached single-molecule magnets.

shows the linear evolving resistivity in dependence of magnetic field superimposed be Shubnikov-de Haas oscillations. Moreover, it is shown that the linear resistivity persist up to room-temperature, while the temperature dependence in zero field is clearly seen in this data.

We can conclude that both Weyl and Dirac semimetals show a strong linear TMR up to highest magnetic fields superimposed by Shubnikov-de Haas oscillations in moderate fields.

Theoretically, a linear magnetoresistance was obtained in Ref. [82] for a 3D Weyl Hamiltonian in the ultra quantum limit, where only the zeroth Landau level contributes to transport. The calculation of this linear TMR is based on scattering off strongly screened Coulomb impurities. With the large magnitude of the TMR in the model of Ref. [82], the model nicely explains the experimentally observed TMR in Weyl semimetals in the ultra quantum limit. However, the linear TMR superimposed by Shubnikov-de Haas oscillations in moderate magnetic fields is not covered in this model. Another theoretical model of a linear TMR involves inhomogeneous semiconductors with macroscopic disorder and relies therefore on a low mobility of the system, cf. Ref. [120]. This is in strong contrast to the high mobility found experimentally for Weyl semimetals.

Motivated by the lack of a theoretical explanation for the strong, linear TMR away from the ultra quantum limit, this thesis proposes a model for an increasing TMR superimposed by strong Shubnikov-de Haas oscillations, Ch. 4. The model includes both pointlike impurities and strongly screened Coulomb impurities emphasizing the importance of Coulomb impurities for the linear TMR in the ultra quantum limit as obtained in Ref. [82].

1.3 Carbon nanotubes

Carbon nanotubes (CNT) are exceptional materials and of particular importance for the fabrication of 1D quantum devices. In this section however, we focus on the structure of CNT and the related band structures as discussed for example in Ref. [76]

First, we identify the different types of CNTs. Due to the infinite amount of ways to roll up the graphene sheet, there are many different carbon nanotube structures. The chiral vector $\mathbf{C}$ defines the lattice sites of the graphene sheet which superpose in the rolled up nanotube cf. Fig. 1.6. Thus, the vector is constructed via the basis vectors of graphene $\mathbf{a}_1$, $\mathbf{a}_2$, reading $\mathbf{C} = n\mathbf{a}_1 + m\mathbf{a}_2$ where n and m are integer numbers conventionally taken in the range $-n/2 < m < n$ to avoid labeling one structure in two different ways. Another way to identify the type of carbon nanotube is to consider the chiral angle θ and the diameter $D = a\sqrt{m^2 + n^2 + mn}/\pi$. The structures are classified in three different categories of carbon nanotubes: (i) the zig-zag structures for $m = 0$ or $\theta = 0$, (ii) the armchair structures for $m = n$ or $\theta = \pi/6$, and (iii) the chiral structures for all other combinations of n and m or $0 < |\theta| < \pi/6$. The different types of carbon nanotubes are visualized in Fig. 1.6. The zig-zag and the armchair structures are named due to the arrangement of atoms at the edge of the nanotube. While zig-zag and armchair nanotubes are inversion symmetric, chiral CNTs lack inversion symmetry.

As build of a sheet of graphene, the band structure of CNT can be derived from the electronic band structure of graphene. However, the effect of rolling up the graphene sheet on the band structure can be drastic and might lead to the introduction of a band gap. This was first derived in Ref. [121, 122]. Mathematically, this is shown by transforming the Cartesian coordinates of momentum of graphene into rotated coordinates of the CNT via

$$\begin{pmatrix} p_x \\ p_y \end{pmatrix} = \begin{pmatrix} \cos(\varphi) & \sin(\varphi) \\ -\sin(\varphi) & \cos(\varphi) \end{pmatrix} \begin{pmatrix} p_\perp \\ p_\parallel \end{pmatrix} \tag{1.24}$$

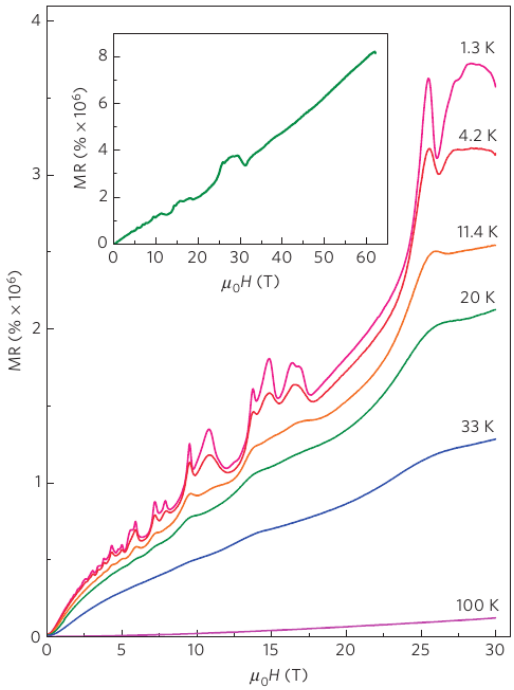

[Reprinted with permission from Springer Nature: Nature Physics **11** (8), 645649, Extremely large magnetoresistance and ultrahigh mobility in the topological Weyl semimetal candidate NbP, Chandra Shekhar, Ajaya K. Nayak, Yan Sun, Marcus Schmidt, Michael Nicklas et al., copyright 2015]

Figure 1.4: Transversal magnetoresistance of the Weyl semimetal NbP as extracted from Ref. [5] for different temperatures. The inset of the figure shows the magnetoresistance up to highest magnetic fields at a temperature of 1.5K where the physics of the ultra quantum limit is clearly seen for magnetic fields above 30T.

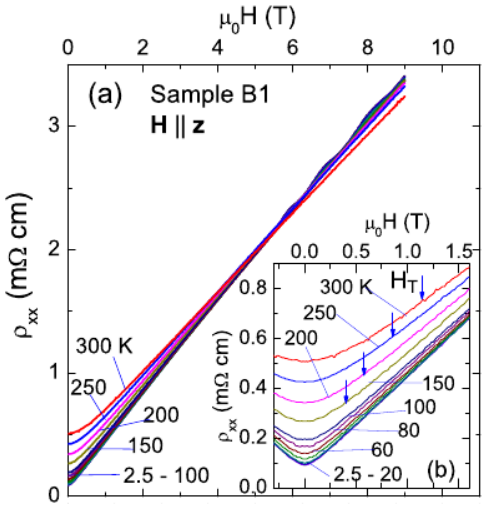

[Reprinted with permission from Springer Nature: Nature Materials **14**, 280284, Ultrahigh mobility and giant magnetoresistance in the Dirac semimetal Cd_3As_2, Tian Liang, Quinn Gibson, Mazhar N. Ali, Minhao Liu, R. J. Cava, N. P. Ong, copyright 2015]

Figure 1.5: Resistivity of the Dirac semimetal Cd_3As_2 as extracted from Ref. [3] in transversal magnetic fields for different temperatures. The inset figure shows the magnetic field at which the linear magnetoresistivity is observed in dependence of temperature.

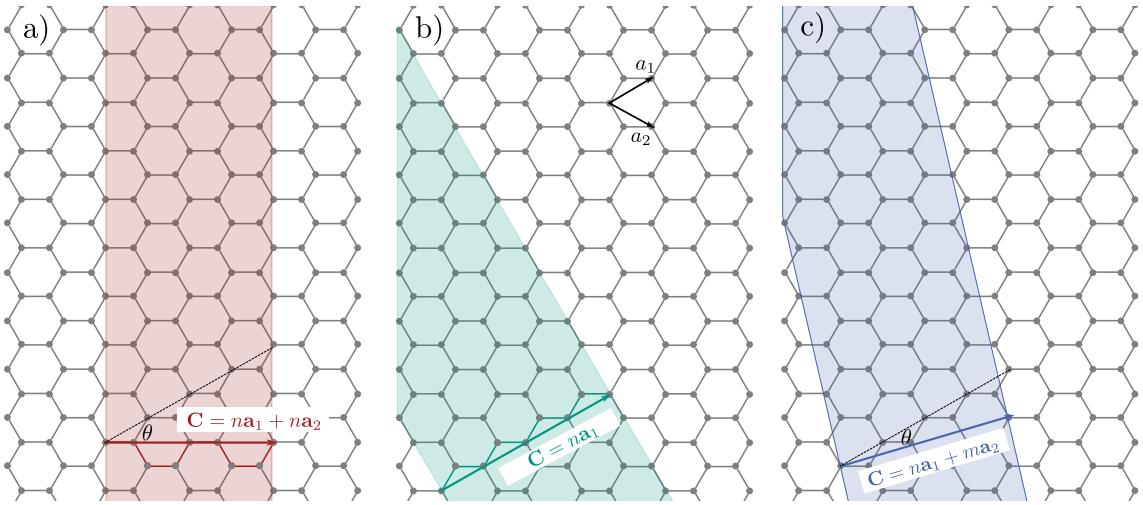

Figure 1.6: Atomic structure of CNTs. In panel a) an example of an armchair nanotube is shown, panel b) depicts a zig-zag nanotube and c) illustrates a chiral CNT. In all three cases, the chiral vector $\mathbf{C}$ and the chiral angle θ are shown. The colored parts correspond the surface of the rolled up nanotube. The basis vectors $\mathbf{a}_1$ and $\mathbf{a}_2$ defined in part b) apply to all panels. In panel a) and b) the edge of the nanotube is marked explaining the names of the structures.

with $\varphi = \pi/6 - \theta$ being the angle between $\mathbf{C}$ and x-direction. In these coordinates, the Hamiltonian of graphene, Eq. (1.13) transforms into

$$\mathcal{H}_{\mathrm{CNT}} = v_F(\tau p_\perp \sigma_x + p_\parallel \sigma_y) \tag{1.25}$$

for the CNT where τ is the valley index. The eigenstates of the Hamiltonian are $\varepsilon(p_\perp, p_\parallel) = \pm\sqrt{p_\perp^2 + p_\parallel^2}$. Clearly, the wave functions of the nanotube have to fulfill periodic boundary conditions, $\Psi_{\mathbf{K}+\mathbf{p}}(\mathbf{r}) = \Psi_{\mathbf{K}+\mathbf{p}}(\mathbf{r}+\mathbf{C})$, resulting in

$$e^{i(\mathbf{K}+\mathbf{p})\cdot\mathbf{C}} = 1. \tag{1.26}$$

A gapless spectrum is present under the condition $p_\perp = 0$. The corresponding condition is $\mathbf{K}\cdot\mathbf{C} = 2\pi M$ which is equivalent to $n - m = 3M$ with M being an integer. Therefore, for arbitrary chiral indices, one third of the nanotubes is metallic. In particular, all armchair CNT are metallic, while the chiral and zig-zag CNT can show both types of the behavior.

The spectrum for the semiconducting CNTs is

$$\varepsilon^{\pm}(p_\parallel) = \pm\sqrt{v_F^2 p_\parallel^2 + E_G^2/4}, \tag{1.27}$$

with a bandgap $E_G = 2v_F|\Delta p_\perp| = 4v_F/(3D)$ dependent on the diameter. The spectra for both metallic and semiconducting CNTs is illustrated in Fig. 1.6 showing also how the 1D mode disperses in the Dirac cone.

The effective mass from the curvature of the spectrum for low energy ($\varepsilon^{\pm}(p_\parallel) < E_G$) is

$$m_{\mathrm{eff}} = \left(\frac{d^2E}{dp_\parallel^2}\right)^{-1} = \frac{E_G}{2v_F^2}. \tag{1.28}$$

For a typical bandgap of 100meV and a Fermi velocity of $8 \cdot 10^5$ m/s, the effective mass is $\sim 0.014 m_e$ (m_e is electron mass) which is much smaller than in many conventional semiconductors. A small effective mass leads to a large level spacing in quantum dots which is preferred in experiment.

Carbon nanotubes in rotated coordinates are described by the 2D massless Dirac Hamiltonian, cf. Eq. (1.25). Due to the boundary conditions of the wave functions, the nanotubes are strictly speaking not a Dirac material. However, the spectrum for the metallic tubes corresponds to the spectrum of the 1D massless Dirac equation while the semiconducting nanotube has the spectrum of the 1D massive Dirac equation.

Due to their high mobility, large current carrying capacities, the dominance of interaction effects over disorder effects, and the long mean-free path, CNTs are a perfect material to study the physics in one spacial dimension, cf. several reviews [76, 123, 124]. Basic electronic devices in nanotechnology are CNTs contacted to metallic leads. In addition to the natural 1D confinement of the electrons in the nanotube, such quantum transport experiments add a further longitudinal confinement by introducing tunnel barriers. The tunnel barriers can be introduced by the contact of the CNT with the leads. Electrons trapped within the barriers build energy levels and form a so-called quantum dot (QD). The properties of the 1D CNT are then reduced to a zero dimensional QD. In the following section, we will consider such a QD system involving a CNT with side-attached single-molecule magnets where a huge spin valve effect is experimentally observed.

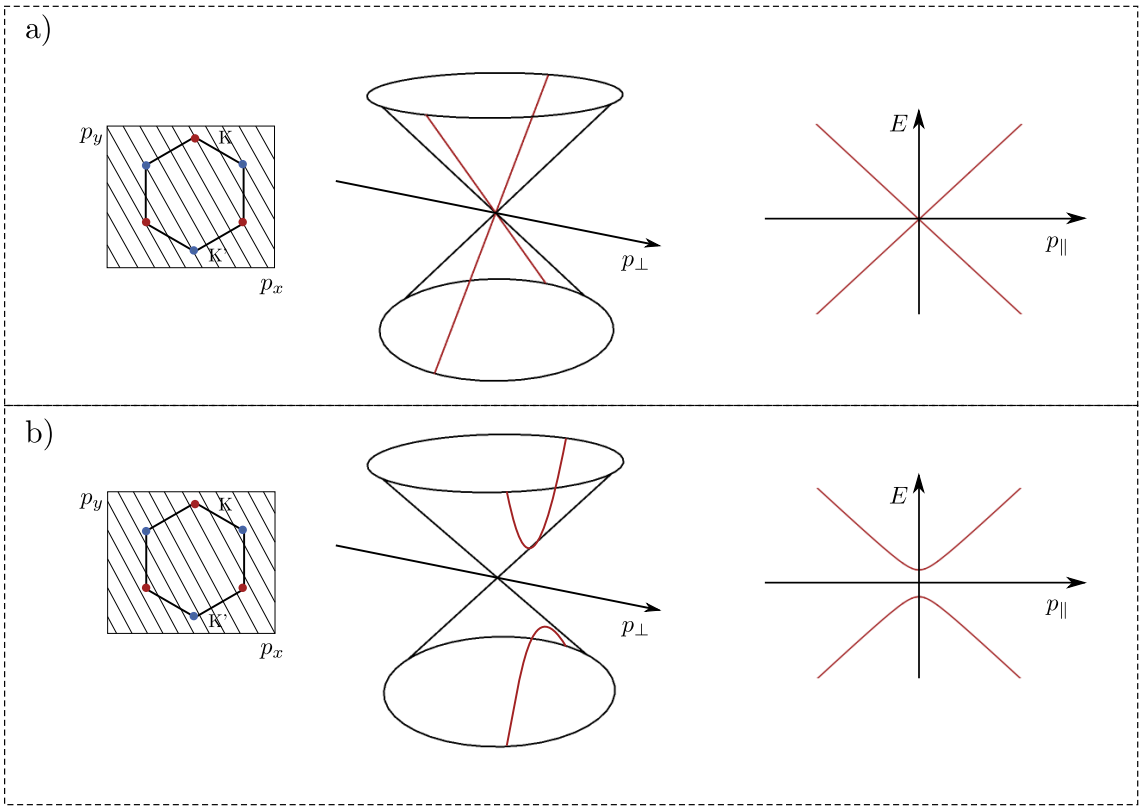

Figure 1.7: Spectrum of carbon nanotubes. Panel a) considers the metallic CNT while panel b) is devoted to the semiconducting case. In both panels on the left, the modes of the wave functions are shown schematically crossing the points K and K' in the metallic case. In the middle of both panels the dispersion relation for a 1D mode (red line) on a Dirac cone is shown. On the right, the resulting spectrum for the 1D mode is depicted for both panels.

1.4 Carbon nanotubes with side-attached single-molecule magnets

Carbon nanotubes are a suitable material to build quantum dots (QDs). This allows to study the electrical current applied to a single carbon nanotube. The QDs are built by contacting the CNT to metallic source and drain electrodes leading to an additional longitudinal confinement of the 1D electrons of the nanotube. The confinement manifest itself by the appearance of barriers introduced by the contact between the metallic lead and the nanotube. The zero dimensional QD has energy levels with a level spacing dependent on the length of the CNT. In such transport structures, a gate is conveniently coupled capacitively to the CNT to allow the electrostatic potential to be tuned. An essential part of this thesis is devoted to a theoretical model of such a QD device built with a single-walled carbon nanotube where single-molecule magnets are side-attached. The CNT in that case serves as a conducting channel. The model was designed to explain the spin-valve effect as observed in experiment [58, 78]. In this section, we introduce the experimental setup, the structure of single-molecule magnets (SMM), and the important features of this system as obtained in experiment.

1.4.1 Structure of single-molecule magnets

In general, single-molecule magnets (SMM) are composed by an inner magnetic core and a surrounding shell of organic ligands [50, 67]. The organic ligands can be designed to couple the SMMs into junctions or on surfaces [68, 70–72]. Magnetic interactions of the core ions can be strengthened by delocalized bonds which are often part of the structure in SMMs and enhance their conducting properties. The variety of shapes and sizes of SMMs allows to study and apply their features in various setups. Furthermore, SMMs permit both a selective substitution of the ligands to change the coupling to the environment [73] and an exchange of the magnetic ion to alter the magnetic properties [52]. These properties manifest their great potential for application in several magnetic devices.

The particular single-molecule magnet of consideration in the thesis is the $TbPc_2$ double decker schematically depicted in Fig. 1.8a). The magnetic features of the $TbPc_2$ molecule appear with a terbium (III) ion with $4f^8$ electrons in the inner shell in the center of the double decker structure. The electrons have a total angular momentum 3 and a total spin 3 resulting in a total angular momentum $J = 6$ due to strong spin-orbit coupling. The easy axis of the structure is determined by the organic ligand. Due to the interaction [125] with the two phthalocyanine (Pc) ligands, a strong magnetic anisotropy allows only two projections on the easy axis $J_z = \pm 6$ for the magnetic moment of terbium at low temperatures, Fig. 1.8b).

Another property of terbium is that its nuclear spin is $3/2$, leading to a hyperfine interaction with electrons of the inner shell. The read-out of the nuclear spin of the SMM is effectively performed by conductance measurements [125, 126] in structures with $TbPc_2$ directly coupled to the leads. By applying a gate voltage, the hyperfine interaction can be manipulated [127]. Furthermore, spin-phonon coupling can change the protection of the terbium spin J [128]. Another magnetic property is that these molecules show a quantum Einstein-de Haas effect [129]. The phthalocyanine ligands in $TbPc_2$ have an electronic state with spin $S = 1/2$ [66]. Strong Coulomb interaction between particles with opposite spins [62] allows only the occupation of one spin orientation [130]. The localized spin S is coupled via exchange interaction [127] to the terbium spin J of $4f$ electrons.

It is relevant to the setup that the magnetic features of $TbPc_2$ remain intact when the magnets are in contact with the sp^2 carbon materials as CNT [131] and graphene [132].

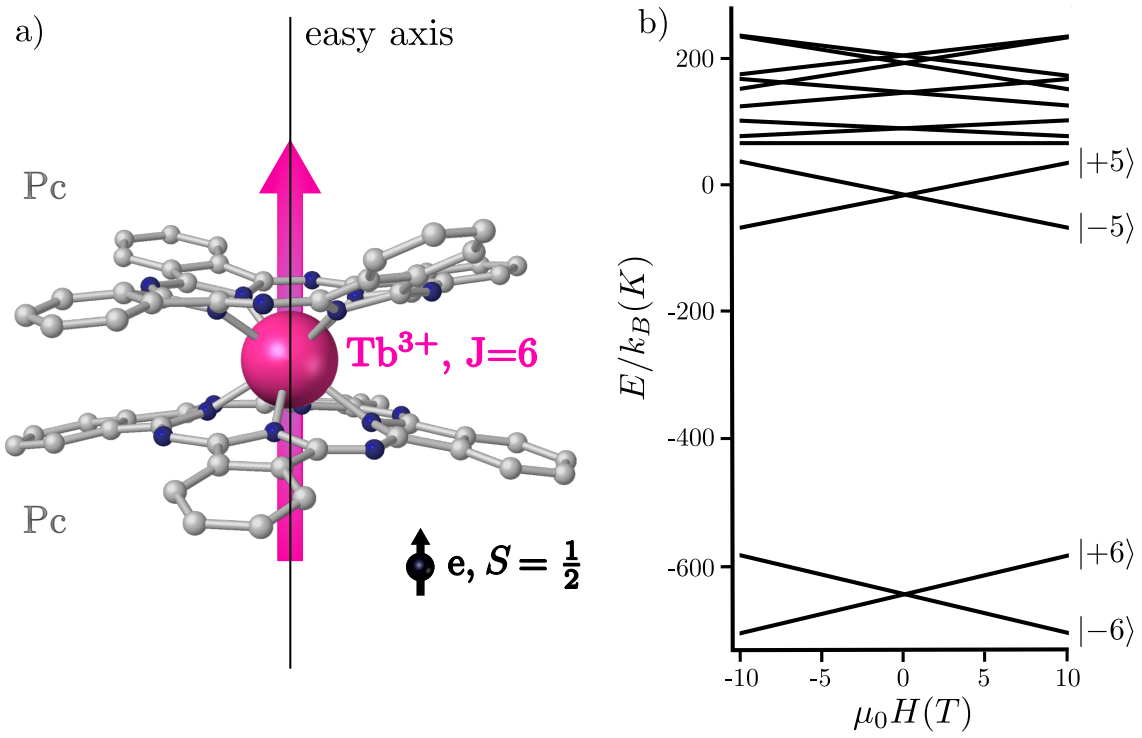

[Reprinted figure with permission from I. V. Krainov, J. Klier, A. P. Dmitriev, S. Klyatskaya, M. Ruben, W. Wernsdorfer, and I. V. Gornyi, ACS Nano, 2017 **11** (7), 6868-6880. Copyright 2017 by the American Chemical Society. DOI: 10.1021/acsnano.7b02014]

Figure 1.8: Schematic structure and energy dispersion of the single molecule magnet $TbPc_2$. Panel a) illustrates the schematic structure of the single molecule magnet $TbPc_2$. The spins of the ion ($J = 6$) and the "resident" electron on the ligands ($S = 1/2$) are shown by the pink and black arrows. In panel b), the energy diagram of $TbPc_2$ in external magnetic field applied in the direction of the easy axis is shown. The ground state has two spin projections ± 6.

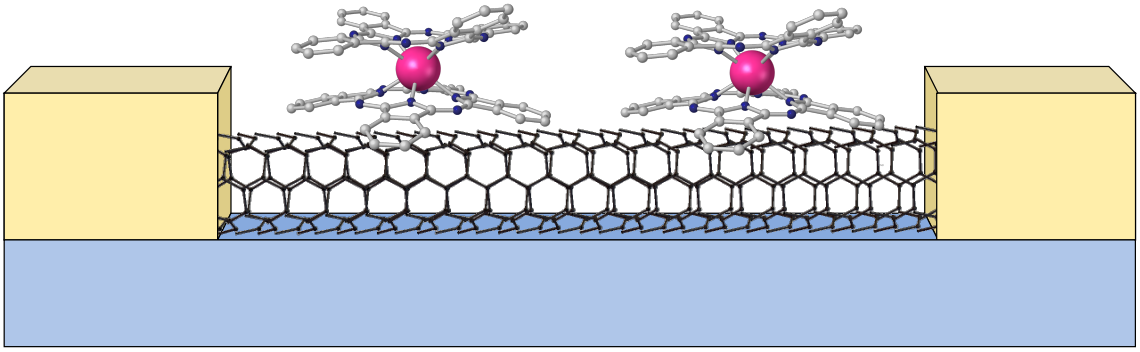

Figure 1.9: Schematic experimental setup for a suspended carbon nanotube tunnel-coupled to the leads with side-attached single molecule magnets in a minimal model of two molecules.

1.4.2 Experimental results

After the discussion of the features of SMMs, we outline how these properties manifest in transport measurements through a CNT. In particular, we will report about a giant magnetoresistance effect for linear transport through the CNT and discuss the differential conductance map in the regime of Coulomb blockade based on the data presented in Ref. [94].

A schematic picture of the experimental setup is shown in Fig. 1.9 with a suspended CNT tunnel-coupled to metallic leads. The carbon nanotube is diluted with a few SMMs. The average number of SMMs was estimated as four [132] in the source drain segment of about 300 nm. However, the theoretical model is designed for a minimal number of two molecules as explained in Ch. 5. The electronic coupling of the terbium spin is mediated by the $S = 1/2$ state of the phthalocyanine ligands via supramolecular π-π interaction with the unpaired π electrons of the nanotube.

A typical conductance measurement is performed by varying the magnetic field in time, as presented in Fig. 1.10 where the gate voltage is fixed at $V_g = -4.63$ V and the source-drain voltage vanishes in linear response, $V_{sd} \to 0$. The magnetic field is swept with a rate of 70 mT·s^{-1}. The blue and red curve depict the conductance for increasing magnetic field B from negative to positive and vice versa, respectively.

The asymmetry of the conductance jumps with respect to $B \to -B$ can be explained by the finite sweep rate. As emphasized in Fig. 1.8b), the ground state of the Tb spin state at negative magnetic fields is $J_z = +6$. The molecular spin resides in this on the branch of $J_z = +6$ also for positive magnetic field until the spin flipping relaxation process takes place if the sweep of magnetic field is sufficiently fast. The relaxation process mainly originates from the spin-phonon coupling in $TbPc_2$ molecule [128]. A relatively low sweep rate however results in a quantum tunneling magnetization by the Landau-Zener mechanism [77].

The maps of the differential conductance, obtained by changing the source-drain voltage V_{sd} at fixed gate voltage V_g and then varying V_g, in units of conductance quantum $\mathcal{G}_0 = e^2/h$ as a function of source-drain and gate voltage are presented for zero magnetic field and for the static magnetic field, $B = 1$T in Fig. 1.11a) and b), respectively. The appearance of Coulomb diamonds in these maps are a signature of Coulomb blockade caused by strong electron-electron interaction between electrons in CNT. The charging energy in the CNT is estimated as $E_C \approx 20$ meV by extrapolating the Coulomb diamonds.

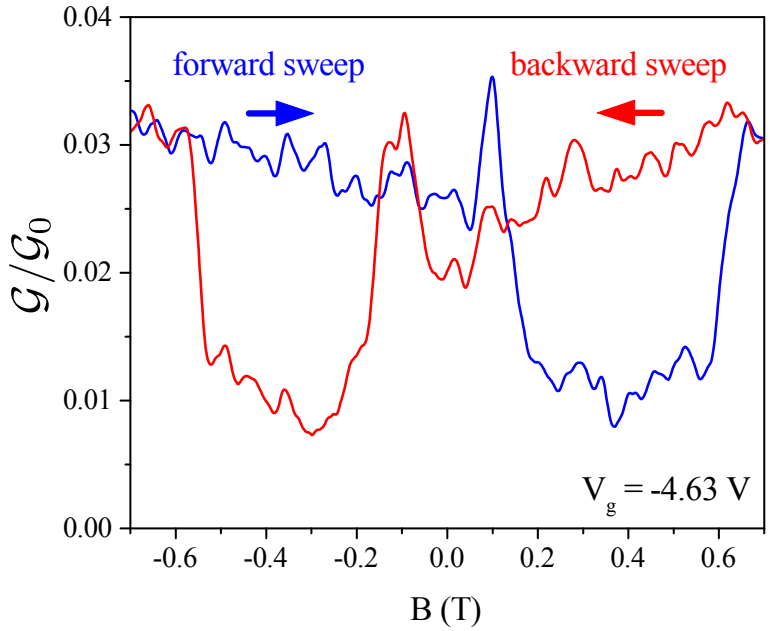

[Reprinted figure with permission from I. V. Krainov, J. Klier, A. P. Dmitriev, S. Klyatskaya, M. Ruben, W. Wernsdorfer, and I. V. Gornyi, ACS Nano, 2017 **11** (7), 6868-6880. Copyright 2017 by the American Chemical Society. DOI: 10.1021/acsnano.7b02014]

Figure 1.10: Linear-response conductance at fixed gate voltage $V_g = -4.63\,\mathrm{V}$ in units of quantum conductance $\mathcal{G}_0$ as a function of dynamically swept magnetic field (sweep rate: 0.07 T/s) with the blue curve corresponding to forward sweep from -0.7 T to 0.7 T and the red curve to backward sweep.

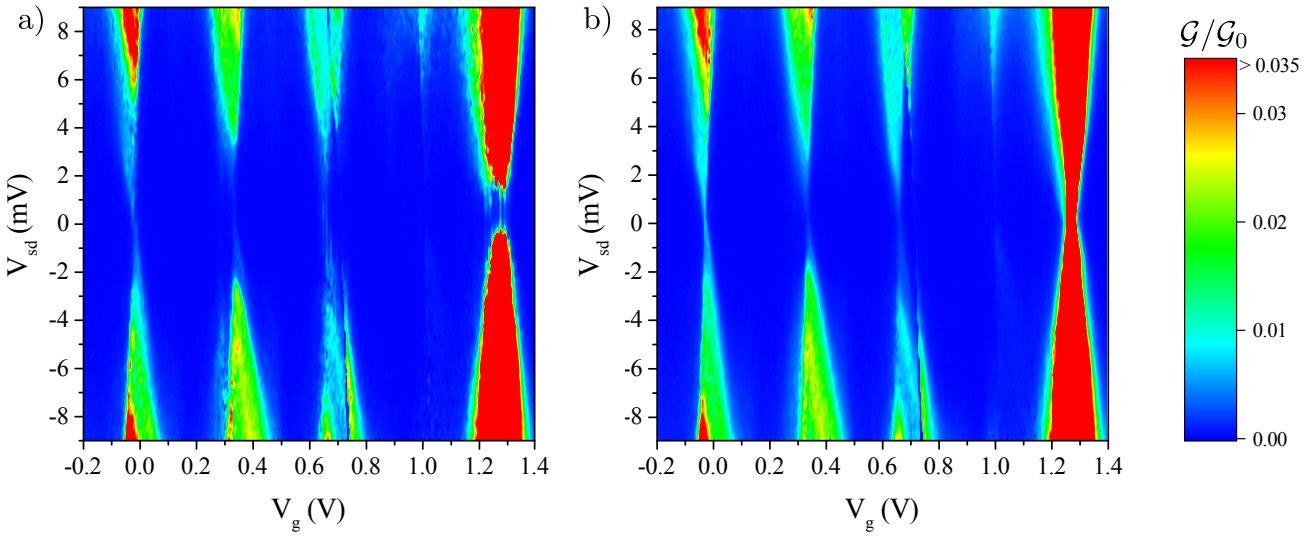

[Reprinted figure with permission from I. V. Krainov, J. Klier, A. P. Dmitriev, S. Klyatskaya, M. Ruben, W. Wernsdorfer, and I. V. Gornyi, ACS Nano, 2017 **11** (7), 6868-6880. Copyright 2017 by the American Chemical Society. DOI: 10.1021/acsnano.7b02014]

Figure 1.11: Experimentally obtained Coulomb blockade maps in the plane of source-drain voltage V_{sd} and gate voltage V_g a) for zero magnetic field and b) in a static magnetic field of $B = 1T$. The differential conductance $\mathcal{G} = dI/dV_{sd}$ is given in units of quantum conductance $\mathcal{G}_0$.

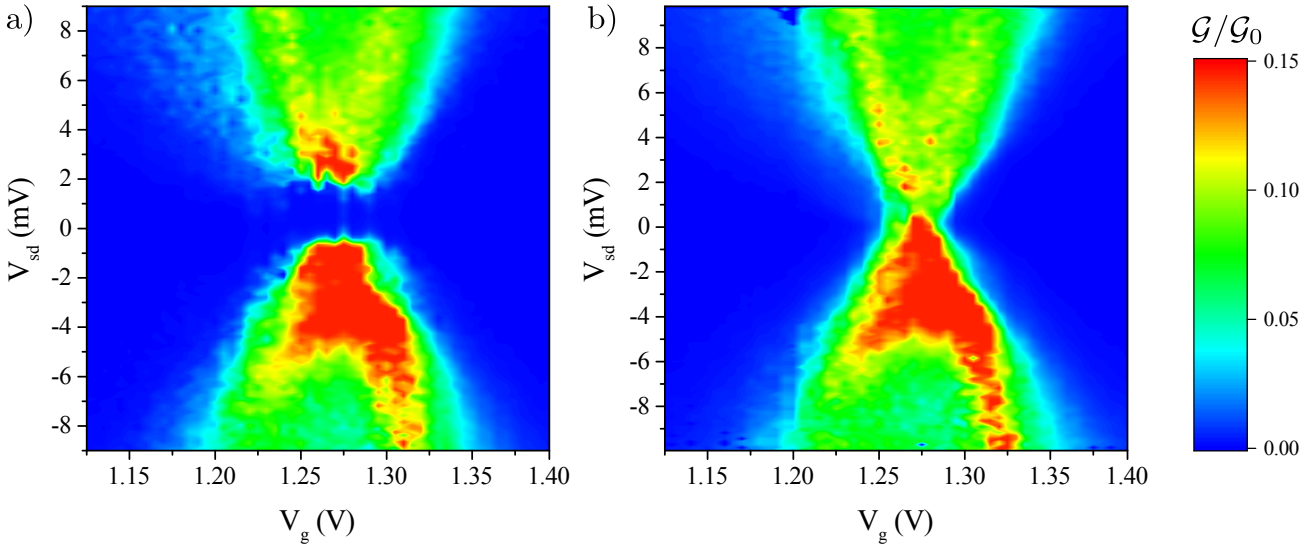

[Reprinted figure with permission from I. V. Krainov, J. Klier, A. P. Dmitriev, S. Klyatskaya, M. Ruben, W. Wernsdorfer, and I. V. Gornyi, ACS Nano, 2017 **11** (7), 6868-6880. Copyright 2017 by the American Chemical Society. DOI: 10.1021/acsnano.7b02014]

Figure 1.12: Zoom into the experimentally obtained Coulomb blockade map around $V_g = 1.25$, at zero magnetic field in panel a) and at $B = 1\,\mathrm{T}$ in panel b). The differential conductance is given in units of $\mathcal{G}_0$.

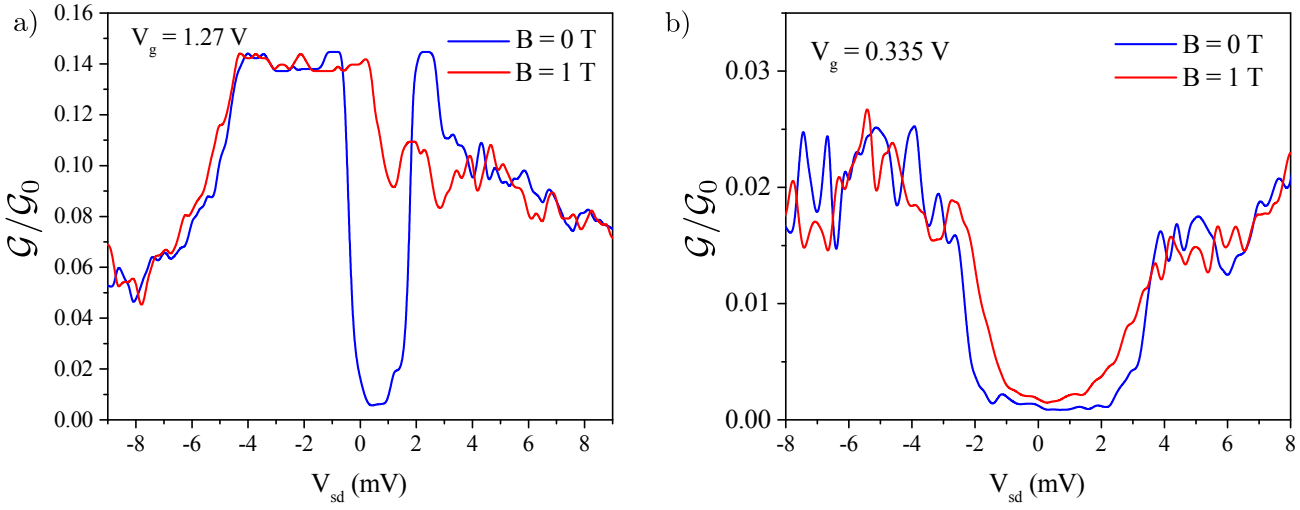

[Reprinted figure with permission from I. V. Krainov, J. Klier, A. P. Dmitriev, S. Klyatskaya, M. Ruben, W. Wernsdorfer, and I. V. Gornyi, ACS Nano, 2017 **11** (7), 6868-6880. Copyright 2017 by the American Chemical Society. DOI: 10.1021/acsnano.7b02014]

Figure 1.13: Conductance as a function of the source-drain voltage V_{sd} at fixed gate voltage with $V_g = 1.27\,\mathrm{V}$ in panel a) and $V_g = 0.335\,\mathrm{V}$ in panel b) in units of $\mathcal{G}_0$. In both panels, the blue curves correspond to $B = 0$ and red curves to $B = 1\,\mathrm{T}$.

Importantly, the broadening of the single-particle levels in the CNT is relatively strong which indicates the observation of a rather homogeneous conduction region. Typically, the conductance map of CNT shows clearly resolved levels in the Coulomb diamonds, cf. Ref. [133].

In contrast to conventional Coulomb blockade maps in quantum dots [134], where the linear conductance is finite at resonant values of V_g for all values of V_{sd}, the conductance of the considered quantum dot is suppressed at $V_{sd} = 0$ for all values of V_g at zero magnetic field, Fig. 1.11a). This transport gap is estimated as $\delta V_{sd} \sim 1 \div 2$ meV and was first observed in Ref. [58]. For strong magnetic fields however, the transport gap in the obtained Coulomb blockade map, cf. Fig. 1.11 b), is closed at certain gate voltages. A zoom conductance map in the Coulomb blockade regime is shown at gate voltages around $V_g \sim 1.25$ V in Fig. 1.12a) and b) for zero magnetic field and $B = 1$ T, respectively, where this feature can be seen pronounced.

To quantify the observed magnetoresistance effect, we present the conductance as a function of the source-drain voltage at fixed gate voltage $V_g = 1.27$ V with and without static magnetic field in Fig. 1.13 a). The GMR effect is of the order of 10^3%: the conductance drops from $\mathcal{G}(B = 1\,\mathrm{T}) = 0.14\,\mathcal{G}_0$ to $\mathcal{G}(B = 0) = 0.006\,\mathcal{G}_0$. Moreover, the low-conductance window is shifted from $V_{sd} = 0$ to the right by $0.5 \div 1$ meV.

Another important experimental feature is that away from the observed GMR for $V_g = 1.25 \div 1.3\,\mathrm{V}$, there is a weaker spin-valve effect observed for other values of the gate voltage in Figs. 1.11a) and b). Let us for example discuss the value $V_g = 0.335\,\mathrm{V}$. The corresponding conductance in dependence on source-drain voltage is depicted in Fig. 1.13b) for zero magnetic field and $B = 1$T. Around zero V_{sd}, the linear conductance is in the same order as the zero field conductance in Fig. 1.13a) for both zero and finite magnetic field, but still with a lower zero field conductance than in finite field, cf. Fig. 1.13

b). Let us further emphasize that the region of suppressed conductance in Fig. 1.13b) is narrower for $B = 1$ T. Thus, we can conclude that the experimentally observed magnetoresistance is dependent on the gate voltage and can be referred to as a gate-controlled supramolecular spin-valve effect.

This gate-controlled supramolecular spin-valve effect was already discussed in Ref. [58] where specifically in the conductance map of Figs. 2a and 2b of Ref. [58], the gate dependence of the spin-valve effect is clearly seen. At gate voltages $V_g = -4.6$ V and $V_g = 2.6$ V, the transport gap closes in strong magnetic field, whereas for $V_g = -4.4$ V, a weak spin-valve effect was observed where the suppressed conductance in the Coulomb blockade map apparently persists in strong B. In Ch. 6, an explanation of the origin of GMR and the gate dependence of the molecular spin-valve effect, as established in Ref. [94], will be presented.

Chapter 2

2 Methods in transport theory

In this chapter, we discuss methods of transport theory which are relevant to this thesis. One important concept is the consideration of disorder in a system. Disorder manifests itself in the scattering of electrons off impurities which are considered to be randomly distributed and non-magnetic. An elegant way to sum up the most important contributions is the self-consistent Born approximation (SCBA). We will discuss this approach and its limitations in the following, Sec. 2.1. Disorder can be characterized by a length scale that determines the average distance which an electron travel can without being scattered, the so-called mean free path l. In transport theory, the response of a system to electrical fields, the conductivity or conductance, is an often considered quantity. The difference between conductance and conductivity is of particular importance. The intrinsic properties of a system are described by the conductivity while the conductance is a sample specific quantity related to the size of the system. Thus, an infinite or large system, compared to other length scales as for example the mean free path, can be studied within Kubo formalism for the conductivity. Kubo formalism describes the linear-response of the system to electrical fields and can be also applied to calculate the Hall conductivity as described in Sec. 2.2. For materials with a homogeneous conductivity, the conductivity and the conductance can be directly related to each other. However, in mesoscopic systems, the system size is typically smaller than the length scale associated with the equilibration energy. Thus, the local description is not applicable. For such finite systems, it is convenient to use the Landauer-Büttiker formalism to calculate the conductance as explained in Sec. 2.3. The Landauer-Büttiker formalism is an application of Kubo formalism and is tailored for mesoscopic systems.

We start now with a description of the theory of impurity scattering in electronic systems, Sec. 2.1. Then, we discuss the Kubo formalism for the conductivity and the Kubo-Streda formula for the Hall conductivity, Sec. 2.2. Finally, we consider the Landauer-Büttiker formalism for the conductance in mesoscopic systems, Sec. 2.3.

2.1 Disorder

This section is devoted to a definition of disorder as it is considered in condensed matter physics. Disorder manifests itself in the scattering of electrons off impurities. It is assumed that the different non-magnetic and randomly distributed impurities share the same disorder potential resulting in the

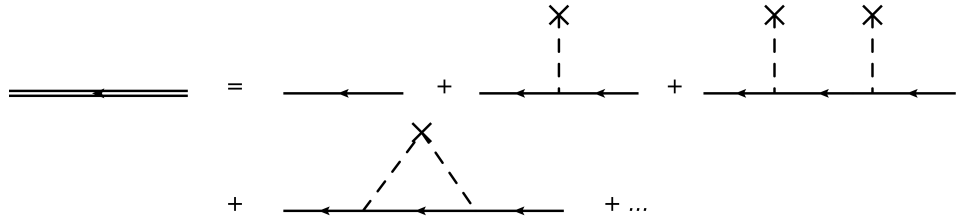

Figure 2.1: Perturbative expansion of the full Green's function in a disorder potential up to second order. Each dashed line corresponds to scattering of a single impurity. The last diagram corresponds to double scattering on the same impurity.

following disorder potential for one particular configuration:

$$V_{\mathrm{dis}}(\mathbf{r}) = \sum_{i=1}^{\mathcal{N}_{\mathrm{imp}}} V_{\mathrm{imp}}\left(\mathbf{r} - \mathbf{R}_i\right). \tag{2.1}$$

Here, the parameter $\mathcal{N}_{\mathrm{imp}}$ is the number of impurities and the vectors $\mathbf{R}_i$ are the positions of the impurities. We treat the Hamiltonian of disorder, defined via

$$\mathcal{H}_{\mathrm{dis}} = \int d\mathbf{r}\Psi^{\dagger}(\mathbf{r})V_{\mathrm{dis}}(\mathbf{r})\Psi(\mathbf{r}), \tag{2.2}$$

as a perturbation to the clean Hamiltonian $\mathcal{H}_0$. This diagrammatic approach is described for example in Ref. [135]. In order to perform the perturbation theory, we use the Green's function of the system. The full Green's function is defined as the resolvent operator

$$\left(\varepsilon - \hat{\mathcal{H}}_0 - \hat{\mathcal{H}}_{\mathrm{dis}}\right)\hat{G} = \hat{1}. \tag{2.3}$$

Within this perturbative approach, the full Green's function is determined by the expansion of the single particle Green's function in powers of the impurity potential. The full Green's function sums up all possibilities for an electron to propagate through the system upon undergoing various scattering processes. The perturbative approach leads to a full Green's function which depends on the positions of impurities. However, for a macroscopic sample, the specific microscopic distribution of impurities will be usually irrelevant since the system shows self-averaging. This is valid if the dephasing length is sufficiently short. The behavior of the system is characterized by an average over an ensemble of macroscopically identical subsystems. The average over all possible impurity realizations of $\mathcal{N}_{\mathrm{imp}}$ randomly distributed impurities of a arbitrary function F is performed as

$$\left\langle F\right\rangle_{\mathrm{imp}} = \frac{1}{V}\int \prod_{i}^{\mathcal{N}_{\mathrm{imp}}} d\mathbf{R}_i F(\mathbf{R}_1, \mathbf{R}_2, ..., \mathbf{R}_N). \tag{2.4}$$

Averaging over impurity configurations restores translation invariance and the Green's function does not depend on the position of the impurities.

We first consider the lowest order terms in momentum representation and transform the resulting terms to position representation in the following. The lowest order expansions of the Green's function

are depicted in Fig. 2.1 and calculated in the following. The first-order term of the disorder-averaged Green's function (the second diagram in Fig. 2.1) in momentum representation reads

$$\left\langle G_1(\mathbf{p},\varepsilon)\right\rangle_{\mathrm{imp}} = N_{\mathrm{imp}} V_{\mathrm{imp}}(\mathbf{p}=\mathbf{0}) \left[G_0(\mathbf{p},\varepsilon)\right]^2, \tag{2.5}$$

where N_{imp} is the concentration of impurities. The first-order term is constant and hence only shifts the chemical potential. Correspondingly, all diagrams with only single scattering processes at each impurity are proportional to $(V_{\mathrm{imp}}(\mathbf{p}=\mathbf{0}))^n$, where n is the number of impurity lines corresponding to single scattering off one impurity. Thus, all diagrams with only single scattering processes shift the chemical potential. We can include this shift if we absorb $N_{\mathrm{imp}}V_{\mathrm{imp}}$ and the corresponding higher order single impurity lines in the renormalized chemical potential.

The first nontrivial diagram corresponds to double scattering off the same impurity which is the fourth diagram in Fig. 2.1. The contribution to the Green's function in momentum representation due to scattering off the same impurity is

$$\left\langle G_2(\mathbf{p},\varepsilon)\right\rangle_{\mathrm{imp}}^{i=j} = N_{\mathrm{imp}} \left[G_0(\mathbf{p},\varepsilon)\right]^2 \frac{1}{V} \sum_{\mathbf{p}'} \left|V_{\mathrm{imp}}(\mathbf{p}-\mathbf{p}')\right|^2 G_0(\mathbf{p}',\varepsilon), \tag{2.6}$$

the so-called Born diagram.

For the analysis in position representation, we neglect multiple scattering off one impurity as will be justified later. Hence, for $\left\langle V(\mathbf{r})\right\rangle = 0$, the impurity average corresponds to pairwise coupling of the impurity potential. By pairwise coupling of the impurity potential, we mean that the impurity correlator is considered to be Gaussian. All higher order diagrams decompose in fully contracted terms. This is analogous to the Wick theorem for expectation values of operator products.

We introduce the impurity correlator in position representation, reading

$$\left\langle V(\mathbf{r})V(\mathbf{r}')\right\rangle = \frac{N_{\mathrm{imp}}}{V^2} \sum_{\mathbf{p}} e^{i\mathbf{p}(\mathbf{r}-\mathbf{r}')} |V_{\mathrm{imp}}(\mathbf{p})|^2 = N_{\mathrm{imp}} \int d\mathbf{x} V_i(\mathbf{r}-\mathbf{x}) V_i(\mathbf{r}'-\mathbf{x}), \tag{2.7}$$

The correlator is proportional to the concentration of impurities N_{imp}. Hereinafter, we will denote the impurity correlator by

$$W(\mathbf{r},\mathbf{r}') = \left\langle V(\mathbf{r})V(\mathbf{r}')\right\rangle = W(\mathbf{r}-\mathbf{r}'). \tag{2.8}$$

Since averaging over the impurity configurations restores translation invariance, the impurity correlator can be written in terms of the difference of $\mathbf{r}$ and $\mathbf{r}'$. Thus, we can write the Fourier transform as

$$W(\mathbf{q}) = \int \frac{d^3q}{(2\pi)^3} e^{-i\mathbf{q}\cdot(\mathbf{r}-\mathbf{r}')} W(\mathbf{r}-\mathbf{r}'). \tag{2.9}$$

With the defined correlators, we can take higher order diagrams into account.

An elegant way to do so is the self-consistent Born approximation (SCBA). In order to perform the SCBA we introduce a self-energy Σ. The self-energy contains all one-particle-irreducible diagrams without incoming and outgoing fermion lines. The full Green's function can be then expressed via the Dyson equation which reads

$$\hat{G}(\varepsilon,\mathbf{p}) = \hat{G}_0(\varepsilon,\mathbf{p}) + \hat{G}_0(\varepsilon,\mathbf{p})\hat{\Sigma}(\varepsilon,\mathbf{p})\hat{G}(\varepsilon,\mathbf{p}). \tag{2.10}$$

In principle, the Dyson equation is so far exact and provides a summation of all possible diagrams. However, in the self-consistent Born approximation, some diagrams are neglected. In the following, we

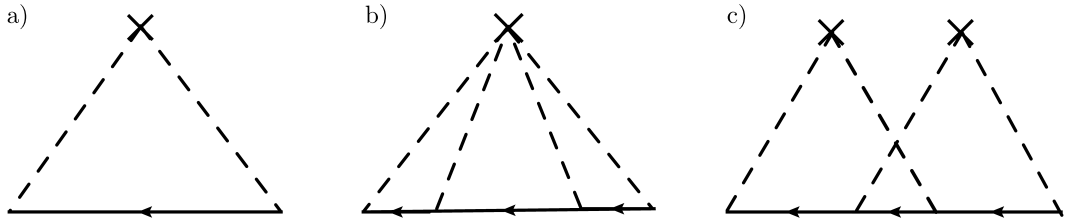

Figure 2.2: Three types of Born diagrams. First non-vanishing order of Born approximation, the so-called simple Born diagram is depicted in panel a), panel b) illustrates the diagram of multiple scattering off one impurity, and c) shows the first order crossing diagram.

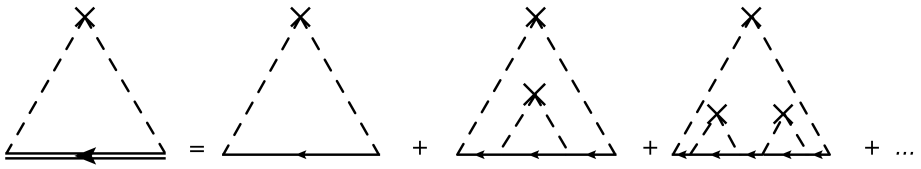

Figure 2.3: Expansion of the full Born diagram for the self-energy in self-consistent Born approximation in lowest orders.

will justify this approximation. The diagrams are classified into three different types which are denoted by: The Born diagrams, Fig. 2.2a), diagrams with multiple scattering off one impurity, Fig. 2.2b), and diagrams with crossed impurity lines, Fig. 2.2c). Diagrams of higher order are taken into account due to the self-consistency of the Dyson equation. In the SCBA approach, diagrams with crossed impurity lines are neglected due to the smallness in the parameter $1/(p_F l)$ (with l being the mean-free path) originating from the following argument: Due to crossed impurity lines, the momentum integrations cannot be performed independently. The relevant contribution stems from the propagations within a thin shell $1/l$ around the Fermi surface p_F. Thus, the diagram Fig. 2.2c) is by a factor $1/(p_F l)$ smaller then the Born type, Fig. 2.2. For Dirac-like systems, the diagram Fig. 2.2c) is by a factor $1/(p_T l)$ smaller then the Born type diagram Fig. 2.2 due to finite temperature. Therefore, for $\mu \to 0$, where $p_F l \lesssim 1$, we expect qualitative agreement of the Born approximation. Furthermore, the diagrams of multiple scattering off one impurity are neglected for $|V_{\mathrm{imp}}| \ll \varepsilon_F p_F^{-3}$, which is the so-called Born criterion.

Within these assumptions, only the Born diagram, Fig. 2.2a), remains in the self-energy. Due to the Dyson equation (2.10), higher-order diagrams are generated by reinserting the Born diagram into itself as illustrated in Fig. 2.3. Therefore, all relevant diagrams are taken into account by substituting the bare Green's function in the simple Born diagram of Fig. 2.2 with the full Green's function resulting in the self-consistent description of the self-energy.

The mathematical description for the Born diagram, Fig. 2.2, is given by Eq. (2.6). The self-energy in SCBA is obtained by the replacement of the bare Green's function by the full Green's function in the Born diagram (2.6), reading

$$\Sigma(\varepsilon, \mathbf{p}) = N_{\mathrm{imp}} \sum_{\mathbf{p}'} \frac{1}{V} \left| V_{\mathrm{imp}}(\mathbf{p} - \mathbf{p}') \right|^2 G(\mathbf{p}', \varepsilon). \tag{2.11}$$

In position representation, the retarded self-energy according to [135] is formally expressed as

$$\Sigma^R(\mathbf{r},\mathbf{r}',\varepsilon) = \left\langle V(\mathbf{r})V(\mathbf{r}')\right\rangle G^R(\mathbf{r},\mathbf{r}',\varepsilon). \tag{2.12}$$

Most generally with the definition of the impurity correlator, Eq. (2.8), the self-energy is expressed in operator language

$$\hat{\Sigma} = \int \frac{d^3q}{(2\pi)^3} W(\mathbf{q}) e^{+i\mathbf{q}\cdot\hat{\mathbf{r}}} \hat{G} e^{-i\mathbf{q}\cdot\hat{\mathbf{r}}}. \tag{2.13}$$

With this definition, the density of states of a disordered system can be calculated as performed in Ch. 3 for Weyl semimetals.

2.2 Kubo-Formalism for the conductivity

In this section, we discuss the Kubo formalism. Kubo formalism relates the linear response function of a physical observable to a certain theoretical correlation function solely determining the equilibrium properties of the system. Thus, the approach is sufficient for the external perturbations of low magnitude. In particular, we study the conductivity of a system meaning the linear response of an electric current density to an applied electrical field and describing the intrinsic properties of a system. In the following section, the term current is used for the current density $\mathbf{j}$ for brevity. Details of the derivation can be found in Refs. [135, 136].

To determine the linear current response to an applied electric field $\mathbf{E}$, we represent the applied electric field by a time dependent vector potential $\mathbf{A}$ which yields

$$\mathbf{E} = -\frac{\partial \mathbf{A}}{\partial t}. \tag{2.14}$$

The linear response of the current is expressed in terms of the current-current response function $Q^R_{\alpha\beta}(\mathbf{r},t,\mathbf{r}',t')$ which yields

$$j_\alpha(\mathbf{r},t) = -\int d^3r' \int dt' Q^R_{\alpha\beta}(\mathbf{r},t,\mathbf{r}',t') A_\beta(\mathbf{r}',t'). \tag{2.15}$$

The current-current response function is given by

$$Q^R_{\alpha\beta}(\mathbf{r},t,\mathbf{r}',t') = \frac{i}{c}\Theta(t-t')\left\langle \left[j_\alpha(\mathbf{r},t), j_\beta(\mathbf{r}',t)\right]\right\rangle_0 - \frac{e^2\rho_0(\mathbf{r},\mathbf{r}',t)}{m}\delta_{\alpha\beta}\delta(\mathbf{r}-\mathbf{r}')\delta(t-t'), \tag{2.16}$$

where terms of quadratic order in the vector potential $\mathbf{A}$ are neglected within linear response.

The connection between the current-current response function and the conductivity is determined with the help of the Fourier transform of Eqs. (2.14) and (2.15) and reads

$$\sigma_{\alpha\beta}(\mathbf{q},\omega) = \frac{Q_{\alpha\beta}(\mathbf{q},\omega)}{i\omega}. \tag{2.17}$$

In the following, we set $\mathbf{q} = 0$.

Therefore, the current-current response function in energy and momentum space is given by

$$Q^R_{\alpha\beta} = T\sum_m \mathrm{Tr}\left[j_\alpha G\left(\mathbf{p},\varepsilon_m+\omega\right) j_\beta G\left(\mathbf{p},\varepsilon_m\right)\right], \tag{2.18}$$

where $\varepsilon_m = \pi T(2m+1)$ are the Matsubara energies. Hereinafter, with the trace Tr[...], we denote

$$\mathrm{Tr}[...] = \int \frac{d^3\mathbf{p}}{(2\pi)^3}\mathrm{Tr}[...] \tag{2.19}$$

in this section.

After analytical continuation of Eq. (2.18) as explained in Ref. [137] and the use of Eq. (2.17), the Kubo formula for the conductivity is given by

$$\sigma_{\alpha\beta}(\omega,T) = -\int \frac{d\varepsilon}{2\pi}\frac{f_T(\varepsilon)}{\omega}\mathrm{Tr}\Big[\Big(\hat{G}^R(\varepsilon,\mathbf{p}) - \hat{G}^A(\varepsilon,\mathbf{p})\Big)\hat{j}_\alpha\hat{G}^A(\varepsilon-\omega,\mathbf{p})\hat{j}_\beta + \hat{G}^R(\varepsilon+\omega,\mathbf{p})\hat{j}_\alpha\Big(\hat{G}^R(\varepsilon,\mathbf{p}) - \hat{G}^A(\varepsilon,\mathbf{p})\Big)\hat{j}_\beta\Big], \tag{2.20}$$

where $f_T(\varepsilon)$ is the Fermi distribution function. Later in this thesis, we will apply this formula for the calculation of the conductivity and the Hall conductivity. The effect of disorder is incorporated via the disorder dressed Green's function. In Dirac materials, in particular in graphene and Weyl semimetals, vertex corrections in the conductivity become important already for the simplest case of pointlike impurities [81]. The vertex corrections for Weyl semimetals are discussed in App. C.

However, for the calculation of the Hall conductivity, it is convenient to use the Kubo-Streda formula [138]. In the following, we will derive the Kubo-Streda formula for the Hall conductivity with the help of the Kubo formula (2.20).

In the limit $\omega \to 0$, Eq. (2.20) can be written as

$$\sigma_{\alpha\beta} = \frac{i\hbar e^2}{2\pi}\int d\varepsilon f_T(\varepsilon)\mathrm{Tr}\left[v_\alpha\frac{dG^\mathrm{R}}{d\varepsilon}v_\beta\mathrm{Im}G - v_\alpha\mathrm{Im}Gv_\beta\frac{dG^A}{d\varepsilon}\right], \tag{2.21}$$

where we used $\hat{j}_\alpha = e\hat{v}_\alpha$. This equation can be split into two terms corresponding to the normal and the anomalous contribution to the Hall conductivity. The two terms are

$$\sigma_{\alpha\beta} = \underbrace{\frac{i\hbar e^2}{2\pi}\int d\varepsilon f_T(\varepsilon)\frac{d}{d\varepsilon}\mathrm{Tr}\left[v_\alpha G^\mathrm{R}v_\beta\mathrm{Im}G - v_\alpha\mathrm{Im}Gv_\beta G^\mathrm{A}\right]}_{\sigma^\mathrm{I}_{\alpha\beta}} \tag{2.22}$$

$$\underbrace{-\frac{i\hbar e^2}{2\pi}\int d\varepsilon f_T(\varepsilon)\mathrm{Tr}\left[v_\alpha G^\mathrm{R}v_\beta\frac{d\mathrm{Im}G}{d\varepsilon} - v_\alpha\frac{d\mathrm{Im}G}{d\varepsilon}v_\beta G^\mathrm{A}\right]}_{\sigma^\mathrm{II}_{\alpha\beta}}, \tag{2.23}$$

where $\sigma^\mathrm{I}_{\alpha\beta}$ is the normal contribution to the Hall conductivity and $\sigma^\mathrm{II}_{\alpha\beta}$ the anomalous contribution. The anomalous contribution can be written in a more compact form which will be derived in the following. Using the commutator

$$v_\alpha = \frac{1}{i\hbar}\left[r_\alpha, \mathcal{H}\right], \tag{2.24}$$

where r_α is the position operator. By using cyclic permutation under the trace, the anomalous contribution to the Hall conductivity is expressed as

$$\sigma^{II}_{\alpha\beta} = \frac{e^2}{2\pi}\int d\varepsilon f_T(\varepsilon)\mathrm{Tr}\left[\frac{d\mathrm{Im}G}{d\varepsilon}(r_\alpha v_\beta - r_\beta v_\alpha)\right]. \tag{2.25}$$

It is obvious here that the diagonal components vanish. Furthermore, we can rewrite the derivative into a derivative with respect to magnetic field H, yielding

$$\frac{d\mathrm{Im}G}{d\varepsilon} = -\frac{dH}{d\mathcal{H}}\frac{d\mathrm{Im}G}{dH}. \tag{2.26}$$

Among others, the Dirac-like Hamiltonian $\mathcal{H}$ in finite magnetic field fulfills the following relation for the derivative with respect to magnetic field:

$$\frac{d\mathcal{H}}{dH} = -\frac{e}{2c}v_\alpha\frac{d}{dH}\left(\sum_{\beta\gamma}\varepsilon_{\alpha\beta\gamma}H_\beta r_\gamma\right) = -\frac{e}{2c}(r_\alpha v_\beta - r_\beta v_\alpha), \tag{2.27}$$

for magnetic field applied perpendicular to α and β. Thus, the anomalous contribution reads

$$\sigma^{II}_{\alpha\beta} = \frac{ec}{\pi}\int d\varepsilon f_T(\varepsilon)\mathrm{Tr}\left[\frac{d\mathrm{Im}G}{dH}\right] = ec\frac{dN(\mu,H)}{dH}. \tag{2.28}$$

Studying disordered systems, it is particularly convenient to separate the Hall conductivity in its normal and anomalous contributions.

2.3 Landauer-Büttiker formalism for the conductance

To derive the Landauer formula, we first consider the scattering of electrons in a quantum dot, as visualized in Fig. 2.4. Thus, we consider a Hamiltonian $\mathcal{H}_\alpha$, where α corresponds to L, R meaning the left and right lead, respectively. The associated eigenstates with energy E are denoted by $\phi^{\pm}_{\alpha,n,E}(x,\mathbf{r}_\perp)$. We introduced the vector $\mathbf{r}_\perp$ perpendicular to the left and right lead which are parallel to the x-axis. Furthermore, the quantum number $\pm$ represents left and right moving particles. The Hamiltonian transverse to the direction of scattering has the eigenenergies ε_n with the corresponding eigenstates denoted by n. For brevity, we introduce the quantum number $\lambda = (\alpha, n, E)$. As illustrated in Fig. 2.4, we can write the eigenstates of the full system including the scattering on the mesoscopic sample with the amplitudes of the eigenfunctions of the leads, reading

$$\psi_E(x,\mathbf{r}_\perp) = \begin{cases} \sum_n b^+\phi^+_{LnE}(x,\mathbf{r}_\perp) + \sum_n b^-\phi^-_{LnE}(x,\mathbf{r}_\perp) & (x,\mathbf{r}_\perp)\in L, \\ \psi_{M,E}(x,\mathbf{r}_\perp) & (x,\mathbf{r}_\perp)\in M, \\ \sum_n d^+\phi^+_{RnE}(x,\mathbf{r}_\perp) + \sum_n d^-\phi^-_{RnE}(x,\mathbf{r}_\perp) & (x,\mathbf{r}_\perp)\in R. \end{cases} \tag{2.29}$$

Here, $\psi_{M,E}(x,\mathbf{r}_\perp)$ is an unknown function in the mesoscopic sample. We can connect the incoming and outgoing waves, $\mathbf{c}_{\mathrm{in}}$ and $\mathbf{c}_{\mathrm{out}}$, with the scattering matrix $\mathbf{S}(E)$, yielding

$$\mathbf{c}_{\mathrm{out}} = \begin{pmatrix}\mathbf{b}^-\\ \mathbf{d}^+\end{pmatrix} = \begin{pmatrix}\mathbf{r}(E) & \mathbf{t}'(E)\\ \mathbf{t}(E) & \mathbf{r}'(E)\end{pmatrix}\begin{pmatrix}\mathbf{b}^+\\ \mathbf{d}^-\end{pmatrix} = \mathbf{S}\mathbf{c}_{\mathrm{in}}. \tag{2.30}$$

In the transmission matrix $\mathbf{t}$, the matrix elements $t_{nn'}$ express the transmission amplitude for an incoming wave from the left in state n' being transmitted into an outgoing wave in the state n on the right side. The transmission in the opposite direction is represented by the transmission element $t'_{nn'}$. The same holds for the reflection matrix $\mathbf{r}$.

Figure 2.4: Geometry of a mesoscopic system considered for the derivation of Landauer formula. The system consists of a left and a right lead where the amplitudes of the wave functions are given by $\mathbf{b}_+, \mathbf{b}_-$ for the left and $\mathbf{d}_+, \mathbf{d}_-$ for the right lead. These four states scatter at the sample.

We use these expressions now to determine the scattering states $\psi_\lambda = \psi_{\alpha n E}$. These states refer to the state n and the lead α where the incoming wave arrives. For the left lead $\alpha = L$, the scattering states read

$$\psi_{LnE}(x, \mathbf{r}_\perp) = \begin{cases} \phi^+_{LnE}(x, \mathbf{r}_\perp) + \sum_{n'} r_{n'n} \phi^-_{LnE}(x, \mathbf{r}_\perp) & (x, \mathbf{r}_\perp) \in L, \\ \psi_{M,E}(x, \mathbf{r}_\perp) & (x, \mathbf{r}_\perp) \in M, \\ \sum_{n'} t_{n'n} \phi^+_{RnE}(x, \mathbf{r}_\perp) & (x, \mathbf{r}_\perp) \in R, \end{cases} \tag{2.31}$$

and for the right lead $\alpha = R$, the states are

$$\psi_{RnE}(x, \mathbf{r}_\perp) = \begin{cases} \sum_{n'} t'_{n'n} \phi^+_{LnE}(x, \mathbf{r}_\perp) & (x, \mathbf{r}_\perp) \in L, \\ \psi_{M,E}(x, \mathbf{r}_\perp) & (x, \mathbf{r}_\perp) \in M, \\ \phi^+_{RnE}(x, \mathbf{r}_\perp) + \sum_{n'} r'_{n'n} \phi^-_{RnE}(x, \mathbf{r}_\perp) & (x, \mathbf{r}_\perp) \in R. \end{cases} \tag{2.32}$$

In general, the conductance of the geometry is determined by $\psi_{M,E}(x, \mathbf{r}_\perp)$. However, we will see in the following that it is possible to calculate the some general results with the S-matrix without knowledge about the exact function $\psi_{M,E}(x, \mathbf{r}_\perp)$. The corresponding approach is the Landauer-Büttiker formalism. There are several ways to derive the so-called Landauer formula, we choose however the derivation in linear response which closely resemblances the Kubo formalism.

For the derivation of Landauer formula, we start with the relation between the conductivity σ and the conductance $\mathcal{G}$, reading

$$\mathcal{G} = \frac{W}{L}\sigma, \tag{2.33}$$

where L is the length of the sample and W the area of the cross-section. However, for mesoscopic systems, this local description is not applicable. To fully consider the geometry of the sample, the conductance is expressed in terms of the current-current correlation function again in linear response, yielding

$$\mathcal{G}(\omega) = -\frac{2e^2}{\omega} \mathrm{Im} \int_{-\infty}^{\infty} dt e^{i(\omega + i\eta)t} (-i)\theta(t) \left\langle \left[I(x,t), I(x,0) \right] \right\rangle, \tag{2.34}$$

where $I(x)$ is the current passing through the system and $\theta(x)$ denotes the Heaviside theta function. This current is equal to the current density integrated through the cross-section. The current in second quantization can be written as

$$I(x) = \sum_{\lambda,\lambda'} j_{\lambda,\lambda'}(x) c_\lambda^\dagger c_{\lambda'}, \tag{2.35}$$

$$j_{\lambda,\lambda'}(x) = \frac{1}{2mi} \int_\Omega d\mathbf{r}_\perp \left\{ \psi_\lambda^*(x,\mathbf{r}_\perp)[\partial_x \psi_{\lambda'}(x,\mathbf{r}_\perp)] - [\partial_x \psi_\lambda^*(x,\mathbf{r}_\perp)]\psi_{\lambda'}(x,\mathbf{r}_\perp) \right\}, \tag{2.36}$$

where the functions $\psi_\lambda(x,\mathbf{r}_\perp)$ are the scattering states, Eq. (2.31) and (2.32).

Evaluating the current-current correlator leads to

$$\mathcal{G}(\omega) = -\frac{2e^2}{\omega} \mathrm{Im} \int_0^\infty dt e^{i(\omega+i\eta)t}(-i) \sum_{\lambda,\lambda'} |j_{\lambda,\lambda'}(x')|^2 e^{i(E_\lambda - E_{\lambda'})t} \left(f_T(E_\lambda) - f_T(E_{\lambda'}) \right), \tag{2.37}$$

Here, we used $\langle c_\lambda^\dagger c_{\lambda'} \rangle = \delta_{\lambda\lambda'} f_T(E_\lambda)$ with the Fermi distribution function $f_T(E)$. Further simplifying the formula provides

$$\mathcal{G}(\omega) = \frac{2e^2}{\omega} \mathrm{Im} \sum_{\lambda,\lambda'} \frac{|j_{\lambda,\lambda'}(x')|^2}{(\omega + i\eta + E_\lambda - E_{\lambda'})} \left(f_T(E_\lambda) - f_T(E_{\lambda'}) \right). \tag{2.38}$$

The consideration of the dc-limit $\omega \to 0$ leads to

$$\mathcal{G}(0) = 2e^2\pi \sum_{\lambda,\lambda'} |j_{\lambda,\lambda'}(x')|^2 \left(-\frac{\partial f_T}{\partial E_\lambda} \right) \delta(E_\lambda - E_{\lambda'}). \tag{2.39}$$

We use now the eigenstates $\lambda = (\alpha, n, E)$ and rewrite the sum over the eigenstates into an integral over energy

$$\sum_\lambda \to \sum_{\alpha n} \frac{m}{2\pi} \int dE. \tag{2.40}$$

Thus, the conductance becomes

$$\mathcal{G}(0) = 2e^2\pi \left(\frac{m}{2\pi} \right)^2 \int_0^\infty dE \sum_{nn',\alpha\alpha'} |j_{\alpha nE,\alpha' n' E}|^2 \left(-\frac{\partial f_T}{\partial E_\lambda} \right). \tag{2.41}$$

Now, we apply the scattering states, Eqs. (2.31) and (2.32), to express the conductance in terms of the S-matrix. This leads to

$$\begin{aligned} \mathcal{G}(0) &= e^2 \frac{m^2}{2\pi} \int_0^\infty dE \sum_{nn'} \left[|j_{LnE,Ln'E}|^2 + |j_{LnE,Rn'E}|^2 + |j_{RnE,Ln'E}|^2 + |j_{RnE,Rn'E}|^2 \right] \left(-\frac{\partial f_T}{\partial E_\lambda} \right) \\ &= e^2 \frac{1}{2\pi} \int_0^\infty dE \left(-\frac{\partial f_T}{\partial E_\lambda} \right) \mathrm{Tr} \left[(\mathbf{t}^\dagger \mathbf{t})^2 + (\mathbf{t}'^\dagger \mathbf{t}')^2 + \mathbf{t}^\dagger \mathbf{r}' \mathbf{r}'^\dagger \mathbf{t} + \mathbf{t}'^\dagger \mathbf{r} \mathbf{r}^\dagger \mathbf{t}' \right]. \end{aligned} \tag{2.42}$$

This results finally in the Landauer formula for the conductance, yielding

$$\mathcal{G}(0) = \frac{2e^2}{h} \int_0^\infty dE \left(-\frac{\partial f_T}{\partial E} \right) \mathrm{Tr} \left[\mathbf{t}^\dagger(E) \mathbf{t}(E) \right]. \tag{2.43}$$

The Landauer formula is applied to calculate the conductance of the carbon nanotube with side-attached single-molecule magnets, cf. Chs. 5 and 6. The mechanism of scattering matrices, briefly discussed in this section, is analyzed in detail for the case relevant to the CNT system in Ch. 5.

Chapter 3

3 Disorder in Weyl semimetals

It was discussed in the last chapter that disorder, as present in condensed matter systems, affects the transport properties. In this chapter, we discuss the effect of disorder on Weyl semimetals within self-consistent Born approximation (SCBA) in three different models of disorder: (i) pointlike impurities, (ii) within a smooth disorder potential, and (iii) for long-range Coulomb impurities which are strongly screened.

The transport properties of Weyl semimetals are highly peculiar especially close to the charge neutrality point. One central aspect of this peculiarity is the appearance of a disordered critical point within the perturbative analysis. This was first pointed out within an mean field approach in Ref. [16, 17], later the fact was confirmed by a renormalization group (RG) analysis in $2-\epsilon$ dimensions [18, 19] and in a numerical analysis [22]. For sufficiently weak disorder below the disorder critical point, the density of states vanishes quadratically in energy around the Weyl point within the perturbation theory. This results in vanishing ac conductivity for zero temperature and external frequency going to zero, while the dc conductivity in the zero temperature limit remains finite, cf. Ref. [30]. However, non-perturbative effects are in discussion to an exponentially small density of states at the Weyl point. This is numerically discussed in Ref. [23–26]. Analytical calculations of rare region effects were performed in Refs. [27] and [28] for resonant scattering and in a T-matrix approach, respectively. However, a recent work, Ref. [29] suggests that rare events do not produce a finite density of states in the weak disorder limit. Instantons in the replica approach, which are known to produce Lifshitz tails Ref. [139], are calculated in higher dimensions ($d = 4$) in Ref. [140]. In the strong disorder regime, the density of states is finite at the Weyl point already without invoking exponentially small contributions.

While the behavior of the density of states in the weak and strong disorder phase seem to be well known for pointlike impurities, the results of the density of states in the critical phase differ in the mean field approach and in the RG analysis performed in $2-\epsilon$ dimensions. The mean field approach results in a density of states as $\varepsilon^{1/2}$ (cf. [16, 17] and below in Sec. 3.1). However, in the RG approach the density of states depends linearly on energy, see Refs. [18, 19].

Moreover, the results in SCBA for strong disorder are also very peculiar. Under an incorporation of the full SCBA, one finds that the system tends to suppress backward scattering. This manifests in the calculations of vertex corrections for the strong disorder regime. They lead to a diffusion dominated conductivity saturating in dependence of disorder strength. To determine this behavior, it is required to consider higher order corrections in energy (ε/Λ with Λ being the ultraviolet cutoff) to the density of states and the real part self-energy in strong disorder compared to Refs. [16, 17]. To justify the validity of SCBA for strong disorder, we consider a model of smooth disorder. In smooth disorder, we

can go to the strong disorder regime within a relatively low impurities potential thus not destroying the complete model. This model also shows the appearance of a disorder critical point and results in the same self-energy of strong disorder than the pointlike model. The consideration of transport as presented in the following is based on our work prepared for submission, Ref. [141].

Another important aspect of disorder in Weyl semimetals can be found in quantizing magnetic fields, meaning in the presence of Landau levels (LL). Since already in the clean limit, the density of states is finite in presence of magnetic field, the features of transport close to the charge neutrality point are expected to be less spectacular. However, it turns out that the vanishing density of states at the Weyl point in absence of magnetic field translates into some unusual behavior of the conductivity and the magnetoresistance, as discussed in Ch. 4. Furthermore, we find by first considering pointlike impurities that the appearance of the disorder critical point maintains for finite magnetic field. In the following analysis of the density of states in presence of magnetic field and disorder, the broadening of Landau levels with respect to disorder is also unusual. With increasing magnetic field, the Landau level broadening occurs faster than the increase of the Landau level distance resulting in the tendency of overlapping Landau levels. Moreover, the background density of states is larger than the density of states of the particular Landau level even for well separated Landau level, as we point out below. Again, these aspects will be crucial for the later calculated magnetoresistance, cf. Ch. 4. Furthermore, we consider Coulomb impurities in presence of finite magnetic field where we find that Coulomb impurities are strongly screened for a large fine structure constant. In 3D systems, Coulomb impurities are relevant since scattering off donors and acceptors are important processes. Due to the linear magnetoresistance in presence of strongly screened Coulomb impurities in the ultra quantum limit [82], the consideration of Coulomb impurities seems to be relevant also in this context. The analysis of disorder in presence of magnetic field, as presented here, is based on Ref. [83] where we established the effects of disorder on LLs.

This chapter is structured as follows: In Sec. 3.1, we introduce self-consistent Born approximation for Weyl semimetals. The chapter continues with an analysis of the full SCBA in the absence of magnetic field, Sec. 3.2. In the resulting limits of weak, critical, and strong disorder, we analyze the conductivity. Furthermore, we consider a model of smooth disorder to justify the SCBA in strongest disorder. Section 3.4 is devoted to an analysis of disorder in presence of finite magnetic field where we study the effect of Landau level broadening on the density of states. In the presence of finite magnetic field, we also consider charged impurities, Sec. 3.5. Finally, we conclude the chapter with a summary and discussion of the results, Sec. 3.6

3.1 Self-consistent Born approximation in Weyl semimetals

In this section, we discuss disorder in Weyl semimetals within the SCBA approach in general. In the following sections, we will then solve the resulting equations both the absence and the presence of a finite magnetic field. As discussed in Sec. 2.1, impurity scattering generates a self-energy $\hat{\Sigma}(\mathbf{p},\varepsilon)$ in the (impurity-averaged) Green's function. For finite magnetic field, the Green's function reads

$$\hat{G}(\mathbf{p},\varepsilon)=\left\langle\frac{1}{\varepsilon-\mathcal{H}}\right\rangle=\frac{1}{\varepsilon-v\boldsymbol{\sigma}\cdot\left(\mathbf{p}-\frac{e}{c}\mathbf{A}\right)-\hat{\Sigma}(\mathbf{p},\varepsilon)}, \tag{3.1}$$

where the magnetic field is aligned in z-direction. Here, the matrix Green's function operates in the pseudospin space of the Pauli matrices σ. Introducing the disorder potential is now performed in the

presence of magnetic field. The simplifications for the resulting Green's functions in the zero-field limit are discussed in the end of this section.

We consider a disorder potential which is diagonal in both spin and pseudospin indices. Furthermore, we neglect scattering between different Weyl nodes. The approximation and its limitations are discussed in the end of this chapter, Sec. 3.6. Clearly, the absence of internode scattering ensures that the structure in node space is trivial for all quantities. We do not show it explicitly below; the calculated quantities (density of states and conductivity) are those per Weyl node.

Under these assumptions, we will first discuss a model of pointlike impurities and later analyze generalization to the case of Coulomb impurities. The impurity potential for pointlike impurities is written as

$$\hat{V}_{\mathrm{dis}}(\mathbf{r}) = u_0 \sum_i \delta(\mathbf{r} - \mathbf{r}_i)\mathbb{1}, \tag{3.2}$$

where $\mathbb{1}$ is the unit matrix in the pseudospin space and u_0 is strength of the disorder potential. In view of the matrix structure of the impurity potential $\hat{V}_{\mathrm{dis}}(\mathbf{r})$, the impurity correlator $\hat{W}$ becomes a rank-four tensor. The self-energy yields

$$\Sigma_{\alpha\beta}(\mathbf{r}, \mathbf{r}') = \int \frac{d^3q}{(2\pi)^3} W_{\alpha\gamma\beta\delta}(\mathbf{q}) e^{i\mathbf{q}\cdot(\mathbf{r}-\mathbf{r}')} G_{\gamma\delta}(\mathbf{r}, \mathbf{r}'). \tag{3.3}$$

A diagonal impurity potential results in a diagonal impurity correlator as well, which reads

$$W_{\alpha\gamma\beta\delta}(\mathbf{q}) = \gamma \delta_{\alpha\gamma}\delta_{\beta\delta}, \tag{3.4}$$

where $\gamma = N_{\mathrm{imp}} u_0^2$. The self-energy is diagonal in the energy-band space. However, the presence of magnetic field effectuates a self-energy being no longer proportional to the unit matrix:

$$\hat{\Sigma} = \mathrm{diag}(\Sigma_1, \Sigma_2). \tag{3.5}$$

This asymmetry has its origin in the asymmetry of states in the zeroth LL. In the clean case, the states of the zeroth LL are chiral meaning they are only present in one energy band. Later, we will show that a strong impurity scattering can eliminate this asymmetry.

Conveniently, we switch to LL representation so that $\hat{G} = \hat{G}(\varepsilon, p_z, n)$ and $\hat{\Sigma} = \hat{\Sigma}(\varepsilon, p_z, n)$ with the LL index n. The diagonal components of the matrix Green's function (3.1) that determine the self-energy are expressed as:

$$G_{11} = \frac{\varepsilon - \Sigma_2 + v p_z}{(\varepsilon - \Sigma_1 - v p_z)(\varepsilon - \Sigma_2 + v p_z) - \Omega^2 n}, \tag{3.6}$$

$$G_{22} = \frac{\varepsilon - \Sigma_1 - v p_z}{(\varepsilon - \Sigma_1 - v p_z)(\varepsilon - \Sigma_2 + v p_z) - \Omega^2 (n+1)}. \tag{3.7}$$

In general, the self-energy depends on energy and on the LL index, $\hat{\Sigma} = \hat{\Sigma}(\varepsilon, p_z, n)$. However, the dependencies on n and p_z drop out in the case of white-noise disorder.

In the absence of magnetic field, the asymmetry in energy band space is of course lifted resulting in equal diagonal components of the Green's function and thus of the self-energy. The Green's function in momentum representation reads

$$G = \frac{\varepsilon - \Sigma}{(\varepsilon - \Sigma)^2 - v^2 |\mathbf{p}|^2}. \tag{3.8}$$

These Green's function will be used in the following to determine the transport properties in Weyl semimetals.

3.2 Critical phenomena in Weyl semimetals

3.2.1 SCBA for pointlike impurities

As shown by $1/N$ expansion [16, 17] or by renormalization group analysis [20], weak disorder is irrelevant in Weyl semimetals and disorder becomes relevant above a critical point. This implies that the density of states remains vanishing at the Weyl point. In the zero magnetic field, the clean density of states vanishes quadratically with energy, yielding

$$\nu(\varepsilon) = \frac{\varepsilon^2}{2\pi^2 v^3}. \tag{3.9}$$

Let us first consider Born approximation for the self-energy in absence of magnetic field. This means that we neglect the self-energy in Eq. (3.8) as explained in Sec. 2.1. The self-energy is obtained by applying Eq. (2.11) to the relevant model of disorder and reads

$$\Sigma^R = \gamma \int \frac{dp}{(2\pi)^3} \frac{\varepsilon + i0}{(\varepsilon + i0)^2 - v^2 p^2} = -i \frac{\gamma \varepsilon^2}{2\pi^2 v^3}. \tag{3.10}$$

Since the density of in Born approximation is equal to the clean density of states, disorder in Born approximation is irrelevant. Moreover, to determine the critical point, it es required to apply self-consistent Born approximation.

To determine the density of states in SCBA, we calculate the self-energy. Using Eqs. (2.11) and (3.8), the self-consistent equation for the self-energy in momentum space reads

$$\Sigma^R(\varepsilon) = \gamma \int \frac{d^3 p}{(2\pi)^3} \frac{\varepsilon - \Sigma^R(\varepsilon)}{(\varepsilon - \Sigma^R(\varepsilon))^2 - v^2 p^2}. \tag{3.11}$$

Due to the divergence of the integral in the ultraviolet regime, we introduce the ultraviolet energy cutoff Λ. The introduction of an ultraviolet cutoff Λ becomes necessary due to the approximation of a true energy dispersion by the Dirac-fermion one, which is, in fact, valid for low-energies. The integration over the radial momentum leads to

$$\Sigma^R(\varepsilon) = \beta(\varepsilon - \Sigma^R) \left[-1 + \frac{(\varepsilon - \Sigma^R)}{2\Lambda} \ln \left(\frac{\varepsilon - \Sigma^R + \Lambda}{\varepsilon - \Sigma^R - \Lambda} \right) \right], \tag{3.12}$$

where we introduced the dimensionless disorder strength

$$\beta = \frac{\gamma \Lambda}{2\pi^2 v^3}. \tag{3.13}$$

A detailed analysis of Eq. (3.12) is performed in App. A.1. Let us here point out the most salient results.

We first consider the case of $\varepsilon = 0$ under the assumption $\mathrm{Re}\Sigma^R(\varepsilon = 0) = 0$ which will be later justified by the numerical results. Under these assumptions, the broadening due to disorder $\Gamma = -\mathrm{Im}\Sigma^R$ is described by the following equation:

$$\frac{\beta - 1}{\beta} = \frac{\Gamma}{\Lambda} \arctan \left(\frac{\Lambda}{\Gamma} \right). \tag{3.14}$$

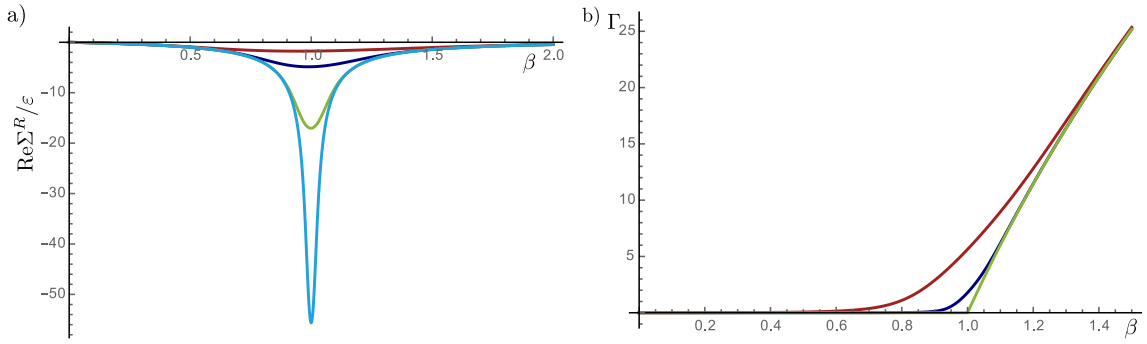

Figure 3.1: Numerical evaluation of the self-energy in dependence of dimensionless disorder strength β. In panel a), equation (A.2) (real part of the self-energy) is depicted in dependence of β for different values of energy. The blue, green, red, and darkblue curves correspond to $\varepsilon/\Lambda = 10^{-4}, 10^{-3}, 10^{-2}, 5\cdot 10^{-2}$, respectively. Equation (A.3) (imaginary part of self-energy) is numerically evaluated in panel b) for $\varepsilon/\Lambda = 0, 10^{-3}, 10^{-2}$ for green, darkblue, and red curve, respectively. The ultra-violet cutoff in both panels is set to $\Lambda = 100$.

As a result, at $\beta = 1$, the left hand site of Eq. (3.14) exhibit a sign change. Since for $\beta < 1$ the allowed values of the imaginary part are $\Gamma = 0$, a critical point strength is present at $\beta = 1$ marking the point where a finite density of states is observed at the Weyl point. The appearance of the disorder critical point is illustrated by a numerical analysis of Eq. (3.14). The numerical evaluation of the self-energy Γ in the full range of disorder at zero energy in dependence of disorder strength is depicted in Fig. 3.1b) by the green curve where the disorder critical point is clearly seen. An analytical solution of Eq. (3.14) for $\beta > 1$ is approximated in the two certain regimes, yielding

$$\Gamma = \begin{cases} \dfrac{2\Lambda}{\pi}\left(1 - \dfrac{1}{\beta}\right), & \Gamma < \Lambda \\ \sqrt{\dfrac{\beta}{3}}\Lambda & \Gamma > \Lambda. \end{cases} \tag{3.15}$$

For finite energy ε, we determine the self-energy in the different regimes of disorder. As we learned from the analysis at the Weyl node, there are the regimes of weak and strong disorder which are separated by the critical point. For finite energy, however, the regimes of weak and strong disorder are separated by a "phase" of critical disorder, cf. Fig. 3.2.

For weak disorder $\beta < 1$, the effect of disorder is irrelevant for the density of states. The self-energy is obtained by an expansion with respect to finite energy of Eq. (3.12) up to the lowest order, leading to

$$\mathrm{Re}\Sigma^R \approx -\frac{\beta}{1-\beta}\varepsilon, \qquad \Gamma \approx \frac{\pi\beta\varepsilon^2}{2(1-\beta)^3\Lambda}. \tag{3.16}$$

For critical disorder $\beta = 1$, the self-energy can be written as

$$\mathrm{Re}\Sigma^R \approx \varepsilon - \sqrt{\left|\frac{2\varepsilon\Lambda}{\pi}\right|}, \quad \Gamma \approx \varepsilon - \mathrm{Re}\Sigma^R = \sqrt{\left|\frac{2\varepsilon\Lambda}{\pi}\right|}. \tag{3.17}$$

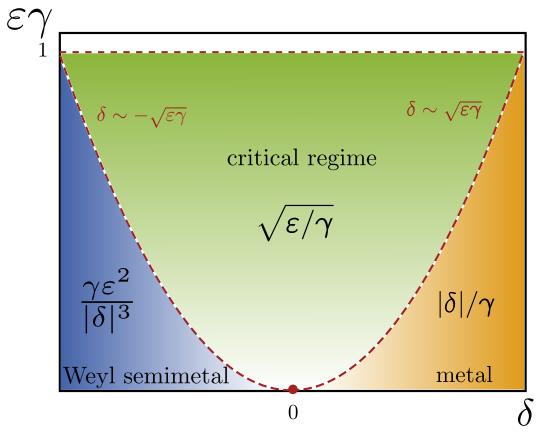

Figure 3.2: Imaginary part of self-energy in the different regimes of disorder. We introduced the parameter $\delta = 1 - \beta$. The diagram clearly shows the "phases" of weak (blue regime), critical (green regime), and strong disorder (yellow regime). The boarders of the regimes are indicated in red, the disorder critical point at zero energy is marked by a red dot.

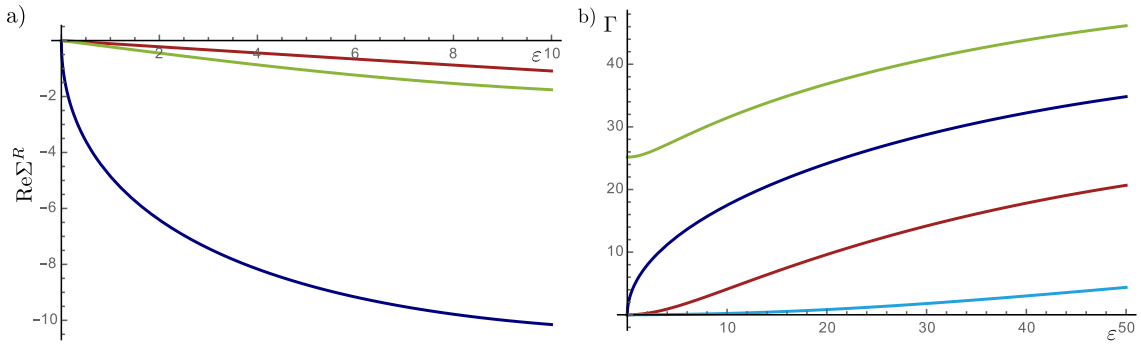

Figure 3.3: Numerical solution of the self-energy in dependence of energy in the three different regimes of disorder. The real part of self-energy is evaluated by Eq. (A.2) in panel a) with weak disorder $\beta = 0.1$ corresponds to the red curve, critical disorder $\beta = 1$ to the darkblue, and strong disorder $\beta = 2.3$ to the green curve. In panel b), the evaluation of Eq. (A.3) in weak disorder ($\beta = 0.1$ and $\beta = 0.5$) is depicted by the blue and red curves, respectively, critical disorder $\beta = 1$ by darkblue, and strong disorder $\beta = 2.3$ by green curve. The ultraviolet cutoff is set to $\Lambda = 100$.

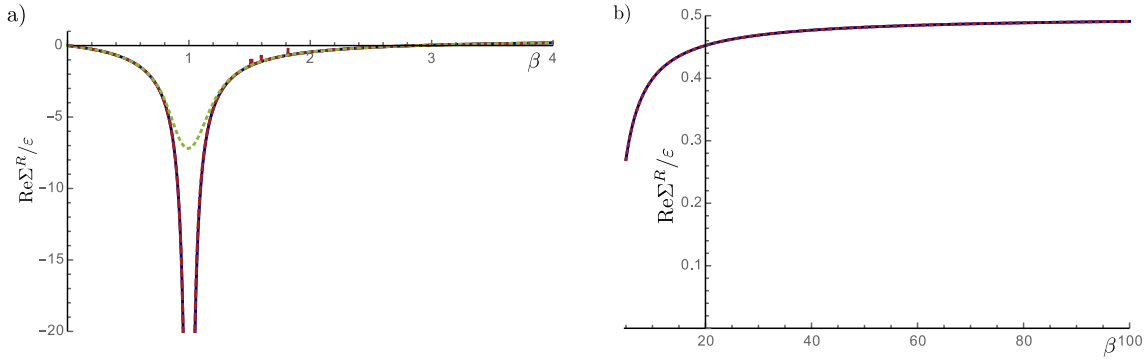

Figure 3.4: Real part of self-energy in dependence of β for $\varepsilon/\Lambda = 5\cdot 10^{-3}$. Panel a) corresponds to the regime $\Gamma/\Lambda < 1$ with the green, dotted curve obtained by the numerical solution of Eq. (A.2), the red, dashed curve depicts Eq. (A.8) for Γ at $\varepsilon = 0$, and the darkblue curve shows Eq. (A.8) determined by the numerical solution of Eq. (A.3) for Γ at $\varepsilon/\Lambda = 5\cdot 10^{-3}$. The divergence around $\beta = 1$ in the red and darkblue curves originate from the application of Eq. (A.8) where formally the critical phase is present. In panel b), the regime of $\Gamma > \Lambda$ is illustrated where the darkblue curve corresponds to the numerical solution of Eq. (A.2) and the red, dashed curve shows Eq. (A.8) with the numerical solution of Γ given by Eq. (A.3). The ultraviolet cutoff in both panels is set to $\Lambda = 100$.

Crucially, we find a linear behavior in energy for the disorder broadening under the assumption that energy is redefined as $\tilde{\varepsilon} = \varepsilon - \mathrm{Re}\Sigma^R$. This assumption was applied in the RG approach [20], where they obtained a linear behavior in energy for the imaginary part of self-energy. This result is valid in the limit $-\sqrt{2\pi\varepsilon/\Lambda} < |\beta - 1| < \sqrt{2\pi\varepsilon/\Lambda}$ which defines the boundaries of the critical regime, cf. Fig 3.2.

Finally, we discuss the case for strong disorder $\beta > 1$. Here, the density of states is mainly determined by the zero energy result, Eq. (3.15). Higher order corrections to the imaginary part of the self-energy are proportional to ε^2. The real part is obtained by an expansion in low energies, as performed in App. A.1, leading to

$$\mathrm{Re}\Sigma^R \approx \frac{(\tilde{\beta} - 2)\varepsilon}{\tilde{\beta} - 1}, \tag{3.18}$$

where the renormalized dimensionless disorder strength is defined as

$$\tilde{\beta} = \beta\left(\frac{2}{\beta} - \frac{1}{1 + (\Gamma/\Lambda)^2}\right). \tag{3.19}$$

This renormalization of the dimensionless disorder will become of particular importance for the consideration of the conductivity. The renormalization ensures that the real part of self-energy saturates at $\mathrm{Re}\Sigma^R/\varepsilon \to 1/2$ for $\beta \to \infty$. This behavior is visualized in Fig. 3.4b).

The self-energy in the disorder-energy plane is visualized in Fig. 3.2, showing that for highest energies the system is in the critical phase leading to a square root behavior in energy. Let us now compare the analytically obtained results with the numerical evaluation of Eq. (3.12). The energy dependence of the self-energy for the real and imaginary part is present in Figs. 3.3a) and b), respectively, in the three different regimes of disorder. We see in both cases that the scaling in energy as shown in Fig. 3.3

matches with the analytical results presented above. Furthermore, Figure 3.3 nicely illustrates the crossover to the critical regime for increased energy in the regime of weak and strong disorder. The crossover can be understood in the "phase-diagram", Fig. 3.2. The linear behavior in energy of the real part of self-energy in the regime of weak and strong disorder is illustrated in Fig. 3.3a). Figure 3.4a) emphasizes the divergent behavior for $\beta \to 1$ of the weak and strong disorder energy renormalization for low energy where the regime of critical disorder is small. The comparison of the analytical and numerical results of the real part, Fig. 3.4a) and b), shows that the analytical nicely matches the numerics away from the critical regime.

3.2.2 Conductivity within SCBA

In the model of pointlike disorder, we calculate now the conductivity σ_{xx} of a Weyl semimetal in weak, strong and critical disorder. We use the Kubo formula for the real part of the conductivity, as discussed in Sec. 2.2, reading

$$\sigma_{xx}(\omega,T) = \int \frac{d\varepsilon}{2\pi}\frac{f_T(\varepsilon)}{\omega}\int \frac{d^3\mathbf{p}}{(2\pi)^3}\mathrm{Tr}\left\{\left[\hat{G}^R(\varepsilon,\mathbf{p})-\hat{G}^A(\varepsilon,\mathbf{p})\right]\hat{j}_x^{\mathrm{tr}}\hat{G}^A(\varepsilon-\omega,\mathbf{p})\hat{j}_x \right. \\ \left. +\hat{G}^R(\varepsilon+\omega,\mathbf{p})\hat{j}_x^{\mathrm{tr}}\left[\hat{G}^R(\varepsilon,\mathbf{p})-\hat{G}^A(\varepsilon,\mathbf{p})\right]\hat{j}_x\right\}, \tag{3.20}$$

where $\hat{j}_x = ev\sigma_x$ is the bare current operator and $\hat{j}_x^{\mathrm{tr}} = V^{\mathrm{tr}}(\omega)\hat{j}_x$ is the current vertex dressed by disorder and dependent on the external frequency ω. The dressed vertex is discussed in App. C. The importance of vertex corrections in Weyl semimetals in the dc limit and for weak disorder was first pointed out in Ref. [81]. Here, we go beyond the limit of Ref. [81] and analyze the effect of vertex correction in both the ac limit and in the full range of disorder. We show below that the vertex corrections are of particular importance in the regimes of critical and strong disorder.

After performing the momentum integration, the conductivity reads

$$\sigma_{xx}(\omega,T) = -\frac{2e^2v^2}{3\gamma}\int_{-\infty}^{\infty}\frac{d\varepsilon}{2\pi}\frac{f_T(\varepsilon)-f_T(\varepsilon+\omega)}{\omega} \\ \mathrm{Re}\left[\frac{1}{1-\frac{v_x^{RR}(\varepsilon,\omega)}{v}}\left(\frac{\Sigma^R(\varepsilon+\omega)-\Sigma^R(\varepsilon)}{\Sigma^R(\varepsilon+\omega)-\Sigma^R(\varepsilon)-\omega}+\frac{\Sigma^R(\varepsilon+\omega)+\Sigma^R(\varepsilon)}{(2\varepsilon+\omega)-(\Sigma^R(\varepsilon+\omega)+\Sigma^R(\varepsilon))}\right)\right. \\ \left.-\frac{1}{1-\frac{v_x^{RA}(\varepsilon,\omega)}{v}}\left(\frac{\Sigma^R(\varepsilon+\omega)-\Sigma^A(\varepsilon)}{\Sigma^R(\varepsilon+\omega)-\Sigma^A(\varepsilon)-\omega}+\frac{\Sigma^R(\varepsilon+\omega)+\Sigma^A(\varepsilon)}{(2\varepsilon+\omega)-(\Sigma^R(\varepsilon+\omega)+\Sigma^A(\varepsilon))}\right)\right], \tag{3.21}$$

where $v_x^{\mathrm{RR/RA}}(\varepsilon,\omega)$ are calculated in App. C and given by Eqs. (C.6) and (C.7), respectively.

Starting with the case of weak disorder $\beta < 1$, we simplify the expression for the conductivity under the assumption $\varepsilon > \Sigma^R, \Sigma^A$. Using Eq. (3.16) for the self-energy, the conductivity is calculated in the two most interesting limits $T = 0$ and $\omega = 0$. We start with the dc limit, $\omega = 0$. The conductivity is

$$\sigma_{xx}(T,\omega=0) = \frac{e^2v^2}{2\pi\gamma}\frac{1-\beta}{1+\beta}, \tag{3.22}$$

constant in temperature and vanishes in the crossover to the regime of critical disorder. For finite ω and $T = 0$, at the point $\varepsilon = -\omega/2$ the conductivity show a singular behavior. We evaluate the integral at this point. The result is

$$\sigma_{xx}(T = 0, \omega) = \frac{e^2}{3\pi v}|\omega|. \tag{3.23}$$

We see that the limit of $\omega = 0$ and $T = 0$ are not interchangeable. Furthermore, we find that the dc conductivity vanishes at the disorder critical point. The ac conductivity however also vanishes at the disorder critical point which only exists for zero temperature and external frequency where the ac conductivity is absent in the full regime of weak disorder. We should emphasize here, that the vanishing ac conductivity as well as the vanishing dc conductivity at the critical point is related to the vanishing density of states in the regime of weak disorder. Rare scattering events may produce a finite density of states already for weak disorder [23, 27] which might eliminate these features and produce a finite conductivity also at the critical point. However, due to recent results [29], it is not clear if rare region effect would have an effect on the conductivity. In Ref. [29], it is shown that the average density of states is not effected by rare events.

For the calculation of the conductivity for critical disorder, we use Eq. (3.17) to evaluate the conductivity. For $\omega = 0$, the result is

$$\sigma_{xx}(T) = \frac{e^2 v^2}{8\gamma\pi}\sqrt{\frac{\pi T}{\Lambda}}. \tag{3.24}$$

In the opposite regime, $T = 0$, the result is

$$\sigma_{xx}(\omega) = \frac{e^2 v^2}{4\gamma\pi}\sqrt{\frac{\omega\pi}{\sqrt{2}\Lambda}}\left(\frac{13}{15} + \frac{\sqrt{2}}{24}\left(-6\mathrm{Arsinh}(1) + \ln(8) - 6\ln(2+\sqrt{2})\right)\right). \tag{3.25}$$

We find that the conductivity in the dc limit for $\omega = 0$ matches with the conductivity for weak disorder for $(1-\beta)^2 \sim T\gamma$ while the ac conductivity in critical disorder does not match due to the disorder independent ac conductivity in the weak disorder limit.

The last remaining regime of strong disorder $\beta > 1$ is discussed in the following. We substitute the result for the self-energy for strong disorder Eq. (3.15) and assume $\mathrm{Re}\Sigma^R = a\varepsilon$. For strong disorder, it is important to consider the vertex correction. For $\omega \to 0$ and $T \to 0$, the vertex corrections (C.6) and (C.7) simplify for strong disorder to

$$v_x^{RR} = -v\frac{a-2}{3(a-1)}, \tag{3.26}$$

$$v_x^{RA} = -v\frac{a+1}{3(a-1)}. \tag{3.27}$$

Vertex corrections need to fulfill $v_x/v < 1$. For $a < 1/2$, this is fulfilled up to highest disorder strength $\beta \to \infty$ as obtained in the numerical calculation in Fig. 3.4. For lowest temperatures and frequencies, the conductivity in both regimes reads

$$\sigma_{xx}(T \sim 0, \omega \sim 0) = -\frac{e^2 v^2}{2\pi\gamma}\frac{(8a-7)}{(2a-1)(4a-5)}. \tag{3.28}$$

We find that the condition $a < 1/2$ for the vertex corrections is manifested again in the calculation of the conductivity, where a positive conductivity without any singularities is obtained under this restriction.

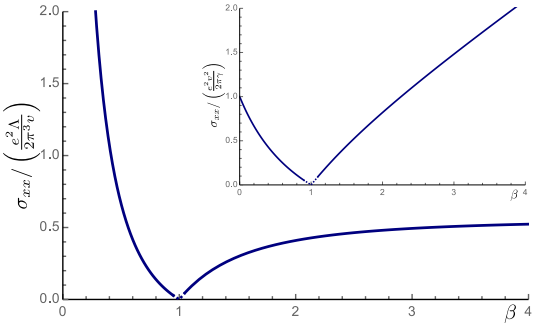

Figure 3.5: Conductivity in the limit $\omega \to 0$ and then $T \to 0$ with the numerically obtained self-energies (real and imaginary part) in dependence of the dimensionless disorder strength β. The dotted part corresponds to the region close to the disorder critical point which cannot be obtained numerically at $T = 0$ due to the divergence of $\mathrm{Re}\Sigma^R$ in weak and strong disorder for $\beta \to 1$. The inset depicts the conductivity in units of the Drude limit of the conductivity emphasizing the effects of vertex corrections. The ultraviolet cutoff in both plots is set to $\Lambda = 100$.

Furthermore, the conductivity vanishes at the disorder critical point with $a = 1 - 1/(\beta - 1) \to -\infty$. The renormalization of dimensionless disorder strength β can be neglected around $\beta = 1$, but gets important for stronger disorder ensuring that the parameter $a < 1/2$. Thus, under fully incorporating the vertex corrections, it is crucial to consider higher orders in the SCBA analysis in particular for strong disorder. This is demonstrated in Fig. 3.5 where the saturating conductivity in dependence of disorder is shown. To justify the SCBA analysis in the regime of strongest disorder, we consider in the following a model of smooth disorder.

3.3 SCBA in a smooth disorder potential

Considering the limit of large β for pointlike impurities on a lattice model corresponds to a large potential on each lattice site which would destroy the model. We can consider a smooth disorder potential where the limit of large β is realized by the correlation length instead of the large potential. The chosen impurity potential should be smooth due to its finite range correction function. Under the purpose to treat the disorder analytically, a rectangular impurity correlator in momentum space is a possible choice.

Thus, we consider the disorder potential with the impurity correlator given by

$$W_{\alpha\gamma\beta\delta}(\mathbf{q}) = \gamma\theta(1 - b|\mathbf{q}|)\delta_{\alpha\gamma}\delta_{\beta\delta}, \tag{3.29}$$

where θ denotes the Heaviside step function and b defines the width of the potential. As for pointlike impurities, we assume that the disorder potential is diagonal in both spin and pseudospin indices and neglect internode scattering.

This impurity correlator relates the disorder strength γ to the disorder potential as

$$\gamma = N_{\mathrm{imp}} u_0^2 b^6, \tag{3.30}$$

where N_{imp} is the impurity density and u_0 the strength of the disorder potential.

Within this model of disorder, the self-energy in SCBA is defined as

$$\Sigma(p,\varepsilon) = \gamma \int \frac{d^3q}{(2\pi)^3} \frac{\theta(1-b|\mathbf{p}-\mathbf{q}|)(\varepsilon-\Sigma(q,\varepsilon))}{(\varepsilon-\Sigma(q,\varepsilon))^2 - v^2q^2}. \tag{3.31}$$

We split the self-energy in terms of large and small momenta, meaning

$$\Sigma(p,\varepsilon) = \Sigma_1(p,\varepsilon)\theta(1-bp) + \Sigma_2(p,\varepsilon)\theta(bp-1), \tag{3.32}$$

where the self-energies Σ_1 and Σ_2 are given by Eqs. (A.14) and (A.15).

In the following, we consider $\varepsilon = 0$ since finite energy leads only to small corrections in the relevant regime of strong disorder. As for pointlike impurities, the real part of self-energy depends linearly on energy and is therefore absent in the considered limit. For the imaginary parts, $\mathrm{Im}\Sigma^R_{1,2}(p) = -\Gamma_{1,2}(p)$, we find the following self-consistent equation

$$\Gamma_1 = \beta_b\Gamma_1 \left[1 - \frac{\Gamma_1}{\Lambda_b}\arctan\left(\frac{\Lambda_b}{\Gamma_1}\right)\right] + \frac{3}{4}bp\Lambda_b\sqrt{\frac{2}{3}\beta_b - 1}\theta\left(2\beta_b - 3\right), \tag{3.33}$$

in the limit $bp \ll 1$ and

$$\Gamma_2 = \theta\left(\frac{2}{3}\beta_b\Lambda_b^2 - v^2p^2\right)\sqrt{\frac{2}{3}\beta_b\Lambda_b^2 - v^2p^2}. \tag{3.34}$$

for $bp \gg 1$. In both regimes, the parameters β_b and Λ_b are given by

$$\beta_b = \frac{\gamma}{(2\pi)^2v^2b}, \quad \Lambda_b = \frac{v}{b}. \tag{3.35}$$

To show that large values of β_b can be realized for relatively low impurity potential, we rewrite the dimensionless disorder strength by the band width Λ and the lattice constant $a = v/\Lambda$, reading

$$\beta_b \sim \left(\frac{u_0}{\Lambda}\right)^2\left(\frac{b}{a}\right)^2. \tag{3.36}$$

This shows that large β_b is achieved for large b already for low impurity potentials.

For small momenta $bp \ll 1$ and $-\mathrm{Im}\Sigma = \Gamma = \Gamma_1$, we recover the SCBA equation for pointlike impurities, Eq. (3.14) where the parameters β and Λ are replaced by the new parameters related to disorder β_b and Λ_b, respectively. The corrections due to finite momenta become apparent for $bp \sim 1$ and $\beta > 3/2$. For large momenta $bp \gg 1$, the self-energy is fully determined by Γ_2 resulting in a momentum dependent critical disorder,

$$\beta_{b,\mathrm{crit}} = (3/2)(pb)^2. \tag{3.37}$$

In this regime, the density of states is only finite for large values of β_b as illustrated in Fig. 3.7b).

In the limit $bp \sim 1$, Eq. (A.14) and (A.15) straightforwardly show that Σ_1 and Σ_2 become equal. The self-consistent equation in this limit $\Gamma_1 = \Gamma_2 = \Gamma$ becomes

$$1 = \beta_b\left[1 - \frac{\Gamma}{\Lambda_b}\arctan\left(\frac{2\Lambda_b}{\Gamma}\right) + \frac{\Gamma^2}{4\Lambda_b}\ln\left(1 + \frac{4\Lambda_b^2}{\Gamma^2}\right)\right]. \tag{3.38}$$

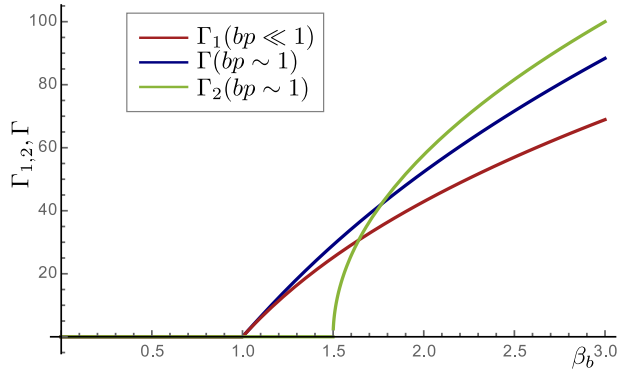

Figure 3.6: Imaginary part of self-energy for smooth disorder in different regimes for the ratio bp in dependence of the dimensionless disorder strength β_b. For $bp < 1$, the self-energy is fully determined by Γ_1 (red curve) obtained by a numerical solution of Eq. (3.33). For $bp > 1$, Γ_2, given by Eq. (3.34) and the green curve, determines the self-energy. The darkblue curve depicts Γ for $bp \sim 1$ given by the numerical solution of Eq. (3.38).

The self-energy in the three regimes is depicted in Fig. 3.6 in dependence of the dimensionless disorder strength. An illustration of the self-energy in dependence of momentum for the to cases $bp \lessgtr 1$ is presented in Figs. 3.7a) and b).

According to these results, the density of states is full determined by Γ_1 since Γ_2 is absent for large momenta cf. Eq. (3.37). The density of states is thus given by

$$\nu(\varepsilon = 0) = \int_0^{1/b} \frac{d^3q}{(2\pi)^3} \frac{\Gamma_1}{\Gamma_1^2 + v^2q^2} = \frac{2\Gamma_1}{\pi\gamma}. \tag{3.39}$$

We find that the behavior of the density of states does not fundamentally change within the model of smooth disorder. The density of states remains vanishing beyond $\beta_b < 1$ for $\varepsilon = 0$ and becomes finite above. In the limit of large β, the broadening can be approximated with $\Gamma_{\text{smooth}} \sim \Lambda_b\sqrt{\beta_b}$ again in full analogy to the case of pointlike impurities fully justifying our results for the conductivity in the limit of large β.

3.4 Disorder in presence of magnetic field

3.4.1 Clean case

Before we analyze disorder in presence of a finite magnetic field, we first discuss the effects of a magnetic field on the density of states without disorder. We introduced the Hamiltonian with the corresponding eigenstates of a single Weyl node in Sec. 1.2. For clarity, the Hamiltonian in the presence of a constant homogeneous magnetic field H in z direction is again states here, reading

$$\mathcal{H}\left(\mathbf{p}\right) = \int d^3\mathbf{r}\Psi^\dagger(\mathbf{r})v\boldsymbol{\sigma}\left(\mathbf{p} - \frac{e}{c}\mathbf{A}\right)\Psi(\mathbf{r}), \tag{3.40}$$

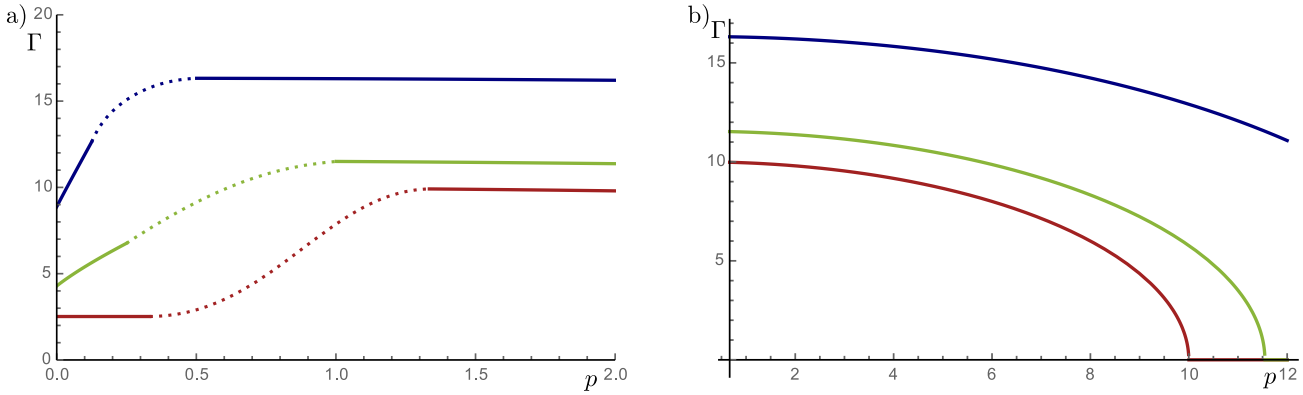

Figure 3.7: Imaginary part of self-energy for smooth disorder in dependence of momentum p for different disorder strengths. Panel a) shows the numerical evaluation of Eq. (3.33) for $bp < 1$ up to $bp = 0.5$ and Eq. (3.34) in the opposite regime $bp > 1$ starting with $bp = 2$. The dotted lines indicate the intermediate regime where the momentum dependence is not completely discussed. Panel b) is devoted to $bp > 1$ and shows the vanishing self-energy for increasing momenta. In both curves, the dimensionless disorder strength β_b is chosen as follows: darkblue curve: $\beta_b = 4$, green curve: $\beta_b = 2$, red curve: $\beta_b = 3/2$. The width of the disorder potential in momentum space is set to $1/b = 10$ in both panels.

with the vector potential $\mathbf{A}(\mathbf{r}) = (0, Hx, 0)$ in Landau gauge. Correspondingly, we reminded the reader that positions of the Landau levels in a clean Weyl semimetal, as discussed in Sec. 1.2, are given by

$$\varepsilon_0 = vp_z, \tag{3.41}$$

$$\varepsilon_n^{(\pm)} = \pm\sqrt{v^2p_z^2 + \Omega^2 n}, \tag{3.42}$$

where $\Omega = v\sqrt{2eH/c}$ is the distance between the zeroth and first LL. The eigenfunctions, which have two components ($\alpha, \beta = 1, 2$) in the space spanned by $\boldsymbol{\sigma}$, are chosen such that the wave function of the clean zeroth Landau level has only component 1 in the pseudospin space resulting in

$$\begin{aligned}\Psi_{n1}^{(\pm)}(\mathbf{r}) &= \frac{1}{\sqrt{2}}\left(1 + \frac{vp_z}{\varepsilon_n^{\pm}}\right)^{1/2} \frac{e^{i(p_y y + p_z z)}}{L}\phi_n(x - l_H^2 p_y),\\ \Psi_{n2}^{(\pm)}(\mathbf{r}) &= \mp\frac{i}{\sqrt{2}}\left(1 - \frac{vp_z}{\varepsilon_n^{\pm}}\right)^{1/2} \frac{e^{i(p_y y + p_z z)}}{L}\phi_{n-1}(x - l_H^2 p_y)\end{aligned} \tag{3.43}$$

for $n > 0$ and $\Psi_{01}^{(\pm)} = \theta(\pm p_z)\phi_0$, $\Psi_{02}^{(\pm)} = 0$ for $n = 0$. With ϕ_n, we denote the normalized eigenfunctions of free electrons in magnetic field, θ is the Heaviside step function, and $l_H = (eH/c)^{-1/2}$.

In the clean system, the retarded bare Green's function $\hat{G}_0$ is conveniently expressed as a matrix in the pseudospin space of bands $\alpha, \beta = 1, 2$:

$$G_{\alpha\beta}^{(0)} = \sum_{n\geq 0, \lambda=\pm} \frac{\Psi_{n\alpha}^{(\lambda)}\Psi_{n\beta}^{(\lambda)*}}{\varepsilon + i0 - \varepsilon_n^{\lambda}}. \tag{3.44}$$

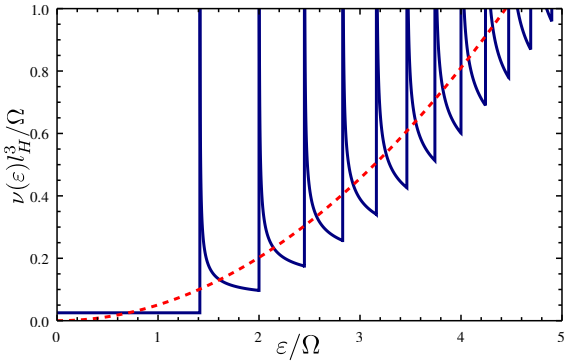

Figure 3.8: Density of states of a clean Weyl semimetal with the darkblue solid line illustrating the density of states in a finite magnetic field, Eq. (3.45), while the red dashed line corresponds to the zero magnetic field, Eq. (3.9).

We note that the summation over λ eliminates the theta-functions $\theta(\pm p_z)$ in the $n = 0$ term in Eq. (3.44). The integration over p_z is always performed from $-\infty$ to ∞ in what follows. However, the absence of states in one energy band manifests itself in a factor $1/2$ in the Green's function and in the density of states for zeroth Landau level compared to higher Landau levels.

In the presence of magnetic field, the density of states is singular at the points $\Omega\sqrt{n}$ for $n > 0$ which have a square root tail originating from the one-dimensional (p_z) dispersion of each Landau band (cf. Ref. [142]) and reads

$$\nu(\varepsilon) = \frac{\Omega^2}{8\pi^2 v^3}\left[1 + 2\sum_{n=1}^{\varepsilon^2/\Omega^2}\frac{|\varepsilon|}{\sqrt{\varepsilon^2 - \Omega^2 n}}\right]. \tag{3.45}$$

We further find, that the density of states in presence of magnetic field is finite already in the clean limit. The density of states is plotted in Fig. 3.8.

3.4.2 Born approximation

For finite magnetic field, we start the analysis of pointlike disorder with the Born approximation meaning we neglect the self-energies in Green's functions (3.6) and (3.7) for the calculation of self-energies:

$$\Sigma_1^R(\varepsilon) = \frac{\gamma\Omega^2}{4\pi v^2}\sum_{n\geq 0}\int_{-\infty}^{\infty}\frac{dp_z}{2\pi}\frac{\varepsilon + vp_z}{(\varepsilon + i0)^2 - \Omega^2 n - v^2 p_z^2}, \tag{3.46}$$

$$\Sigma_2^R(\varepsilon) = \frac{\gamma\Omega^2}{4\pi v^2}\sum_{n\geq 0}\int_{-\infty}^{\infty}\frac{dp_z}{2\pi}\frac{\varepsilon - vp_z}{(\varepsilon + i0)^2 - \Omega^2 (n+1) - v^2 p_z^2}. \tag{3.47}$$

As discussed below and similar to Sec. 3.2, the summation over n should, in fact, be restricted by an upper cutoff $N_{\max}$. We shift the summation over n in Σ_2 and find that the two self-energies only

differ by the absence of the $n = 0$ term in Σ_2:

$$\Sigma_1 - \Sigma_2 = \frac{\gamma\Omega^2}{4\pi v^2}\int_{-\infty}^{\infty}\frac{dp_z}{2\pi}\frac{\varepsilon + vp_z}{(\varepsilon + i0)^2 - v^2p_z^2} \simeq -iA + \frac{2A\varepsilon}{\pi\Lambda}. \tag{3.48}$$

Here, we introduce the parameter

$$A = \frac{\gamma\Omega^2}{8\pi v^3}, \tag{3.49}$$

and denote the bandwidth by Λ. The introduction of an ultraviolet cutoff Λ becomes necessary due to the approximation of a true energy dispersion by the Dirac-fermion one, which is, in fact, valid for low-energies. Our analysis is applicable for $\varepsilon, \Sigma(\varepsilon) \ll \Lambda$.

We learn from Eq. (3.48) that it is sufficient to calculate Σ_1. We obtain Σ_2 with the result of Σ_1 and Eq. (3.48). The term Σ_1 separated in real and imaginary part reads

$$\mathrm{Im}\Sigma_1(\varepsilon) = -A|\varepsilon|\sum_{n=0}^{N_\varepsilon}\frac{1}{\sqrt{\varepsilon^2 - \Omega^2 n}}, \tag{3.50}$$

$$\mathrm{Re}\Sigma_1(\varepsilon) = -A\varepsilon\sum_{n=N_\varepsilon+1}^{N_{\max}}\frac{1}{\sqrt{\Omega^2 n - \varepsilon^2}}. \tag{3.51}$$

The imaginary part of the self-energy under Born approximation is determined by the Landau levels below ε, while the real part is provided by the contribution of the Landau levels above ε. In Eqs. (3.50) and (3.51)

$$N_\varepsilon = \left[\frac{\varepsilon^2}{\Omega^2}\right], \tag{3.52}$$

denotes the Landau level index below energy ε, and the symbol $[\ldots]$ expresses the integer part of a number. The summation in Eq. (3.51) is restricted by the upper cutoff $N_{\max}$ determined by the ultraviolet energy cutoff Λ as follows: $N_{\max} = \Lambda^2/\Omega^2$. Thus, $N_{\max}$ denotes the index of the highest Landau level within the bandwidth Λ.

The sum in $\mathrm{Re}\Sigma_1$ is determined by the upper limit $N_{\max}$ resulting in $\mathrm{Re}\Sigma_1 \sim \varepsilon(A/\Omega)N_{\max}^{1/2}$. We assume that due to LL broadening no Landau quantization is present at the ultraviolet energies $\sim \Lambda$, we can apply the zero-H result

$$\mathrm{Re}\Sigma_1(\varepsilon) \simeq -\frac{\beta}{2}\varepsilon, \tag{3.53}$$

with

$$\beta = \frac{\gamma\Lambda}{2\pi^2 v^3}. \tag{3.54}$$

As in the absence of magnetic field, the parameter β quantifies the strength of disorder. Sufficiently strong disorder produces a real part of Born self-energy larger than ε, which clearly signifies the insufficiency of the simple Born approximation and is resolved by a full consideration of the self-consistent Born approximation, cf. Sec. 3.2. Similar to the zero-field limit, the self-consistent treatment of strong disorder dramatically changes the behavior of the density of states for strong disorder as we will discuss in Sec. 3.4.5 below.

In what follows, however, we mostly focus on the limit of weak disorder, $\beta \ll 1$. We redefine the energy ε with respect to $\mathrm{Re}\Sigma$ meaning $\varepsilon \to \tilde{\varepsilon} = \varepsilon(1 + \beta/2)$, and neglect the difference between $\tilde{\varepsilon}$ and

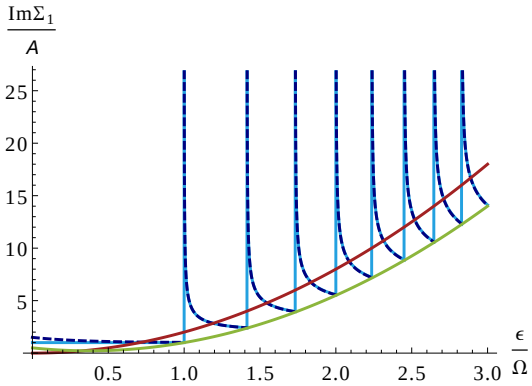

Figure 3.9: Disordered Weyl semimetal in Born approximation. $\mathrm{Im}\Sigma_1(\varepsilon)$ in units of A. The blue curve depicts Eq. (3.50), the darkblue, dashed curve Eq. (3.56), the green curve shows $2(\varepsilon/\Omega)^2 - 3\varepsilon/2\Omega + 1/2$ [minima in Eq. (3.56)], and the red illustrates, $2(\varepsilon/\Omega)^2$, the result without magnetic field.

ε in the calculation of the imaginary part of self-energy. For $|\varepsilon| < \Omega$, the imaginary part of the Born self-energy is expressed as

$$\mathrm{Im}\Sigma_1 = -A, \qquad \mathrm{Im}\Sigma_2 = 0. \tag{3.55}$$

For higher energies, the Euler-Maclaurin formula is applied for the sum over $n < N_\varepsilon - 1$. Thus, the imaginary part of the Born self-energy yields

$$\mathrm{Im}\Sigma_1(\varepsilon) \simeq -A\left[\frac{1}{\sqrt{\varepsilon^2 - \Omega^2 N_\varepsilon}} - \frac{2|\varepsilon|}{\Omega^2}\sqrt{\varepsilon^2 - (N_\varepsilon - 1)\Omega^2} + \frac{1}{2}\left(1 + \frac{|\varepsilon|}{\sqrt{\varepsilon^2 - (N_\varepsilon - 1)\Omega^2}}\right) + \frac{2\varepsilon^2}{\Omega^2}\right]. \tag{3.56}$$

This result is depicted in Fig. 3.9. The terms in Eq. (3.56) resemble the different contributions to the density of states. In particular, the first term yields the square-root divergence at the positions of LLs, while the last term is responsible for the parabolic background similarly to the zero-H case.

Motivated by the square root singularities for LL broadening within the Born approximation (3.56), we consider the Landau level broadening now with the self-consistent Born approximation (SCBA). Introducing disorder-induced self-energies in the Green's functions should resolve these divergences.

The SCBA equations (3.3), (3.6) and (3.7) with the disorder correlator (3.4) within white-noise disorder have the form (below $z = vp_z$):

$$\Sigma_1(\varepsilon) = A\sum_{n\geq 0}\int_{-\infty}^{\infty} dz\, \frac{\varepsilon - \Sigma_2 + z}{(\varepsilon - \Sigma_1 - z)(\varepsilon - \Sigma_2 + z) - \Omega^2 n}, \tag{3.57}$$

$$\Sigma_2(\varepsilon) = A\sum_{n\geq 1}\int_{-\infty}^{\infty} dz\, \frac{\varepsilon - \Sigma_1 - z}{(\varepsilon - \Sigma_1 - z)(\varepsilon - \Sigma_2 + z) - \Omega^2 n}. \tag{3.58}$$

As above within the Born approach, the real parts of self-energies (determined by the ultraviolet cutoff Λ) are absorbed into the shifts of energies $\varepsilon \to \tilde{\varepsilon}$.

The self-consistent equations for separated LLs (the corresponding conditions will be analyzed below) are evaluated as follows. We assume that the energy is close to the bottom of the n_0-th Landau level meaning $N_\varepsilon \simeq n_0$. Thus, the term $n = n_0$ provides the main contribution in the sum over n. This term is therefore treated separately from the sum and we evaluate the sum of the remaining levels and the term $n = n_0$ differently.

3.4.3 Energies close to the lowest Landau level

Let us first consider the case of lowest energies, $|\varepsilon| \ll \Omega$ (i.e., $N_\varepsilon = 0$) in the regime of weak disorder, $\beta \ll 1$. This case is manifested by the asymmetry with respect to the zeroth LL resulting in a strong difference in the two imaginary parts of the self-energy. For the lowest LL being well separated from the others ($\mathrm{Im}\Sigma_{1,2} \ll \Omega$), higher Landau levels in the sum over n can be treated within the Born approximation, while the term of $n = 0$ should be evaluated self-consistently. This procedure immediately leads to $\mathrm{Im}\Sigma_2 = 0$ and

$$\mathrm{Im}\Sigma_1(\varepsilon) \simeq -A \int_{-\infty}^{\infty} dz \, \frac{\mathrm{Im}\Sigma_1(\varepsilon)}{(\varepsilon - z)^2 + [\mathrm{Im}\Sigma_1(\varepsilon)]^2} = -A. \tag{3.59}$$

This result is equivalent to the result of the non-self-consistent Born approximation, Sec. 3.4.2. The condition for a well separated zeroth LL translates into the condition $A < \Omega$. Compared to the absence of magnetic field, the density of states for $\varepsilon \ll \Omega$ is finite and, to the leading order, energy-independent.

First order corrections to the term $\mathrm{Im}\Sigma_2$ can be found by using Eq. (3.59) for $\varepsilon \ll \Omega$, resulting in

$$\mathrm{Im}\Sigma_2(\varepsilon) \simeq -\frac{\pi A^2}{2} \sum_{n=1}^{N_{\max}} \frac{\Omega^2 n}{(\Omega^2 n - \varepsilon^2)^{3/2}} \sim -A\beta. \tag{3.60}$$

Thus, in the limit of weak disorder, $\beta \ll 1$, $\mathrm{Im}\Sigma_2$ can be neglected for $\varepsilon \ll \Omega$. In fact, $\mathrm{Im}\Sigma_2$ becomes of the order of $\mathrm{Im}\Sigma_1$ only in the close vicinity of the first Landau level, $|\varepsilon - \Omega| \sim A$.

Let us emphasize that the self-consistent treatment of the LL broadening is fully justified for weak disorder and $\varepsilon \ll \Omega$. It was shown for 2D Dirac fermions in graphene [143] that all the renormalization effects not captured by the SCBA affect the real part of the self-energy. In the 2D case, the effect of the marginally relevant disorder could be incorporated through the renormalization of parameters (induced by the contributions of higher LLs) entering the SCBA equations for a given Landau level. The renormalization of $\mathrm{Re}\Sigma$ in the present 3D case can be neglected in the regime of weak disorder, $\beta \ll 1$. Even in two dimensions for the lowest LL, the density of states within SCBA is parametrically correct [143]. The exact shape can be calculated as performed in Refs. [144, 145]. The additional integration over the momentum p_z in 3D compared to 2D reduces the difference between the exact and SCBA results further in the limit $\varepsilon \to 0$.

3.4.4 Energies at high Landau levels

We turn now to the consideration of high energies, $\varepsilon \gg \Omega$. Already within the Born approximation, as analyzed in Sec. 3.4.2, the average broadening of LL increases with ε parabolically. This is analogous to the absence of magnetic field: $\propto A(\varepsilon/\Omega)^2 \sim \gamma\varepsilon^2/v^3$, see Fig. 3.9. Therefore, the difference between $\mathrm{Im}\Sigma_1$ and $\mathrm{Im}\Sigma_2$ is manifested by the contribution of $n = 0$ and can be neglected for energies ε away from the zeroth LL. In the following, we use $\Sigma_1 = \Sigma_2 = \Sigma$ for $\varepsilon \gg \Omega$.

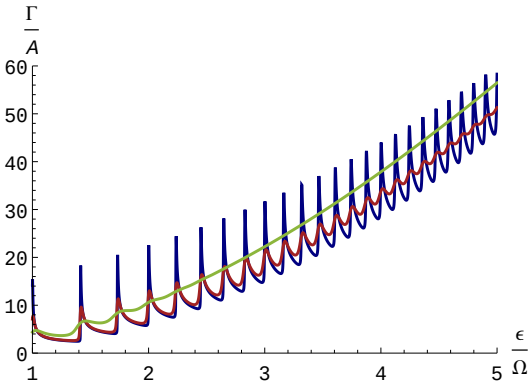

Figure 3.10: Disordered Weyl semimetal in the self-consistent Born approximation for $\varepsilon \gg \Omega$: $\Gamma(\varepsilon)$ in units of A obtained by numerical solution of Eq. (3.62). Blue, red, and green curves correspond to $A/\Omega = 10^{-4},\ 10^{-3},\ 10^{-2}$, respectively. For all curves, we choose $N_{\max} = 100$.

By introducing

$$\Gamma_{1,2}(\varepsilon) = -\mathrm{Im}\Sigma_{1,2}(\varepsilon) \tag{3.61}$$

and setting $\Gamma_1 = \Gamma_2 = \Gamma$, the self-consistent equation for $\Gamma(\varepsilon \gg \Omega)$ is given by

$$\Gamma = \sum_{n=0} \Gamma^{(n)}(\varepsilon), \tag{3.62}$$

$$\begin{aligned} \Gamma^{(n)}(\varepsilon) &= \frac{A\Gamma}{\pi} \int_{-\infty}^{\infty} dz \frac{\varepsilon^2 + \Omega^2 n + \Gamma^2}{(\varepsilon^2 - \Omega^2 n - \Gamma^2 - z^2)^2 + 4\varepsilon^2\Gamma^2} \\ &= A\ \mathrm{Re} \frac{i\varepsilon + \Gamma}{\sqrt{W_n^2 - \varepsilon^2 + 2i\varepsilon\Gamma}}. \end{aligned} \tag{3.63}$$

Here, we have introduced $\Gamma^{(n)}(\varepsilon)$ denoting the contribution of the nth Landau level to the total broadening $\Gamma(\varepsilon)$. Note that each term $\Gamma^{(n)}(\varepsilon)$ of Eq. (3.63) depends on the total broadening Γ rather than the partial $\Gamma^{(n)}$. Furthermore, we find that the position of the nth Landau level is shifted by disorder. This is manifested by the fact that $\Omega^2 n$ appears only in the combination

$$W_n^2 = \Omega^2 n + \Gamma^2. \tag{3.64}$$

In the case of weak disorder, all energies $\Omega \ll \varepsilon \ll \Lambda$ fulfill the condition $\varepsilon \gg \Gamma(\varepsilon)$, so that Eq. (3.63) can be written as

$$\Gamma^{(n)}(\varepsilon) \simeq A\varepsilon \frac{\sqrt{\varepsilon^2 - W_n^2 + \sqrt{(W_n^2 - \varepsilon^2)^2 + 4\varepsilon^2\Gamma^2}}}{\sqrt{2}\ \sqrt{(W_n^2 - \varepsilon^2)^2 + 4\varepsilon^2\Gamma^2}}. \tag{3.65}$$

The limit $\varepsilon \to \infty$ yields $\Gamma^{(n)}(\varepsilon) \to A$, while $\varepsilon \ll W_n$ results in $\Gamma^{(n)}(\varepsilon) \to A\Gamma/W_n$. Thus, the self-energy $\Gamma(\varepsilon)$ of the nth Landau level is increased by A when ε crosses W_n. This can be seen in Fig. 3.10 where the solution of the self-consistent equation (3.62) is shown for $A/\Omega = 10^{-4},\ 10^{-3},\ 10^{-2}$.

We fix now the Landau-level index $n_0 \gg 1$ and consider the range of energies around W_{n_0}. Under the assumption of well separated Landau levels below n_0, we disregard Γ in all terms with $n < n_0$:

$$\sum_{n=0}^{n_0-1} \Gamma^{(n)}(\varepsilon) \simeq A \sum_{n=0}^{n_0-1} \frac{\varepsilon}{\sqrt{\varepsilon^2 - W_n^2}} \simeq 2An_0. \tag{3.66}$$

Landau levels with $n > n_0 + 1$ contribute with the dominant term proportional to $N_{\max}$ hence being negligible for weak disorder:

$$\sum_{n=n_0+1} \Gamma^{(n)}(\varepsilon) \simeq A \sum_{n=n_0+1}^{N_{\max}} \frac{W_n^2 \Gamma}{(W_n^2 - \varepsilon^2)^{3/2}} \sim \Gamma\beta \ll \Gamma. \tag{3.67}$$

Finally, we consider the contribution of the n_0th Landau level (closest to the energy ε) to the self-energy. For $|\varepsilon - W_{n_0}| \ll W_{n_0}$, this can be further simplified, reading

$$\Gamma^{(n_0)}(\varepsilon) \simeq \frac{A\sqrt{W_{n_0}}}{2} \frac{\sqrt{\varepsilon - W_{n_0} + \sqrt{(W_{n_0} - \varepsilon)^2 + \Gamma^2}}}{\sqrt{(W_{n_0} - \varepsilon)^2 + \Gamma^2}}. \tag{3.68}$$

Exactly at $\varepsilon = W_{n_0}$, we particularly find

$$\Gamma^{(n_0)}(\varepsilon = W_{n_0}) \simeq \frac{A\varepsilon^{1/2}}{2\Gamma^{1/2}}. \tag{3.69}$$

To determine the self-consistent equation, we use Eqs. (3.66) and (3.68). When ε is close to W_{n_0}, the self-consistency equation can be written as:

$$\Gamma(\varepsilon) \simeq \frac{2A\varepsilon^2}{\Omega^2} + \frac{A\sqrt{\varepsilon}}{2} \frac{\sqrt{\varepsilon - w_\varepsilon + \sqrt{(w_\varepsilon - \varepsilon)^2 + \Gamma^2(\varepsilon)}}}{\sqrt{(w_\varepsilon - \varepsilon)^2 + \Gamma^2(\varepsilon)}}, \tag{3.70}$$

where $w_\varepsilon \simeq \Omega\sqrt{N_\varepsilon}$ ensures that the right hand side of Eq. (3.70) only depends explicitly on ε, as required.

The self-consistency equation exactly at $\varepsilon = W_{n_0}$ yields:

$$\Gamma = \frac{2A\varepsilon^2}{\Omega^2} + \frac{A\varepsilon^{1/2}}{2\Gamma^{1/2}}. \tag{3.71}$$

We observe that the broadening for sufficiently small energies is determined by the self-consistent contribution of the particular Landau level of consideration, while the broadening for larger energies is dominated by the zero-H result stemming from lower Landau levels. In formulas, this is expressed as

$$\Gamma(\varepsilon = W_{n_0}) \simeq \begin{cases} (A/2)^{2/3}\varepsilon^{1/3}, & \Omega \ll \varepsilon \ll \varepsilon_*, \\ 2A(\varepsilon/\Omega)^2, & \varepsilon \gg \varepsilon_*, \end{cases} \tag{3.72}$$

where

$$\varepsilon_* \sim \Omega(\Omega/A)^{1/5} \propto \frac{H^{2/5}}{\gamma^{1/5}}. \tag{3.73}$$

Below ε_*, Landau levels are fully separated whereas above ε_*, the background density of states is large. As inherited from the clean density of states, each peak in $\Gamma(\varepsilon)$ is non-symmetric with respect to W_{n_0}. This is discussed App. A.3, where shape of the LL broadening is analyzed in detail.

The broadening for high energies should show the same behavior as in absence of magnetic field. Indeed, we recover the zero-H result for $\Gamma(\varepsilon)$ in the limit $\varepsilon > \varepsilon_*$ expressed in terms of the energy:

$$\Gamma(\varepsilon) = \frac{\gamma}{4\pi v^3}\varepsilon^2. \tag{3.74}$$

As expected, the magnetic field has dropped out from the result leading to a LL broadening dominated by the $H = 0$ result for $\varepsilon > \varepsilon_*$. In fact, considering the corrections to the broadening at $\varepsilon > \varepsilon_*$, we observe that the Landau level quantization of the density of states remains intact in a finite range of energies above ϵ_*. This is analyzed in detail in Sec. 3.4.6. The appearance of the energy scale ε_* should be contrasted with the 2D case. In the 2D case of graphene, a single scale distinguishes between the regimes of strong and weak Landau quantization. Finally, it should be emphasized that magnetooscillations in Weyl semimetals were already addressed in Ref. [146] with phenomenological energy-independent broadening. However, we could show, that the energy dependence of Γ is very rich.

3.4.5 Strong Disorder

We discuss now briefly the effect of strong disorder, $\beta \gtrsim 1$, in the presence of a finite magnetic field. As it can be observed by the consideration of the weak-disorder case, cf. Eq. (3.60), the difference between the two self-energies, Σ_1 and Σ_2, becomes subordinate even at $\varepsilon = 0$ for strong disorder. The evaluation of the sum over n in Eqs. (3.57) and (3.58) leads to a qualitative change in the behavior of the imaginary part of self-energy (and thus of the density of states) at $4A\sqrt{N_{max}} = \pi\Omega$. Similar as in absence of magnetic field, cf. Sec. 3.2, this implies the existence of a critical disorder strength, $\gamma_{c,mag} = 2\pi^2 v^3/\Lambda$ separating the two regimes. Remarkably, the critical disorder strength $\gamma_{c,mag}$ found in a strong magnetic field proves to be equal to the zero-field value γ_c. As already discussed in Sec. 3.2, the emergence of this critical disorder strength γ_c in zero-field was reported in Refs. [21, 22, 147, 148] and [18].

The SCBA equation for strong disorder for $\varepsilon \gg \Omega$ is solved by

$$\Gamma \simeq \frac{2\Omega\sqrt{N_{\max}}}{\pi} - \frac{\Omega^2}{2A} = 4\pi v^3 \left(\frac{1}{\gamma_c} - \frac{1}{\gamma}\right), \tag{3.75}$$

which is equal to the zero-H result obtained in Ref. [147] and discussed in Sec. 3.2. When γ is substantially larger than γ_c (i.e., $\gamma - \gamma_c \gtrsim \gamma_c$), the broadening becomes of the order of the ultraviolet cutoff,

$$\Gamma \sim \Lambda, \tag{3.76}$$

which ensures that all Landau levels overlap. A comparison to the results in absence of magnetic field shows that the results matches for $\Gamma < \Lambda$, cf. Eq. (3.15). In the opposite regime, $\Gamma > \Lambda$, the approximations performed within the calculations in presence of magnetic field are no longer valid. Since the effect of magnetic field is already absent close to the disorder critical point, we expect that in strongest disorder, the results of zero magnetic field apply. However, away from strongest disorder, the results presented in this section apply. Further, at $\varepsilon \ll \Omega$, the solution of the SCBA equations yields for the LL broadening

$$\mathrm{Im}\Sigma_1 \simeq \mathrm{Im}\Sigma_2 \sim -\Omega\sqrt{N_{max}} \sim \Lambda. \tag{3.77}$$

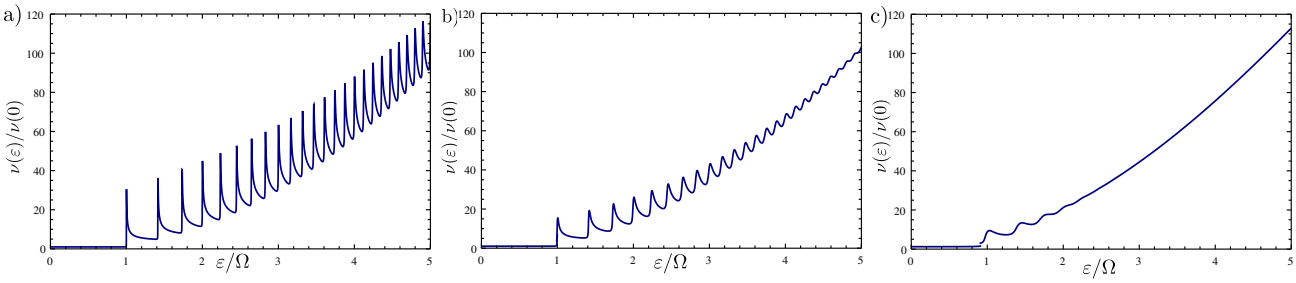

Figure 3.11: Density of states, $\nu(\varepsilon)$, of a Weyl semimetal within self-consistent Born approximation in units of $\nu(0) \propto H$ in presence of magnetic field [Eq. (3.83)], as obtained from Eq. (3.62) for $\varepsilon \gtrsim \Omega$ and Eq. (3.59) for $\varepsilon < \Omega$. The curves corresponds to a) $A/\Omega = 10^{-4}$, b) $A/\Omega = 10^{-3}$, and c) $A/\Omega = 10^{-2}$. The value $N_{\max} = 100$ was used.

Thus, when disorder is substantially stronger than the critical one, even the zeroth LL overlaps with the rest of the spectrum.

The real part of the self energy for $\beta = \gamma/\gamma_c \gg 1$ is given by

$$\mathrm{Re}\Sigma_1 \simeq \mathrm{Re}\Sigma_2 \simeq \frac{\beta - 2}{\beta - 1}\varepsilon, \tag{3.78}$$

in full analogy to the absence of magnetic field, cf. Sec. 3.2, Eq. (3.18). Note, that in absence of magnetic field the parameter β was replaced by $\tilde{\beta}$ where terms of the order of Γ/Λ become important for $\Lambda \sim \Gamma$. These effects are not considered in the presence of magnetic field. Therefore, Eq. (3.78), is applicable close to the disorder order critical point. However, under the consideration of the full SCBA formulas in the presence of magnetic field for strongest disorder, we would expect similar terms providing a diffusion dominated conductivity.

In this thesis, we do not address the critical regime near the transition from weak to strong disorder at $\beta \sim 1$ in finite magnetic field. The effect of magnetic field near the transition remains a very interesting question for future work.

3.4.6 Density of States

In this section, we address the density of states in finite magnetic field which is related to the self-energy as follows:

$$\nu(\varepsilon) = -\frac{1}{\pi}\mathrm{Tr}\ \mathrm{Im}G = -\frac{1}{\pi\gamma}\left(\mathrm{Im}\Sigma_1 + \mathrm{Im}\Sigma_2\right). \tag{3.79}$$

We apply this formula by plotting the numerically obtained solutions of the SCBA equation in the case of weak disorder in Fig. 3.11. The three figures illustrate the evolution of the density of states for different parameters $\gamma\Omega/v^3$ (proportional to the disorder strength and to the square root of the magnetic field) increasing from Fig. 3.11a)–c).

Due to the integration over p_z, the Landau levels are broadened even in the clean case, cf. Fig. 3.8, resulting in divergent peaks at $\varepsilon_n(p_z)$ located on top of the background density of states. In the clean limit, however, these peaks are well resolved for all energies. Finite disorder suppresses the peaks

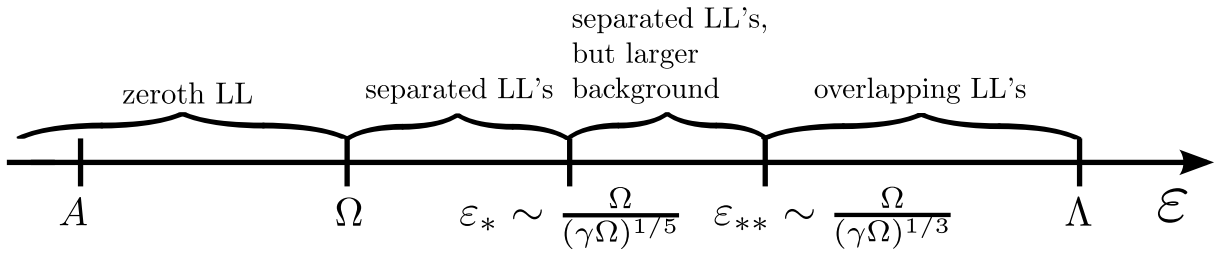

Figure 3.12: Relevant energy scales and dominant contributions to the density of states of a disordered Weyl semimetal (for brevity, we have set $v = 1$).

with increasing energy such that the Landau levels eventually fully overlap at high energies. In the following, we analyze the characteristic values of the Landau level index where the density of states changes qualitatively.

For $\varepsilon \gtrsim \varepsilon_*$, the broadening of Landau levels is dominated by the background (zero-H) contribution. From Eq. (3.73), we find that the corresponding LL index $N_* = \varepsilon_*^2/\Omega^2$ decreases with increasing H:

$$N_* \sim (\Omega/A)^{2/5} \propto \frac{1}{\gamma^{2/5} H^{1/5}}. \tag{3.80}$$

In order to determine if LLs are resolved, we need to check the corresponding condition $\varepsilon_{n+1}(p_z = 0) - \varepsilon_n(p_z = 0) > \Gamma$. For energies $\Omega \ll \varepsilon \ll \Omega(\Omega/A)^{1/5}$, this condition is fulfilled with the width of high Landau levels being smaller than the distance Ω^2/ε between them. As a consequence, at $\varepsilon \sim \varepsilon^*$, Landau levels are still resolved on top of the large background, but the height of the small peaks $A^{1/2}\Omega/\varepsilon^{1/2}$, Eq. (3.71), is lower than the height of the background. Thus, the latter then dominates the broadening.

In the regime $\varepsilon > \varepsilon_{**} > \varepsilon_*$, the neighboring peaks fully overlap and the broadening is given by the zero-H result. The corresponding energy is given by

$$A\frac{\varepsilon^2}{\Omega^2} \sim \frac{\Omega^2}{\varepsilon} \quad \Rightarrow \quad \varepsilon \sim \varepsilon_{**} = \Omega \left(\frac{\Omega}{A}\right)^{1/3}, \tag{3.81}$$

with the LL index associated with

$$N_{**} = \frac{\varepsilon_{**}^2}{\Omega^2} = \left(\frac{\Omega}{A}\right)^{2/3} \propto \frac{1}{\gamma^{2/3} H^{1/3}}. \tag{3.82}$$

Similarly to N_*, the LL index for overlapping LLs decreases with increasing magnetic field. We emphasize that in contrast to conventional expectations, the number of separated LLs is decreasing for increasing magnetic field.

For fixed disorder strength, the Landau level index N_{**}, corresponding to the starting point of overlapping, becomes smaller with an increase of magnetic field. This behavior is very exceptional since it is opposite to the case in conventional semiconductors. The energy ε_{**} associated with the start of overlapping of LL increases with H as $H^{1/3}$. However, the behavior with disorder strength

qualitatively confirms with intuitive expectations. This means specifically that with increasing disorder the number of separated Landau levels decreases corresponding to a decreasing energy range.

An important feature of the density of states in presence of magnetic field is that even in weak disorder the density of states at the Weyl node (zero energy) is finite. Specifically, the density of states at $\varepsilon = 0$ is linear in magnetic field:

$$\nu(0) = \frac{A}{\pi\gamma} = \frac{\Omega^2}{8\pi^2 v^3} \propto H. \tag{3.83}$$

It is worth to stress that a finite value of the density of states at the degeneracy point will result in a finite conductivity independently of the order of limits $\omega \to 0$ and $T \to 0$. From this perspective, a finite magnetic field has the same effect as a strong disorder.

All analytically obtained features of the density of states (cf. Fig. 3.12) are perfectly observed in Figs. 3.11a)–c). First, it can be observed that for weak disorder and weak magnetic field many LLs are separated. Furthermore, the number of separated Landau levels decreases with increasing magnetic field or with increasing disorder. Second, in an intermediate range of energies, the density of states is mainly determined by the background value but Landau levels are still well resolved. Third, one can see that the background density of states is equal to that in the absence of magnetic field (quadratic in energy). Finally, a finite density of states at the degeneracy point dependent on the magnetic field is created by a finite magnetic field.

3.5 Coulomb impurities

In the previous section, we discussed the density of states in a model of white-noise disorder in finite magnetic field. We are now going to introduce a model of the more realistic case of screened Coulomb impurities. Coulomb impurities are relevant since scattering on donors and acceptors are important processes in a 3D system. The model will be of particular importance in finite magnetic field for the magnetoresistance where strongly screened Coulomb impurities provide a linear magnetoresistance in the ultra quantum limit [82]. Thus, we focus on this case in the proceeding section. The potential of charged (Coulomb) impurity is given by

$$U(\mathbf{k}) = \frac{4\pi e^2}{\epsilon_\infty (k^2 + \kappa^2)}, \tag{3.84}$$

where ϵ_∞ is the background dielectric constant. The parameter κ denotes the inverse Debye screening radius, defined via

$$\kappa^2 = \frac{4\pi e^2}{\epsilon_\infty}\frac{\partial N(\Omega,\mu,T)}{\partial\mu} = \frac{e^2}{\pi\varepsilon_\infty v^3}\begin{cases} \Omega^2, & \Omega \gg T,\mu, \\ \pi^2 T^2/3, & T \gg \Omega,\mu, \\ \mu^2/2 & \mu \gg \Omega, T. \end{cases} \tag{3.85}$$

Here, $\partial N/\partial\mu$ is the fermion compressibility with the effect of disorder on the thermodynamic density of states being neglected. However, in the limit $T, H, \mu \to 0$, the impurity contribution can be included in a self-consistent way, as we will discuss below.

Hereinafter, we shall assume that the "fine-structure" constant is relatively large,

$$e^2/v \gtrsim 1. \tag{3.86}$$

In a realistic situation, the fine-structure constant is of order of unity leading to κ being of the order of characteristic values $k_{\text{typical}} \sim \max(\Omega, T)/v$ of the wave vector k. By applying condition (3.86), it is possible to describe the screened Coulomb disorder by an effective pointlike correlator

$$\left\langle U(\mathbf{r})U(\mathbf{r}')\right\rangle \simeq \gamma(H,T)\delta(\mathbf{r}-\mathbf{r}') \tag{3.87}$$

to govern the parametric dependence of the conductivity (without numerical prefactors).

Thus, the correlator (3.87) is associated with a white-noise disorder strength dependent on magnetic field, temperature and chemical potential,

$$\gamma(H,T,\mu) = N_{\text{imp}}\left(\frac{\partial N(\Omega,T,\mu)}{\partial\mu}\right)^{-2} \sim N_{\text{imp}}v^6\begin{cases}\Omega^{-4}, & \Omega \gg T,\mu,\\ T^{-4}, & T \gg \Omega,\mu,\\ \mu^{-4} & \mu \gg \Omega,T.\end{cases} \tag{3.88}$$

The parameter N_{imp} denotes the density of impurities. The appearance of a divergent disorder strength in the limit $T,H,\mu \to 0$ of Eq. (3.88) implies the necessity to treat the impurity screening self-consistently. In particular, at

$$\max(\Omega,T,\mu) \sim \varepsilon_{\text{imp}} = N_{\text{imp}}^{1/3}v, \tag{3.89}$$

the quasiparticle broadening $\gamma(H,T,\mu)\max(T^2,\Omega^2,\mu^2)/v^3$ becomes of the order of $\max(\Omega,T,\mu)$. Then, the screening will be dominated by the impurity-induced density of states, yielding

$$\gamma(H,T,\mu) \sim \gamma_0 = N_{\text{imp}}^{-1/3}v^2 \ll \gamma_c. \tag{3.90}$$

The comparison of the obtained disorder strength with γ_c emphasizes that for Coulomb impurities, the density of states is always finite at zero energy. This result is in agreement with the numerically obtained result in Ref. [149]. Note, that the weak-disorder approach is formally applicable under the condition $\max(\Omega,T,\mu) \gtrsim \varepsilon_{\text{imp}}$.

The case of Coulomb impurities can be employed by replacing γ with $\gamma(H,T,\mu)$ in the results of the previous section. Let us emphasize, however, that for screened Coulomb impurities Landau quantization is favored for increasing magnetic field opposite to the case of white-noise disorder. We underline this statement by using Eq. (3.88) and analyzing the condition for separation of the zeroth LL, $A < \Omega$, reading

$$\Omega > v^3/\gamma_0 = \varepsilon_{\text{imp}}. \tag{3.91}$$

Particularly, the zeroth LL is always separated in the limit $H \to \infty$. This demonstrates the crucial role of the H dependent screening. The results for Coulomb impurities are of particular importance for the magnetoresistance. Hence, we apply the above discussed disorder strength $\gamma(H,T\mu)$ in the final steps in the calculations of the magnetoresistance in Ch. 4.

3.6 Summary of Chapter 3

To conclude this chapter, we summarize and discuss the results. In general, we discussed disorder in Weyl semimetals within self-consistent Born approximations (SCBA) within three different models of disorder: (i) point-like impurities, (ii) smooth disorder, and (iii) long-range Coulomb impurities. A compact summary of the results in absence of magnetic field is provided in Tab. 3.1 where we compare the three different models of disorder.

First, we calculated the density of states in absence of magnetic field within the SCBA in Sec. 3.2, as performed in Refs. [18] for weak and strong disorder. Of particular importance for disorder in Weyl semimetals is the appearance of a disorder critical point at charge neutrality, cf. Fig. 3.1. For finite energies, weak and strong disorder are separated by a "phase" of critical disorder, cf. 3.2. In weak and strong disorder, the results for the density of states are consistent with the results obtained in Ref. [18]. This means that in the weak disorder limit, the clean density of states $\propto \varepsilon^2$ is applicable, cf. Eq. (3.16) and for strong disorder, the density of states is energy independent, cf. Eq. (3.15). In the regime of critical disorder, the obtained density of states $\propto \varepsilon^{1/2}$, cf. Eq. (3.17), is consistent with the $1/N$ expansion as obtained in Refs. [16, 17]. In the renormalization group (RG) analysis performed in $2-\epsilon$ dimensions, cf. Refs. [18, 20], the regime of critical disorder shows a linear dependence on energy in contrast to our results and those of the mean field analysis [16, 17]. However, we assume that the SCBA approach is more reliable also in the regime of critical disorder since the RG analysis is performed far from the critical dimension with $\epsilon = -1$. The prove of this statement is delegated to further work.

In the absence of magnetic field, we further evaluated the conductivity in the three regimes considering the dc limit and the ac conductivity at zero temperature. As already shown in Ref. [30], the limits of temperature to zero and external frequency to zero do not interchange in the regime of weak disorder, Eqs. (3.22) and (3.23), while for critical and strong disorder those limits are interchangeable, Eq. (3.24), (3.25), and (3.28). In Weyl semimetals, it is crucial to include vertex corrections already for pointlike impurities. This was shown in Ref. [81] for weak disorder in the dc limit. We discuss vertex corrections in the full range of disorder and for the ac conductivity. As a result, we obtain that the vertex corrections are of particular importance in the limit of strong disorder. In the limit of strongest disorder, the conductivity saturates with disorder strength originating from a diffusion dominated conductivity with a suppression of backscattering, cf. Fig. 3.5.

The limit for very strong disorder with the strongly diffusive conductivity is justified within a model of smooth disorder where strong disorder is manifested by the correlation length instead of a rather strong impurity potential. For smooth disorder, we find that the appearance of the disorder critical point persists at the Weyl point cf. Fig. 3.6. The density of states is thus vanishing below $\beta_b \sim 1$ and can be approximated with $\Gamma_{\text{smooth}} \sim \Lambda_b \sqrt{\beta_b}$ for $\beta \gg 1$ in full analogy to the case of pointlike impurities. The results in absence of magnetic field are prepared to be submitted for publication [141].

We further analyzed the density of states in pointlike impurities in the presence of a magnetic field, Sec. 3.4. The analysis was performed in the Born approximation as well as in the SCBA. We find that the broadening of Landau levels is not described in the Born approximation. To analyze the Landau level broadening in dependence of disorder, magnetic field, and energy, it is required to consider self-consistent Born approximation. This can be related to the absence of magnetic field, where the Born limit does not lead to critical disorder. The appearance of critical disorder survives in the presence of magnetic field. In the regime of strong disorder in presence of finite magnetic field, however, all Landau levels overlap, Eq. (3.76). Moreover, it is important to emphasize that the density of states at the Weyl point in presence of magnetic field is finite already without disorder, Eq. (3.83). This means that finite magnetic field has a similar effect on the density of states as strong disorder. Another salient aspect of Landau level broadening is that the magnetic field dependent broadening leads to an increase of broadening for increasing magnetic field, Fig. 3.12, which stands in strong contrast to conventional materials. Related to disorder, the Landau level broadening increases with increasing disorder strength as expected. Moreover, we find that the background density of states becomes larger than the density of states of the peaks of Landau levels before the Landau levels overlap, cf. Fig. 3.11, leading to a interesting physics in the magnetoconductivity, cf. Ch. 4. We published the results for the density of

Table 3.1: Disorder in Weyl semimetals in absence of magnetic field in the three different models of disorder: (i) pointlike impurities, (ii) smooth disorder, and (iii) long-range Coulomb impurities. The comparison is based on the differences and similarity in the density of states at the Weyl node and in the conductivity.

	$\Gamma(\varepsilon = 0)$, Density of states		conductivity	
Coulomb impurities	finite at the Weyl node, Eq. (3.90)		limits $\omega \to 0$ and $T \to 0$ interchangeable	
	weak	strong	weak	strong
pointlike, smooth disorder	zero, Eqs. (3.14), (3.39), and Figs. 3.1, 3.38	finite, Eqs. (3.14), (3.39), and Figs. 3.1, 3.38	$\omega \to 0$ and $T \to 0$ non-interchangeable, Eqs. (3.22) and (3.23)	$\omega \to 0$ and $T \to 0$ interchangeable, Eq. (3.28)

states in the presence of magnetic field in Ref. [83].

In Sec. 3.5, we introduced a model of screened Coulomb impurities as relevant due to scattering on donors and acceptors is important in 3D. We find that screening is dominant in the disorder potential for "fine-structure" constants in the order of unity or larger. In addition, screening depends on temperature, magnetic field and chemical potential. In particular, the magnetic field dependent screening is present in the zeros Landau level and will play an important role in the consideration of the magnetoresistance as discussed in Ch. 4.

In the presented analysis of disorder, internode scattering between the different Weyl nodes is neglected. Internodal scattering is believed to be smaller than the intranode scattering as discussed here. However, even weak internode scattering will become important for the effects as the chiral anomaly. Since this thesis is restricted to the discussion of the transversal magnetoresistance where the chiral anomaly does not play an important role, we assume that the obtained results will not be crucially affected by internode scattering.

Chapter 4

4 Magnetoresistance in Weyl semimetals

One of the main goals of the present thesis is to calculate the transversal magnetoresistance (TMR) in Weyl semimetals as it was measured in several experiments [3–9]. Transversal magnetoresistance in this case means that the magnetic field is perpendicular to the measured current and the applied electric field. In experiment, a positive, linear magnetoresistance up to high magnetic fields is observed. The linear behavior starts at very low magnetic field, where Shubnikov-de Haas oscillations (SdHO) are observed, and persists in highest fields, where the system is in the ultra quantum limit meaning only the zeroth Landau level contributes to transport. Of particular interest is also the magnitude of the measured magnetoresistance ranging from $10^4 - 10^6\%$.

Theoretically, the quantum linear magnetoresistance was obtained by Abrikosov [82] for Dirac semimetals when only the zeroth Landau level is filled. As we showed in Ref. [83], the magnetoresistance in the quantum limit strongly depends on the chosen model of disorder. This result will be reviewed in the following chapter. The linear behavior in Ref. [82] originates from the magnetic field dependent screening of Coulomb impurities which matches to our results. For pointlike impurities in the quantum limit, the magnetoresistance vanishes with $1/H$ at the charge neutrality point as discussed in Ref. [83]. This result was recently confirmed by a numerical calculation in Ref. [87]. For lower magnetic fields and at charge neutrality, the broadening of the Landau levels leads to a rich structure of regimes in particular for finite temperature. The broadening due to finite temperature was established in Ref. [83] and is presented in the proceeding chapter. Furthermore, we discuss the effects of SdHO where we considered finite chemical potential. We analyze the magnetoresistance for Coulomb impurities for a large fine structure constant, cf. Sec. 3.5. This should be contrasted to Ref. [85], where the magnetoresistance is evaluated for small fine structure constant. However, the results in Ref. [85] are consistent with our results.

Another important aspect of magnetotransport for Weyl semimetals is the chemical potential. As we will discuss below in this chapter, a finite Hall conductivity cancels the magnetoresistance (except at the peaks of the Landau levels). In real materials however, the different pairs of Weyl nodes are shifted in energy with respect to each other. This means that the whole system is close to the charge neutrality point while the different pairs of Weyl nodes can have a comparably large chemical potential. Therefore, in Sec. 4.5 we consider a model of Weyl nodes shifted in energy such that the system is at the complete charge neutrality point, cf. Fig. 4.12. The presented results for the magnetoresistance in the case of finite chemical potential and for shifted nodes is based on Ref. [84]. There is a certain overlap of our results with the results obtained in Ref. [86], where the magnetoresistance was calculated for finite chemical potential and finite temperature in Born approximation. We however go beyond these

results by using self-consistent Born approximation and consider both pointlike and charged impurities. Moreover, we consider the magnetoresistance with fixed chemical potential and fixed particle density. It is worth mentioning that the analysis is performed for non-interacting particles discarding possible contributions to the magnetoresistance by the classical memory effect, cf. Ref [88], or interactions.

In this chapter, we present the calculation of the conductivity, Sec. 4.1, and the Hall conductivity, Sec. 4.2, of a disordered Weyl semimetal. The conductivity is discussed for both finite temperature and finite chemical potential. While the Hall conductivity is absent at the charge neutrality point, we discuss the Hall conductivity for finite chemical potential and low temperature. With the results for the conductivity and Hall conductivity, we determine the magnetoresistance and compare our results with the experimental findings. The magnetoresistance is calculated within two different models of disorder: (i) pointlike impurities and (ii) charged impurities. Furthermore, the calculation is performed in several regimes of temperature and chemical potential: (i) finite temperature and zero chemical potential, Sec. 4.3, (ii) finite chemical potential and zero temperature Sec. 4.4, and (iii) a model of shifted Weyl nodes in energy corresponding to complete charge neutrality, Sec. 4.5. In each regime, we start with the analysis of pointlike impurities and continue with charged impurities. In Sec. 4.5, we discuss the results most relevant to experiment qualitatively according to the experimental observations. We summarize our findings in the end of this chapter, Sec. 4.6.

4.1 Conductivity

Using the model of disorder for finite magnetic field as introduced in Sec. 3.4, we calculate now the conductivity σ_{xx} of a Weyl semimetal within Kubo formalism, cf. Sec. 2.2. We concentrate on the case of weak disorder, $\beta \ll 1$ and will briefly discuss the case of strong disorder in end of this section. The real part of the conductivity within Kubo formalism reads

$$\sigma_{xx}(\omega,T) = \int \frac{d\varepsilon}{2\pi}\frac{f_T(\varepsilon)}{\omega}\int \frac{d^3\mathbf{p}}{(2\pi)^3}\mathrm{Tr}\left\{\left[\hat{G}^R(\varepsilon,\mathbf{p})-\hat{G}^A(\varepsilon,\mathbf{p})\right]\hat{j}_x^{\mathrm{tr}}\hat{G}^A(\varepsilon-\omega,\mathbf{p})\hat{j}_x \right.$$
$$\left. +\hat{G}^R(\varepsilon+\omega,\mathbf{p})\hat{j}_x^{\mathrm{tr}}\left[\hat{G}^R(\varepsilon,\mathbf{p})-\hat{G}^A(\varepsilon,\mathbf{p})\right]\hat{j}_x\right\}, \tag{4.1}$$

where $\hat{j}_x = ev\sigma_x$ is the bare current operator and $\hat{j}_x^{\mathrm{tr}} = V^{\mathrm{tr}}\hat{j}_x$ is the current vertex dressed by disorder with

$$V^{\mathrm{tr}} \simeq \frac{\Omega^2 + 4i\varepsilon\Gamma}{\Omega^2 + \frac{8}{3}i\varepsilon\Gamma}. \tag{4.2}$$

Here, Ω is the distance between zeroth and first LL and Γ is the LL broadening, cf. App. C.2 for the details of the calculation of the current vertex. The effect of disorder manifests itself in the use of the impurity-averaged Green's function and in the vertex corrections V^{tr}. In Weyl semimetals, the calculation of the conductivity requires to take vertex corrections into account already at the level of pointlike impurities (similar to graphene) as already discussed in Ref. [81]. For weak disorder and in the absence of magnetic field, the difference of transport scattering time and quantum scattering time is marked by the inclusion of vertex corrections which is $\tau^{\mathrm{tr}} = 3/2\tau^q$ as calculated in Ref. [81]. Therefore, we can first calculate the conductivity and include the effect of vertex corrections in the final steps of the calculation.

For $V^{\rm tr}=1$, the evaluation of the trace and the use of the orthogonality of the wave functions of the different LLs transforms Eq. (4.1) into

$$\sigma_{xx}^{(0)}\left(T\right)=\frac{e^2v^2}{T}\int\frac{d\varepsilon}{2\pi}\frac{1}{\cosh^2\left(\frac{\varepsilon-\mu}{2T}\right)}\sum_n\frac{eH}{2\pi c}\int\frac{dp_z}{2\pi}\,\mathrm{Im}G_{11}^R(\varepsilon,n,p_z)\,\mathrm{Im}G_{22}^R(\varepsilon,n,p_z), \tag{4.3}$$

where the Green's functions are written in the Landau level representation. Since the self-energy of the zeroth Landau level differs from those of the other, the following calculations are performed separately for the zeroth LL and higher LLs. For both regimes, zeroth LL and higher LLs, we derive the integral over energy and then evaluate this integral first for $\mu=0$ and then for $T=0$. For small chemical potential, $\mu<\Omega$, and low temperatures, $T<\Omega$, excitations to higher LLs are exponentially suppressed and the conductivity is dominated by the contribution of the zeroth LL. For higher temperatures, excitations to higher Landau levels are possible and therefore, the conductivity is determined by contributions of zeroth LL, separated and overlapping LLs. For $\mu>\Omega$ however, the conductivity is determined by the position of the chemical potential with respect to separated and overlapping LLs.

4.1.1 Small chemical potential, $\mu<\Omega$, and low temperature, $T<\Omega$: Zeroth Landau level

We start with the consideration of the situation when the zeroth Landau level, broadened due to disorder by the parameter $A\sim\gamma\Omega^2$, is the dominant contribution to the conductivity. This is realized under the following assumptions: (i) the zeroth LL is separated from the first one, which is fulfilled under the condition $A\ll\Omega$; (iia) for zero chemical potential $\mu=0$, temperature must fulfill $T<\Omega$; (iib) the chemical potential satisfies $\mu<\Omega$, while the temperature is close to zero, $T\to0$. The current vertex corrections are calculated in App. C.2 which are small under the conditions for transport dominated by the zeroth LL with $V^{\rm tr}(\varepsilon\ll\Omega)\sim A/\Omega\ll1$ for energies close to the Weyl node. The difference between quantum and transport scattering time in the regime of the dominant zeroth LL contribution can be disregarded in the following calculations. With a negligible real part of self-energy ($\mathrm{Re}\Sigma\sim\beta\varepsilon\ll\varepsilon$, see Sec. 3.4, and the imaginary parts $\mathrm{Im}\Sigma_1\simeq A$ and $\mathrm{Im}\Sigma_2\simeq0$, the Green's functions read

$$G_{11}^R(\varepsilon,n,p_z)\;\simeq\;\frac{\varepsilon+vp_z}{(\varepsilon+iA-vp_z)(\varepsilon+vp_z)-\Omega^2n}, \tag{4.4}$$

$$G_{22}^R(\varepsilon,n,p_z)\;\simeq\;\frac{\varepsilon+iA-vp_z}{(\varepsilon+iA-vp_z)(\varepsilon+vp_z)-\Omega^2(n+1)}. \tag{4.5}$$

Substituting Eqs. (4.4) and (4.5) in Eq. (4.3) and separating the $n=0$ term in the sum over all LLs, the conductivity is written as

$$\sigma_{xx}=\frac{e^2\Omega^4A^2}{(2\pi)^2v}\int d\varepsilon\frac{\partial f_T(\varepsilon)}{\partial\varepsilon}\int\frac{dz}{2\pi}\left\{\frac{1}{\left[(\varepsilon-z)^2+A^2\right]}\frac{1}{\left[(\varepsilon^2-z^2-\Omega^2)^2+A^2(\varepsilon+z)^2\right]}\right.$$
$$\left.+\sum_{n=1}^{N_{\max}}\frac{(\varepsilon+z)^2(n+1)}{\left[(\varepsilon^2-z^2-\Omega^2n)^2\right]\left[(\varepsilon^2-z^2-\Omega^2(n+1))^2\right]}\right\}, \tag{4.6}$$

where $N_{\max}$ is the number of LLs within the energy bandwidth Λ.

We consider first the case of zero chemical potential, $\mu = 0$, and low temperature, $T < \Omega$. Under these assumptions, we can set $\varepsilon = 0$ and arrive at ($z = vp_z$)

$$\sigma_{xx} = \frac{e^2\Omega^4A^2}{2\pi^2 v}\sum_{n=0}^{\infty}\int\frac{dz}{2\pi}\left\{\frac{z^2}{\left[(z^2+\Omega^2 n)^2+A^2z^2\right]}\frac{(n+1)}{\left[(z^2+\Omega^2(n+1))^2+A^2z^2\right]}\right\}. \tag{4.7}$$

Evaluating the remaining integral under the condition $A < \Omega$ (condition for separation of the zeroth and first Landau level), we find that the sum for $n > 0$ converges and contributes as $e^2A^2/(\Omega v)$. The terms for $n = 0$ provide however a contribution as e^2A/v. Thus, the conductivity for $\mu = 0$ and $T < \Omega$ is dominated by the zeroth Landau level, yielding

$$\sigma_{xx}(T < \Omega < v^3/\gamma) \simeq \frac{e^2A}{(2\pi)^2 v} = \frac{e^2}{16\pi^3}\frac{\gamma\Omega^2}{v^4} \propto \gamma H. \tag{4.8}$$

The resulting conductivity is proportional to both disorder strength and magnetic field.

For finite chemical potential, $\mu < \Omega$, the integration over ε is performed for $T = 0$. As for finite temperature, we find that the contribution of non-zero Landau levels, $n > 0$ in the summation above, is of the order $e^2A^2/(\Omega v)$. The dominant term is coming from the zeroth LL, reading

$$\sigma_{xx} = \frac{e^2\Omega^4A^2}{(2\pi)^2 v}\int\frac{dz}{2\pi}\frac{1}{\left[(\mu-z)^2+A^2\right]\left[(z^2+\Omega^2)^2\right]} \simeq \frac{e^2A}{(2\pi)^2 v}, \tag{4.9}$$

which is equal to the result of $\mu = 0$, see Eq. (4.8). The corrections to Eq. (4.9) for a finite but small chemical potential, $\mu < \Omega$, are small in the parameter $A\mu^2/\Omega^3$ and do not essentially affect σ_{xx}.

4.1.2 Large chemical potential, $\mu > \Omega$, and high temperature, $T > \Omega$

For high temperatures, $T > \Omega$ or large chemical potentials, $\mu > \Omega$, the situation is more subtle. As analyzed in Sec. 3.4, the spectrum is subdivided in three domains for a given magnetic field: (i) in the spectrum of the low-energy part the Landau levels are separated, (ii) the intermediate region consists of separated Landau levels, but the height of an individual LL is small compared to the background density of states, and, finally, (iii) the LLs overlap for higher energies. For high temperatures, $T > \Omega$, energies $\varepsilon > \Omega$ are involved in thermal averaging such that these three domains will contribute to the conductivity. At low temperatures, the three domains become apparent due to the position of the chemical potential which will strongly affect the conductivity. The unusual broadening of LLs will lead to an unconventional shape of the SdHO.

In the following, we will derive the general properties of the conductivity within Kubo formalism. In view of this result, we will analyze the conductivity first for finite temperature and $\mu = 0$ and second for low temperature $T \sim 0$ and finite chemical potential. In both regimes, the structure of the spectrum leads to a distinction between the three different cases: (i) fully separated LLs, (ii) separated LLs, but large background density of states, and (iii) fully overlapping LLs. For all three regimes, we can neglect the energy band asymmetry and write the self-energy in terms of LL broadening: $\mathrm{Im}\Sigma_1 = \mathrm{Im}\Sigma_2 = -i\Gamma$. The Green functions are of the form

$$G^R_{11}(\varepsilon, n, p_z) \simeq \frac{\varepsilon + vp_z + i\Gamma}{(\varepsilon+i\Gamma)^2 - v^2p_z^2 - \Omega^2 n}, \tag{4.10}$$

$$G^R_{22}(\varepsilon, n, p_z) \simeq \frac{\varepsilon + vp_z + i\Gamma}{(\varepsilon+i\Gamma)^2 - v^2p_z^2 - \Omega^2(n+1)}, \tag{4.11}$$

We substitute these Green functions into the formula for the conductivity (4.3) and perform the summation over n and integration over p_z. The details of the calculation can be found in App. B.1. The result is given by

$$\sigma_{xx} = \frac{e^2\Omega^2}{2\pi^2 v}\int d\varepsilon \frac{df_T(\varepsilon)}{d\varepsilon}\frac{2\Gamma\varepsilon^4}{\Omega^2\left[\Omega^4+(4\varepsilon\Gamma)^2\right]}\left[\frac{4}{3}+\frac{\Omega^2}{\varepsilon}\left(\frac{\Gamma}{A\varepsilon}-\frac{2\varepsilon}{\Omega^2}\right)\right]. \tag{4.12}$$

The magnetoconductivity can be expressed by the semiclassical Drude formula in the three domains of the spectrum of the density of states with an energy-dependent transport scattering time τ^{tr} and an effective cyclotron frequency $\omega_c(\varepsilon)$, reading

$$\sigma_{xx}^{D} = \frac{e^2v^2}{6\pi}\int \frac{d\varepsilon}{4T\cosh^2\left(\frac{\varepsilon-\mu}{2T}\right)}\,\frac{\nu(\varepsilon)\tau_{\mathrm{tr}}(\varepsilon)}{1+\omega_c^2(\varepsilon)[\tau_{\mathrm{tr}}(\varepsilon)]^2}. \tag{4.13}$$

Here, the transport scattering time, $\tau_{\mathrm{tr}}(\varepsilon)$, takes into account the current vertex corrections in j_x^{tr}, calculated in App. C.2. The transport scattering time is related to the quantum time $\tau_q = (2\Gamma)^{-1}$ via $\tau_{\mathrm{tr}} = (3/2)\tau_q$.

The above statement, that the magnetoconductivity can be expressed by the semiclassical Drude formula, can be understood by the following relations: the Landau level broadening for energies $\varepsilon \gg \varepsilon^*$, which holds for overlapping Landau levels and for large background density of states compared to the particular Landau levels, is given by

$$\Gamma(\varepsilon) = 2A\frac{\varepsilon^2}{\Omega^2} = \frac{3}{4\tau_{\mathrm{tr}}(\varepsilon)}. \tag{4.14}$$

The SCBA relation between the density of states and the scattering time is

$$\nu(\varepsilon)\tau_{\mathrm{tr}}(\varepsilon) = \frac{3}{4\pi\gamma}, \tag{4.15}$$

and the semiclassical expression for the cyclotron frequency in the linear spectrum yields

$$\omega_c(\varepsilon) = \frac{v^2}{l_H^2\varepsilon} = \frac{\Omega^2}{2\varepsilon}. \tag{4.16}$$

Using Eq. (4.14), we can express the conductivity for energies $\varepsilon \gg \varepsilon^*$ as:

$$\sigma_{xx} \simeq \frac{e^2}{\pi^2}\,\frac{A\Omega^2}{vT}\int \frac{d\varepsilon}{\cosh^2\left(\frac{\varepsilon-\mu}{2T}\right)}\frac{\varepsilon^6}{(8A\varepsilon^3)^2+9\Omega^8/4}. \tag{4.17}$$

Now, we use Eq. (4.17) to evaluate the conductivity for $\mu = 0$ and finite temperature.

For high temperatures, $T > \Omega$, in the energy range $\Omega < \varepsilon < \varepsilon_*$, where Landau levels are separated, thermal averaging effectuates that the conductivity is still dominated by the low-lying LLs with $n < N_\varepsilon$, leading to Eq. (4.17) also in this regime. This argument is presented in App. B.1. Therefore, the semiclassical Drude formula (4.13) can be applied for all temperatures $T \gg \Omega$. For graphene, a similar result was obtained at the charge neutrality point in Refs. [150] and [151].

In the following, we analyze the magnetic-field dependence of the conductivity for $T > \Omega$. For fully separated Landau levels and separated Landau levels with large background, $\varepsilon < \varepsilon_{**} = \Omega(\Omega/A)^{1/3}$, the denominator of the integrand in Eq. (4.17) is dominated by Ω^8, leading to

$$\sigma_{xx} \simeq \frac{4e^2}{9\pi^2} \frac{A\Omega^2}{vT} \int \frac{d\varepsilon}{\cosh^2\left(\frac{\varepsilon}{2T}\right)} \frac{\varepsilon^6}{\Omega^8} = \frac{62\pi^3}{189} \frac{e^2\gamma T^6}{v^4\Omega^4} \propto \frac{1}{H^2} \tag{4.18}$$

for $\Omega < T < \varepsilon_{**}$. For higher temperatures, $T > \varepsilon_{**}$, the term proportional to Ω^8 in the denominator of the integrand is negligible in Eq. (4.17), which results in

$$\sigma_{xx} \simeq \frac{e^2}{\pi^2} \frac{A\Omega^2}{vT} \int \frac{d\varepsilon}{\cosh^2\left(\frac{\varepsilon}{2T}\right)} \frac{\varepsilon^6}{(8A\varepsilon^3)^2} = \frac{e^2v^2}{2\pi\gamma}. \tag{4.19}$$

Here, we obtained just the conductivity in the absence of magnetic field. The magnetic field dependent correction to this result, determining the low-field magnetoresistance, yields

$$\delta\sigma_{xx} \simeq -\frac{e^2v^3}{4} \left(\frac{\pi}{18}\right)^{1/3} \frac{\Omega^{2/3}}{\gamma^{4/3}T} \propto -\frac{H^{1/3}}{\gamma^{4/3}T}. \tag{4.20}$$

This correction is non-analytic in H.

The behavior of all regimes in the temperature-magnetic field plane is visualized in Fig. 4.1 where the scaling of the dominant contribution(s) to the conductivity is shown. We find that the conductivity is dominated by the Drude formula (4.13) down to the lowest Landau level, $T \sim \Omega$. The conductivity in the different regimes is summarized as

$$\sigma_{xx} \sim \begin{cases} \dfrac{e^2\gamma\Omega^2}{v^4} \propto H, & T \ll \Omega, \\ \dfrac{e^2\gamma T^6}{v^4\Omega^4} \propto \dfrac{1}{H^2}, & \Omega \ll T \ll \varepsilon_{**} = \dfrac{v\Omega^{2/3}}{\gamma^{1/3}}, \\ \dfrac{e^2v^2}{\gamma}, & T \gg \varepsilon_{**}. \end{cases} \tag{4.21}$$

The magnetic field dependent correction to the conductivity in the last regime, $T \gg \varepsilon_{**}$, is described by Eq. (4.20).

Figure 4.1 shows moreover that the limits $H \to 0$ and $T \to 0$ are not interchangeable for weak disorder. Expressed in formulas, performing first the limit $H \to 0$ and then $T \to 0$ yields

$$\lim_{T\to 0} \lim_{H\to 0} \sigma_{xx}(H,T) = \frac{e^2v^2}{2\pi\gamma}, \tag{4.22}$$

while for setting first $T \to 0$ and then $H \to 0$, we obtain

$$\lim_{H\to 0} \lim_{T\to 0} \sigma_{xx}(H,T) = 0. \tag{4.23}$$

This emphasizes the peculiar transport properties at the Weyl point. As discussed in Sec. 3.2 and first considered in Ref. [30], a similar behavior was also found in the absence of magnetic field. Specifically, in absence of magnetic field, a distinction between the order of the limits $T \to 0$ and $\omega \to 0$ was mandatory

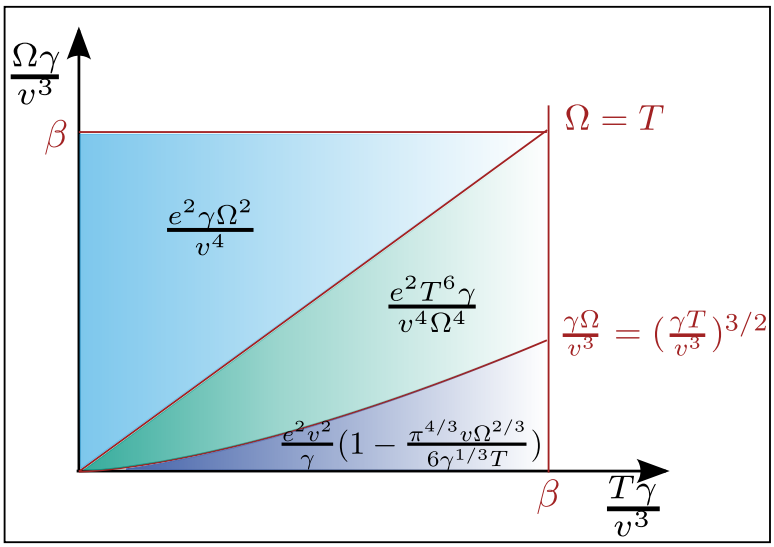

Figure 4.1: Dominant scaling behavior of the conductivity σ_{xx} in a Weyl semimetal for weak white-noise disorder as a function of temperature and magnetic field in each of the parameter regime is shown. Equations describing borderlines between the domains are also indicated.

for weak disorder, while in the strong disorder regime, the order of the limits was interchangeable (cf. Refs. [152] and [30] and Sec. 3.2 for details). Due to a finite density of states at the Weyl point in the presence of magnetic field, the limits $\omega \to 0$ and $T \to 0$ become interchangeable also for weak disorder. The elimination of the non-interchangeability of two limits by magnetic field (for any disorder strength) or by strong disorder is reasoned by the generation of a finite density of states at the Dirac point ($\varepsilon = 0$).

Now, we turn to the consideration of finite, large chemical potential, $\mu > \Omega$ and low temperature. The definition of low temperature differs for the domains of fully separated and overlapping Landau levels. We will discuss the exact condition in the corresponding paragraphs. As for finite temperature, Eqs. (4.12) and (4.17) apply for the magnetoconductivity. First, let us consider the domain of fully separated LLs. The relevant energies to ensure the separation of Landau levels satisfy $\Omega \ll \varepsilon \ll \Omega(\Omega/A)^{1/5}$. Under the assumption that the chemical potential is located within one of the LLs and the temperature is low (lower then Landau level width), the conductivity for a general LL broadening is given by the second term in Eq. (4.12), reading

$$\sigma_{xx} \simeq \frac{e^2\Omega^2}{\pi^2 v A}\int_{-\infty}^{\infty} d\varepsilon \delta(\varepsilon-\mu)\frac{4\Gamma^2\varepsilon^2}{9\Omega^4} \simeq \frac{4e^2\mu^2\Gamma^2}{9\pi^2 v A\Omega^2}. \tag{4.24}$$

The broadening of the LLs in Weyl semimetals in general is discussed in App. A.3. In the following, we will however distinguish between the Landau levels broadening at the peak of the Landau level and the background density of states. At the peak of one particular Landau level, the broadening is given by $\Gamma = (A/2)^{2/3}\varepsilon^{1/3}$, which results in the conductivity in the center of LLs (in the following denoted by $\sigma_{xx}^{\text{peak}}$) of

$$\sigma_{xx}^{\text{peak}} \sim \frac{\gamma^{1/3}\mu^{8/3}}{\Omega^{4/3}}. \tag{4.25}$$

With a broadening of $\Gamma \sim \gamma\varepsilon^2$ of the background density of states, the conductivity of the background, denoted by σ_{xx}^{bg}, reads

$$\sigma_{xx}^{\text{bg}} \simeq \frac{2e^2\gamma\mu^6}{9\pi^3 v^4\Omega^4}. \tag{4.26}$$

For the location of the chemical potential of $\Omega(\Omega/A)^{1/5} \ll \epsilon \ll \Omega(\Omega/A)^{1/3}$, the Landau levels are separated, but the background density of states is already large. Here, the Ω^8-term in the denominator of Eq. (4.17) dominates, leading to

$$\sigma_{xx} \simeq \frac{4e^2A\Omega^2}{9\pi^2 vT}\int \frac{d\varepsilon}{\cosh\left(\frac{\varepsilon-\mu}{2T}\right)}\frac{\varepsilon^6}{\Omega^8} = \frac{2e^2\gamma}{9\pi^3v^4\Omega^4}\left(\mu^6 + 5\pi^2\mu^4T^2 + 7\pi^4\mu^2T^4 + \frac{31}{21}\pi^6T^6\right) \simeq \frac{2e^2\gamma\mu^6}{9\pi^3v^4\Omega^4}. \tag{4.27}$$

The last step in Eq. (4.27) corresponds to the low-temperature limit (here the condition $T \ll \mu$ is sufficient).

Finally, in the regime of overlapping LLs valid for higher chemical potential, $\varepsilon > \Omega(\Omega/A)^{1/3}$, we neglect Ω^8 in the denominator of Eq. (4.17), which leads to

$$\sigma_{xx} = \frac{e^2A\Omega^2}{\pi^2 vT}\int \frac{d\varepsilon}{\cosh^2\left(\frac{\varepsilon-\mu}{2T}\right)}\frac{\varepsilon^6}{(8A\varepsilon^3)^2} = \frac{e^2v^2}{2\pi\gamma}. \tag{4.28}$$

Similar as for finite temperature, the conductivity of overlapping Landau levels and finite chemical potential coincides with the conductivity $\sigma_{xx,0}$ in the absence of magnetic field and does not depend on the chemical potential.

A summary of the results for the conductivity in the different regimes with respect to magnetic field, chemical potential, and disorder strength are given by

$$\sigma_{xx} = \frac{e^2}{\pi^2 v} \begin{cases} \dfrac{v^3\pi}{2\gamma}, & \Omega \ll \mu^{3/2}\gamma^{1/2} \\ \dfrac{2\gamma\mu^6}{9\pi v^3\Omega^4}, & \mu^{3/2}\gamma^{1/2} \ll \Omega \ll \mu^{5/4}\gamma^{1/4}, \\ \dfrac{32\pi v^3\mu^2\Gamma^2(\mu)}{9\gamma\Omega^4}, & \mu^{5/4}\gamma^{1/4} \ll \Omega < \mu, \\ \dfrac{\gamma\Omega^2}{32\pi v^3}, & \mu < \Omega \ll \gamma^{-1}. \end{cases} \tag{4.29}$$

As usual, a comparison between the results for finite temperature, Eq. (4.21), and finite chemical potential, Eq. (4.29), shows that the differences are manifested in the thermal averaging. The consequences of the thermal averaging for magnetotranstranport are discussed in more detail in Sec. 4.4.

This paragraph is concluded by a discussion of magnetooscillations for overlapping Landau levels. Magnetooscillations of the conductivity are caused by the oscillations of the density of states $\nu(\varepsilon)$ and of the transport scattering time $\tau_{\mathrm{tr}}(\varepsilon)$, see Ref. [153]. The density of states with magnetooscillations for Weyl semimetals is given by

$$\nu(\varepsilon) = \nu_0 \left\{ 1 + \sum_{k=1}^{\infty} \sqrt{\frac{\omega_c(\varepsilon)}{2k\varepsilon}}\, \delta^k \left[\cos\frac{\pi k\varepsilon}{\omega_c(\varepsilon)} + \sin\frac{\pi k\varepsilon}{\omega_c(\varepsilon)} \right] \right\}, \tag{4.30}$$

where

$$\delta = \exp\left[-\frac{\pi}{\omega_c(\varepsilon)\tau_q(\varepsilon)} \right]$$

is the Dingle factor determined by the quantum scattering time τ_q. Note that the frequency of the oscillations for a conventional 3D material with parabolic dispersion (see Ref. [154]) is a factor of 2 larger then in the case of Weyl semimetals. In the 2D case of graphene [151], a similar behavior is encountered in comparison to conventional 2D materials. Via the energy dependent cyclotron frequency ω_c, the non-equidistant behavior of the LLs for relativistic dispersion relations is expressed . The first harmonics, $k = 1$ is the least damped term and therefore sufficient to consider for $\omega_c(\varepsilon)\tau_q(\varepsilon) \ll 1$, which corresponds exactly to the condition of overlapping LLs.

Using Eqs. (4.30) and (4.15), the oscillatory contribution to the conductivity (the SdHO) for the case of overlapping LLs results in

$$\sigma_{xx} \simeq \sigma_{xx,0} \left\{ 1 + \frac{3\gamma\mu^2}{2\pi v^3\Omega} \exp\left(-\frac{\gamma\mu^3}{v^3\Omega^2} \right) \left[\cos\left(\frac{2\pi\mu^2}{\Omega^2} \right) + \sin\left(\frac{2\pi\mu^2}{\Omega^2} \right) \right] \right\}, \tag{4.31}$$

where $\sigma_{xx,0}$ is the smooth part of the conductivity calculated above [Eq. (4.28)]. In contrast to the case of separated LLs, the SdHO are exponentially damped in the regime of overlapping LLs as it is the usual situation.

4.1.3 Magnetoconductivity for strong disorder

We conclude this section by a brief discussion of the magnetoconductivity in the case of strong disorder, $\beta = \gamma/\gamma_c \sim \gamma\Lambda/v^3 \gg 1$. As discussed in Sec. 3.4.5, the strong broadening of all Landau levels (broadening is in the order of the ultraviolet cutoff) leads to the fact that all Landau levels overlap. The conductivity can be calculated under applying the semiclassical Drude formula (4.13) complemented by Eqs. (3.76), (3.78), (4.15), and (4.16). The magnetic-field dependence of the conductivity is now governed by the parameter

$$\omega_c(\tilde{\varepsilon})\tau(\tilde{\varepsilon}) \sim \frac{\Omega^2}{\Gamma^2} \sim \frac{\Omega^2}{\Lambda^2}. \tag{4.32}$$

Here, the energy $\tilde{\varepsilon}$ is replaced by the level broadening $\Gamma \sim \Lambda$. The conductivity is mainly dominated by a magnetic-field independent term with a weak quadratic-in-H correction for finite magnetic field (here we do not write the numerical prefactor in the H-dependent correction)

$$\begin{aligned} \sigma_{xx} &\sim \frac{e^2v^2}{\gamma_c}\int\frac{d\varepsilon}{T}\frac{1}{1+\Omega^4/\Lambda^4} \sim \frac{e^2v^2}{\gamma_c}\left(1-\frac{\Omega^4}{\Lambda^4}\right), \\ \delta\sigma_{xx} &\sim -\frac{e^2\Omega^4}{v\Lambda^3} \propto -H^2. \end{aligned} \tag{4.33}$$

The quadratically in H vanishing correction to the conductivity in strong disorder should be contrasted to the conductivity for weak disorder which vanishes non-analytically (proportional to $H^{1/3}$).

4.2 Hall conductivity

This section is devoted to the analysis of the Hall conductivity. The Hall conductivity is described by the Kubo-Streda formula [138], reading

$$\sigma_{xy} = \frac{i}{2\pi}\int d\varepsilon f_T(\varepsilon)\mathrm{Tr}\left[\hat{j}_x^{\mathrm{tr}}\frac{dG^{\mathrm{R}}}{d\varepsilon}\hat{j}_y\mathrm{Im}G - \hat{j}_x^{\mathrm{tr}}\mathrm{Im}G\hat{j}_y\frac{dG^{A}}{d\varepsilon}\right], \tag{4.34}$$

where $\hat{j}_x = ev\sigma_x$ and $\hat{j}_y = ev\sigma_y$ are the bare current operators. As for the calculation of the conductivity, $\hat{j}_x^{\mathrm{tr}} = V^{\mathrm{tr}}\hat{j}_x$ with V^{tr} being the current vertex dressed by disorder. The vertex corrections are given by Eq. (4.2) which will be included in the final steps of the calculation. The Hall conductivity is split up into a normal, σ_{xy}^{I}, and an anomalous, $\sigma_{xy}^{\mathrm{II}}$, contribution. This is particularly convenient for the calculation with disorder. The normal contribution can be simplified by using the orthogonality of the wave functions of different LLs, leading to

$$\sigma_{xy}^{\mathrm{I}} = \frac{e^2\Omega^2}{(2\pi)^2}\int d\varepsilon\frac{df_T(\varepsilon)}{d\varepsilon}\int\frac{dp_z}{2\pi}\sum_n\left[G_{22}^{\mathrm{R}}\mathrm{Im}G_{11} - G_{11}^{\mathrm{R}}\mathrm{Im}G_{22} - \mathrm{Im}G_{22}G_{11}^{\mathrm{A}} + \mathrm{Im}G_{11}G_{22}^{\mathrm{A}}\right]. \tag{4.35}$$

This contribution is determined by the states near the Fermi level. The anomalous contribution, as discussed in Sec. 2.2, reflecting the thermodynamic properties of the system in the presence of magnetic field, can be written as

$$\sigma_{xy}^{\mathrm{II}} = e\frac{\partial N(H,\mu)}{\partial H}. \tag{4.36}$$

Here, the electron density N is defined as

$$N(H,\mu) = \frac{1}{V}\sum_{\mathbf{p}} f_T(\varepsilon_{\mathbf{p}}) = \int_{-\infty}^{\infty} d\varepsilon \frac{\nu(\varepsilon)}{\exp\left(\frac{\varepsilon-\mu}{T}\right)+1}. \tag{4.37}$$

In the following, the Hall conductivity is first calculated in the clean case, and then disorder is incorporated via the density of states $\nu(\varepsilon)$ and the transport scattering time τ^{tr}.

4.2.1 Clean case

As a first step, we calculate the Hall conductivity in the clean case and discuss in the proceeding section how disorder affects the Hall conductivity. The Green's functions in Landau level representation without disorder can be expressed as

$$G_{11}(\varepsilon, p_z, n) = \sum_{\lambda}\left(1+\frac{\lambda v p_z}{\varepsilon_n}\right)\frac{1}{\varepsilon-\lambda\varepsilon_n+i0}, \tag{4.38}$$

$$G_{22}(\varepsilon, p_z, n) = \sum_{\lambda}\left(1-\frac{\lambda v p_z}{\varepsilon_{n+1}}\right)\frac{1}{\varepsilon-\lambda\varepsilon_{n+1}+i0}. \tag{4.39}$$

First, we perform the calculation for the normal part of Hall conductivity and substitute the Green's function from Eqs. (4.38) and (4.39) in Eq. (4.35). Evaluating the integral over energy ε and the summation over energy bands λ leads to the normal contribution to the Hall conductivity of

$$\sigma_{xy}^{\mathrm{I}} = -\frac{e^2\Omega^2}{4\pi T}\int\frac{dp_z}{2\pi}\sum_{n=1}^{\infty}\mathrm{Re}\left(\frac{n}{\varepsilon_n}\left[\frac{1}{\cosh^2\left(\frac{\varepsilon_n+\mu}{2T}\right)}-\frac{1}{\cosh^2\left(\frac{\varepsilon_n-\mu}{2T}\right)}\right]\right). \tag{4.40}$$

For zero temperature, $T=0$, the normal contribution is expressed as the following sum over Landau levels:

$$\sigma_{xy}^{\mathrm{I}} = \frac{e^2\Omega^2}{2\pi^2 v}\sum_{n=1}^{(\mu/\Omega)^2}\frac{n}{\sqrt{\mu^2-\Omega^2 n}}. \tag{4.41}$$

For chemical potential located at the center of one particular LL, $\mu=\Omega\sqrt{n}$, the normal contribution to the Hall conductivity shows singularities, cf. Fig. 4.2a).

To obtain the anomalous contribution to the Hall conductivity, we use Eq. (4.36) and the density of states $\nu(\varepsilon)$ of a Weyl semimetal in the clean case, Eq. (3.45). The evaluation of the integral in Eq. (4.37) for $T=0$ and the calculation of the derivative of N with respect to magnetic field H results in

$$\sigma_{xy}^{\mathrm{II}} = -\frac{e^2\Omega^2}{2\pi^2 v}\sum_{n=1}^{\mu^2/\Omega^2}\frac{n}{\sqrt{\mu^2-\Omega^2 n}} + \frac{e^2}{4\pi^2 v}\left[\mu+2\sum_{n=1}^{\mu^2/\Omega^2}\sqrt{\mu^2-\Omega^2 n}\right]. \tag{4.42}$$

The singularities of the first term of Eq. (4.42), when the chemical potential is at the center of one particular LL, are opposite of those of the normal contribution from Eq. (4.41), cf. Fig. 4.2b). Thus, in

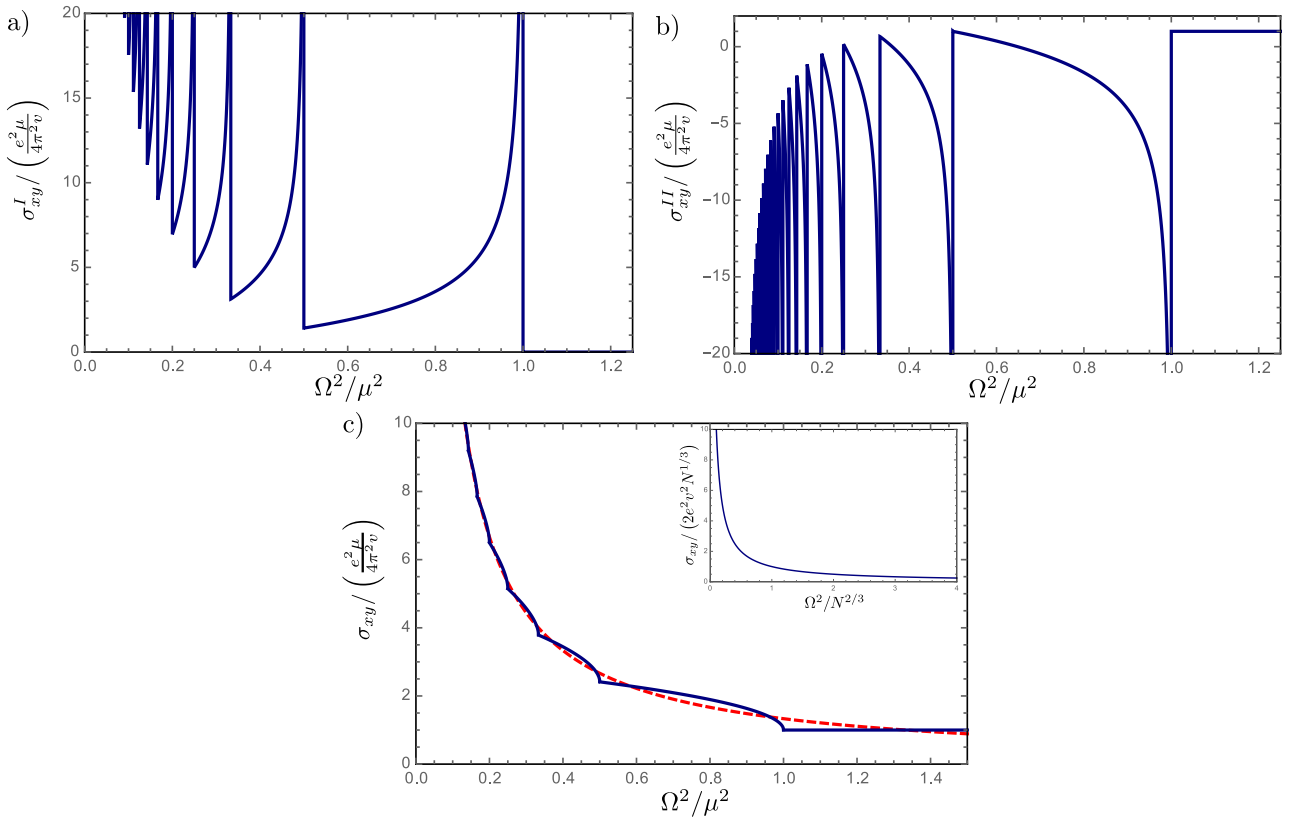

[Reprinted figure with permission from J. Klier, I. V. Gornyi, A. D. Mirlin, Physical Review B, **96**, 214209 (2017) Copyright 2017 by the American Physical Society. http://dx.doi.org/10.1103/PhysRevB.96.214209]

Figure 4.2: Normal part of the Hall conductivity a), anomalous part b), and the total Hall conductivity c) of a clean Weyl semimetal. In all three panels, the curves correspond to fixed chemical potential and are plotted as functions of magnetic field ($\Omega^2 \propto H$). The Hall conductivity for fixed particle density is visualized in the inset of panel c) The red dashed curve in panel c) corresponds to the smoothened Hall conductivity (with SdHO subtracted).

the total Hall conductivity, these singularities are exactly canceled. The cancellation of the singularities is not a feature due to zero temperature, but occurs in the clean case for arbitrary T, as demonstrated in App. B.3.

In leading order, the evaluation of the sum over LLs with Euler-Maclaurin formula results in

$$\sigma_{xy} \simeq \frac{e^2}{4\pi^2 v} \begin{cases} \mu, & \mu < \Omega, \\ \dfrac{4\mu^3}{3\Omega^2}, & \mu > \Omega. \end{cases} \tag{4.43}$$

Equation (4.43) describes the smoothened part of the Hall conductivity in the limit $\mu > \Omega$. On top of this background contribution, an oscillatory part is induced by the Landau quantization. In Fig. 4.2, where the Hall conductivity (normal and anomalous part and the total Hall conductivity) without disorder is presented, the oscillations induced by Landau quantization can be seen clearly in case of fixed chemical potential. Already from the results in the clean case, one can expect that disorder changes the total Hall conductivity only weakly since the disorder-induced broadening would only smoothen the oscillatory part of the curve.

Further, the Hall conductivity can be expressed in terms of a fixed particle density N instead of a fixed chemical potential, as relevant to experiments. We find that the magneto-oscillations in the chemical potential are exactly canceled by the oscillations in the particle density:

$$\sigma_{xy} = 2e^2 v^2 \frac{N}{\Omega^2}, \tag{4.44}$$

cf. inset in Fig. 4.2c). Here, the density N is chosen in such a way that $N = 0$ corresponds to the chemical potential located at the Dirac point, $\mu = 0$.

Before considering the effects of disorder on the Hall conductivity, we will briefly discuss the effect of finite temperature on the Hall conductivity. For $T < \mu$, the Hall conductivity is essentially unaffected by temperature. However, for comparably large temperatures, $\mu < T$, the Hall conductivity is given by the Sommerfeld expansion. The Hall conductivity is given by

$$\sigma_{xy} \simeq \frac{e^2}{4\pi^2 v} \begin{cases} \mu & T < \Omega, \\ \dfrac{\pi^2}{3}\dfrac{\mu T^2}{\Omega^2} & T > \Omega. \end{cases} \tag{4.45}$$

In contrast to the Hall conductivity for zero temperature, the oscillations in Landau levels for temperatures $T > \Omega$ are smeared due to temperature.

4.2.2 Normal part of the Hall conductivity in the presence of disorder

Now, we analyze the effects of disorder on the normal part of the Hall conductivity. As explained in Sec. 3.4, it is relevant to distinguish again between the cases of chemical potential positioned below the first zeroth LL or positioned at higher LLs. We consider low temperatures, $T \to 0$, throughout the whole section.

We start with the case of the Hall conductivity of the zeroth Landau level. The calculation is performed under the following conditions: (i) the zeroth LL is separated from higher LLs, $A \ll \Omega$; (ii) excitations to higher LLs are suppressed, $\mu < \Omega$. Substituting the Green functions for energies close

to the zeroth LL, Eqs. (4.4) and (4.5), into the normal part to the Hall conductivity, Eq. (4.35), the equation transforms to

$$\sigma_{xy}^{\mathrm{I}} = -\frac{e^2\Omega^2 A}{(2\pi)^2 v}\int\frac{dz}{2\pi}\sum_n\left\{\frac{A^2(\mu+z)^3+(\mu+z)^2(\mu-z)[\mu^2-z^2-\Omega^2(n+1)]}{\left[(\mu^2-z^2-\Omega^2 n)^2+A^2(\mu+z)^2\right]\left[(\mu^2-z^2-\Omega^2(n+1))^2+A^2(\mu+z)^2\right]}\right.$$
$$\left.-\frac{(\mu+z)(\mu^2-z^2-\Omega^2 n)\Omega^2(n+1)}{\left[(\mu^2-z^2-\Omega^2 n)^2+A^2(\mu+z)^2\right]\left[(\mu^2-z^2-\Omega^2(n+1))^2+A^2(\mu+z)^2\right]}\right\}, \tag{4.46}$$

where $z = vp_z$.

As in the evaluation of the conductivity of the zeroth Landau level, Eq. (4.6), we will split the summation over the LL index into the term with $n = 0$ and the terms with $n > 0$. In contrast to Eq. (4.6), the terms with $n > 0$ and the term $n = 0$ are of the same order in σ_{xy}^{I}. Under the assumptions $A \ll \Omega$ and $\mu < \Omega$, the leading order gives

$$\sigma_{xy}^{\mathrm{I}} \simeq \frac{5e^2 A\mu}{4(2\pi)^2 v\Omega} \sim \frac{e^2}{v^4}\gamma\mu\Omega. \tag{4.47}$$

Compared to a clean system, where the normal part is absent for a chemical potential positioned in the zeroth Landau level, this rather small result (linear in disorder) matches. It will turn out in the proceeding section that the term (4.47) is negligible in comparison with the anomalous contribution to the Hall conductivity.

Now, we proceed with higher chemical potential $\mu > \Omega$ and analyze the contribution of higher LLs to σ_{xy}^{I}. As already discussed for the conductivity, Sec. 4.1, the difference between the self-energies of the two bands can be neglected for $\varepsilon \gg \Omega$. Thus, the Green's functions (4.10) and (4.11) are applicable in Eq. (4.35). For the detailed calculation, we refer the reader to App. B.2. The normal part of the Hall conductivity yields

$$\sigma_{xy}^{\mathrm{I}} \simeq \frac{e^2\Omega^2}{2\pi^2 v}\int d\varepsilon\frac{df_T(\varepsilon)}{d\varepsilon}\frac{\varepsilon^3}{\Omega^4+(4\varepsilon\Gamma)^2}\left[\frac{4}{3}+\frac{\Omega^2}{\varepsilon}\left(\frac{\Gamma}{A\varepsilon}-\frac{2\varepsilon}{\Omega^2}\right)\right]. \tag{4.48}$$

In the limit of vanishing disorder, $\Gamma \to 0$, the clean case is reproduced in Eq. (B.30) before the sum of all Landau levels is evaluated. Similarly to σ_{xx}, we can express the normal contribution to the Hall conductivity in the form of a semiclassical Drude formula:

$$\sigma_{xy}^{\mathrm{I,D}} \simeq \frac{e^2 v^2}{6\pi}\int\frac{d\varepsilon}{4T\cosh^2\left(\frac{\varepsilon-\mu}{2T}\right)}\frac{\nu(\varepsilon)\tau_{\mathrm{tr}}(\varepsilon)\omega_c(\varepsilon)[\tau_{\mathrm{tr}}(\varepsilon)]}{1+\omega_c^2(\varepsilon)[\tau_{\mathrm{tr}}(\varepsilon)]^2}. \tag{4.49}$$

For fully separated Landau levels, $\Omega \ll \mu \ll \Omega(\Omega/A)^{1/5}$, Eq. (4.48) is dominated by the second term. In the limit $T \to 0$, the normal part reads

$$\sigma_{xy}^{\mathrm{I}} = \frac{e^2\Omega^2}{2\pi^2 v}\int d\varepsilon\delta(\varepsilon-\mu)\frac{2\Omega^2\varepsilon^2}{\Omega^4+(4\varepsilon\Gamma)^2}\frac{\Gamma}{A\varepsilon} \simeq \frac{e^2\mu\Gamma(\mu)}{2\pi^2 vA}. \tag{4.50}$$

We continue with the evaluation of the Hall conductivity for a larger chemical potential, i.e. in the regime where the LLs are separated but the contribution of the background density of states

dominates corresponding to $\Omega(\Omega/A)^{1/5} \ll \mu \ll \Omega(\Omega/A)^{1/3}$. In this case, the expressions for the density of states, transport scattering time, and cyclotron frequency are given by Eqs. (4.14), (4.15), and (4.16), respectively. Substituting these expressions in Eq. (4.48), we find

$$\sigma_{xy}^{\mathrm{I}} = \frac{e^2}{\pi^2 v} \int d\varepsilon \frac{1}{4T \cosh^2\left(\frac{\varepsilon-\mu}{2T}\right)} \frac{\varepsilon^3}{\Omega^2} = \frac{e^2\mu^3}{\pi^2 v \Omega^2} \left(1 + \frac{\pi^2 T^2}{\mu^2}\right). \tag{4.51}$$

For fully overlapping LLs, $\mu \gg \Omega(\Omega/A)^{1/3}$, the normal contribution to the Hall conductivity is

$$\sigma_{xy}^{\mathrm{I}} \simeq \frac{3e^2\Omega^2}{2\pi^2 v} \int d\varepsilon \frac{1}{4T \cosh^2\left(\frac{\varepsilon-\mu}{2T}\right)} \frac{\pi^2 v^5}{\gamma^2 \varepsilon^3} = \frac{3e^2 v^5 \Omega^2}{2\mu^3 \gamma^2}, \tag{4.52}$$

where Eq. (4.48) was evaluated under the condition $\Omega^4 < (4\varepsilon\Gamma)^2$ with the use of Eqs. (4.14), (4.15), and (4.16).

4.2.3 Anomalous part of the Hall conductivity in the presence of disorder

In this Section, we discuss the anomalous contribution to the Hall conductivity in the presence of disorder. The anomalous part to the Hall conductivity is calculated by Eqs. (4.36) and (4.37). In order to apply this definition of the anomalous part, we subtract the contribution of states below the charge neutrality point in the calculation of the particle density. These states do not contribute to the Hall conductivity as it is shown explicitly in App. B.3 for the clean case. However, the statement holds for finite but weak disorder under the condition, $\gamma\Lambda < 1$, as considered here. The density of states of a disordered Weyl semimetal can be expressed as

$$\nu(\varepsilon) = -\frac{1}{\pi\gamma} \left(\mathrm{Im}\Sigma_1 + \mathrm{Im}\Sigma_2\right). \tag{4.53}$$

As in the former parts of the chapter, we distinguish between the zeroth LL and higher LLs in the self-energy. For the zeroth LL, the self-energy, as analyzed in Sec. 3.4, is

$$\mathrm{Im}\Sigma_1 = -A \qquad \text{and} \qquad \mathrm{Im}\Sigma_2 = 0, \tag{4.54}$$

which is valid in the regime $\mu < \Omega$. In this regime and for weak disorder, $\gamma\Lambda \ll 1$, the anomalous Hall conductivity is disorder independent, yielding

$$\sigma_{xy}^{\mathrm{II}} \simeq e\frac{\partial}{\partial H} \int_0^\infty d\varepsilon \frac{1}{\exp\left(\frac{\varepsilon-\mu}{2T}\right) + 1} \frac{A}{\pi\gamma} = \frac{e^2\mu}{4\pi^2 v}, \tag{4.55}$$

The result for the ac anomalous Hall conductivity $\sigma_{xy}(\omega)$, obtained in Ref. [155], matches to the result obtained here in the limit $\omega \to 0$.

For $\mu > \Omega$, we need to consider again the three domains of the density of states: (i) fully separated Landau levels, (ii) separated Landau levels, but large background density of states compared to the value of the particular Landau level, (iii) overlapping Landau levels. In particular for separated Landau levels, $\mu < \Omega(\Omega/A)^{1/3}$, the density of states depends strongly on the actual position of the chemical potential with respect to the center of a given LL. The shape of one Landau level consists of the peak at the center of the LL, the tail of the LL, and the background, as visualized and discussed in App. A.3.

In the case of separated LLs with large background and for overlapping LLs, the main contribution of the density of states comes from the background. The anomalous Hall conductivity for $\mu > \Omega$ in its general form reads

$$\sigma_{xy}^{\mathrm{II}} = e\frac{\partial}{\partial H}\int_0^\mu d\varepsilon \frac{2\Gamma(\varepsilon)}{\pi\gamma}, \tag{4.56}$$

where $\Gamma(\varepsilon)$ is given by Eq. (3.65) and includes the complete shape of the density of states for $\mu > \Omega$.

Applying the same approximations as in the calculation of σ_{xy}^{I}, the anomalous Hall conductivity in the disordered case results in

$$\sigma_{xy}^{\mathrm{II}} \simeq \sum_n \frac{e^2}{2\pi^2 v}\frac{A\mu}{\Gamma_n(\mu)} - \frac{e^2\mu\Gamma(\mu)}{2\pi^2 vA} = \sum_n \frac{e^2}{2\pi^2 v}\frac{A\mu}{\Gamma_n(\mu)} - \sigma_{xy}^{\mathrm{I}}, \tag{4.57}$$

where Γ_n is defined in Eq. (3.65). The limit of vanishing disorder is reproduced by the limit $\Gamma \to 0$ in Eq. (3.65). Moreover, for non-overlapping LLs, in the sum over all Landau levels, the broadening of LLs in Eq. (4.57) is only important in the term of the particular LL where the chemical potential is located; for all other n one can replace $A\mu/\Gamma_n(\mu)$ with $\sqrt{\mu^2 - \Omega^2 n}$, as in Eq. (4.42). As in the limit without disorder, the smoothened part of the Hall conductivity for separated LLs, $\mu^{3/2}\gamma^{1/2} \ll \Omega < \mu$, reads

$$\sigma_{xy} \simeq \frac{e^2}{4\pi^2 v}\frac{4\mu^3}{3\Omega^2}. \tag{4.58}$$

We find that oscillations are minor compared to the smoothened Hall conductivity. Thus, in the calculation of the magnetoresistance, we will neglect the effect of oscillations in the Hall conductivity and use Eq. (4.58) in the following sections. The effects of disorder on the Hall conductivity is depicted in Fig. 4.3, where the oscillatory part of the Hall conductivity is shown.

For overlapping LLs, the main term in the broadening, given by $\Gamma = 2A\varepsilon^2/\Omega^2$, is independent of magnetic field and results in an absent anomalous Hall conductivity in leading order. As described above for the conductivity, corrections due to magnetic field for overlapping LLs are governed by the Dingle factor. Therefore, the particle density for zero temperature reads

$$N(H,\mu) = \int_0^\mu d\varepsilon \nu(\varepsilon)\left\{1 + \sqrt{\frac{\omega_c(\varepsilon)}{2\varepsilon}}\delta\left[\cos\frac{\pi\varepsilon}{\omega_c(\varepsilon)} + \sin\frac{\pi\varepsilon}{\omega_c(\varepsilon)}\right]\right\}. \tag{4.59}$$

This results in an exponentially decaying anomalous contribution to the Hall conductivity due to the exponentially small Dingle factor for overlapping Landau levels. The same applies to the transversal magnetoresistance. The magnetoresistance will therefore always be dominated by effects of finite temperature for overlapping Landau levels which is discussed in the following section.

4.3 Magnetoresistance at finite temperature

The magnetoresistance quantifies the difference between the resistivity $\rho_{xx}(H)$ in a finite magnetic field and the zero-field resistivity $\rho_{xx}(0)$ and is defined as

$$\Delta_\rho(H) = \frac{\rho_{xx}(H) - \rho_{xx}(0)}{\rho_{xx}(0)}. \tag{4.60}$$

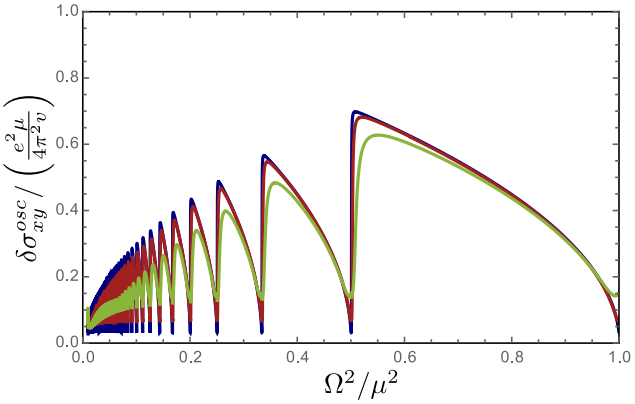

Figure 4.3: Numerically calculated oscillatory part of the anomalous part of the Hall conductivity in presence of disorder obtained by the numerical solution of the equation for the self-energy, Eq. (4.57). Blue, red, and green curves correspond to $A\mu/\Omega^2 = 10^{-5}, 10^{-4}, 10^{-3}$, respectively. For all three curves, the ultraviolet cutoff was set to $\Lambda/\Omega = 100$.

The resistivity is given by $\rho_{xx} = \sigma_{xx}/(\sigma_{xx}^2 + \sigma_{xy}^2)$. Thus, with the results of the previous sections, it is straightforward to calculate the magnetoresistance. The transversal magnetoresistance (TMR), expressed in terms of the conductivity and the Hall conductivity, reads

$$\Delta_\rho(H) = \frac{\sigma_{xx}(0)\sigma_{xx}(H)}{\sigma_{xx}^2(H) + \sigma_{xy}^2(H)} - 1 \tag{4.61}$$

In this section, we focus on the case of finite temperature with zero chemical potential $\mu = 0$. Therefore, the Hall conductivity is zero and the magnetoresistance simplifies to

$$\Delta_\rho(H) = \frac{\sigma_{xx}(0)}{\sigma_{xx}(H)} - 1. \tag{4.62}$$

In the following, this relative magnetoresistance is calculated for both models of disorder, pointlike impurities and charged impurities.

4.3.1 Pointlike Impurities

For pointlike impurities, the conductivity is summarized in Eq. (4.21). We keep the value of $T\gamma$ constant and analyze the evolution of the magnetoresistance with increasing magnetic field by the use of Eq. (4.21). This corresponds to a vertical cross-section in Fig. 4.1. The magnetoresistance in different regimes of Landau level broadening yields

$$\Delta_\rho = \begin{cases} \dfrac{\pi^{4/3}}{12^{2/3}} \dfrac{v\Omega^{2/3}}{\gamma^{1/3}T}, & \Omega \ll \dfrac{\gamma^{1/2}T^{3/2}}{v^{3/2}}, \\ \dfrac{189}{124\pi^4} \dfrac{v^6\Omega^4}{\gamma^2 T^6} - 1, & \dfrac{\gamma^{1/2}T^{3/2}}{v^{3/2}} \ll \Omega \ll T, \\ 8\pi^2 \dfrac{v^6}{\gamma^2\Omega^2} - 1, & T \ll \Omega \ll \dfrac{v^3}{\gamma}. \end{cases} \tag{4.63}$$

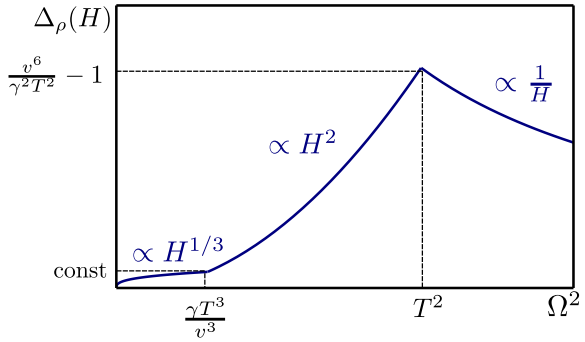

Figure 4.4: Schematic magnetoresistance for the case of white-noise disorder in the weak disorder regime (the parameter $\Omega^2 \propto H$ shows the dependence on magnetic field). The range of magnetic field for the depicted magnetoresistance is relatively weak, $\Omega \ll v^3/\gamma$. For larger fields, the magnetoresistivity would vanish. The dominant scaling of the magnetoresistance in different regimes, boundaries of the regimes and the corresponding values of $\Delta\rho$ are indicated.

Increasing the magnetic field further than $\Omega > v^3/\gamma$, the Landau levels overlap again leading to a vanishing magnetoresistance. A schematic plot of the magnetoresistance in different regimes is shown in Fig. 4.4.

We should stress that the vanishing density of states of Weyl semimetals at $\varepsilon = 0$ in zero H translates into the non-analytic, $H^{1/3}$, behavior of the magnetoresistance for weak pointlike impurities, which survives in the limit of $H = 0$. The non-analytic behavior in Weyl semimetals should be contrasted to the case of graphene, where a $H^{1/2}$-magnetoresistance was found in Ref. [150]. There, the square-root magnetoresistance does not actually persist down to $H \to 0$ due to the fact that even weak white-noise scalar disorder is marginally relevant in graphene establishing a finite density of states at the Dirac point. Although the $H^{1/2}$ behavior of the magnetoresistance in graphene may persist to very weak magnetic fields, the true $H \to 0$ asymptotics of the magnetoresistance is parabolic. Weak white-noise disorder in 3D systems with linear spectrum is by contrast irrelevant and cannot establish a finite density of states at $\varepsilon = 0$ leading to the remarkable observation of the non-analyticity of the TMR. This non-analyticity is another manifestation of the unconventional behavior at the Weyl node similar to the non-commutativity of the limits $T \to 0$ and $\omega \to 0$ in zero magnetic field. A non-analytic behavior of the magnetoconductivity in Weyl semimetals is also found in Ref. [156]. The non-analytic function of the magnetic field proportional to $|H|^{3/2}$ in this work originates from a singularity of the Berry curvature at small momenta.

It is worth emphasizing that in the limit of low temperatures $T \to 0$, the TMR for pointlike impurities is very sharp, cf. Fig. 4.4. The maximum of the magnetoresistance is at $H \propto T^2$ with $\Delta_\rho \propto 1/T^2$ resulting in an infinite magnetoresistance at zero magnetic field for $T \to 0$. This manifests the non-commutativity of the limits $T \to 0$ and $H \to 0$ discussed in Sec. 4.1.

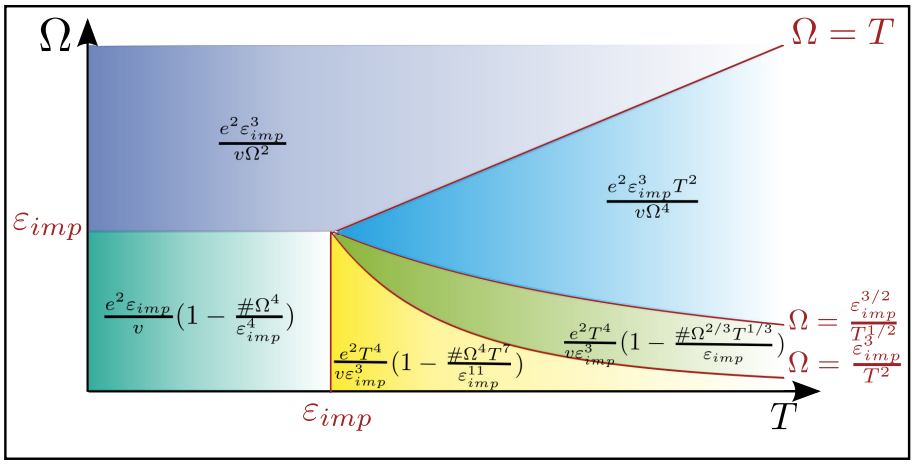

[Reprinted figure with permission from J. Klier, I. V. Gornyi, A. D. Mirlin, Physical Review B, **92**, 205113 (2015) Copyright 2015 by the American Physical Society. http://dx.doi.org/10.1103/PhysRevB.92.205113]

Figure 4.5: Conductivity σ_{xx} in a Weyl semimetal with Coulomb impurities in the temperature-magnetic field-plane. Dominant scaling of conductivity in each parameter regime is shown (the Fermi velocity v is set to unity). Equations describing borderlines between the regimes are also indicated. Numerical coefficients are denoted by the symbol #.

4.3.2 Charged Impurities

In order to calculate the magnetoresistance of charged impurities, we need to consider first the conductivity for this model of disorder, discussed in Sec. 3.5. To find the conductivity, we should substitute $\gamma(H,T) \sim \gamma_0^{-3}[\max(\Omega,T)]^{-4}$ for γ in the results for the conductivity of a system with white-noise disorder. Therefore, we first consider the conductivity for Coulomb impurities and then turn to the magnetoresistance. As discussed in Sec. 3.5, we do not keep numerical factors and thus also disregard the vertex corrections (they only modify these factors for weak disorder). We start the consideration with the low-temperature regime, $T \ll \Omega$, when the screening is controlled by the magnetic field. In contrast to the conductivity of pointlike impurities, all LLs overlap for low magnetic field $\Omega < \varepsilon_{\rm imp}$, and the conductivity is essentially equal to that at zero magnetic field, see below. For larger magnetic fields, $\Omega > \varepsilon_{\rm imp}$, only the zeroth LL contributes. With $A \sim N_{\rm imp}v^3/\Omega^2$, the conductivity of the zeroth Landau level yields

$$\sigma_{xx} \sim \frac{e^2 A}{v} \sim \frac{e^2\varepsilon_{\rm imp}^3}{v\Omega^2} \sim \frac{e^2 N_{\rm imp} v^2}{\Omega^2} \propto \frac{1}{H}. \tag{4.64}$$

This result agrees with the result obtained by Abrikosov in Ref. [82]. We find that the magnetic field dependence of the conductivity for Coulomb impurities differs strongly from that of white-noise disorder.

For higher temperatures, $T > \Omega$, the conductivity is characterized by a temperature-dependent screening. For such temperatures, contributions of higher LLs become important. The conductivity is evaluated by the use of the semiclassical expression (4.13), the cyclotron frequency (4.16) and the scattering time due to temperature-dependent screening

$$\frac{1}{\tau(\varepsilon)} \sim \frac{\gamma(T)\varepsilon^2}{v^3} \sim \frac{\varepsilon_{\rm imp}^3\varepsilon^2}{T^4}. \tag{4.65}$$

A more detailed analysis reveals the necessity to distinguish between several regimes. The regime of separated Landau levels (fully separated and separated with large background) translates into the condition $\varepsilon < \Omega^{2/3}T^{4/3}/\varepsilon_{\rm imp}$. In the Drude formula for the conductivity (4.13), one can neglect the unity in the denominator of the integrand. Therefore, the conductivity of a system with screened Coulomb impurities for $T > \varepsilon_{\rm imp}^3/\Omega^2$ results in

$$\sigma_{xx} \sim \frac{e^2T^2\varepsilon_{\rm imp}^3}{v\Omega^4} \sim \frac{e^2T^2N_{\rm imp}v^2}{\Omega^4} \propto \frac{1}{H^2}. \tag{4.66}$$

For lower temperatures, $T < \varepsilon_{\rm imp}^3/\Omega^2$, magnetic field can be neglected in the range of ε which dominates the conductivity:

$$\sigma_{xx} \sim \frac{e^2v^2}{\gamma(T)} \sim \frac{e^2T^4}{v\varepsilon_{\rm imp}^3} \sim \frac{e^2T^4}{v^4N_{\rm imp}}. \tag{4.67}$$

The H-dependent correction to this result needs to be divided in two different subregimes. First, the subregime defined by $\varepsilon_{\rm imp}^3/T^2 < \Omega < \varepsilon_{\rm imp}^{3/2}/T^{1/2}$ provides a result similar to Eq. (4.20):

$$\delta\sigma_{xx} \sim -\frac{e^2v^2}{\gamma(T)}\frac{\Omega^{2/3}T^{1/3}}{\varepsilon_{\rm imp}} \sim -\frac{e^2T^{13/3}}{v^5N_{\rm imp}^{4/3}}\Omega^{2/3} \propto -H^{1/3}. \tag{4.68}$$

In weakest magnetic fields, $\Omega < \varepsilon_{\rm imp}^3/T^2$, the parameter $\varepsilon_{\rm imp}$ is larger then the energies dominating the magnetic-field dependence of the conductivity. Thus, ε needs to be replaced by $\varepsilon_{\rm imp}$ in the parameter $\omega_c\tau$:

$$\omega_c\tau \sim \frac{\Omega^4T^8}{\varepsilon_{\rm imp}^{12}}. \tag{4.69}$$

The correction to the conductivity caused by magnetic field in lowest magnetic field, $\Omega < \varepsilon_{\rm imp}^{3/2}/T^{1/2}$, yields

$$\delta\sigma_{xx} \sim -\frac{e^2\Omega^4T^{11}}{v\varepsilon_{\rm imp}^{14}} \propto -H^2. \tag{4.70}$$

As a consequence, we find that the non-analytic ($H^{1/3}$) magnetoresistance does not persist in the limit $H \to 0$ for the case of charged impurities, in contrast to the case of white-noise disorder.

For low temperatures, $T < \varepsilon_{\rm imp}$, and weak magnetic fields, $\Omega < \varepsilon_{\rm imp}$, all Landau levels overlap. Thus, a zero-H calculation, as performed in Refs. [149] and [157], should be applicable. The result of those papers, expressed in our notations, is

$$\sigma_{xx} \sim e^2N_{\rm imp}^{1/3} \sim \frac{e^2\varepsilon_{\rm imp}}{v}. \tag{4.71}$$

This regime corresponds to strong disorder meaning that the H-dependent correction to the conductivity can be calculated under the assumption that $1/\tau \sim \Gamma \sim \varepsilon_{\rm imp}$ and $\omega_c \sim \Omega^2/\Gamma$ as discussed in Sec. 4.1.3. Therefore, similar to Eq. (4.33), the H-dependent correction to Eq. (4.71) for $\Omega \ll T \ll \varepsilon_{\rm imp}$ reads:

$$\delta\sigma_{xx} \sim -\frac{e^2\Omega^4}{v\varepsilon_{\rm imp}^3} \propto -H^2. \tag{4.72}$$

Finally, in the regime $T \ll \Omega \ll \varepsilon_{\mathrm{imp}}$ an analogous consideration with $1/\tau \sim \Omega^2/\varepsilon_{\mathrm{imp}}$ yields no H dependent correction to the leading order.

The conductivity in all regimes is visualized in the temperature-magnetic field-plane in Fig. 4.5 where the dominate scaling in each regime is shown. Furthermore, the results are summarized according to the parameter $T/\varepsilon_{\mathrm{imp}}$, yielding

$$\sigma_{xx} \sim \begin{cases} \dfrac{e^2\varepsilon_{\mathrm{imp}}^3}{v\Omega^2} \propto \dfrac{1}{H}, & \Omega \gg T, \\ \dfrac{e^2\varepsilon_{\mathrm{imp}}}{v}\left(1 - \dfrac{\Omega^4}{\varepsilon_{\mathrm{imp}}^4}\right), & \Omega \ll T \end{cases} \tag{4.73}$$

for $T/\varepsilon_{\mathrm{imp}} < 1$. In the opposite limit for higher temperatures, more regimes are relevant

$$\sigma_{xx} \sim \begin{cases} \dfrac{e^2\varepsilon_{\mathrm{imp}}^3}{v\Omega^2} \propto \dfrac{1}{H}, & \Omega \gg T, \\ \dfrac{e^2\varepsilon_{\mathrm{imp}}^3 T^2}{v\Omega^4}, & \dfrac{\varepsilon_{\mathrm{imp}}^{3/2}}{T^{1/2}} \ll \Omega \ll T, \\ \dfrac{e^2T^4}{v\varepsilon_{\mathrm{imp}}^3}\left(1 - \dfrac{\#\Omega^{2/3}T^{1/3}}{\varepsilon_{\mathrm{imp}}}\right), & \dfrac{\varepsilon_{\mathrm{imp}}^3}{T^2} \ll \Omega \ll \dfrac{\varepsilon_{\mathrm{imp}}^{3/2}}{T^{1/2}}, \\ \dfrac{e^2T^4}{v\varepsilon_{\mathrm{imp}}^3}\left(1 - \dfrac{\#\Omega^4T^7}{\varepsilon_{\mathrm{imp}}^{11}}\right), & \Omega \ll \dfrac{\varepsilon_{\mathrm{imp}}^3}{T^2}. \end{cases} \tag{4.74}$$

The symbol # denotes numerical coefficients in these equations and in Fig. 4.5. In contrast to pointlike impurities, the limits $T \to 0$ and $H \to 0$ are interchangeable for Coulomb impurities.

Now, we can use the obtained results for the conductivity to calculate the magnetoresistance, similar to the calculation with white-noise disorder in Sec. 4.3.1. More specifically, we fix the parameter $T/\varepsilon_{\mathrm{imp}}$ and then consider the magnetoresistivity for an increasing magnetic field.

For $T/\varepsilon_{\mathrm{imp}} < 1$, the magnetoresistivity is obtained by using Eq. (4.73), leading to

$$\Delta_\rho \sim \begin{cases} \dfrac{\Omega^4}{\varepsilon_{\mathrm{imp}}}, & \Omega \ll \varepsilon_{\mathrm{imp}}, \\ \dfrac{\Omega^2}{\varepsilon_{\mathrm{imp}}} - 1, & \varepsilon_{\mathrm{imp}} \ll \Omega. \end{cases} \tag{4.75}$$

The behavior in the high field limit obtained here was identified in an early work by Abrikosov, Ref. [82]. For lower magnetic fields, the magnetoresistance is dominated by overlapping Landau levels. This implies that the conductivity is in leading order given by the conductivity in the absence of magnetic field resulting in a quadrically vanishing magnetoresistance. The magnetoresistance for low temperatures and charged impurities is schematically visualized in Fig. 4.6.

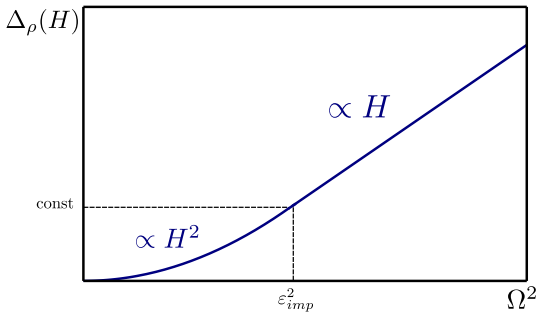

[Reprinted figure with permission from J. Klier, I. V. Gornyi, A. D. Mirlin, Physical Review B, **92**, 205113 (2015) Copyright 2015 by the American Physical Society. http://dx.doi.org/10.1103/PhysRevB.92.205113]

Figure 4.6: Schematic magnetoresistivity for a Weyl semimetal with Coulomb impurities in the limit of low temperatures, $T < \varepsilon_{\text{imp}}$. The parameter $\Omega^2 \propto H$ shows the dependence on magnetic field. The dominant scaling of the magnetoresistance in different regimes, boundaries of the regimes and the corresponding values of $\Delta\rho$ are indicated.

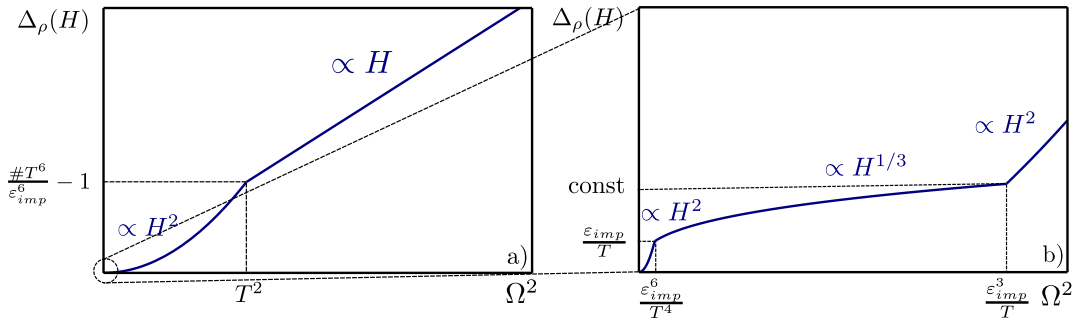

[Reprinted figure with permission from J. Klier, I. V. Gornyi, A. D. Mirlin, Physical Review B, **92**, 205113 (2015) Copyright 2015 by the American Physical Society. http://dx.doi.org/10.1103/PhysRevB.92.205113]

Figure 4.7: Magnetoresistvity of a Weyl semimetal with Coulomb impurities in the temperature limit, $T > \varepsilon_{\text{imp}}$, in the full range of magnetic fields a). Panel b) shows the magnified low-field region. In both panels, the parameter $\Omega^2 \propto H$ shows the dependence on magnetic field. The dominant scaling of the magnetoresistance in different regimes, boundaries of the regimes and the corresponding values of $\Delta\rho$ are indicated.

For sufficiently high temperatures, $T/\varepsilon_{\rm imp} > 1$, we find the magnetoresistivity by using Eq. (4.74)

$$\Delta_\rho \sim \begin{cases} \dfrac{\Omega^4 T^7}{\varepsilon_{\rm imp}^{11}}, & \Omega \ll \dfrac{\varepsilon_{\rm imp}^3}{T^2}, \\ \dfrac{\Omega^{2/3} T^{1/3}}{\varepsilon_{\rm imp}}, & \dfrac{\varepsilon_{\rm imp}^3}{T^2} \ll \Omega \ll \dfrac{\varepsilon_{\rm imp}^{3/2}}{T^{1/2}}, \\ \dfrac{T^2\Omega^4}{\varepsilon_{\rm imp}^6} - 1, & \dfrac{\varepsilon_{\rm imp}^{3/2}}{T^{1/2}} \ll \Omega \ll T, \\ \dfrac{\Omega^2 T^4}{\varepsilon_{\rm imp}^6} - 1, & T \ll \Omega. \end{cases} \tag{4.76}$$

The magnetoresistivity in highest magnetic fields shows again a linear behavior in magnetic field. In the low-field limit, a quadratic dependence on magnetic field dominates the magnetoresistance. The behavior in the full range of magnetic field is visualized in Fig. 4.7. We continue this section by an analysis of the Shubnikov-de Haas oscillations in the magnetoresistance, which cannot be described in the model with zero chemical potential as considered in this section since the zero chemical potential already sits in the zeroth LL.

4.4 Magnetoresistance at finite chemical potential

The magnetoresistance is in general given by Eq. (4.61) which is stated again for clarity

$$\Delta_\rho(H) = \frac{\sigma_{xx}(H)\sigma_{xx}(0)}{\sigma_{xx}^2(H) + \sigma_{xy}^2(H)} - 1.$$

Since we consider now finite chemical potential, we need to employ the results for the conductivity, Sec.4.1, and the Hall conductivity, Sec. 4.2.

The magnetoresistance is either dominated by a large conductivity, $\sigma_{xx} \gg \sigma_{xy}$, resulting in

$$\Delta_\rho(H) \simeq \frac{\sigma_{xx}(0)}{\sigma_{xx}(H)} - 1 \tag{4.77}$$

or dominated by a large Hall conductivity, $\sigma_{xy} \gg \sigma_{xx}$, leading to

$$\Delta_\rho(H) \simeq \frac{\sigma_{xx}(H)\sigma_{xx}(0)}{\sigma_{xy}^2(H)} - 1. \tag{4.78}$$

The proceeding section is divided in two parts, one considering pointlike impurities and another discussing charged impurities. In both parts, we will distinguish between fixed chemical potential and fixed particle density. Let us start with pointlike impurities.

4.4.1 Pointlike impurities

We start this section with the analysis of the magnetoresistance for pointlike impurities and fixed chemical potential. In this case, in lowest magnetic fields, $\Omega^2 < \mu^3\gamma$, all LLs overlap. In this regime, Drude formula, Eqs. (4.28) and (4.52), determines the conductivity and the normal Hall conductivity,

leading to a vanishing TMR. Corrections in this regime are given by the exponentially small anomalous Hall conductivity, cf. Eq. (4.59). This means that effects of a finite temperature (as discussed in the previous section) will dominate the magnetoresistance.

For larger magnetic fields, $\mu^3\gamma < \Omega^2 < \mu^{5/2}\gamma^{1/2}$, the separated LLs are dominated by the large background density of states compared to the peaks of the Landau levels. In this region, we find that the conductivity, Eq. (4.27), is smaller than the Hall conductivity, Eq. (4.58). With Eq. (4.78), the magnetoresistance remains zero.

In the range, $\mu^{5/2}\gamma^{1/2} < \Omega^2 < \mu^2$, of magnetic field, the Landau levels are pronounced. Still, Eq. (4.78) applies for the magnetoresistance meaning that the conductivity is small compared to the Hall conductivity. However, the oscillations in the conductivity are strong due to the strong oscillations of the scattering rate while the Hall conductivity is nearly unaffected by the oscillations. Using Eq. (4.24) for the conductivity and Eq. (4.58) for the Hall conductivity, the TMR is

$$\Delta_\rho(H) \sim \frac{\Gamma^2(\mu)}{\gamma^2\mu^4} - 1. \tag{4.79}$$

This leads to

$$\Delta_\rho^{\max}(H) \sim \frac{\Omega^{8/3}}{\mu^{10/3}\gamma^{2/3}} \tag{4.80}$$

at the peak (with the conductivity at the peak given by Eq. (4.25)) and zero background TMR (as in the previous region).

Stronger magnetic fields, $\mu < \Omega < \gamma^{-1}$, result in a TMR determined by carriers at the zeroth LL. In this domain, the TMR determined by the conductivity, Eq. (4.9), and the Hall conductivity, Eq. (4.55) is split into two subregions. For magnetic fields up to $\Omega^2 < \mu\gamma^{-1}$, σ_{xy} is larger than σ_{xx}, resulting in

$$\Delta_\rho \sim \frac{\Omega^2}{\mu^2} - 1, \tag{4.81}$$

where Eq. (4.78) is applied. For yet higher magnetic fields, $\mu^{1/2}\gamma^{-1/2} < \Omega < \gamma^{-1}$, the opposite limit becomes valid. Using Eq. (4.77), we obtain

$$\Delta_\rho \sim \frac{v^6}{\gamma^2\Omega^2} - 1. \tag{4.82}$$

We summarize the results for the magnetoresistance for fixed values of μ and γ and increasing the magnetic field:

$$\Delta_\rho(H) \sim \begin{cases} \dfrac{\Gamma^2(\mu)}{\gamma^2\mu^4} - 1, & \dfrac{\mu^{5/4}\gamma^{1/4}}{v^{3/4}} \ll \Omega < \mu, \\ \dfrac{\Omega^2}{\mu^2} - 1, & \mu < \Omega \ll \dfrac{\mu^{1/2}v^{3/2}}{\gamma^{1/2}}, \\ \dfrac{v^6}{\gamma^2\Omega^2}, & \dfrac{\mu^{1/2}v^{3/2}}{\gamma^{1/2}} \ll \Omega \ll \dfrac{v^3}{\gamma}. \end{cases} \tag{4.83}$$

In the first line, for $\mu > \Omega \gg \mu^{5/4}\gamma^{1/4}v^{-3/4}$, the function $\Gamma(\mu)$ is given by Eq. (3.65), determining the oscillations in the TMR ranging from zero to a maximum value proportional to $H^{4/3}$. This oscillatory behavior is visualized in Fig. 4.8.

Let us point out that the TMR is only sizable for the zeroth LL (for magnetic fields $\Omega > \mu$). In lower magnetic fields, only the different shape of the oscillations in the conductivity and the Hall conductivity provides a small magnetoresistance. In a smoothened curve, the TMR is absent. In the regime of the zeroth LL, we find a linearly growing magnetoresistance as long as σ_{xy} is larger than σ_{xx}, and then a decaying TMR (being proportional to H^{-1}) for larger fields H, where $\sigma_{xx} \gg \sigma_{xy}$. The TMR is schematically visualized in Fig. 4.9a).

The calculation of the TMR was so far limited to either zero temperature or zero chemical potential. In the following, we will briefly analyze the effect of finite temperatures together with a finite chemical potential. Landau levels are smeared for temperatures $T > \Omega/\sqrt{n}$. We consider now fully separated LLs in the regime of low chemical potential, $\Omega < \mu < \Omega(\Omega/A)^{1/5}$, since the other regimes remain nearly unaffected by temperatures $T < \mu$. For temperatures $T > \mu$, the scaling of the conductivity and the Hall conductivity changes with respect to temperature and chemical potential while the scaling with respect to magnetic field is not affected.

However, the contribution of the LLs in the vicinity of the chemical potential $\mu - T < \Omega\sqrt{n} < \mu + T$ is affected by such temperatures and will be analyzed in the following. The corresponding contribution to the conductivity is estimated by replacing the integral over energy by a sum over regions of width $\Gamma^{(n)}(W_n)$ around Landau levels, and using for $\Gamma^{(n)}(\epsilon)$ its maximal value $\Gamma^{(n)}(W_n) \equiv \Gamma_n \sim A^{2/3}\Omega^{1/3}n^{1/6}$, resulting in

$$\sigma_{xx}^{(n)} \sim \frac{e^2\Omega^2}{ATv} \sum_{n=\mu(\mu-T)/\Omega^2}^{\mu(\mu+T)/\Omega^2} \Gamma_n \frac{\Gamma_n^2 W_n^2}{(4W_n\Gamma_n)^2 + \Omega^4} \sim \frac{e^2\gamma\mu^4}{\Omega^2 v^4} \propto \frac{\gamma\mu^4}{H}. \tag{4.84}$$

Similar as in Sec. 4.3, the thermally averaged conductivity of separated Landau levels is smaller than the background conductivity Eq. (4.27), but is important for the otherwise vanishing TMR.

For $T < \mu$, the effect of finite temperature on the Hall conductivity is negligible, cf. Sec. 4.2. The magnetoresistance is still determined by the Hall conductivity according to Eq. (4.78), yielding

$$\Delta_\rho(H) \sim \frac{\Omega^2}{\mu^2}. \tag{4.85}$$

The obtained linear magnetoresistance, valid for $\Omega < \mu < \Omega(\Omega/A)^{1/5}$, is small and shows exponentially suppressed SdHO.

In the limit $T > \mu$, the Hall conductivity is given by Eq. (4.45). The magnetoresistance is either determined by the Hall conductivity, Eq. (4.78), for $\Omega^2 > \gamma T^4/\mu$ or by the conductivity, Eq. (4.77), in the opposite limit. For $\Omega^2 > \gamma T^4/\mu$, the magnetoresistance reads

$$\Delta_\rho(H) \sim \frac{T^2}{\mu^2} + \frac{\Omega^2}{\mu^2}. \tag{4.86}$$

and for $\Omega^2 < \gamma T^4/\mu$, the magnetoresistance is determined by the result of finite temperature at charge neutrality, Eq. (4.63).

We proceed this section with TMR for the experimentally more relevant situation of a fixed particle

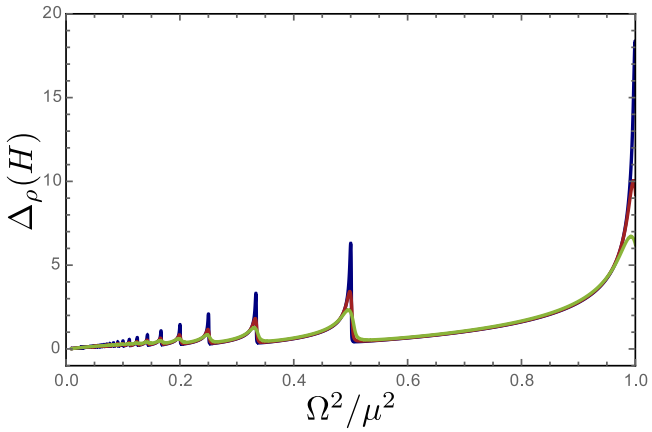

Figure 4.8: Numerical evaluation of the TMR for pointlike impurities and fixed chemical potential in the regime of separated LLs. The figure is based the numerical analysis of the density of states in Eq. (4.79). Blue, red, and green curves correspond to $A\mu/\Omega^2 = 5 \cdot 10^{-5}, 3 \cdot 10^{-4}, 1 \cdot 10^{-3}$, respectively. The ultraviolet cutoff is $\Lambda/\Omega^2 = 100$ for all curves.

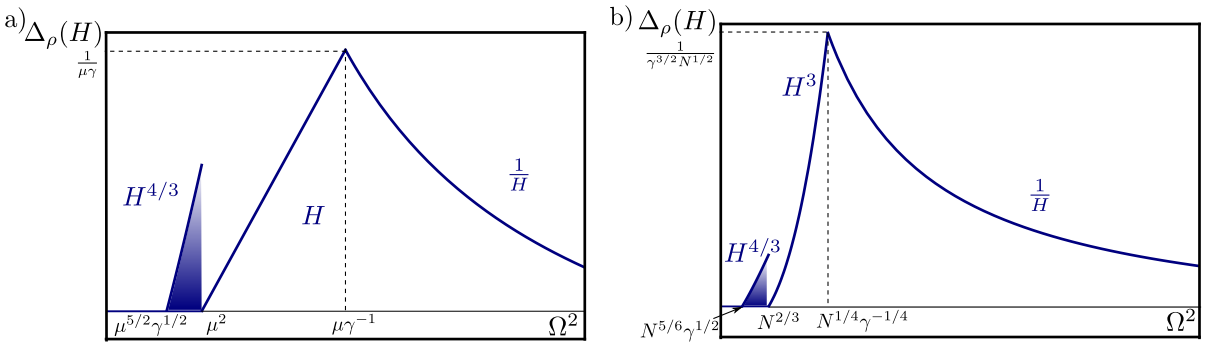

Figure 4.9: Schematic illustration of the TMR for pointlike impurities. Panel a) depicts the magnetoresistance for fixed chemical potential as given in Eq. (4.83) where the shaded region corresponds to oscillations of separated LLs described in Eq. (4.80) and plotted in Fig. 4.8. In panel b), the magnetoresistance for fixed particle density is shown with the shaded region corresponding to the oscillations of separated Landau levels as given by Eq. (4.90).

density N [1]. The particle density was defined in Eq. (4.37) and is evaluated as

$$N(\mu,\Omega)=\begin{cases}\dfrac{\mu\Omega^2}{4\pi^2v^3} & \Omega>\mu,\\ \dfrac{\mu^3}{12\pi^2v^3} & \Omega<\mu.\end{cases} \tag{4.87}$$

for different relations between magnetic field and chemical potential. We directly observe that the magnetic-field dependence of the resistivity is only changed for the zeroth LL (in both conductivity and Hall conductivity) by the particle density. For completeness, we analyze the magnetoresistance from the lowest relevant magnetic fields, $N^{5/6}\gamma^{1/2}>\Omega^2$ (below no TMR emerges to the leading order within the SCBA).

In magnetic fields $N^{5/6}\gamma^{1/2}<\Omega^2<N^{2/3}$, the finite TMR at the center of the LLs, Eq. (4.80) transforms with Eq. (4.87) to

$$\Delta_\rho^{\max}(H)\sim\frac{\Omega^{8/3}}{N^{10/9}\gamma^{2/3}} \tag{4.88}$$

for a fixed particle density

For increasing magnetic fields, $N^{1/3}<\Omega<\gamma^{-1}$, Eq. (4.87) modifies the magnetic field dependence of the conductivity, Eq. (4.9), and the Hall conductivity, Eq. (4.55), for the zeroth Landau level. The Hall conductivity is larger than the conductivity up to magnetic fields of $\Omega<N^{1/4}\gamma^{-1/4}$, resulting in

$$\Delta_\rho\sim\frac{\Omega^6}{N^2}-1. \tag{4.89}$$

for the TMR. For stronger magnetic fields, $N^{1/4}\gamma^{-1/4}<\Omega<\gamma^{-1}$, Eq. (4.82) remains unaffected for a fixed particle density.

The result for fixed N, fixed γ, and increasing magnetic field are summarized as

$$\Delta_\rho(H)\sim\begin{cases}\dfrac{\Gamma^2(N^{1/3})}{\gamma^2N^{4/3}}-1, & \dfrac{N^{5/12}\gamma^{1/4}}{v^{3/4}}\ll\Omega<N^{1/3},\\ \dfrac{\Omega^6}{N^2}-1, & N^{1/3}<\Omega\ll\dfrac{N^{1/4}v^{3/4}}{\gamma^{1/4}},\\ \dfrac{v^6}{\gamma^2\Omega^2}, & \dfrac{N^{1/4}v^{3/4}}{\gamma^{1/4}}\ll\Omega\ll\dfrac{v^3}{\gamma}.\end{cases} \tag{4.90}$$

We find that the behavior of the TMR at the fixed particle density only changes in the zeroth LL while for higher LLs, the particle density does not depend on magnetic field. In Fig. 4.9b), the schematic behavior of the magnetoresistance is illustrated.

To conclude this subsection, we briefly discuss the Hall resistivity ρ_{xy} for fixed particle density, reading

$$\rho_{xy}=\frac{\sigma_{xy}}{\sigma_{xx}^2+\sigma_{xy}^2}. \tag{4.91}$$

[1] In some materials, the Fermi energy might cross additional bands. In this case, the total density is fixed rather than the density in the Weyl bands. From the point of view of the Weyl bands, this is an intermediate situation between fixed chemical potential and particle density, see, e.g., Ref. [8].

We start with lowest magnetic fields, where the Landau levels overlap. In this regime, the anomalous Hall conductivity is exponentially small, see Eq. (4.59). Thus, the conductivity, Eq. (4.28), and the normal Hall conductivity, Eq. (4.52) give rise to

$$\rho_{xy} \sim \frac{\Omega^2}{e^2 v^2 N}. \tag{4.92}$$

The Hall conductivity, Eq. (4.44), is larger than σ_{xx} for separated Landau levels and also for the zeroth Landau level in magnetic fields up to $\Omega \sim N^{1/4}\gamma^{-1/4}$. This results again in Eq. (4.92) for the Hall resistivity. For further increasing fields $\Omega > N^{1/4}\gamma^{-1/4}$, the conductivity of the lowest LL, Eq. (4.9), has a large contribution, leading to

$$\rho_{xy} \sim \frac{\gamma \Omega^6}{e^2 v^7 N^2}. \tag{4.93}$$

Therefore, the Hall resistivity shows a linear behavior up to the highest fields where a rapid increase as a third power of magnetic field is found.

4.4.2 Charged impurities

Similar as in Sec. 4.3.2, we substitute $\gamma(H,\mu) \sim \varepsilon_{\text{imp}}^3 v^3 [\max(\Omega,\mu)]^{-4}$ for γ in the conductivity and Hall conductivity, in order to find the TMR. The detailed parameters for the substitution are discussed in Sec. 3.5. Since we do not keep numerical coefficients, the vertex corrections can be neglected (since they only change these coefficients). In the following, we will first discuss the modifications of the conductivity due to charged impurities and then use these results to calculate the magnetoresistance. Since the Hall conductivity does not depend on disorder in the full parameter regime, it remain unaffected by these modifications.

Of particular importance for the magnetoresistance, is the substitution for the lowest LL, $\Omega > \mu$, where the screening depends on magnetic field. With the replacement $\gamma \to \varepsilon_{\text{imp}}^3 \Omega^{-4}$, the conductivity for the zeroth LL, Eq. (4.9), modifies to

$$\sigma_{xx} \sim \frac{e^2 \varepsilon_{\text{imp}}^3}{v \Omega^2}. \tag{4.94}$$

For higher LLs, $\mu > \Omega$, the dependence of the conductivity on disorder strength is dependent on the shape of the Landau level (e.g. the peak, the tail, or the background), cf. App. A.3 for details. Therefore, we transform the self-consistent equation for the LL broadening, Eq. (3.65), into the case of Coulomb impurities $\gamma \to \varepsilon_{\text{imp}}^3 \mu^{-4}$, reading

$$\Gamma_C(\mu,\Omega) \sim \frac{\varepsilon_{\text{imp}}^3 \Omega^2}{\mu^3} \sum_n \frac{\sqrt{\mu^2 - W_n^2 + \sqrt{(W_n^2-\mu^2)^2 + 4\mu^2\Gamma_C^2}}}{\sqrt{2}\,\sqrt{(W_n^2-\mu^2)^2 + 4\mu^2\Gamma_C^2}} \tag{4.95}$$

As for pointlike impurities, the equation is solved in certain parameter regimes. Most important for the amplitude of the later discussed Shubnikov-de Haas oscillation in TMR will be the value of Γ_C at the center of a particular LL and the background value of Γ_C, which are given by

$$\Gamma_C^{\text{peak}} \sim \frac{\varepsilon_{\text{imp}}^2 \Omega^{4/3}}{\mu^{8/3}} \varepsilon^{1/3}, \qquad \Gamma_C^{\text{bg}} \sim \frac{\varepsilon_{\text{imp}}^3}{\mu^3}\varepsilon. \tag{4.96}$$

For separated Landau levels, we transform the conductivity for pointlike impurities in this regime, Eq. (4.24), which is valid for $\mu^{3/2}\gamma^{1/2} < \Omega < \mu$ into

$$\sigma_{xx} \sim \frac{\mu^2\Gamma^2}{A\Omega^2} \qquad \rightarrow \qquad \sigma_{xx} \sim \frac{\mu^6\Gamma_C^2}{\varepsilon_{\mathrm{imp}}^3\Omega^4}. \tag{4.97}$$

for charged impurities. Expressed in terms of chemical potential, magnetic field and disorder strength, the conductivity at the background and at the peak, respectively, is

$$\sigma_{xx}^{\mathrm{bg}} \sim \frac{\mu^2\varepsilon_{\mathrm{imp}}^3}{\Omega^4}, \qquad \sigma_{xx}^{\mathrm{peak}} \sim \frac{\mu^{4/3}\varepsilon_{\mathrm{imp}}}{\Omega^{4/3}}. \tag{4.98}$$

The background contribution is valid in the full regime of separated Landau levels, $\varepsilon_{\mathrm{imp}}^{3/2}\mu^{-1/2} \ll \Omega < \mu$ while the peaks apply only for $\mu^{1/4}\varepsilon_{\mathrm{imp}}^{3/4} < \Omega < \mu$ where pronounced Landau levels are present.

Equation (4.28) covers the conductivity for overlapping Landau levels in the model of pointlike impurities. For Coulomb impurities, the regime of overlapping Landau levels is in a regime of high chemical potential $\mu \gg \varepsilon_{\mathrm{imp}}$, where screening due to chemical potential leads to

$$\sigma_{xx} \sim \frac{e^2\mu^4}{v\varepsilon_{\mathrm{imp}}^3}, \tag{4.99}$$

and in a regime of low chemical potential, $\mu < \varepsilon_{\mathrm{imp}}$, where the zero magnetic field calculations as discussed in Sec. 4.3.2 apply,

$$\sigma_{xx} \sim \frac{e^2\varepsilon_{\mathrm{imp}}}{v}. \tag{4.100}$$

We summarize the results for the conductivity in the case of charged impurities for increasing magnetic field for low chemical potential $\mu \ll \varepsilon_{\mathrm{imp}}$

$$\sigma_{xx} \sim \frac{e^2}{v}\begin{cases} \varepsilon_{\mathrm{imp}}, & \Omega \ll \varepsilon_{\mathrm{imp}}, \\ \dfrac{\varepsilon_{\mathrm{imp}}^3}{\Omega^2}, & \varepsilon_{\mathrm{imp}} \ll \Omega, \end{cases} \tag{4.101}$$

and in the opposite regime of large chemical potential $\mu \gg \varepsilon_{\mathrm{imp}}$

$$\sigma_{xx} \sim \frac{e^2}{v}\begin{cases} \dfrac{\mu^4}{\varepsilon_{\mathrm{imp}}^3}, & \Omega \ll \dfrac{\varepsilon_{\mathrm{imp}}^{3/2}}{\mu^{1/2}}, \\ \dfrac{\mu^6\Gamma_{\mathrm{C}}^2(\mu)}{\varepsilon_{\mathrm{imp}}^3\Omega^4}, & \dfrac{\varepsilon_{\mathrm{imp}}^{3/2}}{\mu^{1/2}} \ll \Omega < \mu, \\ \dfrac{\varepsilon_{\mathrm{imp}}^3}{\Omega^2}, & \mu < \Omega. \end{cases} \tag{4.102}$$

Now, we proceed with the calculation of the magnetoresistance which is dominated either by σ_{xx} or σ_{xy}. We start with small chemical potential, $\mu < \varepsilon_{\mathrm{imp}}$, where the regimes of overlapping Landau levels and of the lowest Landau level are present. As for pointlike impurities, the TMR is exponentially

small for overlapping Landau levels, valid for magnetic field $\Omega \ll \varepsilon_{\text{imp}}$. In strongest magnetic fields, $\Omega \gg \varepsilon_{\text{imp}}$, the behavior of the magnetoresistance is divided into two subregions: (i) the conductivity, Eq. (4.94), is larger than the Hall conductivity Eq. (4.55), for $\Omega \ll \varepsilon_{\text{imp}}^{3/2}\mu^{-1/2}$, leading to

$$\Delta_\rho(H) \sim \frac{\Omega^2}{\varepsilon_{\text{imp}}^2} - 1; \tag{4.103}$$

and (ii) magnetic fields, $\Omega \gg \varepsilon_{\text{imp}}^{3/2}\mu^{-1/2}$, result in a TMR determined by a large Hall conductivity, yielding

$$\Delta_\rho(H) \sim \frac{\varepsilon_{\text{imp}}^4}{\Omega^2\mu^2} - 1. \tag{4.104}$$

We summarize the results for the TMR of charged impurities for fixed μ and ε_{imp} in the parameter regime $\mu < \varepsilon_{\text{imp}}$. For increasing magnetic field, the TMR reads

$$\Delta_\rho(H) \sim \begin{cases} \dfrac{\varepsilon_{\text{imp}}^4}{\mu^2\Omega^2}, & \dfrac{\varepsilon_{\text{imp}}^{3/2}}{\mu^{1/2}} \ll \Omega, \\ \dfrac{\Omega^2}{\varepsilon_{\text{imp}}^2}, & \varepsilon_{\text{imp}} \ll \Omega \ll \dfrac{\varepsilon_{\text{imp}}^{3/2}}{\mu^{1/2}}. \end{cases} \tag{4.105}$$

In contrast to the case of finite temperatures for Coulomb impurities, cf. Sec. 4.3.2, we find that the linear magnetoresistance persist up to highest magnetic fields for fixed chemical potential in fields smaller than $\varepsilon_{\text{imp}}^{3/2}\mu^{-1/2}$. In the opposite regime, the TMR at fixed chemical potential vanishes as H^{-1}. However, the behavior of the TMR in the ultra-quantum limit differs for the case of a fixed density, where the TMR keeps growing linearly as discussed below.

In the opposite regime, $\mu > \varepsilon_{\text{imp}}$, the TMR is finite for fields larger than $\mu^{1/4}\varepsilon_{\text{imp}}^{3/4}$. In lower fields, the density of states is either dominated by overlapping Landau levels or the background of separated Landau levels. Both cases lead to a negligible TMR for the reasons discussed in Sec. 4.4.1. For $\mu^{1/4}\varepsilon_{\text{imp}}^{3/4} \ll \Omega \ll \mu$, the Landau levels are pronounced which gives rise to a finite TMR at the center of Landau levels. Since the Hall conductivity, Eq. 4.58, is still larger than σ_{xx}, a finite TMR corresponds to the peaks of the conductivity, Eq. (4.98):

$$\Delta_\rho(H) \sim \frac{\Omega^{8/3}}{\mu^{2/3}\varepsilon_{\text{imp}}^2} - 1. \tag{4.106}$$

In high magnetic fields, $\Omega > \mu$, the TMR of the quantum limit is now fully determined by the Hall conductivity. The parameters for the relation $\sigma_{xy} > \sigma_{xx}$ are $\Omega > \varepsilon_{\text{imp}}^{3/2}\mu^{-1/2}$ [cf. Eq. (4.94) and (4.55)] which is valid in the complete domain of the zeroth Landau level. Thus, the TMR is given by (using Eq. (4.78))

$$\Delta_\rho(H) \sim \frac{\mu^2}{\Omega^2} - 1. \tag{4.107}$$

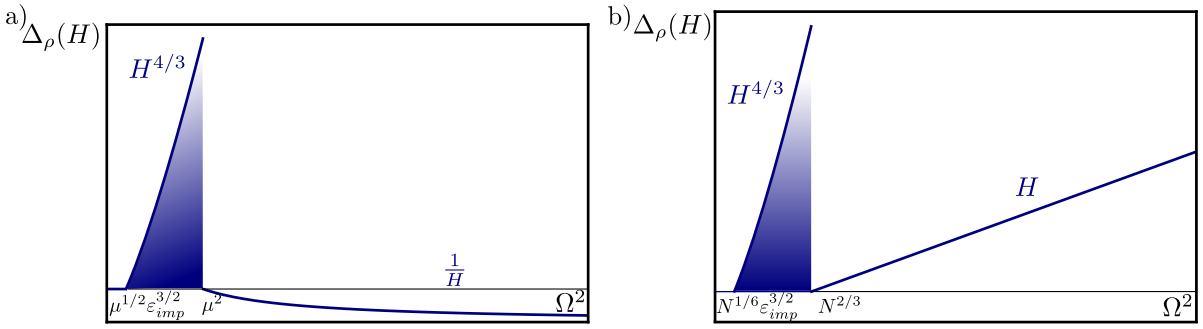

Figure 4.10: Schematic illustration of TMR for Coulomb impurities. Panel a) visualizes the magnetoresistance at a fixed chemical potential, $\mu \gg \varepsilon_{\rm imp}$. The dominant scaling of the magnetoresistance corresponds to Eq. (4.108). Panel b) illustrates the magnetoresistance for fixed particle density, $N \gg \varepsilon_{\rm imp}^3$. The scaling of the different regimes is given by Eq. (4.112). In both panels, the shaded regions corresponds to separated Landau levels and gives rise to the peaks of the Shubnikov-de Haas oscillations.

The regimes of a sizable TMR for $\mu > \varepsilon_{\rm imp}$ are summarized for fixed values of μ and $\varepsilon_{\rm imp}$ and increasing magnetic field as

$$\Delta_\rho(H) \sim \begin{cases} \dfrac{\Gamma_C^2\mu^4}{\varepsilon_{\rm imp}^6} - 1, & \mu^{1/4}\varepsilon_{\rm imp}^{3/4} \ll \Omega < \mu, \\ \dfrac{\mu^2}{\Omega^2} - 1, & \mu < \Omega, \end{cases} \tag{4.108}$$

where $\Gamma_C(\mu, \Omega)$ is defined in Eq. (4.95) defining the magnetooscillations of the conductivity. Compared to pointlike impurities, the TMR changes essentially only for the lowest Landau level, $\Omega > \mu$, where the screening is magnetic-field dependent. For higher LLs, the screening dominated by chemical potential transforms only the dependence on chemical potential and disorder strength $\varepsilon_{\rm imp}$ in Fig. 4.8. The schematic behavior of the TMR is illustrated in Fig. 4.10a). Moreover, the behavior of the TMR in the chemical potential-magnetic field plane is presented in Fig. 4.11a).

We continue the discussion of the TMR for fixed particle density as relevant for experiments as discussed in the previous section. The particle density is unaffected by the model of disorder and is given by Eq. (4.87). For $N^{1/3} \ll \varepsilon_{\rm imp}$, a non-negligible TMR is found for $\Omega \gg \varepsilon_{\rm imp}$ where the zeroth Landau level is important. The conductivity of the zeroth LL, Eq. (4.94), is larger than σ_{xy}, in the full parameter regime. Therefore, the magnetic-field dependence of the resistivity of the zeroth LL is modified due to the magnetic-field dependence of the particle density. The TMR for $N^{1/3} < \varepsilon_{\rm imp}$ reads

$$\Delta_\rho(H) \sim \frac{\Omega^2}{\varepsilon_{\rm imp}^2}, \qquad \Omega \gg \varepsilon_{\rm imp}. \tag{4.109}$$

This linear TMR in the limit of highest magnetic fields agrees with the results of Refs. [82] and our findings in Sec. 4.3.2.

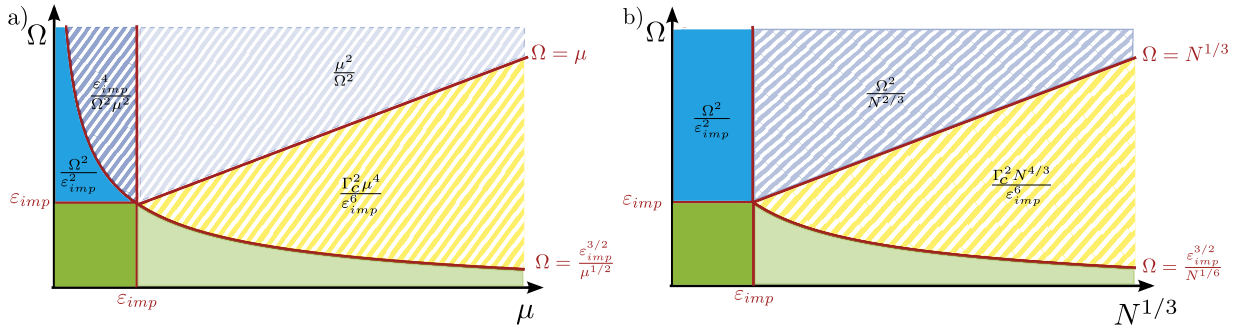

Figure 4.11: Behavior of the TMR $\Delta_\rho(H)$ in a Weyl semimetal with Coulomb impurities for fixed chemical potential a) and for fixed particle density b). Scaling of dominant contribution to the TMR in each of the parameter regimes (the Fermi velocity v is set to unity) and equations for borderlines between the regimes are indicated. The striped (filled) parts indicate the regions where σ_{xy} (σ_{xx}) dominates the denominator in Eq. (4.61) for the TMR $\Delta_\rho(H)$. The regions correspond to the regimes as: blue – zeroth LL, yellow – separated LLs, and green – overlapping LLs. In the yellow regions of panel a) and b), the contribution describes the magneto-oscillations of the scattering rate Γ_C defined in Eq. (4.95).

In the opposite limit of $N^{1/3} \gg \varepsilon_{\rm imp}$, a finite TMR at the center of the particular LL is present for fields larger then $N^{1/12}\varepsilon_{\rm imp}^{3/4}$, yielding at those peaks

$$\Delta_\rho(H) \sim \frac{\Omega^{8/3}}{N^{2/9}\varepsilon_{\rm imp}^2} - 1. \tag{4.110}$$

In strongest magnetic fields $\Omega > N^{1/3}$, the comparison of the conductivity Eq. (4.94) and the Hall conductivity, Eq. (4.55), reveals that this regime is dominated by the Hall conductivity (the exact condition is $\Omega > \varepsilon_{\rm imp}^{3/2} N^{-1/6}$). Applying Eq. (4.78), the TMR is

$$\Delta_\rho(H) \sim \frac{\Omega^2}{N^{2/3}} - 1. \tag{4.111}$$

The results for $N^{1/3} > \varepsilon_{\rm imp}$ by increasing magnetic field, merge to

$$\Delta_\rho(H) \sim \begin{cases} \dfrac{\Gamma_C^2 N^{4/3}}{\varepsilon_{\rm imp}^6} - 1, & N^{1/12}\varepsilon_{\rm imp}^{3/4} \ll \Omega < N^{1/3}, \\ \dfrac{\Omega^2}{N^{2/3}} - 1, & N^{1/3} < \Omega. \end{cases} \tag{4.112}$$

We find a linear TMR in highest magnetic fields in agreement with Eq. (4.109), the results of Sec. 4.3.2, and with Refs. [82, 86]. Compared to Eq. (4.109), the difference is the replacement of the disorder scale $\varepsilon_{\rm imp}$ in the slope of the TMR with $N^{1/3}$. In lower fields, the TMR remains vanishing with small

oscillations, see Fig. 4.10b). As for fixed chemical potential, the resulting "phase diagram" for TMR for fixed density is presented in Figs. 4.11b).

Furthermore, we briefly address finite temperature under the conditions $T < \mu$ and $T > \Omega/\sqrt{n}$. The magnetoresistance calculated for pointlike impurities in Sec. 4.4.1 applies here. For fixed particle density and the regime of separated Landau levels $N^{1/12}\varepsilon_{\text{imp}}^{3/4} \ll \Omega < N^{1/3}$, the magnetoresistance given by Eq. (4.85) scales in the same way as the linear magnetoresistance for the zeroth LL [cf. second line of Eq. (4.112)]:

$$\Delta_\rho(H) \sim \frac{\Omega^2}{N^{2/3}}. \tag{4.113}$$

Finally, we consider the Hall resistivity, Eq. (4.91), for fixed particle density. Away from the quantum limit, the conductivity and Hall conductivity combine into

$$\rho_{xy} \sim \frac{\Omega^2}{e^2 v^2 N} \tag{4.114}$$

similar to the case of pointlike impurities. In the quantum limit, $\Omega > N^{1/3}$, the scaling of the conductivity, Eq. (4.94), and Hall conductivity, Eq. (4.44), with magnetic field is identical. Therefore, the Hall resistivity is

$$\rho_{xy} \sim \frac{N\Omega^2}{e^2 v^2 \varepsilon_{\text{imp}}^4} \tag{4.115}$$

for $\varepsilon_{\text{imp}} > N^{1/3}$ and

$$\rho_{xy} \sim \frac{\Omega^2}{e^2 v^2 N} \tag{4.116}$$

for $\varepsilon_{\text{imp}} < N^{1/3}$. When a finite particle density is induced by donors (charged impurities), $\varepsilon_{\text{imp}} \sim N^{1/3}$, which is the physically most relevant situation, the Hall resistivity and the TMR are of the same order.

We conclude this section by outlining its main findings:

(i) For Coulomb impurities and fixed particle density, a linear TMR is present in the ultra-quantum limit;

(ii) In the experimentally relevant case, $\varepsilon_{\text{imp}} \sim N^{1/3}$, the Hall resistivity is of the same order as the TMR;

(iii) In moderate magnetic fields, strong Shubnikov-de Haas oscillations are observed together with a negligible background TMR.

All presented findings agree with the numerical results of Ref. [86]. The experimental observations [5] of a strong linear TMR in the order of the Hall resistivity is in agreement with the results (i) and (ii). However, the above model treated within the SCBA does not elucidate the origin of the emergence of the Shubnikov-de Haas oscillations on top of a strongly increasing background TMR as observed in experiments, contrary to (iii). The next section is devoted to a model that can explain such a behavior.

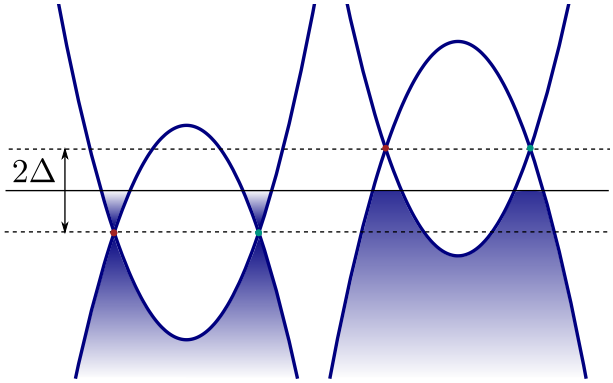

[Reprinted figure with permission from J. Klier, I. V. Gornyi, A. D. Mirlin, Physical Review B, **96**, 214209 (2017) Copyright 2017 by the American Physical Society. http://dx.doi.org/10.1103/PhysRevB.96.214209]

Figure 4.12: Schematic energy band structure of the material with two pairs of Weyl nodes shifted in energy with respect to each other. The carriers belonging to the two pairs of nodes have a chemical potential (counted from the corresponding node) of Δ (electron-type carriers) and $-\Delta$ (hole-type), respectively. Thus, the considered system is at the total charge compensation point.

4.5 Magnetoresistance and Shubnikov-de Haas oscillations for shifted Weyl nodes

We discuss now the magnetoresistance and the Shubnikov-de Haas oscillations of a Weyl semimetal in a third parameter regime namely a model with Weyl nodes shifted in energy, see Fig. 4.12. This model applies to various experiments [5, 6], where the different pairs of Weyl nodes are shifted in energy with respect to each other. In Sec. 1.2, the presented bandstructure of NbP, Fig. 1.2, as extracted from Ref. [5] emphasizes the relevance of this model further. This shift occurs such that some pairs of nodes are characterized by a positive chemical potential, whereas other nodes by a negative chemical potential counted from the corresponding nodal points.

The conductivity, σ_{xx}, as an even function of chemical potential, does not depend on the sign of the chemical potential in a particle-hole symmetric spectrum. Thus, the contributions of different nodes to σ_{xx} can be summed up. The conductivity of each pair of nodes, even exactly at the total charge compensation, is determined by a finite density of quasiparticles (electrons or holes, N_+ and N_-, respectively). This is similar to the consideration of a single node in the previous sections. Let us emphasize that away from charge neutrality the Shubnikov-de Haas oscillations show a superposition of oscillations from the pairs of nodes characterized by the different chemical potentials. In contrast, since the Hall conductivity is an odd function of chemical potential, the Hall conductivity vanishes at charge neutrality. Thus, for the Hall response, the distance to the complete charge compensation point is of crucial significance. In realistic cases, this distance is typically smaller than the chemical potential of each pair of Weyl nodes (see discussion in Ref. [5]).

We essentially analyze a system characterized by a vanishing Hall conductivity, $\sigma_{xy} = 0$, meaning the chemical potentials of the different nodes correspond to the total charge compensation point. The

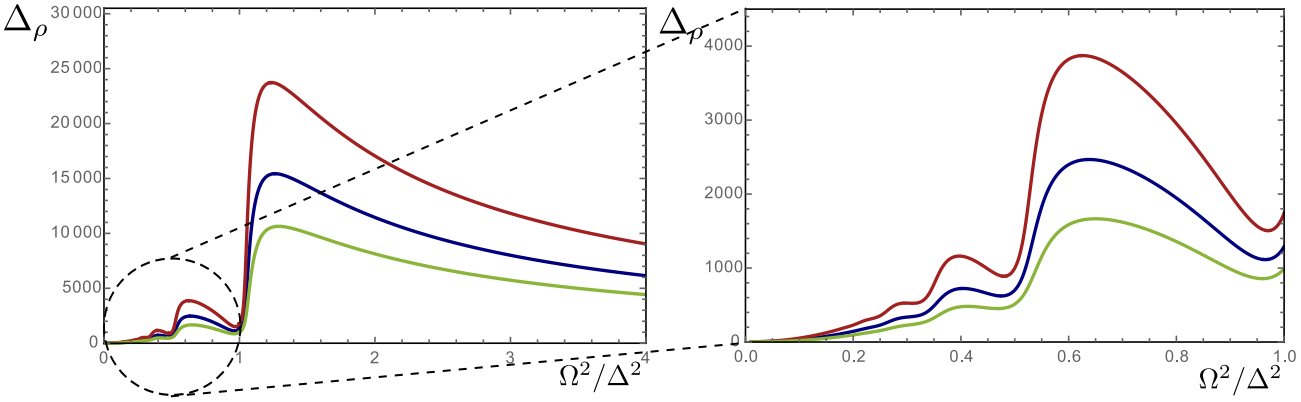

Figure 4.13: Numerically obtained TMR as a function of Ω^2/Δ^2 for pointlike impurities and for Weyl nodes shifted in energy by 2Δ. The enlarged panel shows the TMR for separated Landau levels and focuses on the Shubnikov-de Haas oscillations. The results are obtained by using Eq. (4.9) for $\Delta < \Omega$ and Eq. (4.24) for $\Delta > \Omega$. In both panels red, blue, and green lines correspond to $A\Delta/\Omega^2 = 5 \cdot 10^{-3}, 6 \cdot 10^{-3}, 7 \cdot 10^{-3}$, respectively. For all curves $\Lambda/\Omega^2 = 100$.

magnetoresistance is then fully identified by the conductivity σ_{xx},

$$\Delta_\rho(H) = \frac{\sigma_{xx}(0)}{\sigma_{xx}(H)} - 1 \tag{4.117}$$

In the considered model, the carriers in one pair of Weyl nodes have chemical potential Δ while the other pair is characterized by the chemical potential of $-\Delta$, cf. Fig 4.12, leading to the multiplication with the number of Weyl nodes in the total TMR. In proceeding sections, we consider the limit of lowest temperatures, $T \sim 0$.

4.5.1 Pointlike impurities

The TMR for the case of zero Hall conductivity and lowest temperatures is evaluated by inverting the conductivity, Eq. (4.29), in the different regimes. For fixed values of Δ and γ, we analyze the evolution of the TMR with increasing magnetic field, yielding

$$\Delta_\rho \sim \begin{cases} \dfrac{v^6\Omega^4}{\Delta^6\gamma^2} - 1, & \dfrac{\gamma^{1/2}\Delta^{3/2}}{v^{3/2}} \ll \Omega \ll \dfrac{\gamma^{1/4}\Delta^{5/4}}{v^{3/4}}, \\ \dfrac{\Omega^4}{\Delta^2\Gamma^2(\Delta)} - 1, & \dfrac{\gamma^{1/4}\Delta^{5/4}}{v^{3/4}} \ll \Omega < \Delta, \\ \dfrac{v^6}{\gamma^2\Omega^2}, & \Delta < \Omega \ll \dfrac{v^3}{\gamma}. \end{cases} \tag{4.118}$$

In the regime of separated LLs, $\gamma^{1/4}\Delta^{5/4}v^{-3/4} \ll \Omega \ll \Delta$, the minima of the Shubnikov-de Haas oscillations show a sublinear ($H^{2/3}$) behavior, while the maxima of the TMR scale quadratically with

magnetic field. In lowest magnetic fields, the TMR vanishes quadratically. Obtained via a numerical solution of the SCBA equations, we depict the Shubnikov-de Haas oscillations and the TMR in Fig. 4.13. In highest magnetic fields, we find a TMR decaying as $1/H$, similarly to the case of non-shifted Weyl nodes.

4.5.2 Charged impurities

For charged impurities, the sample can be at the complete charge compensation point ($N_+ = N_-$) for a finite concentration of Coulomb impurities when the concentration of positively and negatively charged impurities is equal. The conductivity for Coulomb impurities, as analyzed in Sec. 4.4.2 for finite chemical potential, is given by Eqs. (4.101) and (4.102). For fixed values of Δ and ε_{imp}, we first calculate the TMR for $\Delta < \varepsilon_{\text{imp}}$:

$$\Delta_\rho \sim \frac{\Omega^2}{\varepsilon_{\text{imp}}^2}, \quad \varepsilon_{\text{imp}} \ll \Omega. \tag{4.119}$$

For $\Delta > \varepsilon_{\text{imp}}$, the evolution of the TMR with increasing magnetic field is described by

$$\Delta_\rho \sim \begin{cases} \dfrac{\Omega^4\Delta^2}{\varepsilon_{\text{imp}}^6} - 1, & \dfrac{\varepsilon_{\text{imp}}^{3/2}}{\Delta^{1/2}} \ll \Omega \ll \Delta^{1/4}\varepsilon_{\text{imp}}^{3/4}, \\ \dfrac{\Omega^4}{\Delta^2\Gamma_C^2(\Delta,\Omega)} - 1, & \Delta^{1/4}\varepsilon_{\text{imp}}^{3/4} \ll \Omega < \Delta, \\ \dfrac{\Omega^2\Delta^4}{\varepsilon_{\text{imp}}^6}, & \Delta < \Omega. \end{cases} \tag{4.120}$$

In the quantum limit, where only the zeroth Landau level contributes to transport, the large TMR shows a linear behavior in both limits. The linear TMR in highest magnetic fields is very robust and is unaffected by the shift of Weyl nodes in energy compared to the case of a single node (cf. Secs. 4.3.2 and 4.4.2).

In lower magnetic fields, the results remain essentially unaffected by the model of disorder. As for pointlike impurities, the minima of the TMR evolve as $H^{2/3}$ and the maxima as H^2 in magnetic field. The numerically evaluated results of TMR are presented in Fig. 4.14 for both the regime of magneto-oscillations and in the ultra-quantum limit of the TMR. Compared to experiments, the overall picture of the TMR agrees by showing strong Shubnikov-de Haas oscillations on top of the rapidly increasing background and crossing over into a purely linear TMR without magneto-oscillations in the limit of highest magnetic field.

Close to the exact compensation point, the Hall resistivity is finite. However, the above picture for the TMR with magneto-oscillations on top of strong TMR applies as long as $\sigma_{xx} \gg \sigma_{xy}$. We denote by $\delta\mu \propto (N_+ - N_-)^{1/3} \ll \Delta$ the distance from the neutrality point. This translates into a Hall conductivity of

$$\sigma_{xy} \sim \frac{e^2\delta\mu}{v} \begin{cases} 1, & \Delta < \Omega, \\ \dfrac{\Delta^2}{\Omega^2}, & \Delta > \Omega. \end{cases} \tag{4.121}$$

The condition $\sigma_{xx} \gg \sigma_{xy}$ with the background conductivity given by Eq. (4.98) for $\Delta > \Omega$ converts into

$$\frac{\varepsilon_{\text{imp}}^3}{\Omega^2} \gg \delta\mu. \tag{4.122}$$

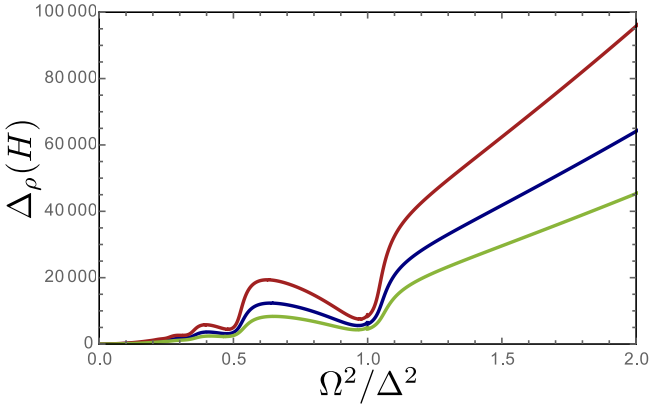

Figure 4.14: Numercially obtained TMR for Coulomb impurities and shifted Weyl nodes as a function of Ω^2/Δ^2. The results are obtained from Eq. (4.94) for $\Omega > \Delta$ and from Eq. (4.97) for $\Omega < \Delta$. These results nicely match at the border of the regimes in the numerical evaluation. Red, blue and green lines correspond to $\varepsilon_{\text{imp}}^3/\Delta^3 = 5 \cdot 10^{-3}, 6 \cdot 10^{-3}, 7 \cdot 10^{-3}$, respectively. For all curves $\Lambda/\Omega^2 = 100$.

For similar concentrations of positively and negatively charged impurities, this condition can be fulfilled in a wide range of magnetic fields.

4.5.3 Shubnikov-de Haas oscillations and comparison to experiment

In contrast to the model of non-shifted Weyl nodes, the model of shifted Weyl nodes provides an increasing TMR superimposed by strong Shubnikov-de Haas oscillations. The maxima of the magnetooscillations for shifted Weyl nodes correspond to H^2 with respect to magnetic field. This is in contrast to the model of non-shifted nodes where the vanishing TMR shows spikes corresponding to the center of Landau levels in the density of states. The maxima of these spikes increase with magnetic field as $H^{4/3}$.

Before concluding this chapter, we quantitatively compare our results for the TMR for shifted nodes to the data of the experiment on magnetotransport in NbP [5]. In this experiment, a strong TMR was measured in a very wide range of magnetic fields up to highest fields where quantum oscillations were no longer observed. We start with the comparison of the value of magnetic field where oscillations disappear in the experimentally measured TMR curve, $H \sim 32\text{T}$, with the value of magnetic field where transport is manifested by the ultra-quantum limit in our calculation. The value of magnetic field is determined by the distance between the zeroth and the first Landau level leading to the condition $\Omega = \Delta$. The shift of chemical potential, as presented in the band structure calculations of Ref. [5], is estimated by $\Delta \sim 0.1eV$. As extracted from Ref. 4.14 by the analysis of the magnetooscillation, the Fermi velocity is $v \simeq 4.8 \times 10^7 \text{cm/s}$. The Fermi velocity together with $\Delta = 0.1eV$, the condition $\Omega = \Delta$ translates into a magnetic field of $H \sim 30\text{T}$, which is in good agreement with the experimental observation. Furthermore, the slope of the linear TMR in experiment [5] of $1.3 \cdot 10^5\%$ per 1T is again in a good agreement with our result presented in Fig. 4.14. The magnitude in our calculation is

determined by $\Delta/\varepsilon_{\text{imp}}$, which is extracted from the zero-field resistivity in experiment: $\Delta/\varepsilon_{\text{imp}} \sim 7$. The parameters in Fig. 4.14 are $\Delta/\varepsilon_{\text{imp}} \sim 5.2 - 5.8$. Since the magnitude in Fig.4.14 is compatible to the one in experiment, the parameter nicely compares. A similar slope of the TMR is found in Ref. [40] where the range of magnetic field in measurement corresponds to the part of Fig. 4.14 where $\Omega < \Delta$.

4.6 Summary of Chapter 4

We conclude this chapter by a summary of the main results. We have studied the transversal magnetoresistivity (TMR) in two different models of disorder: (i) pointlike impurities and (ii) charged impurities. We considered finite temperatures where, away from the lowest Landau level, even moderate temperatures $T > \Omega/\sqrt{n}$ result in a broadening of Landau levels such that the conductivity is described by the classical Drude formula. The analysis of magnetotransport away from the charge neutrality point includes the calculation of the Hall conductivity and the consideration of Shubnikov-de Haas oscillations. Furthermore, we discuss a realistic model of Weyl nodes shifted in energy (as found in various Weyl and Dirac semimetals) with chemical potential corresponding to total charge compensation. A compact summary of the most important results is provided in Tab. 4.1 where we point out the differences and similarities within the two disorder models.

The behavior of the TMR in strongest magnetic field is very robust. In all considered cases, the magnetoresistance vanishes as $1/H$ for pointlike impurities. For charged impurities, a magnetic field dependent screening leads to a linearly evolving magnetoresistance in the ultra quantum limit for both finite temperatures and for the model of shifted Weyl nodes. However, it should be noted that the magnetoresistance for Coulomb impurities in the presence of a finite chemical potential for non-shifted Weyl nodes is different for the cases of fixed chemical potential and fixed particle density. For fixed chemical potential and Coulomb impurities, the magnetoresistance in strongest magnetic field vanishes as $1/H$ due to the dominant Hall conductivity. The linear magnetoresistance for charged impurities is, however, restored for the consideration of fixed particle density which is the relevant case in experiment.

In low magnetic fields and for finite temperature, we find a non-analytically $\sim H^{1/3}$ vanishing magnetoresistance in lowest fields for pointlike impurities, Eq. (4.63), while for charged impurities the TMR vanishes quadratically, Eq. (4.76). The non-analyticity gives rise to the unconventional behavior of transport at the charge neutrality point.

Away from charge neutrality, we identify a rich variety of regimes related to a competition between the conductivity and the Hall conductivity. In both models of disorder, this manifests in a negligible magnetoresistance in lower magnetic fields (even for separated Landau levels) showing peaks at the center of Landau levels.

In the most sophisticated model (but experimentally relevant) of pairs of Weyl nodes shifted in energy with respect to each other, we find a huge TMR superimposed by strong magneto-oscillations away from the lowest Landau level and for both models of disorder. This model is manifested by a fully or partly compensated Hall conductivity while the conductivity corresponds to the finite particle density in each pair of Weyl nodes. The strong background TMR evolves as $H^{2/3}$ with Shubnikov-de Haas oscillations increasing quadratically with magnetic field. Together with the linearly increasing high-field TMR for the lowest Landau level in the model of Coulomb, we find an increasing magnetoresistance in a wide range of magnetic field as observed in experiment. The results for shifted nodes are visualized in Figs. 4.13 and 4.14. A qualitative comparison with experiment, cf. Sec 4.5.3, shows that the magnitude of the calculated TMR within the model of shifted Weyl nodes nicely agrees with the magnitude observed in experiment, cf. Sec. 1.2. It should be noted that we considered two idealized cases: (i) no

charge compensation between the pair of Weyl nodes, (ii) full charge compensation between the nodes. The intermediated case of partial compensation as present in experiment [5, 6] would show a variety of regimes due to the competition between σ_{xx} and σ_{xy}. Furthermore, a superposition of Shubnikov-de Haas oscillations from the different nodes would be present.

It should be noted that this chapter does not cover the calculations in the full range of temperatures. We discuss either the case of high temperatures, where magneto-oscillations are exponentially suppressed due to thermal smearing or the case of vanishing temperature, where thermal smearing is neglected. Our results without thermal smearing are well applicable for temperatures smaller then the distance between the Landau levels where strong Shubnikov-de Haas oscillations are observed. However, thermal smearing leads to a finite magnetoresistance even in the model without shifted nodes. For temperatures smaller than the chemical potential, we find a small linear magnetoresistance (cf. Eqs. (4.85) and (4.113)), while the magnetoresistance is large for temperatures where the Hall conductivity gets negligible.

Finally, we discuss briefly the limitations of the presented model. Effects in the TMR stemming from mechanisms beyond SCBA were not considered here. The mechanism of classical memory effect was recently addressed for Weyl semimetals [88] and obtained a magnetoresistance in the order of $1-2$ orders of magnitude compared to the the 5 orders of magnitude in experiment [5]. This mechanism requires a large correlation radius of disorder which is realized in 3D by a small "fine-structure" constant, Eq. (3.86) (assumed to be $\gtrsim 1$ in the previously discussed case). Moreover, the classical memory effect is assumed to be suppressed in the ultra-quantum limit compared to conventional materials [158]. In Weyl semimetals, the chiral zeroth LL requires internodal scattering (inactive for Weyl semimetals) for finite backscattering. However, a further interesting aspect would be to calculated these memory effects in the presence of Coulomb impurities and compare the results with those presented here. Another interesting aspect would be the consideration of interactions. In particular, possible Lutteringer liquid interactions in the 1D channel in the ultra quantum-limit or the electron-hole recombination in compensated systems with finite geometry, cf. Ref. [159]. These effects might be important in the regime where no finite magnetoresistance was observed here, cf. Sec. 4.4, meaning specifically low temperatures $T < \Omega/\sqrt{n}$. However, we do not expect that these additional mechanisms change the overall picture of the TMR presented here.

Table 4.1: Summary of the most important results for the TMR in Weyl semimetals. We compare the results for pointlike impurities and Coulomb impurities in the two columns. The results between the two columns apply to both disorder models. Moreover, we compare the model of Weyl nodes shifted in energy with respect to each other with the model of non-shifted nodes.

	pointlike impurities	Coulomb impurities
non-shifted Weyl nodes	• non-analytic lowest field TMR $\propto H^{1/3}$ at finite T, Eq. (4.63) and Fig. 4.4	• lowest field TMR $\propto H^2$ at finite T, Eq. (4.76) and Fig. 4.7
	• TMR vanishing as $\propto 1/H$ in the quantum limit for fixed N, Eq. (4.90) and Fig. 4.9	• linear TMR $\propto H$ in the quantum limit for fixed N, Eq. (4.112) and Fig. 4.10
	• vanishing TMR in moderate fields • peaks in the center of LLs for TMR in moderate fields, Fig. 4.8	
shifted Weyl nodes	• TMR vanishing as $\propto 1/H$ in the quantum limit, Eq. (4.118) and Fig. 4.13	• linear TMR $\propto H$ in the quantum limit, Eq. (4.120) and Fig. 4.14
	• TMR evolving with $H^{2/3}$ in moderate fields, Figs. 4.13 and 4.14 • strong Shubnikov-de Haas oscillations in moderate fields, Figs. 4.13 and 4.14	

5 Chapter 5
Magnetoresistance in carbon nanotubes with SMMs

This chapter is devoted to a theoretical model for the magnetoresistance (MR) in carbon nanotubes with the side-attached single-molecule magnets (SMM). As discussed in Sec. 1.4, a giant MR was observed in these systems [58, 77, 78]. The MR is characterized by the ratio $[\mathcal{G}(B) - \mathcal{G}(0)]/\mathcal{G}(0)$, where $\mathcal{G}(B)$ and $\mathcal{G}(0)$ denote the conductance with and without magnetic field, respectively. With a slow variation of magnetic field, the magnetic moments of the molecules become parallel oriented to each other resulting in the observation of reproducible sharp jumps for the conductance of the CNTs tunnel-coupled to the leads. By varying the gate voltage, the MR effect in such nanotube systems can reach $10^3\%$. This spin-valve effect can be by its manifestation compared with the most prominent giant MR effect in thin metallic films with magnetic contract which is widely used in the field of spintronics. Other examples for the observation of a similar spin-valve effect are thin graphene strips with SMMs [79] and in CNTs with permalloy contacts [80].

Theoretically, nanostructures involving SMMs, such as molecular quantum dots coupled to metallic leads, were discussed in several works. Specifically, the measurement of the spin current as a possible read-out for the local spin orientation [89], asymmetries in the Coulomb diamonds and Kondo peaks [90], and the spin-blockade effect associated with a change of magnetic anisotropy [91] were addressed. The analysis of the tunnel magnetoresistance for a single-walled CNT with side-attached molecule in Ref. [93] led to the result that the tunneling magnetoresistance may depend on the exchange interaction between the CNT and the SMMs [93]. A proposal of a mechanism for the spin-valve effect for (effectively infinite) CNTs with SMMs was performed in Ref. [92].

In this chapter, we analyze the MR for the CNT with side-attached SMMs tunnel-coupled to leads. The proposed theoretical model is based on spin-dependent resonant scattering of conducting electrons on the bound state inside a molecule (Fano resonance) [92, 160, 161]. In order to propose this model, we first need to consider the effect of the leads on the transport through the Fano state. We proposed this model of the spin-valve effect in Ref. [94]. There, scattering of electrons on Fano resonances was addressed in the classical limit. The classical limit is sufficient to explain the spin-valve effect and thus the MR since the important ingredient, the blocking of transport in the resonant energy region, is fully described already in the classical limit. Moreover, the classical limit is fully justified in the case of strong dephasing as discussed below. However, in this chapter, we go beyond the classical limit and discuss also quantum effects of the leads on a Fano state. The quantum effects are addressed in the three different approaches, two approaches, where the Fano states is treated perturbatively and the

conventional scattering matrix approach. The results are in preparation to be published [162].

The chapter is structured as follows. First, we revise the transmission across a Fano state in an infinite system, Sec. 5.1. Then, we continue the chapter with an analysis of a Fano state in a confined geometry meaning within two barriers, Sec. 5.2, where we discuss the transmission amplitude in presence of strong dephasing, Sec. 5.2.1, and in the full quantum mechanical limit, Sec. 5.2.2. In Sec. 5.3, we apply the consideration of Fano-resonances to SMMs attached to a CNT which is coupled to leads. Section 5.3.1 explains then the origin of the MR within the model of Fano-resonances. Finally, the results are summarized and discussed in Sec. 5.4.

5.1 Transmission across Fano state

Fano resonances originate from the quantum mechanical interference of a discrete state and a continuum of states [160]. Specifically, the electronic wave scattered on the discrete state acquires a phase shift compared to the waves that do not pass the discrete state. At the Fano resonance, the two waves interfere destructively resulting in a zero transmission.

Let us start with the Hamiltonian of one-dimensional electrons which are tunnel coupled to a localized state. We will study the effect of transport in this system without Coulomb interaction. The Hamiltonian of such a system reads:

$$\hat{\mathcal{H}} = E_0|\varphi\rangle\langle\varphi| + \sum_k \Big(E_k|\psi_k\rangle\langle\psi_k| + t_k|\varphi\rangle\langle\psi_k| + t_k^*|\psi_k\rangle\langle\varphi| \Big), \tag{5.1}$$

where E_0 denotes the energy of the localized state with the corresponding wave function φ, $E_k = \hbar^2 k^2/(2m)$ and ψ_k are energy and wave function of the state k in the one-dimensional channel, $t_k = \langle\varphi|\hat{T}|\psi_k\rangle$ is the Bardeen tunneling matrix element [163]. The wave functions φ and ψ_k are assumed to be orthogonal to each other.

In an infinite channel, the transmission (t_M) and reflection (r_M) amplitudes for the scattering off the localized Fano state are given by [161] (the subscript "M" stand for the molecular state of the single molecule magnets as required later in this chapter):

$$t_M = \frac{E_k - E_M(k)}{E_k - E_M(k) + i\Gamma_M(k)}, \tag{5.2}$$

$$r_M = \frac{-i\Gamma_M(k)}{E_k - E_M(k) + i\Gamma_M(k)}, \tag{5.3}$$

where

$$E_M(k) = E_0 + P\int_0^\infty dp\ \frac{|t_p|^2}{E_k - E_p}, \tag{5.4}$$

$$\Gamma_M(k) = \pi \int_0^\infty dp\ \delta(E_p - E_k)|t_p|^2. \tag{5.5}$$

At the resonance point, $k_0 = \sqrt{2mE_0/\hbar^2}$, we denote $E_0 = E_M(k_0)$ and $\Gamma_M = \Gamma_M(k_0)$. For an infinite channel, it is sufficient to take $E_M(k)$ and $\Gamma_M(k)$ at the resonant point. The energy scale Γ_M describes the broadening of the localized state originating from the coupling between the 1D channel and localized state. At the resonance point, it is clearly seen that the Fano state suppresses the transmission in the window of resonant energy $E_k \sim (E_0 - \Gamma_M, E_0 + \Gamma_M)$. For a confined geometry,

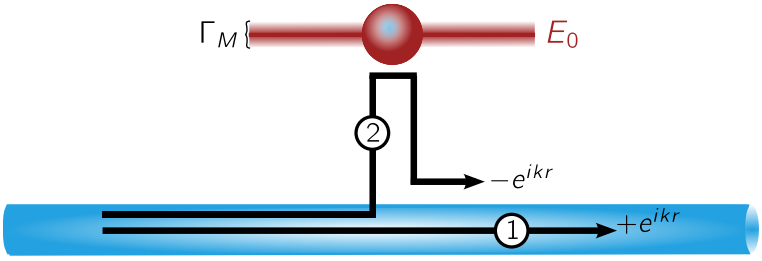

[Reprinted figure with permission from I. V. Krainov, J. Klier, A. P. Dmitriev, S. Klyatskaya, M. Ruben, W. Wernsdorfer, and I. V. Gornyi, ACS Nano, 2017 **11** (7), 6868-6880. Copyright 2017 by the American Chemical Society. DOI: 10.1021/acsnano.7b02014]

Figure 5.1: Schematic illustration of the origin of the Fano resonance in transmission though an infinite one-dimensional channel tunnel-coupled with a discrete state (red level). The destructive interference of waves passing the discrete level without visiting it (path 1) and the waves visiting the Fano state (path 2) leads to a vanishing transmission for electrons with the resonant energy ($E_k = E_0$).

however, the broadening of the Fano-resonance is changed by the properties of the boundaries and may also be momentum dependent, as we will discuss in the proceeding chapter.

A schematic illustration of the appearance of the Fano resonance is depicted in Fig. 5.1. It shows the interference of the electronic wave that passes the 1D continuum directly without scattering and the wave that passes via scattering on the discrete state (paths 1 and 2 in Fig. 5.1, respectively). Exactly at the resonance $E_k = E_0$, path 2 acquired a phase of π leading to zero transmission since the sum of the two waves vanishes $e^{ikx} + e^{ikx+i\pi} = 0$. Accordingly, the reflection coefficient reaches maximum (unity) at the resonance. As a result, the discrete level acts as an effective barrier with a transparency depending on the energy of scattered electrons.

5.2 Fano-resonance in a double-barrier structure

If the 1D channel is tunnel-coupled to external leads, the coupling to the leads is described by barriers. The barriers are characterized by the transmission coefficient $\mathcal{T}_{L,R}$ and the reflection coefficient $\mathcal{R}_{L,R}$. Here, the index "L" stands for the left barrier and "R" for the right. If we consider just two equal barriers, there are resonances in the transmission dependent on the momentum of the carriers of the channel and length of the system. The resonances originate from destructive interference of the states between the barriers and the reflected states. Those resonances form energy levels which are broadened by the strength of the barriers and describe the level spacing in a 1D quantum dot. In the presence of strong dephasing, the classical transmission and reflection amplitudes apply to the system. In the following, we will analyze those aspects in the presence of a Fano state and define the conditions to explain the magnetoresistance in the CNT with side-attached SMMs.

5.2.1 Role of dephasing for tunneling

In real structures, some dephasing is always present. In this section, we illustrate the effect of dephasing on transport in a one-dimensional case for a simple model with two barriers characterized by the

transmission/reflection amplitudes $t_{L,R}, r_{L,R}$. The transmission coefficients for two barriers can be found by a summation over all paths with transmissions and reflections at the barriers:

$$t = t_L e^{ikL} t_R + t_L e^{ikL} r_R e^{ikL} r_L e^{ikL} t_R + \ldots = t_L t_R e^{ikL} \sum_{n=0}^{\infty} \left(r_L r_R e^{i2kL} \right)^n = \frac{t_L t_R e^{ikL}}{1 - r_L r_R e^{i2kL}}. \tag{5.6}$$

To model dephasing, we include a random potential $V_r(t)$ in the Hamiltonian. Specifically, we include dephasing for a particle moving from one barrier to another by replacing $r_L r_R e^{i2kL} \to r_L r_R e^{i2kL} e^{i\phi}$. The phase ϕ is random and has the distribution

$$P(\phi) = \frac{e^{-\frac{\phi^2}{4\gamma_\phi}}}{2\sqrt{\pi\gamma_\phi}}. \tag{5.7}$$

Within this simple model of dephasing the transmission amplitude for a given realization of phases ϕ_m is given by

$$t(\{\phi\}) = t_L t_R e^{ikL} \sum_{n=0}^{\infty} \left(r_L r_R e^{i2kL} \right)^n e^{i \sum_{m=0}^{n} \phi_m}. \tag{5.8}$$

Now we calculate the transmission coefficient $\mathcal{T} = |t|^2$ for a double-barrier structure and average it over the random phases:

$$\langle \mathcal{T} \rangle = \int \prod_i d\phi_i P(\phi_i)\ t(\{\phi\}) t^*(\{\phi\}) = \frac{\mathcal{T}_L \mathcal{T}_R \left(1 - \mathcal{R}_L \mathcal{R}_R e^{-2\gamma_\phi} \right)}{\left| 1 - r_L r_R e^{i2kL - \gamma_\phi} \right|^2 \left(1 - \mathcal{R}_L \mathcal{R}_R \right)}. \tag{5.9}$$

Here, we denote $\mathcal{R}_{L,R} = |r_{L,R}|^2$, $\mathcal{T}_{L,R} = |t_{L,R}|^2 = 1 - \mathcal{R}_{L,R}$. Moreover, γ_ϕ characterize the dephasing due to the accumulation of the random phase.

Without dephasing ($\gamma_\phi = 0$), the transmission coefficients at resonances, $\mathcal{T}_{\text{res}}$, and away from the resonances, $\mathcal{T}_{\text{non-res}}$, strongly differ from each other for $\mathcal{T}_{L,R} \ll 1$:

$$\mathcal{T}_{\text{res}} = \frac{\mathcal{T}_L \mathcal{T}_R}{(1 - \sqrt{\mathcal{R}_L \mathcal{R}_R})^2} \approx \frac{4 \mathcal{T}_L \mathcal{T}_R}{(\mathcal{T}_L + \mathcal{T}_R)^2}, \tag{5.10}$$

$$\mathcal{T}_{\text{non-res}} = \frac{\mathcal{T}_L \mathcal{T}_R}{(1 + \sqrt{\mathcal{R}_L \mathcal{R}_R})^2} \approx \frac{\mathcal{T}_L \mathcal{T}_R}{4}. \tag{5.11}$$

In the opposite case of strong dephasing, $\gamma_\phi \gg 1$, one obtains the classical result $\langle \mathcal{T} \rangle_{\text{class}}$ which can be calculated from the kinetic/rate equations [134]:

$$\mathcal{T}_{\text{class}} = \frac{\mathcal{T}_L \mathcal{T}_R}{1 - \mathcal{R}_L \mathcal{R}_R} \approx \frac{\mathcal{T}_L \mathcal{T}_R}{\mathcal{T}_L + \mathcal{T}_R}. \tag{5.12}$$

This result can also be obtained by considering a classical particle propagating from one barrier to another with a summation of all transmissions/reflections. The main effect of dephasing is the absence of strong resonances. In particular, for equal strong barriers, $\mathcal{T}_L = \mathcal{T}_R \ll 1$, Eq. (5.10) yields ideal transmission $\mathcal{T}_{\text{res}} = 1$, whereas the classical result (5.12) gives $\mathcal{T}_{\text{class}} \ll 1$.

We apply now this concept to such a double barrier system in presence of a discrete state. The transmission and reflection coefficients of this state are denoted by $\mathcal{T}_M$ and $\mathcal{R}_M$ which are given by

the absolute value of the amplitudes (5.2) and (5.3), respectively. It is assumed that the state is located between barriers. We use classical expression (5.12) for the transmission through a double-barrier structure and first replace the right barrier by the Fano state. The transmission and reflection coefficient of the composite system consisting of the left barrier and the Fano state reads

$$\mathcal{T}_{LM} = \frac{\mathcal{T}_L \mathcal{T}_M}{1 - \mathcal{R}_L \mathcal{R}_M}, \tag{5.13}$$

$$\mathcal{R}_{LM} = \frac{\mathcal{R}_M + \mathcal{R}_L(\mathcal{T}_M - \mathcal{R}_M)}{1 - \mathcal{R}_L \mathcal{R}_M}. \tag{5.14}$$

Now, we calculate the transmission coefficient for the whole structure replacing $\mathcal{T}_L$ and $\mathcal{R}_L$ by $\mathcal{T}_{LM}$ and $\mathcal{R}_{LM}$ in Eqs. (5.13) and (5.14) and find

$$\mathcal{T}_{BMB} = \frac{\mathcal{T}_{LM}\mathcal{T}_R}{1 - \mathcal{R}_{LM}\mathcal{R}_R} = \frac{\mathcal{T}_L \mathcal{T}_R (E_k - E_0)^2}{(\mathcal{T}_L + \mathcal{T}_R - \mathcal{T}_L\mathcal{T}_R)(E_k - E_0)^2 + \mathcal{T}_L\mathcal{T}_R\Gamma_M^2}. \tag{5.15}$$

In addition, we can write the transmission coefficient in terms of the transmission coefficient of the double barrier system $\mathcal{T}_{BB}$. The expression is given by

$$\mathcal{T}_{BMB} = \frac{\mathcal{T}_{BB}(E_k - E_0)^2}{(E_k - E_0)^2 + \mathcal{T}_{BB}\Gamma_M^2}. \tag{5.16}$$

Compared to the system with the infinite channel, the transmission coefficient is now multiplied by the transmission coefficient of the double barrier system without molecule. Moreover, the region of reduced transmission shrinks in the presence of the two barriers, $E_k \sim (E_0 - \sqrt{\mathcal{T}_{BB}}\Gamma_M, E_0 + \sqrt{\mathcal{T}_{BB}}\Gamma_M)$. The transmission amplitude in the case of strong dephasing is visualized by the lower panel of Fig. 5.2.

5.2.2 Quantum interference in a double barrier structure in presence of a Fano state

In order to discuss several methods to consider quantum interference in a double barrier structure in presence of a Fano state, we briefly introduce the wave functions for the simple problem of two δ-shaped barriers located at $x = \pm L$ and strength η in absence of the Fano state, cf. Fig. 5.3. We can decompose the wave functions in symmetric and antisymmetric functions. The symmetric function reads

$$\Psi_{k+}(x) = \begin{cases} \cos(kx) + \frac{\eta}{k}\cos(kL)\sin(k(x-L)), & x \geq L \\ \cos(kx), & |x| \leq L \\ \cos(kx) - \frac{\eta}{k}\cos(kL)\sin(k(x+L)) & x \leq -L \end{cases} \tag{5.17}$$

and the asymmetric is given by

$$\Psi_{k-}(x) = \begin{cases} \sin(kx) + \frac{\eta}{k}\sin(kL)\sin(k(x-L)), & x \geq L \\ \sin(kx), & |x| \leq L \\ \sin(kx) + \frac{\eta}{k}\sin(kL)\sin(k(x+L)) & x \leq -L \end{cases} \tag{5.18}$$

Thus, the right moving wave is described by

$$\phi_{Rk}(x) = a_+(k)\Psi_{k+}(x) + a_-(k)\Psi_{k-}(x), \tag{5.19}$$

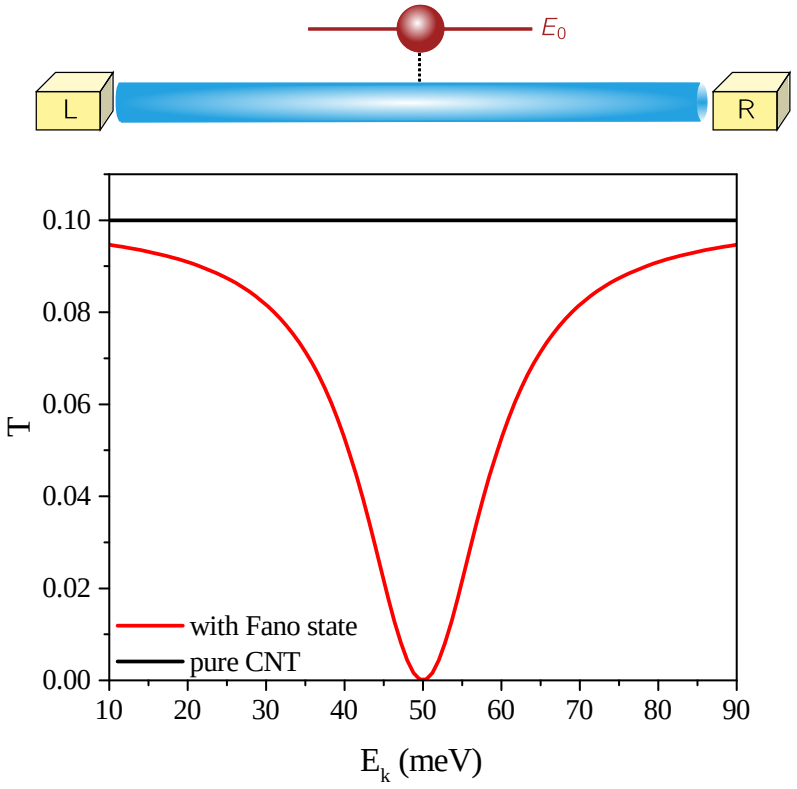

[Reprinted figure with permission from I. V. Krainov, J. Klier, A. P. Dmitriev, S. Klyatskaya, M. Ruben, W. Wernsdorfer, and I. V. Gornyi, ACS Nano, 2017 **11** (7), 6868-6880. Copyright 2017 by the American Chemical Society. DOI: 10.1021/acsnano.7b02014]

Figure 5.2: (Upper panel) Schematic illustration of the setup with an 1D channel coupled to the leads by tunneling barriers in presence of a Fano state. (Lower panel) Transmission coefficient for this setup as a function of the carrier energy E_k in the classical case (strong dephasing) with symmetric barriers. The red curve shows the transmission $\mathcal{T}_{BMB}$ for the structure with barriers and one molecule, the black one shows the transmission for two barriers without the molecule ($\mathcal{T}_{BB}$). The chosen parameters are as follows: the energy of the localized state is $E_0 = 50$ meV; the transmission coefficients across the contacts to the leads are $\mathcal{T}_L = \mathcal{T}_R = 0.17$; the hybridization of conducting electrons with the Fano state is characterized by $\Gamma_M = 30$ meV.

and the left moving wave is given by

$$\phi_{Lk}(x) = a_+(k)\Psi_{k+}(x) - a_-(k)\Psi_{k-}(x). \tag{5.20}$$

Here, the prefactors denote

$$a_+(k) = \frac{ik}{ik - \eta\cos(kL)\exp(ikL)}, \qquad a_-(k) = \frac{ik}{k + \eta\sin(kL)\exp(ikL)}. \tag{5.21}$$

Including the Fano state into the double barrier system, we can consider a Hamiltonian similar to Eq. (5.1). We couple now the Fano state to the left and right moving waves of the double barrier structure. Thus, the Hamiltonian reads

$$\begin{aligned}\hat{\mathcal{H}} = \hat{\mathcal{H}}_0 + E_0|\varphi\rangle\langle\varphi| + \int_0^\infty dk\left(V_{Lk}|\psi_{Lk}\rangle\langle\varphi| + V_{Lk}^*|\varphi\rangle\langle\psi_{Lk}|\right) \\ + \int_0^\infty dk\left(V_{Rk}|\psi_{Rk}\rangle\langle\varphi| + V_{Rk}^*|\varphi\rangle\langle\psi_{Rk}|\right),\end{aligned} \tag{5.22}$$

where $\hat{\mathcal{H}}_0$ is the Hamiltonian of a one dimensional wire within the two barriers with the corresponding eigenfunctions $\psi_{Lk,Rk}(x,\mathbf{r}_\perp) = \phi_{Rk,Lk}(x)\xi(\mathbf{r}_\perp)$. Here, the functions $\phi_{Rk,Lk}(x)$ are the right and right moving waves of the double barrier structure, Eqs. (5.19) and (5.20), respectively. The function $\xi(\mathbf{r}_\perp)$ describes the eigenfunction transverse to the scattering. These functions are chosen similar to the functions introduced in Sec. 2.3. The energy E_0 is the energy of the discrete level located at position $x = a$ with the corresponding wave function $\varphi(x,\mathbf{r}_\perp)$. The functions $\psi_{Lk,Rk}(x,\mathbf{r}_\perp)$ and $\varphi(x,\mathbf{r}_\perp)$ are assumed to be orthogonal to each other. The operator V describes the coupling to the wire where the subscript "L" describes the coupling to left moving particles and "R" to right moving.

The equation for the eigenfunctions Φ_{Rk} of the full Hamiltonian, corresponding to electrons moving through the system from left to right, can be written as

$$\Phi_{Rk}(x,\mathbf{r}_\perp) = \psi_{Rk}(x,\mathbf{r}_\perp) + \int G_k(x,\mathbf{r}_\perp;x',\mathbf{r}'_\perp)V\Phi_{Rk}(x',\mathbf{r}'_\perp)dx'd\mathbf{r}'_\perp. \tag{5.23}$$

Here, the Green's function of the operator $H_0 + E_0|\varphi\rangle\langle\varphi|$ is given by

$$\begin{aligned}G_k(x,\mathbf{r}_\perp;x',\mathbf{r}'_\perp) = \frac{\varphi(x,\mathbf{r}_\perp)\varphi(x',\mathbf{r}'_\perp)}{E_k - E_0} + \int_0^\infty dk'\frac{\psi_{Rk'}(x,\mathbf{r}_\perp)\psi_{Rk'}^*(x',\mathbf{r}'_\perp)}{E_k - E_{k'} + i0} \\ + \int_0^\infty dk'\frac{\psi_{Lk'}(x,\mathbf{r}_\perp)\psi_{Lk'}^*(x',\mathbf{r}'_\perp)}{E_k - E_{k'} + i0}.\end{aligned} \tag{5.24}$$

To solve the self-consistent equation for the right moving function Eq. (5.23), we expand the full function of the system in terms of the eigenfunctions of the Hamiltonian without coupling. With the orthogonality of the functions $\psi_{Lk,Rk}(x,\mathbf{r}_\perp)$ and $\varphi(x,\mathbf{r}_\perp)$, we can then solve the self-consistent equation and obtain

$$\begin{aligned}\Phi_{Rk}(x,\mathbf{r}_\perp) = \psi_{Rk}(x,\mathbf{r}_\perp) + \frac{V_{Lk}}{E_k - E_0 - \Sigma(k)}\varphi(x,\mathbf{r}_\perp) + \frac{V_{Rk}}{E_k - E_0 - \Sigma(k)}\int_0^\infty dk'\frac{V_{Rk'}\psi_{Rk'}(x,\mathbf{r}_\perp)}{E_k - E_{k'} + i0} \\ + \frac{V_{Rk}}{E_k - E_0 - \Sigma(k)}\int_0^\infty dk'\frac{V_{Lk'}\psi_{Lk'}(x,\mathbf{r}_\perp)}{E_k - E_{k'} + i0}\end{aligned} \tag{5.25}$$

with

$$\Sigma(k) = \int_0^\infty dk' \frac{|V_{Rk'}|^2 + |V_{Lk'}|^2}{E_k - E_{k'} + i0} = P \int_0^\infty dk' \frac{|V_{Rk'}|^2 + |V_{Lk'}|^2}{E_k - E_{k'} + i0} + \frac{i\pi m}{k}(|V_{Rk'}|^2 + |V_{Lk'}|^2). \tag{5.26}$$

For a symmetric operator V and the Fano state located at position $x = a$, the coupling to left and right moving waves is given by

$$V_{Rk} = V(a_+(k)\cos(ka) + a_-(k)\sin(ka)), \qquad V_{Lk} = V(a_+(k)\cos(ka) - a_-(k)\sin(ka)) \tag{5.27}$$

Here, $a_+(k)$ and $a_-(k)$ are again given by Eq. (5.21).

To calculate now the transmission amplitude t_{BMB}, we evaluate the remaining integrals in Eq. (5.25) at the pole of the denominator since the other contributions decrease strongly with x and determine the coefficient of the outgoing wave. The coefficient of the outgoing wave is then the transmission amplitude, reading

$$t_{\mathrm{BMB}}(k) = \frac{E_k - E_0' + (i\pi m/k)(|V_{Lk}|^2 - |V_{Rk}|^2)}{E_k - E_0' + (i\pi m/k)(|V_{Lk}|^2 + |V_{Rk}|^2)} t_{\mathrm{BB}}(k) + \frac{(2i\pi m/k)|V_{Lk}V_{Rk}^*}{E_k - E_0' + (i\pi m/k)(|V_{Lk}|^2 + |V_{Rk}|^2)} r_{\mathrm{BB}}(k), \tag{5.28}$$

where $E_0' = E_0 + \mathrm{Re}\Sigma(k)$ and t_{BB} and r_{BB} are the transmission and reflection coefficients of the double barrier structure given by

$$t_{\mathrm{BB}}(k) = \frac{1}{2}\left\{\frac{a_+(k)}{a_+^*(k)} - \frac{a_-(k)}{a_-^*(k)}\right\}, \tag{5.29}$$

$$r_{\mathrm{BB}}(k) = \frac{1}{2}\left\{\frac{a_+(k)}{a_+^*(k)} + \frac{a_-(k)}{a_-^*(k)}\right\}. \tag{5.30}$$

The resulting transmission coefficient is illustrated in Fig. 5.4. Compared to the classical results, Fig. 5.2, the features the molecule are quite similar in the region of reduced transmission. However, away from the reduced transmission region the resonances of the double barrier structure are still affected by the Fano state.

In a next step, we develop a quite similar approach involving Green's functions. Instead of relating the transmission amplitude to the prefactor of the right moving function, we related it to the matrix Green's functions. Green's functions have the advantage that they can be used to describe interacting systems.

We can relate the Green's function of the clean system to the full Green's function, where the electrons scattered off the Fano resonance, by the Dyson equation, reading

$$\hat{\mathbf{G}} = \hat{\mathbf{G}}_0 + \hat{\mathbf{G}}_0 \hat{\mathbf{\Sigma}} \hat{\mathbf{G}}. \tag{5.31}$$

Here, Σ is the self-energy of perturbation. Note, that we can consider in principle any system which is described by plain waves as the clean system even the system itself is scattered at some obstacle. The matrix Green's function is written in the space of left and right moving particles. In the clean system, the Green's function is diagonal in the space of left and right moving particles while scattering of the Fano state introduces off-diagonal components, yielding

$$\hat{\mathbf{G}}_0 = \begin{pmatrix} G_{0,\mathrm{RR}} & 0 \\ 0 & G_{0,\mathrm{LL}} \end{pmatrix} \text{ and } \hat{\mathbf{G}} = \begin{pmatrix} G_{\mathrm{RR}} & G_{\mathrm{RL}} \\ G_{\mathrm{LR}} & G_{\mathrm{LL}} \end{pmatrix}. \tag{5.32}$$

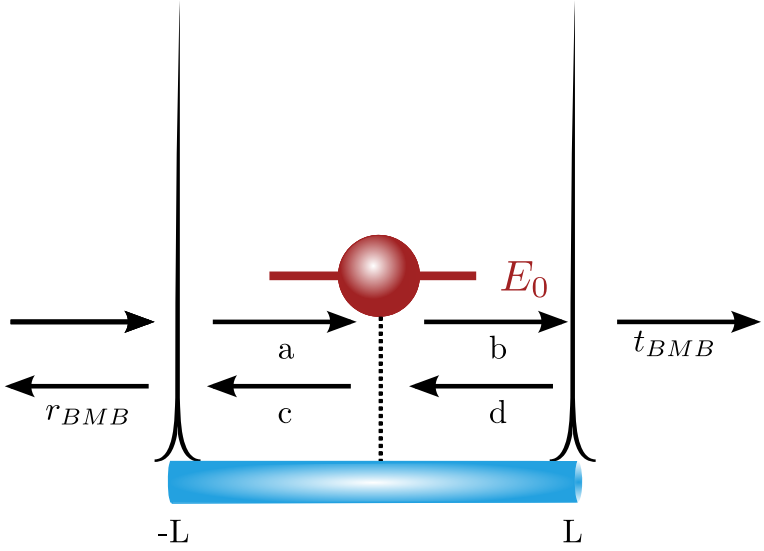

Figure 5.3: Scattering off a Fano state in a system of two symmetric barriers. The coefficients of the wave functions are indicated. The barriers are of height η and located at $\pm L$. The Fano state has the energy E_0 and is located at position a.

We solve the Dyson equation for a particle moving from x' to x with the position of the Fano state at a. Moreover, we assume that the scattering potential does not depend on the direction of the incoming wave, meaning $\Sigma_{11} = \Sigma_{12} = \Sigma_{21} = \Sigma_{22} = \Sigma$. The Green's functions can be thus written as

$$G_{\mathrm{RR}}(x',x) = G_{0,\mathrm{RR}}(x',x) + \frac{G_{0,\mathrm{RR}}(x',a)\Sigma G_{0,\mathrm{RR}}(a,x)}{1 - G_{0,\mathrm{LL}}(a,a)\Sigma - G_{0,\mathrm{RR}}(a,a)\Sigma}, \tag{5.33}$$

$$G_{\mathrm{LL}}(x',x) = G_{0,\mathrm{LL}}(x',x) + \frac{G_{0,\mathrm{LL}}(x',a)\Sigma G_{0,\mathrm{LL}}(a,x)}{1 - G_{0,\mathrm{LL}}(a,a)\Sigma - G_{0,\mathrm{RR}}(a,a)\Sigma}, \tag{5.34}$$

$$G_{\mathrm{LR}}(x',x) = \frac{G_{0,\mathrm{LL}}(x',a)\Sigma G_{0,\mathrm{RR}}(a,x)}{1 - G_{0,\mathrm{LL}}(a,a)\Sigma - G_{0,\mathrm{RR}}(a,a)\Sigma}, \tag{5.35}$$

$$G_{\mathrm{RL}}(x',x) = \frac{G_{0,\mathrm{RR}}(x',a)\Sigma G_{0,\mathrm{LL}}(a,x)}{1 - G_{0,\mathrm{LL}}(a,a)\Sigma - G_{0,\mathrm{RR}}(a,a)\Sigma}. \tag{5.36}$$

For a Fano state, the self-energy is given by

$$\Sigma = \frac{|V|^2}{E_k - E_0}. \tag{5.37}$$

The Green's function of the clean system are written in the spectral representation

$$G_{0,\mathrm{RR/LL}}(x',x) = \int_0^\infty dk' \frac{\Phi_{\mathrm{R/L}k}(x)\Phi^*_{\mathrm{R/L}k}(x')}{E_k - \frac{k'^2}{2m} + i0}. \tag{5.38}$$

We consider now the system of the two barriers as the clean system and the Fano state as the perturbation. For the two barrier located at $\pm L$ and height η, we use the functions of the right and left moving particles given by Eqs. (5.19) and (5.20), respectively. These functions for right and left

moving particles can be written in terms of plane waves with the information about the two barriers stored in a prefactor which is related to the transmission and reflection amplitudes of the double barrier system. The functions in the three sectors, in the left of the barrier, in the right of barriers, and between the barriers, are given by

$$\begin{aligned}
\text{for } x > L: \quad & \Phi_{\mathrm{R}k}(x) = e^{ikx} t_{BB}(k) \\
& \Phi_{\mathrm{L}k}(x) = e^{-ikx} + e^{ikx} r_{BB}(k) \\
\text{for } x < -L: \quad & \Phi_{\mathrm{R}k}(x) = e^{ikx} + e^{-ikx} r_{BB}(k) \\
& \Phi_{\mathrm{L}k}(x) = e^{-ikx} t_{BB}(k) \\
\text{for } x = a: \quad & \Phi_{\mathrm{R}k}(a) = a_+(k)\cos(ka) + a_-(k)\sin(ka) \\
& \Phi_{\mathrm{L}k}(a) = a_+(k)\cos(ka) - a_-(k)\sin(ka)
\end{aligned}$$

The transmission and reflection amplitudes for the double barrier structure in terms of the parameter $a_+(k)$ and $a_-(k)$ are given by Eqs. (5.29) and (5.30).

To evaluate the Green's functions in the corresponding sectors, we preform the integration in Eq. (5.38). This integral has in general a real and an imaginary part. However, the real part can be neglected in all integrals containing wave functions for $x > L$ and $x > -L$. To show this, we calculate the Green's function of a plane wave in 1D and in energy-coordinate representation is for $x > L$ and $x' < -L$, yielding

$$\begin{aligned}
G_{0,\mathrm{RR}}(E_k, x', x) =& \int_0^\infty \frac{dk'}{2\pi} \frac{e^{ik'(x'-x)}}{E_k - k'^2/(2m) + i0} = i\frac{m}{k} e^{ik(x'-x)} - \frac{im}{\pi} \int_0^\infty d\kappa \frac{e^{-\kappa(x'-x)}}{k^2+\kappa^2} \\
=& i\frac{m}{k} e^{ik(x'-x)} - \frac{im}{k\pi} \Big(2\mathrm{Ci}(k(x'-x))\sin(k(x'-x)) \\
& + (\pi - 2\mathrm{Si}(k(x'-x))\cos(k(x'-x)) \Big),
\end{aligned} \tag{5.39}$$

where $\mathrm{Si}(kx)$ and $\mathrm{Ci}(kx)$ are the sine respectively the cosine integral. The second term vanishes in the limit $x \to \infty$ and $x' \to -\infty$ and can thus be neglected as a contribution to the transmission and reflection coefficients.

Applying these assumptions, the relevant Green's functions of the problem without perturbations read

$$G^{\mathrm{trans}}_{0,\mathrm{RR}}(x', x) = \frac{2\pi i m}{k} \left(t_{BB}(k) e^{ik(x-x')} + t_{BB}(k) r^*_{BB}(k) e^{ik(x+x')} \right) \tag{5.40}$$

$$G^{\mathrm{trans}}_{0,\mathrm{LL}}(x', x) = \frac{2\pi i m}{k} \left(t^*_{BB}(k) e^{-ik(x-x')} + t^*_{BB}(k) r_{BB}(k) e^{-ik(x+x')} \right) \tag{5.41}$$

$$G^{\mathrm{trans}}_{0,\mathrm{RR}}(0, x) = \frac{2\pi i m}{k} (a^*_+(k)\cos(ka) + a^*_-(k)\sin(ka)) t_{BB}(k) e^{ikx} \tag{5.42}$$

$$G^{\mathrm{trans}}_{0,\mathrm{RR}}(x', 0) = \frac{2\pi i m}{k} (a_+(k)\cos(ka) + a_-(k)\sin(ka)) \left(e^{-ikx'} + r^*_{BB}(k) e^{ikx'} \right) \tag{5.43}$$

$$G^{\mathrm{trans}}_{0,\mathrm{LL}}(0, x) = \frac{2\pi i m}{k} (a^*_+(k)\cos(ka) - a^*_-(k)\sin(ka)) \left(e^{-ikx} + r_{BB}(k) e^{ikx} \right) \tag{5.44}$$

$$G^{\mathrm{trans}}_{0,\mathrm{LL}}(x', 0) = \frac{2\pi i m}{k} (a_+(k)\cos(ka) - a_-(k)\sin(ka)) t^*_{BB}(k) e^{ikx'}. \tag{5.45}$$

Here, the Green's functions are all obtained for $x > L$ and $x' < -L$. These Green's function can thus be applied to the calculation of the transmission amplitude.

For the reflection amplitude, however, the Green's functions are evaluated for $x < -L$ and $x' < -L$. Thus, the Greens functions are obtained by using Φ_{Rk} and Φ_{Lk} for $x < -L$ for both x and x'. This leads to the following relevant Green's functions

$$G^{\text{ref}}_{0,\text{RR}}(x',x) = \frac{2\pi i m}{k}\left(e^{ik(x-x')} + |r_{BB}|^2 e^{-ik(x-x')} + r^*_{BB}(k)e^{ik(x+x')} + r_{BB}e^{-ik(x+x')}\right), \tag{5.46}$$

$$G^{\text{ref}}_{0,\text{LL}}(x',x) = \frac{2\pi i m}{k}|t_{BB}(k)|^2 e^{-ik(x-x')}, \tag{5.47}$$

$$G^{\text{ref}}_{0,\text{RR}}(0,x) = \frac{2\pi i m}{k}(a^*_+(k)\cos(ka) - a^*_-(k)\sin(ka))\left(e^{ikx} + r_{BB}(k)e^{-ikx}\right), \tag{5.48}$$

$$G^{\text{ref}}_{0,\text{RR}}(x',0) = \frac{2\pi i m}{k}(a_+(k)\cos(ka) + a_-(k)\sin(ka))\left(e^{-ikx'} + r^*_{BB}(k)e^{ikx'}\right), \tag{5.49}$$

$$G^{\text{ref}}_{0,\text{LL}}(0,x) = \frac{2\pi i m}{k}(a^*_+(k)\cos(ka) - a^*_-(k)\sin(ka))t_{BB}(k)e^{-ikx}, \tag{5.50}$$

$$G^{\text{ref}}_{0,\text{LL}}(x',0) = \frac{2\pi i m}{k}(a_+(k)\cos(ka) + a_-(k)\sin(ka))t^*_{BB}(k)e^{ikx'}. \tag{5.51}$$

Here, the Green's functions are valid for $x, x' < -L$.

Using these introduced Green's functions, we are now able to obtain the Green's of the double barrier structure with a molecule between the barriers. The Green's functions provide also the transmission and reflection amplitudes. We use now the perturbative Green's function (5.33)-(5.36). As clean Green's functions, we use these obtained in the previous paragraph Eqs. (5.40)-(5.45). To show the form of the obtained Green's function, we state here the full Green's function for a right moving particle before and after the scattering. The other Green's functions are given in App. D by Eqs. (D.7)-(D.10). The Green's function thus reads

$$\begin{aligned} G^{\text{trans}}_{\text{RR}}(x',x) = &\frac{E_k - E'_0 - \frac{4\pi i m}{k}|V|^2 \text{Re}(a_+(k)a_-(k))\cos(ka)\sin(ka))}{E_k - E'_0 - \frac{2\pi i m}{k}|V|^2(|a_+(k)|^2\cos^2(ka) + |a_-(k)|^2\sin^2(ka))} \\ &\cdot \frac{2\pi i m}{k}\left(t_{BB}(k)e^{ik(x-x')} + t_{BB}(k)r^*_{BB}(k)e^{ik(x+x')}\right), \end{aligned} \tag{5.52}$$

The local Green's function at the position of the Fano state has a non-negligible real part, which is absorbed into the energy renormalization of the Fano state, reading

$$E'_0 = E_0 + P\int_0^\infty \frac{|V|^2(|a_+(k')|^2\cos^2(ka) + |a_-(k)|^2\sin^2(ka))}{E_k - E_{k'}}dk'. \tag{5.53}$$

To obtain the transmission amplitude from these Green's functions, we need to take into account all terms proportional to $e^{ik(x-x')}$. This results in the transmission amplitude for the double barrier structure with a molecule at position a of

$$\begin{aligned} t_{BMB}(k) = &\frac{E_k - E'_0 - \frac{4i|V|^2\pi m}{k}\text{Re}(a_+a^*_-)\cos(ka)\sin(ka)}{E_k - E'_0 - \frac{2i|V|^2\pi m}{k}(|a_+|^2\cos^2(ka) + |a_-|^2\sin^2(ka))}t_{BB} \\ &- \frac{\frac{2i|V|^2\pi m}{k}(|a_+|^2\cos^2(ka) - |a_-|^2\sin^2(ka) - 2\text{Im}(a_+a^*_-)\cos(ka)\sin(ka))}{E_k - E'_0 - \frac{2i|V|^2\pi m}{k}(|a_+|^2\cos^2(ka) + |a_-|^2\sin^2(ka))}r_{BB}. \end{aligned} \tag{5.54}$$

The corresponding result for the reflection amplitude is presented in App. D.

We directly see that the resulting transmission amplitude coincides with the transmission amplitude in Eq. (5.28). Moreover, we can write the transmission amplitude in a more compact form which enables us to see the effect of the Fano state clearly in contrast to the classical approach. However, comparing both results, Eqs. (5.28) and (5.54) to the conventional scattering matrix approach, it is not obvious that both approaches provide the same result.

Let us briefly employ the scattering matrix approach and compare the results with the Green's function approach. This means, we determine the coupled equations for the probability of finding a left or right moving wave in each sector as illustrated in Fig. 5.3. The matching of the probabilities at each scatterer are

$$b\exp(-ika)t = t_{BMB}\exp(-ikL), \tag{5.55}$$
$$b\cdot r = d\exp(-ik(L-a)), \tag{5.56}$$
$$t + c\exp(ik(a+L))r = a\exp(-ik(a+L)), \tag{5.57}$$
$$r + c\exp(ik(a+L))t = r_{BMB}, \tag{5.58}$$
$$a\cdot t_M + d\cdot r_M = b, \tag{5.59}$$
$$a\cdot r_M + d\cdot t_M = c, \tag{5.60}$$

where $t = k/(k+i\eta)^{-1}$ and $r = i\eta/(k+i\eta)^{-1}$ are the transmission and reflection amplitudes of the barriers. The transmission and reflection amplitudes of the Fano state are given by Eqs. (5.2) and (5.3).

Using the transmission and reflection amplitudes and the coupled equations, the solution for the transmission amplitude yields

$$\begin{aligned} t_{BMB} =& \exp(2ikL)k^2(E_k-E_0)\Big[(E_k-E_0)[k^2+(-1+\exp(4ikL))\eta^2+2ik\eta] \\ &+\Gamma_M[ik^2+k\eta(-2+\exp(2ik(L+a))+\exp(2ik(L-a))) \\ &+ i\eta^2(-1-\exp(4ikL)+\exp(2ik(L+a))+\exp(2ik(L-a))]\Big]^{-1}, \end{aligned} \tag{5.61}$$

and the solution for the reflection amplitude is

$$\begin{aligned} r_{BMB} =& \big[i\exp(4ikL)(-i\Gamma_M+E_k-E_0)(k-i\eta)\eta \\ &+(\Gamma_M-i(E_k-E_0))(k+i\eta)\eta - i\exp(2ik(L-a))\Gamma_M\eta^2 \\ &+\exp(2ik(L+a))\Gamma_M(k-i\eta)(-ik+\eta)\big]\Big[(E_k-E_0)[k^2+(-1+\exp(4ikL))\eta^2+2ik\eta] \\ &+\Gamma_M[ik^2+k\eta(-2+\exp(2ik(L+a))+\exp(2ik(L-a))) \\ &+ i\eta^2(-1-\exp(4ikL)+\exp(2ik(L+a))+\exp(2ik(L-a))]\Big]^{-1}. \end{aligned} \tag{5.62}$$

We will show now that the obtained transmission amplitude in the three different approaches are equal. For that purpose, we write the transmission coefficient in a more compact form. Thus, we define $2|V|^2\pi m/k = \Gamma_M$. In the following, we will derive the connections between $a_+(k), a_-(k)$ and t_{BB}, r_{BB}. First of all, we use

$$\frac{r_{BB}}{t_{BB}} = \frac{\mathrm{Re}(a_+a_-^*)}{\mathrm{Im}(a_+a_-^*)} \tag{5.63}$$

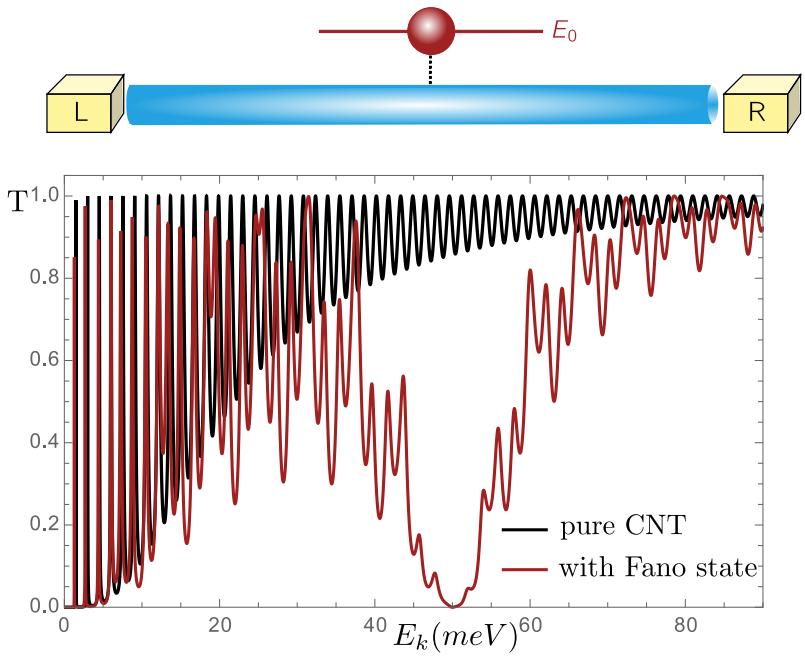

[Upper panel: Reprinted figure with permission from I. V. Krainov, J. Klier, A. P. Dmitriev, S. Klyatskaya, M. Ruben, W. Wernsdorfer, and I. V. Gornyi, ACS Nano, 2017 **11** (7), 6868-6880. Copyright 2017 by the American Chemical Society. DOI: 10.1021/acsnano.7b02014]

Figure 5.4: (Upper panel) Schematic illustration of the setup with an 1D channel coupled to the leads by tunneling barriers in presence of a Fano state. (Lower panel) Transmission coefficient for this setup as a function of the carrier energy E_k in the quantum mechanical case with symmetric barriers. The red curve shows the transmission $\mathcal{T}_{BMB}$ for the structure with barriers and one molecule, the black one shows the transmission for two barriers without the molecule ($\mathcal{T}_{BB}$). The chosen parameters are as follows: the energy of the localized state is $E_0 = 50$ meV; the transmission coefficients across the contacts to the leads is characterized by the barrier strength $\eta_L = \eta_R = 3.16$ meV; the hybridization of conducting electrons with the Fano state is characterized by $\Gamma_M = 30$ meV.

to simplify Eq. (5.54), leading to

$$t_{BMB}(k) = \frac{E_k - E_0'}{E_k - E_0' + i\Gamma_M(|a_+|^2\cos^2(ka) + |a_-|^2\sin^2(ka))} t_{BB} - \frac{i\Gamma_M(|a_+|^2\cos^2(ka) - |a_-|^2\sin^2(ka))}{E_k - E_0' + i\Gamma_M(|a_+|^2\cos^2(ka) + |a_-|^2\sin^2(ka))} r_{BB}. \tag{5.64}$$

To determine the renormalization of the energy of the Fano state, as defined in Eq. (5.53), we use the following relations of the real and imaginary part of the fraction of $a_+(k)$ and $a_-(k)$, reading

$$\mathrm{Im}\left(\frac{a_+(k)}{a_-(k)}\right) = -|a_+(k)|^2, \qquad \mathrm{Re}\left(\frac{a_+(k)}{a_-(k)}\right) = -i|a_+(k)|^2\frac{r_{BB}}{t_{BB}}, \tag{5.65}$$

$$\mathrm{Im}\left(\frac{a_-(k)}{a_+(k)}\right) = -|a_-(k)|^2, \qquad \mathrm{Re}\left(\frac{a_-(k)}{a_+(k)}\right) = i|a_-(k)|^2\frac{r_{BB}}{t_{BB}}. \tag{5.66}$$

Therefore, we can directly evaluate the principle value integral (5.53) via the Kramers Kronig relation. The definition of Kramer Kronig relation is given by

$$\mathrm{Re}F(x) = \frac{2}{\pi}P\int_0^\infty \frac{t\mathrm{Im}F(t)}{t^2 - x^2}dt \tag{5.67}$$

Applying now the Kramers Kronig relation to the relevant terms in Eq. (5.53) results in

$$P\int_0^\infty dk' \frac{|a_+(k')|^2}{E_k - E_k'} = -P\int_0^\infty dk' \frac{k'}{E_k - E_k'}\mathrm{Im}\left(\frac{a_+(k')}{k'a_-(k')}\right) \overset{\text{K.K.}}{=} -\pi m\mathrm{Re}\left(\frac{a_+(k)}{ka_-(k)}\right) = i\frac{\pi m}{k}|a_+(k)|^2\frac{r_{BB}}{t_{BB}}, \tag{5.68}$$

and

$$P\int_0^\infty dk' \frac{|a_-(k')|^2}{E_k - E_k'} = -P\int_0^\infty dk' \frac{k'}{E_k - E_k'}\mathrm{Im}\left(\frac{a_-(k')}{k'a_+(k')}\right) \overset{\text{K.K.}}{=} -\pi m\mathrm{Re}\left(\frac{a_-(k)}{ka_+(k)}\right) = -i\frac{\pi m}{k}|a_-(k)|^2\frac{r_{BB}}{t_{BB}}. \tag{5.69}$$

Thus, the transmission amplitude, Eq. (5.54), can be expressed in a very compact form, reading

$$t_{BMB}(k) = \frac{E_k - E_0}{E_k - E_0 + \Gamma_M\left[\frac{a_+}{a_-}\cos^2(ka) + \frac{a_-}{a_+}\sin^2(ka)\right]} t_{BB} \tag{5.70}$$

In this form, it is straightforward to show the transmission amplitude obtained by the scattering matrix approach is equal to the obtained result by the Green's functions. Applying the same relations to the reflection amplitude (D.23), it is also straightforward to see that both approaches provide the same results.

We define

$$\Sigma(k) = \Gamma_M \left[\frac{a_+}{a_-} \cos^2(ka) + \frac{a_-}{a_+} \sin^2(ka) \right], \tag{5.71}$$

where the real part of $\Sigma(k)$ shifts the resonant energy of the Fano state and the imaginary part broadens the Fano state.

The transmission coefficient reads:

$$\mathcal{T}_{BMB} = \frac{\mathcal{T}_{BB}\ (E_k - E_0)^2}{\left[E_k - E_0 + \mathrm{Re}\Sigma(k)\right]^2 + \left[\mathrm{Im}\Sigma(k)\right]^2}. \tag{5.72}$$

In this notation, the transmission coefficient for the two barriers without the molecule reads:

$$\mathcal{T}_{BB} = \frac{1}{2} - \frac{1}{2}\mathrm{Re}\frac{a_+ a_-^*}{a_- a_+^*}. \tag{5.73}$$

In this very compact, we can nicely see the features of the Fano state on the double barrier structure as visualized in Fig. 5.4. In Fig. 5.4, we can see the shift of reduced transmission due to $\mathrm{Re}\Sigma(k)$ and the momentum dependence of $\mathrm{Im}\Sigma(k)$ resulting in the affected resonances of the double barrier transmission also away from the regime of reduced transmission. A comparison with the classical result for strong barriers shows that the resonant energy E_0 is shifted and the window of suppressed transmission is changed. Due to quantum effects, the window of suppressed transmission is momentum dependent and dependent on the position of the Fano state.

5.3 Fano-resonances with single-molecule magnets

As observed in Raman measurements [132] and found in various density-functional calculations [92, 130], for example, $TbPc_2$ SMMs host a delocalized state on its ligands. For SMMs in contact with the CNTs, tunneling between the electronic states of the CNT and the state localized on ligands occurs and leads to a hybridization of these states. Due to the fact that the hybridization of the conduction electrons with the localized states leads to a Fano resonance [92, 160, 161], transport through the CNT is strongly affected with side-attached molecules.

It was pointed out in Ref. [92] that Fano resonances are particular important for transport through a CNT with attached SMMs. However, the analysis in that paper was limited to infinite systems without the consideration of coupling to leads. As we showed in Ref. [94] and present in Ch. 6, the description of all experimentally observed features requires the consideration of Coulomb blockade. Coulomb blockade is caused by charge quantization in a finite-length CNT with sufficiently high contact resistance and is therefore absent in the infinite system.

In the next step, we will adept the transport properties of the system with Fano resonances, as discussed the preliminary sections of this chapter, to the system of a CNT with side-attached SMMs. Specifically, we consider the transmission coefficient of a nanotube of length L coupled to the leads in the presence of a the localized state of SMMs, the Fano state (upper panel in Fig. 5.2). The two barriers separate the nanotube from the leads and are characterized by the transmission and reflection coefficients $\mathcal{T}_{L,R}$, $\mathcal{R}_{L,R} = 1 - \mathcal{T}_{L,R}$. The Fabry-Pérot-type interference inside the CNT results in Breit-Wigner resonances in the transmission through the structure at energies corresponding to the quantization energy for infinite barriers.

In the following, we will consider the physics of the double-barrier system in the presence of the Fano state in the classical case. This is sufficient for strong dephasing such that the single-particle levels inside the CNT overlap, cf. Sec. 5.2.1. At the same time, the typical time $\hbar/\Gamma_M$ that a particle spends on the localized Fano state is assumed to be shorter than the dephasing time. Thus, the Fano quantum interference is not destroyed. Motivated by the experimental results for the CNT system as introduced in Sec. 1.4, we can conclude that the single-particle levels inside the dot overlap which fully justifies the application of the classical results. The transmission coefficient $\mathcal{T}_{BMB}$ for the structure "barrier-molecule-barrier" (BMB) can be expressed in a classical manner by the quantum expression for the transmission and reflection amplitudes of the Fano state on the molecule, cf. Sec. 5.2:

$$\mathcal{T}_{BMB} = \mathcal{T}_{BB}\frac{(E_k - E_0)^2}{(E_k - E_0)^2 + \mathcal{T}_{BB}\Gamma_M^2}, \tag{5.74}$$

$$\mathcal{T}_{BB} = \frac{\mathcal{T}_L\mathcal{T}_R}{1 - \mathcal{R}_R\mathcal{R}_L}, \tag{5.75}$$

with $\mathcal{T}_{BB}$ describing the classical transmission coefficient for the two barriers without molecule. As discussed in Ch. 5.2, in the presence of the leads compared to the infinite system the window of suppressed transmission due to the Fano effect is reduced to $E_k \sim (E_0 - \sqrt{\mathcal{T}_{BB}}\Gamma_M, E_0 + \sqrt{\mathcal{T}_{BB}}\Gamma_M)$, and the transmission probability $\mathcal{T}_M$ is also reduces by the multiplication with the transmission coefficient for the two barriers, $\mathcal{T}_{BB}$. In the lower panel of Fig. 5.2, the classical transmission coefficient for the CNT with one Fano center is shown.

In the general case of arbitrary dephasing (including the zero-dephasing case), the structure of the total transmission probability $\mathcal{T}_{BMB}$ is similar to Eq. (5.74) in the sense that the double-barrier transmission coefficient is modulated by the Fano-resonance envelope. For the case of symmetric barriers, the transmission coefficient of the whole structure is presented in Sec. 5.2.2. In the following, the important feature is the suppressed transmission in the presence of the Fano state in the range of energies $E_k \sim (E_0 - \Gamma_0, E_0 + \Gamma_0)$ around E_0 of the width Γ_0 controlled by both the strength of the coupling Γ_M and the transmission probability $\mathcal{T}_{BB}$ for the two barriers which is nicely reflected in the classical picture. In the presence of two and more molecules, the overall picture remains the same: in the range of Fano-resonance energies, the transmission is strongly suppressed. In other words, the molecules can be considered as strong barriers for electrons in this energy range. At the same time, away from the Fano resonance, molecules do not essentially affect the transport.

5.3.1 Including spin: Splitting of Fano resonances

In this section, we analyze the role of the spins of the molecule and the electron for transport through the CNT structure with attached SMMs. The ferromagnetic exchange interaction between the electrons localized on the ligands and the $4f$ electrons of Tb [127] was discussed in Sec. 1.4 and is mathematically described by

$$\hat{V}_{ex} = A(\hat{\mathbf{J}} \cdot \hat{\mathbf{S}}), \tag{5.76}$$

where J and S denote the spins of terbium and of localized electrons, respectively. The exchange interaction constant A is determined by a value of around -0.2 meV. Furthermore, localized electronic states on Pc ligands of the SMM are characterized by a large Coulomb energy U_0. With these conditions, the energy of spin-up and spin-down electrons on Pc ($E_\uparrow$ and $E_\downarrow$, respectively) yields

$$E_{\uparrow,\downarrow} = E_0 \pm AJ_z/2 + U_0 n_{\downarrow,\uparrow}. \tag{5.77}$$

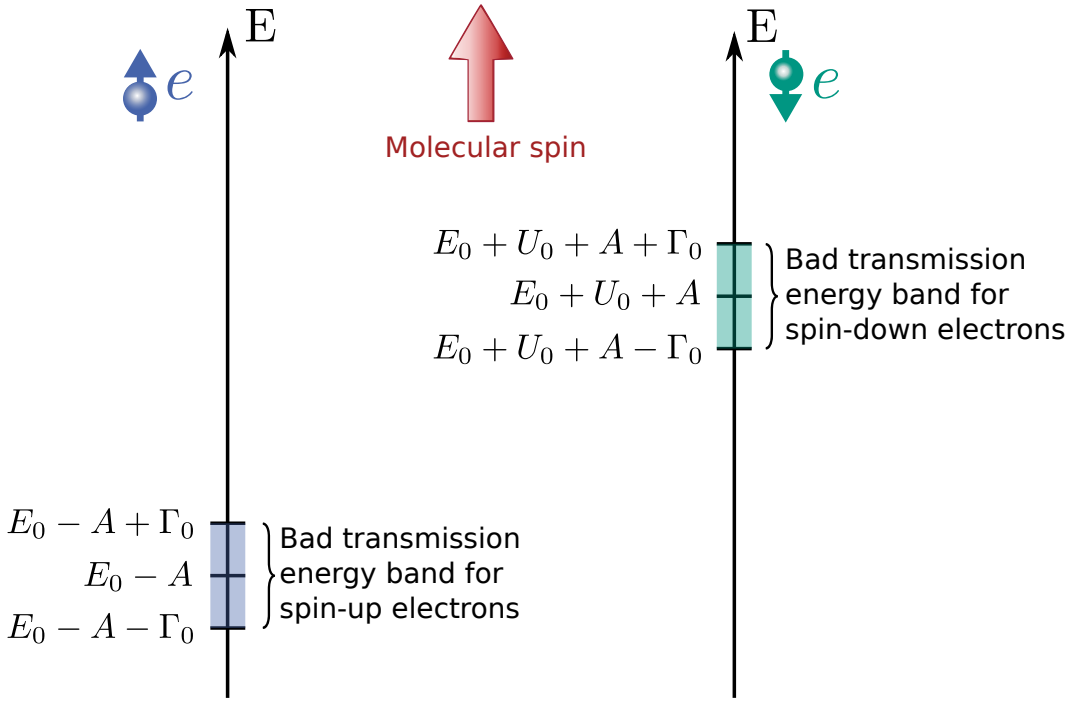

Figure 5.5: Schematic diagram of electron scattering on SMMs. When a spin-down electron occupies the localized state on the ligand, two regions of bad transmission for electrons are formed due to exchange interaction with the molecular spin.

The strong repulsive Coulomb interaction U_0 strongly prevents tunneling of an electron into $TbPc_2$ if already an electron of opposite spin occupies the SMM. The exchange interaction determines the orientation of the spin of the localized electron with respect to the Tb spin. The orientation of the spin of terbium itself in the considered system is analyzed in Sec. 6.3. The magnetic moment of the molecule is fix by magnetic anisotropy of the SMMs in one direction. The effect of electron scattering on the molecule is analyzed in the following. A schematic illustration of this is depicted in Fig. 5.5.

For given molecular spin $\mathbf{J}$, the transmission of an electron through the molecule depends on energy and spin of the electron. Let us now introduce the relevant energy scales for a CNT of the length $L \sim 300$ nm. The level spacing for such a nanotube due to the confined geometry is about $\Delta \sim 1 \div 2$ meV. The energy of Coulomb interaction between the electrons in the CNT is also related to the length of the nanotube via $E_C \sim e^2/L$ resulting in a numerical estimate of $E_C \sim 15 \div 20$ meV. The conductance map of transport through a single molecule [127] allows to use for the Fano level broadening $\Gamma_0 \sim 10 \div 20$ meV. The repulsive Coulomb energy on Pc ligands can be approximated as $U_0 \sim 100$ meV, as calculated in Ref. [130]. According to these estimates, we assume the following hierarchy of the energy scales in the proceeding section:

$$\Delta \ll E_C \lesssim \Gamma_0 \ll U_0. \tag{5.78}$$

The hierarchy of the energy scales means that a few levels of the size quantization of the CNT fall into the regime of bad transmission caused by the molecular magnet.

In this parameter regime, the spin dependent scattering can be understood with the following example. We consider the case of the Fermi level located in the energy band of poor transmission for electrons with spin up orientation, cf. the left axis of Fig. 5.5. In this case, a single molecule magnet serves as an effective barrier splitting the nanotube in two quantum dots for spin up electrons. Thus, spin-up electrons are affected by three barriers, including the two tunneling barriers due to the connection of the CNT with source and drain contact, while spin-down electrons remain unaffected by the presence of the molecule and feel only the two outer barriers.

Hence, due to the spin dependent Fano resonances, a "spin-valve-effect" emerges for the minimal model of two molecules similar to the effect described in Ref. [92]. In particular, an anti-parallel orientation of the two molecular spins results in a resonant backscattering of conduction electrons with both spin projections and thus in suppressed transport for all electrons. Two parallel aligned SMMs, however, block transport for electrons in one spin orientations while electrons with opposite spin orientation are not affected by the molecules leading to a higher conductance of the system. This means that in absence of magnetic field, where the spins can be aligned either parallel or anti-parallel the conductance is reduced compared to the conductance in finite magnetic field, cf. Fig. 5.7a). However, the resulting magnetoresistance of the reduced conductance is not giant. Moreover, the observed plateaus of lower conductance in experiment, cf. Figs. 1.13 and 1.10, can only be explained within a dynamically swept magnetic field. For a dynamically swept magnetic field, the plateaus in the conductance appear due to the time it takes for the spin to feel the magnetic field. This retarded process of spin relaxation is seen for a sufficiently fast sweeping rate. However, the conductance of the plateaus is much larger than expected in experiment. A schematic illustration of the conductance in a dynamically swept magnetic field can be found in Fig. 5.7b).

The present model differs from the model of Ref. [92] by the presence of strong tunneling barriers separating the CNT and the leads. The tunneling barriers lead to the consideration of the CNT as a sequence of quantum dots with number of dots depending on the spins of carriers and molecules. In particular, two SMM with parallel aligned spin-up break the CNT into three quantum dots for spin-up carriers while spin-down carriers behave as in a single quantum dot, cf. Fig. 5.5. Anti-parallel aligned spins of SMMs break the CNT in both spin orientation of the carriers into two quantum dots, each type of carriers blocked by one molecule.

The described splitting of the CNT into quantum dots is illustrated in Fig. 5.6. This theoretical model relies on the assumption that the Fermi level is located in the lower energy band in Fig. 5.5, such that carriers with spin parallel to the molecular spin show suppressed transmission. For different capacitances of the CNT and the molecule, this assumption can be satisfied by varying the gate voltage.

However, the simple model of spin-dependent Fano resonances regulating the suppression of transmission as presented in this section and illustrated in Fig. 5.6 cannot explain all experimentally observed phenomena without considering Coulomb interaction. Due to charging effects, the transport properties are strongly affected by the presence of several quantum dots in the system showing the characteristics of Coulomb blockade. In particular, the explanation of the spin-valve effect is manifested by the magnetic ordering of the molecular spins in zero magnetic field which is governed by the Coulomb interaction. The next chapter, Ch. 6, is devoted to the incorporation of these effects.

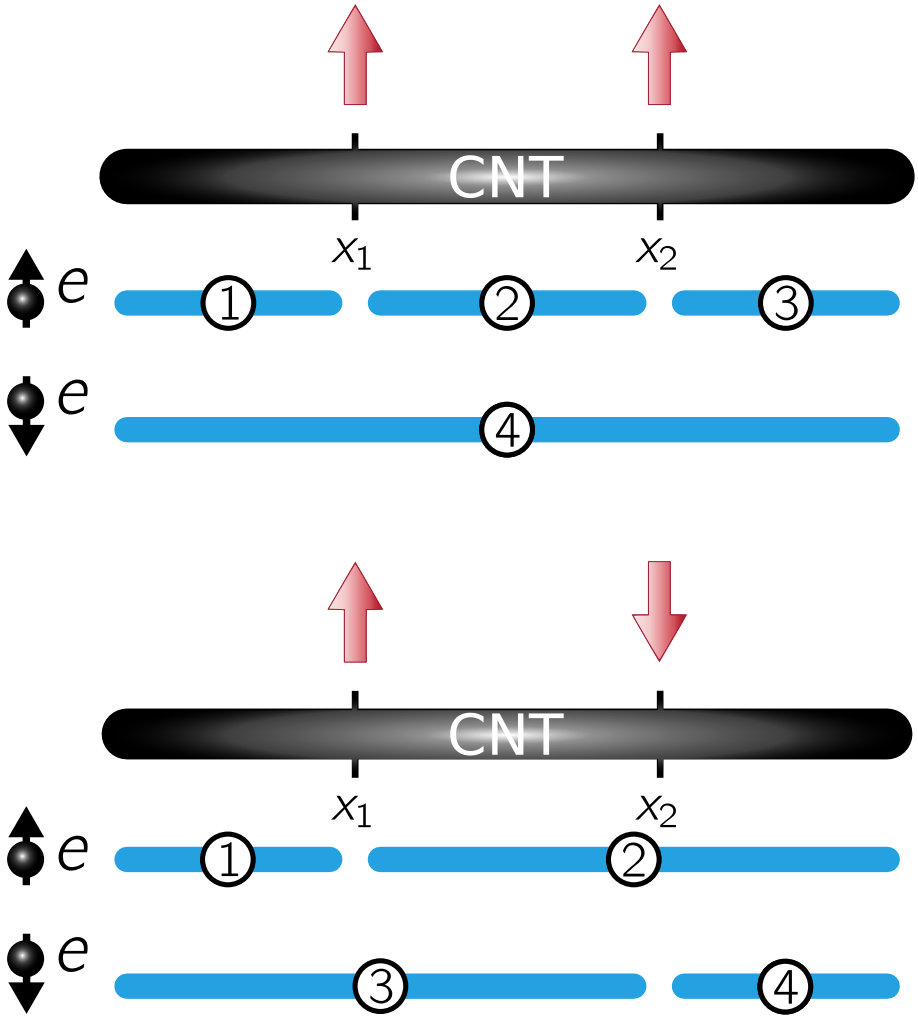

[Reprinted figure with permission from I. V. Krainov, J. Klier, A. P. Dmitriev, S. Klyatskaya, M. Ruben, W. Wernsdorfer, and I. V. Gornyi, ACS Nano, 2017 **11** (7), 6868-6880. Copyright 2017 by the American Chemical Society. DOI: 10.1021/acsnano.7b02014]

Figure 5.6: Scheme of quantum dots for electrons in the CNT with energies close to the Fermi energy. The CNT effectively breaks into four quantum dots with the configuration depending on spin orientation of the electrons and molecules. The Fermi level lies in the region of bad transmission for the carriers electrons aligned in the direction of the parallel molecular spins.

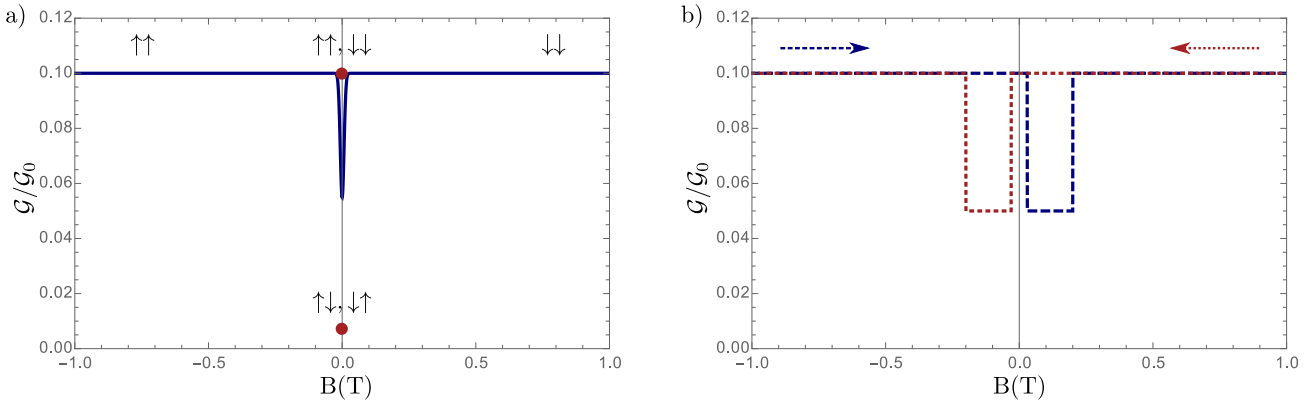

Figure 5.7: Schematic diagram for the conductance of the CNT with two side-attached SMMs as a function of magnetic field. Panel a) depicts the conductance as a function of static magnetic field showing the reduced conductance. The red dots indicate conductance for parallel or anti-parallel spin configurations. In panel b), the conductance as a function of a dynamically swept magnetic field is schematically shown illustrating steps of lower conductance. The steps originate from the retarded process of spin relaxation in a dynamically swept magnetic field.

5.4 Summary of Chapter 5

In this chapter, we discussed the origin of a magnetoresistance due to spin-dependent resonance scattering on Fano states. For this purpose, we started to revise the appearance of Fano resonances in an infinite system in Sec. 5.1. In Sec. 5.2, we considered a Fano state between two barriers. We first calculated the transmission coefficient in presence of strong dephasing where the classical results can be applied for the transmission coefficient. However, the quantum nature of the Fano state is not destroyed. This means that the transmission is reduced in the energy region of the resonance of the Fano state while for other energies the transmission remains energy independent. In Sec. 5.2.2, we considered the quantum mechanical limit for a Fano state located between two barriers. In this case, we apply three different approaches to determine the transmission amplitude. First, we determined the wave function of the full system which is obtained by the coupling of the Fano state to the wave functions of the double barrier system. Then, we developed a Green's function approach. Within the Green's function approach, we can straightforwardly express the transmission amplitude by the transmission amplitude of the double barrier system and a term related to the Fano state. Finally, we compare the results to the conventional scattering matrix approach. We find that the region of suppressed transmission due to the Fano resonance is shifted by the barriers. In the quantum mechanical consideration, the energy shift and the width of suppressed transmission is both momentum dependent and dependent on the position of the Fano state while the classical consideration provides only a region of suppressed transmission dependent on the barriers, cf. Figs. 5.3 and 5.4.

The results of reduced transmission can thus be applied to the CNT with side-attached molecules as follows: The localized electronic states of phthalocyanine ligands in $TbPc_2$ magnetic molecules near the Fermi level ($S = 1/2$ state in Fig. 1.8), which are assumed to couple well to the electronic states of the CNT, serve as a Fano state. These localized states for spin-up and spin-down carriers are split by both exchange interaction between electrons localized on the molecule and the $4f$ electrons in the terbium shell, cf. Fig. 5.5. The electrons, in the energy window depending on the relative orientation of the

spins of the electron and the SMM, cf. Fig. 5.5, are strongly backscattered due to the Fano resonance induced by the side-attached molecule, see Fig. 5.2. Under the consideration of a minimal model of two SMMs attached to the CNT, backscattering due to the Fano-resonance breaks the nanotube into four quantum dots. The four quantum dots correspond either to a single quantum dot for one spin species and three quantum dots for the other spin species in the case of parallel aligned spins of the SMMs, or to two quantum dots for each spin species of electrons for anti-parallel molecular spins, cf. Fig. 5.6. Thus, for anti-parallel aligned molecular spins, transport is blocked for both spins of carrier electrons while one spin species is not affected by the molecules on the case of parallel molecular spins. This leads to a MR due to the fact that the spins can be either parallel or anti-parallel in the absence of magnetic field while they are parallel aligned in the presence of magnetic field, cf. Fig. 5.7. In contrast to the experimental findings for the carbon nanotube with side-attached $TbPc_2$ molecules [58], the MR is giant which is not the case in the present theoretical model. Moreover, the appearance of a plateau of low conductance around zero magnetic field can only be explained for a dynamical sweep of magnetic field, cf. Fig. 5.7b). In the next chapter, we will therefore include Coulomb interaction where we can explain both the magnitude of the MR and the alignment of spins with respect to magnetic field. Moreover, Coulomb interaction also provides an explanation for the appearance of the gaps in the Coulomb map in the considered setup.

Chapter 6

6 Coulomb blockade and Spin-Valve Effect in Nanotubes with $TbPc_2$ molecules

In the last chapter, Ch. 5, we have seen that the magnetoresistance (MR) and the spin-valve effect of a nanotube with side-attached single-molecule magnets can be explained by spin-dependent resonant scattering of conducting electrons on a Fano state. However, the described ingredients of the theory do not provide a giant magnetoresistance (GMR) with a magnitude of $10^3\%$ as obtained in the experiment of Ref. [58] and discussed in Sec. 1.4 with $TbPc_2$ molecules. Moreover, the obtained MR in the model of Ch. 5 shows a lower conductance only in the absence of magnetic field. In the experiment, a plateau of lower conductance around zero magnetic field is observed, Fig. 1.10. Certainly, the gaps in the Coulomb map around zero source-drain voltage can also be not described by the proposed model without including Coulomb interaction.

In this chapter, we extend to theoretical model proposed in Ch. 5 by the consideration of Coulomb interaction. Of particular importance for the GMR, will be the effect of Coulomb blockade [164] inside the nanotube. The Coulomb interaction between electrons inside the CNT gives rise to Coulomb blockade with the linear transport blocked for the anti-parallel orientation of molecular spins at all values of gate voltage. A long-range interaction between SMMs is responsible for a stable magnetic ordering of the inner spins of the molecules as predicted by the presented theory. The magnetic ordering explains the GMR of the considered device. We published the presented results in Ref. [94].

Remarkably, the gate voltage can manipulate both the sign and the strength of the molecular spin-spin interaction. This implies that the arrangement of the spins of the SMMs can be varied by external gate and explains the experimentally obtained gate-controlled spin-valve effect as presented in Sec. 1.4. More generally speaking, the magnetic properties of the supramolecular nanostructures can be effectively designed by external gates. These effects are expected to lead to further breakthroughs in the field of quantum electronics and spintronics.

The chapter is structured as follows. In Sec. 6.1, we present the theoretical model to obtain the free energy and the current through a multidot quantum system. This model is then applied to relevant case of SMMs attached to a CNT where the system breaks into four quantum dots with different configurations depending on the spin of the molecules, Sec. 6.2. Further, we continue with the analysis of the effect of Coulomb interaction on the alignment of the molecular spin, Sec. 6.3. The results of Ch. 5 combined with the incorporation of Coulomb interaction, Sec. 6.2 and 6.3 can be applied to calculate the conductance and the GMR, Sec. 6.4. Finally, the results are summarized and discussed in Sec. 6.5.

6.1 Free energy and current in multidot systems

It has been discussed in the previous chapter that SMMs may split the CNT into several quantum dots (QDs). Furthermore, Coulomb interaction, as well as charge quantization should become important for the transport properties of the structure by the following arguments: Coulomb blockade was observed in pure CNTs, cf. Ref. [165], and the conductance maps obtained in experiment for the CNT system with side-attached CNT, cf. Fig. 1.11 and 1.12 of Sec. 1.4 also shows signatures of Coulomb blockade. Coulomb blockade is identified by a strongly suppressed conductance for certain ranges of the gate voltage V_g and of the source-drain voltage V_{sd}. In the following, we construct the conductance maps including Coulomb blockade for the different configurations of QDs determined by the molecular spins.

Before we discuss the particular cases of Coulomb blockade in the system of CNTs with SMMs, we consider the basic properties of a single dot system and multidot systems. In a finite electronic system, Coulomb interaction leads to the emergence of the charging energy E_C. For an electron tunneling into a QD, energy conversation involves this interaction energy. Thus, an electron needs to overcome the charging energy to pass through the QD, otherwise transport through the QD is blocked. The phenomenon is described in terms of electrostatic scheme [164], where the charging energy is represented by introducing the capacitors, as illustrated for a single QD in Fig. 6.1a).

By considering the free energy of a QD, the effects of Coulomb blockade are quantitatively characterized by the free energy of the system [166]. For the zero source-drain voltage V_{sd}, the free energy of a single quantum dot reads

$$F_1(N, V_g) = \frac{\Big(eN + C_g V_g\Big)^2}{2(C_g + C_L + C_R)}, \tag{6.1}$$

where N is the number of electrons on the dot. The capacitance between the dot and the gate is denoted by C_g and the capacitances between the dot and the leads are $C_{L,R}$. For $V_{sd} \to 0$, increasing the number of electrons on the QD, increases in general the free energy,

$$F_1(N) < F_1(N+1),$$

and tunneling through the quantum dot is avoided.

However, for certain "resonant" gate voltages V_g^*, the free energy remains unchanged for the addition of an extra electron to the quantum dot, $F(N, V_g^*) = F(N+1, V_g^*)$, resulting in a finite, linear conductance for those values of V_g. For a finite source-drain voltage, the resonant conditions for the free energy of the system define the boundaries of the "Coulomb diamonds" in the Coulomb map, with Coulomb-blocked regions shown in blue color in Fig. 6.1c). To obtain a finite current through the system, corresponding to red regions in Fig. 6.1c), in general, the change of electrons in the course of the complete tunneling process (to and from the dot) needs to decrease the free energy (with the energy conservation maintained by inelastic scattering).

For transport through two or more QDs, there is a crucial difference compared to a single quantum dot leading to the strong spin-valve effect in our system. The boundary conditions of Coulomb blockade for a system more than one QD are rather sophisticated. As discussed in Refs. [166, 167], conductance maps for a double dot system, with an equivalent scheme shown in Fig. 6.1b), show generically gaps in the Coulomb diamond around zero source-drain voltage for all gate voltages V_g. Thus, there is a region around $V_{sd} = 0$ where no current passes through the QD system as illustrated for a typical Coulomb map with two quantum dots in Fig. 6.1d).

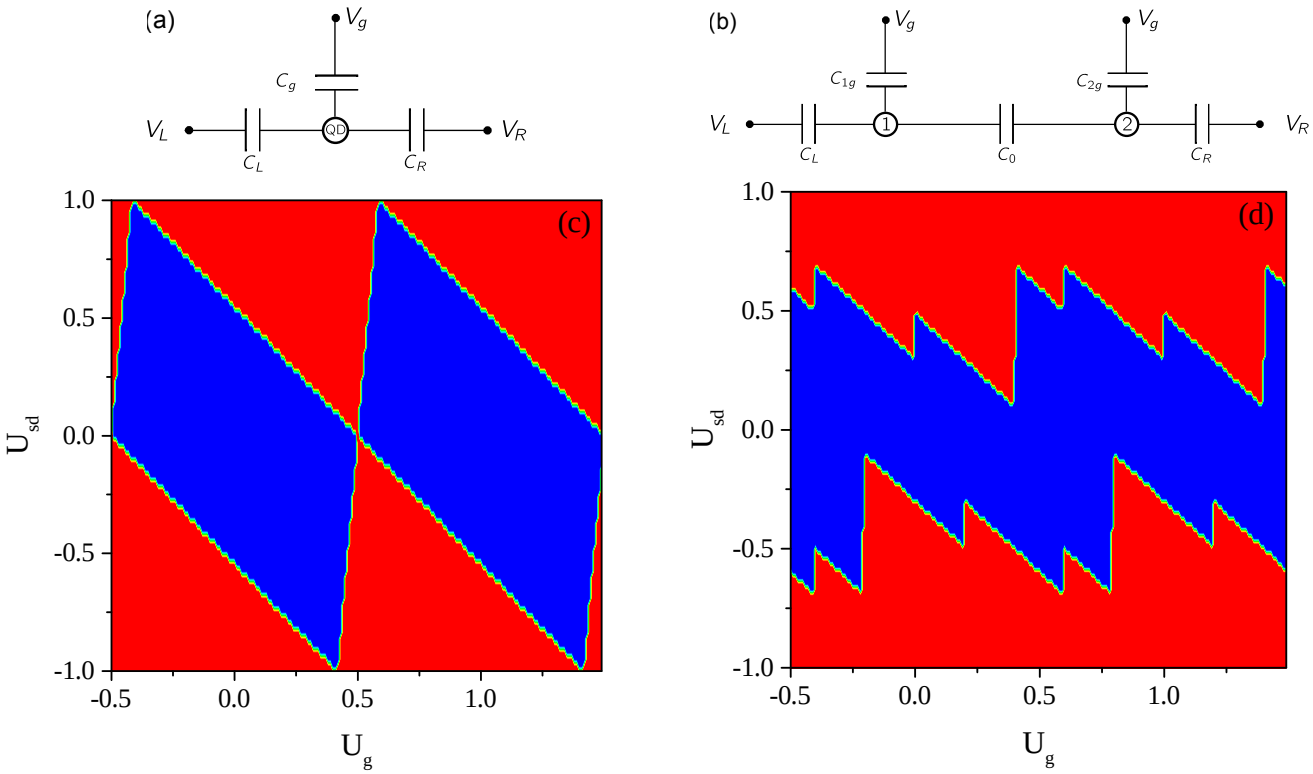

[Reprinted figure with permission from I. V. Krainov, J. Klier, A. P. Dmitriev, S. Klyatskaya, M. Ruben, W. Wernsdorfer, and I. V. Gornyi, ACS Nano, 2017 **11** (7), 6868-6880. Copyright 2017 by the American Chemical Society. DOI: 10.1021/acsnano.7b02014]

Figure 6.1: Illustration of equivalent schemes and Coulomb maps for single and double quantum dot systems. a) Equivalent electrostatic scheme for a single quantum dot; b) Equivalent electrostatic scheme for a double quantum dot; c) and d) Typical Coulomb-blockade maps for the single and double quantum dots, respectively, at $T = 0$. Blue and red regions correspond to the zero and finite current, respectively.

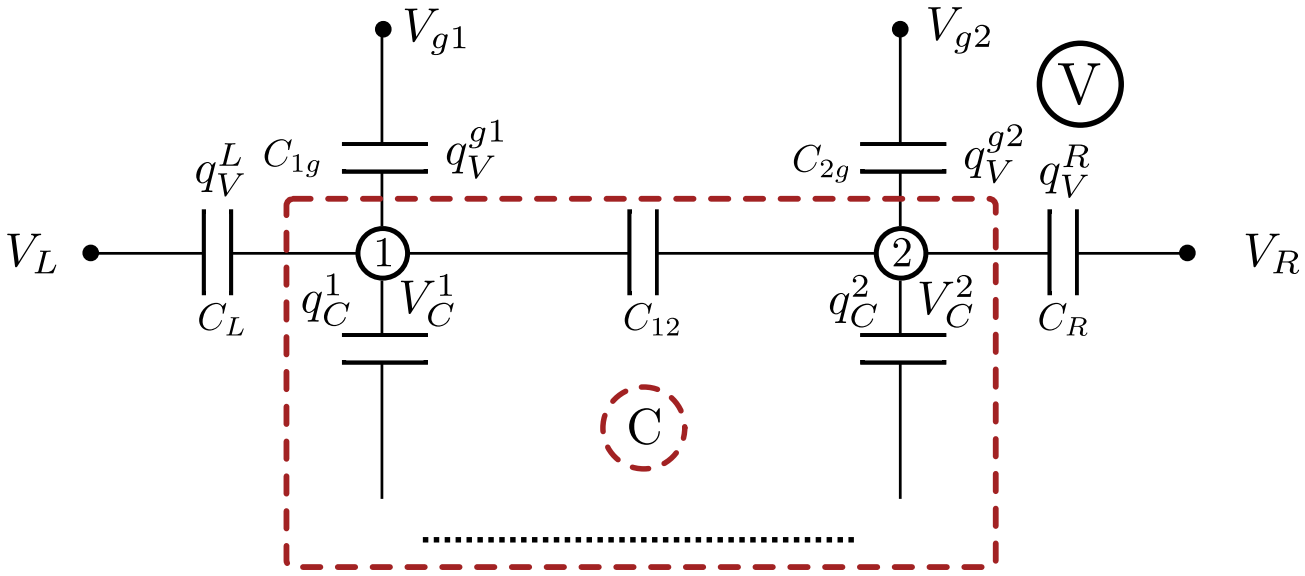

Figure 6.2: Equivalent scheme for quantum dots. The inner and outer regions labeled by "C" and "V" correspond to the QDs and the "environment", respectively.

For a double-dot system, the electron needs to first tunnel in the first dot, then in the second dot, and finally to the lead to contribute to a finite conductance. As a result, the conditions account for the energy difference for adding an electron in the first and in the second QD, as well as for the tunneling between the two dots. Therefore, a finite conductance at $V_{sd} \to 0$ requires equal free energies F_2 for QDs with initially different numbers of electrons:

$$F_2(N_1, N_2, V_g) = F_2(N_1 + 1, N_2, V_g) = F_2(N_1, N_2 + 1, V_g). \tag{6.2}$$

These conditions (6.2) can only be fulfilled in the fully symmetric double-dot system [166, 167] leading to a gapless conductance map while any asymmetry (as in the generic case) fully blocks transport and hence opens a transport gap at all gate voltages. By varying the gate voltages, the differences between the free energies, Eq. (6.2), can be minimized by changing the gate voltage. Thus, the magnitude of transport gaps $e\,\delta V_{sd} = \Delta F_{2\,\mathrm{dots}}$ is a function of V_g, see Fig. 6.1d).

To fully understand these features, we discuss a general approach to calculate the free energy of an electrostatically coupled system of QDs in the following. It is important to emphasize that the electrostatic energy of QDs (i.e., the sum of all capacitor's energies in the equivalent electric scheme) cannot be directly used for the analysis of the transport properties. This is caused by the changes of the environment of the system when the number of electrons in QDs is varied due to the charge transfer. This is associated with the processes in batteries (the sources of the gate and source-drain voltages) where the charge of capacitors is changed when the current flows. To subtract the work performed by voltage sources, we need to calculate the free energy of the QDs in terms of the numbers of electrons on the QDs, N_i, gate voltage, and source-drain voltage.

We describe the system consisting of the QDs and the "environment" by an equivalent electrostatic scheme in Fig. 6.2. The total electrostatic energy of the system is given by

$$E = \frac{1}{2}\left[\mathbf{V}_c\mathbf{Q}_c + \mathbf{V}_v\mathbf{Q}_v\right], \tag{6.3}$$

where $\mathbf{V}_c$ and $\mathbf{Q}_c$ are the voltage and the charge of the QDs, $\mathbf{V}_v$ and $\mathbf{Q}_v$ the voltage and the charge of the environment capacitors (gate and source-drain leads), cf. Fig. 6.2.

The voltages on QDs can be found from the relation

$$\mathbf{Q}_c = \hat{\mathbf{C}}_{cc}\mathbf{V}_c + \hat{\mathbf{C}}_{cv}\mathbf{V}_v. \tag{6.4}$$

The diagonal elements of $\hat{\mathbf{C}}_{cc}$ are given by the sum of capacitances of all capacitors connected to the particular node

$$(\hat{\mathbf{C}}_{cc})_{ii} = \sum_j C_{ij}, \tag{6.5}$$

while the off-diagonal elements are given by the capacitance (taken with the minus sign) of the capacitor that connects the two nodes,

$$(\hat{\mathbf{C}}_{cc})_{ij} = -C_{ij}. \tag{6.6}$$

The product $\hat{\mathbf{C}}_{cv}\mathbf{V}_v$ contains all voltages multiplied by the capacitances connecting the nodes with the environment:

$$(\hat{\mathbf{C}}_{cv}\mathbf{V}_v)_i = \sum_j C_{ij}V_v^j. \tag{6.7}$$

The work of batteries is associated with the change of $\mathbf{Q}_v$ for the process of the electron transfer across the system, reading

$$dA = \mathbf{V}_v d\mathbf{Q}_v, \quad d\mathbf{Q}_v = \hat{\mathbf{C}}_{vc}d\mathbf{V}_c. \tag{6.8}$$

The total differential of the free energy is then given by

$$dF = dE - dA = \frac{1}{2}d\left[\mathbf{V}_c\mathbf{Q}_c + \mathbf{V}_v\mathbf{Q}_v\right] - \mathbf{V}_v d\mathbf{Q}_v. \tag{6.9}$$

The free energy of the QD system is

$$F(\{N\}_i, V_g, V_{sd}) = \frac{1}{2}\mathbf{V}_c\hat{\mathbf{C}}_{cc}\mathbf{V}_c, \tag{6.10}$$

$$\mathbf{V}_c = \hat{\mathbf{C}}_{cc}^{-1}\left(\mathbf{Q}_c - \hat{\mathbf{C}}_{cv}\mathbf{V}_v\right). \tag{6.11}$$

The calculation of the current through a system of QDs requires to solve the quantum tunneling problem for a system with weak dephasing while a system with strong dephasing is treated via the solution of the master equation. In general, this is a very challenging task. However, for low temperatures (smaller than the single-particle level spacing), the calculation is simplified. In this case, it is sufficient to construct the Coulomb-blockade map by finding the number of open current channels as a function of the gate and source-drain voltages.

We consider now a system of N QDs as presented in Fig. 6.3. We will operate in the space of the numbers of electrons in the QDs $\left\{N\right\}_i = (N_1, N_2, \cdots, N_N)$, where i denotes the ith basic vector. First, we obtain the conditions for the current flow for a fixed particle number $\left\{N\right\}_i$ in QDs. In what follows,

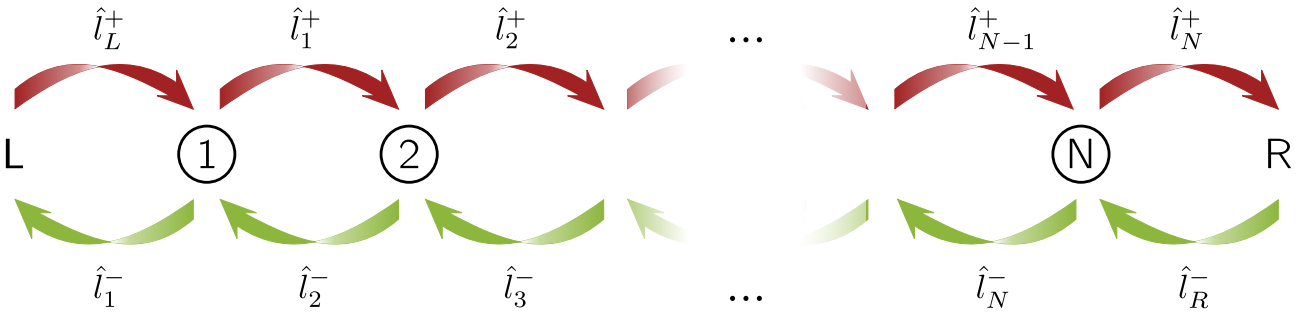

Figure 6.3: Illustration of transport in a structure with N QDs. Operators $\hat{l}_j^{\pm}$ denote the tunneling of an electron from one dot to another.

the chemical potential of the left and right leads is chosen to be $\mu_L = eV_L$, $\mu_R = eV_R$, respectively. The leads are symmetric with respect to adding and extracting particles. The transmission process of an electron from left to right lead is required to be energetically favorable at each step of the process. In the first step, the particle tunnels from the left lead to the first QD. Extracting a particle from the left lead reduces the energy of the system in accordance to the definition of chemical potential. The change in the occupation of the first QD is reflected by the change of the argument of the free energy from $\{N\}_i$ to $\{N\}_i + 1_1$. Hereinafter, $\pm 1_j$ means an increase/decrease of the amount of electrons by 1 at the position j in the setup. For a flow of the current, the sum of these two contributions, $\Delta E_{L\to 1}$ being the variation of the energy of the system, has to be negative, cf. Eq. (6.12). In the next step, the electron tunnels from the first to the second quantum dot. The energy change of this process for the system is denoted by $\Delta E_{1\to 2}$ which is given by the difference of the free energies with $\{N\}_i + 1_2$ and $\{N\}_i + 1_1$, Eq. (6.13). This construction is repeated up to Nth QD. The last step of the process, $\Delta E_{N\to R}$, is the tunneling of the particle from the Nth QD to the right lead. This step results in a difference of free energy and an increase of the chemical potential of the right lead, μ_R, cf. Eq. (6.14). Explicitly, the energy differences read:

$$\Delta E_{L\to 1}(\{N\}_i) = -\mu_L + F(\{N\}_i + 1_1) - F(\{N\}_i) < 0, \tag{6.12}$$

$$\Delta E_{1\to 2}(\{N\}_i) = F(\{N\}_i + 1_2) - F(\{N\}_i + 1_1) < 0, \tag{6.13}$$

$$\dots$$

$$\Delta E_{N\to R}(\{N\}_i) = \mu_R + F(\{N\}_i) - F(\{N\}_i + 1_N) < 0. \tag{6.14}$$

Hereinafter, we disregard the arguments V_g, V_L, V_R in the free energy to simplify the notation . The sum of all energy differences $\Delta E_{j\to j+1}$ is equal to the energy difference of an electron transferred from the left to the right lead, $\mu_R - \mu_L$.

We define the current channel in terms of the basic vector $\{N\}_i$ consisting of the particle numbers arranged consecutively from the left to right lead as:

$$J_{L\to R}(\{N\}_i) = \Theta(\Delta E_{L\to 1})\,\Theta(\Delta E_{1\to 2})\cdots\Theta(\Delta E_{N\to R}) = \prod_j \Theta\Big(\Delta E_{j\to j+1}\Big)\,,$$

where $\Theta(x) = 1-\theta(x)$ with $\theta(x)$ the Heaviside step function, and $\{j\} = (L, 1, 2, \cdots, N, R)$ enumerates leads and QDs acting on the channel. The value of current channel $J_{L\to R}(\{N\}_i)$ is equal to zero if the current cannot flow from the $\{N\}_i$ state and equal to unity in the opposite case. The tunneling of an electron from the right to the left lead, as expressed by the current channel $J_{R\to L}(\{N\}_i)$, contributes to the total current. The tunneling process from the right to the left lead is described in the same manner.

Now, we need to find the relevant states $\{N\}_i$ which might produce a nonzero current. In order to do so, we define the operators describing the evolution of the basis states $\{N\}_i$, reading

$$\hat{l}_j = 1 + \Theta\Big(\Delta E_{j\to j+1}\Big)\,\hat{P}^+_{j+1}\hat{P}^-_j + \Theta\Big(\Delta E_{j\to j-1}\Big)\,\hat{P}^+_{j-1}\hat{P}^-_j = 1 + \hat{l}^+_j + \hat{l}^-_j, \tag{6.15}$$

$$\hat{P}^\pm_j\{N\}_i = \{N\}_i \pm 1_j, \quad \hat{P}^\pm_{L,R} = 1, \quad \hat{l}^-_L = \hat{l}^+_R = 0. \tag{6.16}$$

Here, the operator $\hat{P}^\pm_j$ changes the number of electrons in QD j by unity, the operators $\hat{l}^\pm_j$ describe the tunneling of an electron from QD j to one of the adjacent QDs, and $P_{\{N\}}$ is a vector in the space of electron numbers, i.e. $P_{\{N\}}(i) = \{N\}_i$. The states, for which the current needs to be calculated, $P^0_{\{N\}}$, are all possible variations of the state which minimizes the free energy of the configuration at fixed gate and source-drain voltage and are given by

$$\begin{gathered}\min_{\{N\}} F(\{N\}) = F(P^{\min}_{\{N\}}(i_{\min})),\\ \hat{\mathcal{L}} = \sum_j \hat{l}_j,\\ \lim_{m\to\infty}\hat{\mathcal{L}}^m P^{\min}_{\{N\}} = P^0_{\{N\}}.\end{gathered} \tag{6.17}$$

Finally, the total current is expressed in terms of the different current channels, yielding

$$\mathcal{I}(V_g, V_{sd}) = \sum_i P^0_{\{N\}}(i)\left[J_{L\to R}(\{N\}_i) + J_{R\to L}(\{N\}_i)\right]. \tag{6.18}$$

For low temperatures and positive source-drain bias, $\mu_L > \mu_R$, the current flows only from the left to the right lead, $J_{L\to R}$. A generalization of this method for multiple channels in each direction of tunneling is done by the summation over all channels in Eq. (6.18). This consideration is now applied to the the minimal model of two SMMs side-attached to a nanotube.

6.2 Coulomb blockade in the nanotube with SMMs

In order to obtain the conductance maps for the CNT with two SMMs, we apply the formalism discussed in the previous section to the calculation of the free energy [164, 166] with both parallel, $\uparrow\uparrow$, and anti-parallel, $\uparrow\downarrow$ orientation of the molecular spin. In both cases, the full system of spin up and down orientation of the carriers is split into four QDs, cf. Fig. 5.6. The free energy is therefore expressed as function of the number of electrons in the different quantum dots, $\{N\}_i = \{N_1, N_2, N_3, N_4\}$, the gate and source-drain voltages, and the charging energy E_C. Furthermore, we introduce a dimensionless function $\phi_{\alpha\beta}$ with $\alpha = \uparrow, \downarrow$, $\beta = \uparrow, \downarrow$ resulting in the following expression for the free energy:

$$F_{\alpha\beta}(\{N\}_i, V_g, V_{sd}) = E_C\ \phi_{\alpha\beta}\left(\{N\}_i, \frac{eV_g}{E_C}, \frac{eV_{sd}}{E_C}\right) = E_C\ \phi_{\alpha\beta}(\{N\}_i, U_g, U_{sd}), \tag{6.19}$$

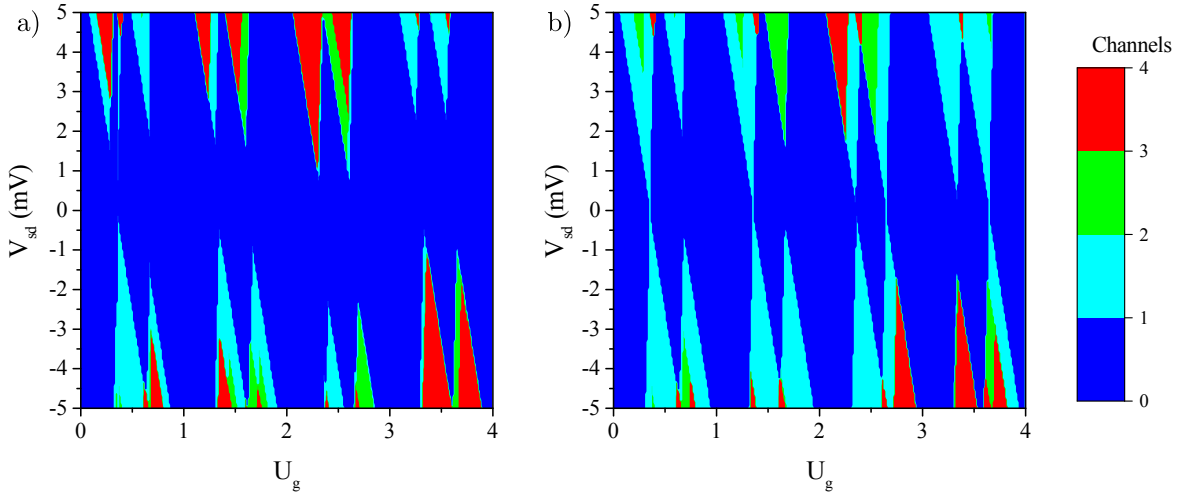

[Reprinted figure with permission from I. V. Krainov, J. Klier, A. P. Dmitriev, S. Klyatskaya, M. Ruben, W. Wernsdorfer, and I. V. Gornyi, ACS Nano, 2017 **11** (7), 6868-6880. Copyright 2017 by the American Chemical Society. DOI: 10.1021/acsnano.7b02014]

Figure 6.4: Calculated current map $\mathcal{I}(V_g, V_{sd})$ a) at zero magnetic field and b) above the critical fields B_c in terms of current channels. Positions of molecules: $x_1 = 0.2$, $x_2 = 0.6$; $\kappa = 25$.

where U_g and U_{sd} are the dimensionless gate and source-drain voltages (measured in units of $E_C = e^2/L$), respectively. The derivation and the explicit expressions for $\phi_{\uparrow\uparrow}$ and $\phi_{\uparrow\downarrow}$ are presented in App. E. In the following, we normalize all the capacitances to the CNT length $C_i \to C_i/L$ and define the positions of the two molecules, x_1, x_2, in the range $(0, 1)$.

The capacitances between the gate and the QD are proportional to length of the particular quantum dot, $C_{ig} \sim l_i$. The coupling to the leads is determined by the spatial overlap between the leads and the quantum dot, $C_{iR,L} \sim l_{R,L}$ since in experiment, the metallic contacts cover the ends of the CNT. Hereinafter, the parameter defining the capacitances between the leads and the QD is set to $l_{L,R} = 0.2$. However, it will turn out that the results are not too sensitive to this parameter. The different spin channels are connected by capacitances determined by their spatial overlap. For the capacitances between the QDs of the same spin channel of the electrons, we introduce a phenomenological parameter κ that characterizes the electrostatic properties of the molecules. The parameter can be identified by atomistic numerical simulations of a SMM attached to a CNT, but is in the following only applied as a fitting parameter. Hence, the capacitances with the same electron spin yield $C_{ij} \simeq \kappa l_i l_j/(l_i + l_j)$.

The parameter κ signifies the correlation between a single-dot and a double-dot system. In the limit $\kappa \to \infty$, the double-dot free energy $F_2(N_1, N_2)$ reduces to the free energy of a single-dot system, $F_1(N_1 + N_2)$ with $C_g = C_{1g} + C_{2g}$. This indicates the requirement of a large fitting parameter, $\kappa \sim 20 \div 30$ which is experimentally justified by small transport gaps $\delta V_{sd} \sim 1 \div 2$ meV $\ll E_C$ compared to the charging energy. In this parameter regime, the calculation provides transport gaps of $\delta(eV_{sd}) = E_C \delta U_{sd} \sim 1 \div 2$ meV which is in a good agreement with the experimental observation.

The calculated transport maps for anti-parallel and parallel molecular spin orientation is presented in Fig. 6.4 a) and b), respectively with the two molecules located at $x_1 = 0.2$ and $x_2 = 0.6$. The current is obtained in terms of current channels which are discussed in App. E. There, we introduced the function $\mathcal{I}(V_g, V_{sd})$ which expresses the amount of distinct configurations $\{N\}_i$ of electron numbers

in the QDs participate in transport. For blocked transport, the absence of conducting states leads to zero for the function $\mathcal{I}(V_g, V_{sd})$ while in the conducting region, the function is finite, $\mathcal{I} = M \geq 1$,, and equal to the integer number M, which counts the contributing configurations $\{N\}_i$ to the current (the number of non-blocked current channels).

Figure 6.4 illustrates that the anti-parallel spin orientation of the SMMs leads to a gap around $V_{sd} = 0$ for all gate voltages V_g. The appearance of the transport gap is analogous to that in double-dot systems, cf. Fig. 6.1d), since for each spin orientation of the carrier electrons, the CNT is divided into two quantum dots, as depicted in the lower panel of Fig. 5.6.

For parallel aligned molecular spins (upper panel in Fig. 5.6), the transport gaps around $V_{sd} = 0$ close at some values of V_g which is associated with the Coulomb map of the single-dot, Fig. 6.1c). However, generically, the system of coupled quantum dots is more complex than a conventional single-dot system. Electrostatic interaction between electrons tunneling through the single QD with electrons tunneling through three quantum dots change the conditions for blocked transport in the single dot depending on the population of the three other quantum dots where the carriers have opposite spin. As a result, some transport gaps remain open in the Coulomb map although they decrease, as seen in Fig. 6.4b). This is in contrast to the simplest single-dot case (Fig. 6.1c). At such gap closing gate voltages, one encounters a strong spin-valve effect. The obtained conductance maps are consistent with experiment as described in Fig. 1.11a) and b).

This feature originates from the change of the electron numbers in the non-conducting channel with three quantum dots by varying the gate voltage. By varying the numbers of electrons N_1, N_2, or N_3, the free energy might be affected in such a way that the transport conditions for finite current for the single dot channel are no longer fulfilled (the free energies at the degeneracy point for $\{N\}_i$ and $\{N\}_i + 1_4$ should be equal) and at $V_{sd} \to 0$ opens a gap. The described feature is fully consistent with the existence of weak and strong spin-valve effects observed at different values of V_g, as described in Sec. 1.4 and shown Figs. 1.13a) and b).

6.3 Interaction between molecular spins

In the previous sections, we showed that different spin configurations of the SMMs result in different quantum dot systems with different free energy and transport maps. This section is now devoted to the orientation of the molecular spins determining the spin orientation of the localized electrons on the ligands. In the following, the interaction energy between the spins of the electrons localized on the ligands is defined as the free energy difference between anti-parallel and parallel spin orientation,

$$E_{SS}(x_1, x_2, V_g) = F_{\uparrow\downarrow} - F_{\uparrow\uparrow}, \tag{6.20}$$

where x_1 and x_2 are again the positions of the two molecules. The interaction is caused by the repulsive Coulomb interaction in the presence of the Fano scattering close to the energy region of the localized state of the molecule and hence mediated by the conducting electrons of the CNT.

The interaction between localized spins is a non-monotonous function of the molecule positions. This is demonstrated in Fig. 6.5a), where the dependence of interaction energy E_{SS} (in units of the charging energy E_C) on the position of the second molecule x_2 with the first molecule localized at $x_1 = 0.2$ is plotted for two distinct values of the dimensionless gate voltages. For $U_g = 1$, we find an anti-ferromagnetic type of interaction independently of the position of the second molecule corresponding to the experimental observation of the low conductance in zero magnetic field around zero source drain

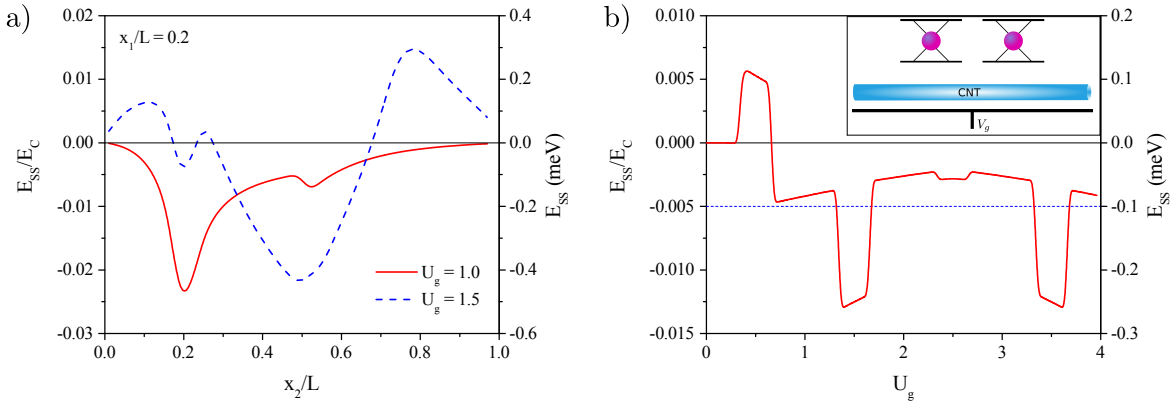

[Reprinted figure with permission from I. V. Krainov, J. Klier, A. P. Dmitriev, S. Klyatskaya, M. Ruben, W. Wernsdorfer, and I. V. Gornyi, ACS Nano, 2017 **11** (7), 6868-6880. Copyright 2017 by the American Chemical Society. DOI: 10.1021/acsnano.7b02014]

Figure 6.5: Panel a) depicts the interaction energy between localized spins as a function of position x_2 with fixed $x_1 = 0.2$ and $\kappa = 25$ for two values of the gate voltages. Negative (positive) values correspond to the anti-ferromagnetic (ferromagnetic) interaction. Panel b) shows the interaction energy (red curve) between localized spins as function of gate voltage U_g at fixed positions of the molecules, $x_1 = 0.2$ and $x_2 = 0.6$, and $\kappa = 25$. Negative (positive) values correspond to the anti-ferromagnetic (ferromagnetic) interaction. The dashed blue line corresponds to the interaction energy estimated from experiment. Inset of panel b): Schematics of the gated CNT with two $TbPc_2$.

voltage. The anti-ferromagnetic ordering of the molecular spin is related to the appearance of two quantum dots for both spin-up and spin-down electrons, lower panel of Fig. 5.6).

At the same time, for a gate voltage of $U_g = 1.5$, it depends on the position of the second molecule if the effective spin-spin interaction between the SMM is anti-ferromagnetic or ferromagnetic, cf. Fig. 6.5a). The dependence of the spin-spin interaction on gate voltage is depicted in Fig. 6.5b) for molecules located at the fixed positions, $x_1 = 0.2$ and $x_2 = 0.6$. We find that almost all gate voltages lead to an anti-ferromagnetic type of interaction which is in a good agreement with the experimental value of ~ 1 K indicated by the thin blue dashed line at Fig. 6.5b). In all regimes, the typical interaction energy is of the order of $E_{SS} \sim 0.1 \div 0.2$ meV.

In finite magnetic fields, the effective spin Hamiltonian describing the CNT with two side-attached SMMs yields

$$\hat{\mathcal{H}}_{\text{eff}} = -\frac{E_{SS}}{2S^2}\left(\hat{S}_{1z}\hat{S}_{2z}\right) + A\left(\hat{S}_{1z}\hat{J}_{1z}\right) + A\left(\hat{S}_{2z}\hat{J}_{2z}\right) + \mu_B\left(g_T\hat{\mathbf{J}}_1 + g_T\hat{\mathbf{J}}_2 + g_S\hat{\mathbf{S}}_1 + g_S\hat{\mathbf{S}}_2\right)\cdot\mathbf{B}, \tag{6.21}$$

with the g-factors of terbium and the localized electrons denoted by $g_T = 1.5$ and g_S, respectively. Due to the small spin of the electrons localized on the Pc ligands compared to the terbium spin, we can neglect the Zeeman terms of those electrons to simplify the model.

We set the easy axis of the molecules to the z direction in the Hamiltonian. Strong repulsive Coulomb interaction U_0 acting on the ligands of the molecule forces the spin of the localized electrons

$S_{1,2}$ to align in z direction. The molecular spins become parallel for fields larger than the characteristic magnetic field B_c which is related to the fact that the Zeeman energy exceeds the interaction energy E_{SS}. For an applied magnetic field in z direction, we use the effective Hamiltonian (6.21) to obtain the critical field described by

$$B_c = \frac{E_{SS}}{\mu_B g_T J} \sim 0.2 \div 0.3 \text{ T}. \tag{6.22}$$

Compared to the experimental data of the jump in conductance when the magnetic field is swept from -1 T to 1 T, cf. Fig. 1.10 of Sec. 1.4, the obtained critical field nicely matches.

6.4 Conductance and GMR

The conductance in the regime of Coulomb blockade can be calculated by the use of kinetic equations for the distribution function of the quantum dot system [134, 167]. This powerful approach is, however, not exactly solvable for case of finite source-drain voltage addressed here, in contrast to the linear regime of Ref. [134]. As relevant to experiment, we focus on low temperatures $T \ll \Delta$ where the tunneling current can be calculated without solving kinetic equations. Instead the conductance is obtained by calculating the current-channel function $\mathcal{I}(V_g, V_{sd})$ as already performed in Figs. 6.4a) and b).

The explanation for the GMR effect summarizes the results obtained in the previous sections and is manifested as follows: The spins of the SMMs are anti-parallel aligned for vanishing magnetic field, while above a critical magnetic field $B > B_c$, the stable orientation of molecular spins is parallel. Due to Coulomb blockade, the conductance around zero source-drain voltage is strongly suppressed for the anti-parallel configurations of the spins of the SMMs. The gap in the transport map can be estimated as $\delta V_{sd} \sim 1 \div 2$ meV in the absence of magnetic field for the locations of the molecules of $x_1 = 0.2$, $x_2 = 0.6$ and the parameter $\kappa = 25$, as seen in Fig. 6.4a), in agreement with experimental observation, Fig. 1.11a). For magnetic field above the critical field, however, the parallel aligned spins of the SMMs lead to a closing of some transport gaps. For gate voltages where the transport gap closes, a strong spin-valve effect and hence a GMR emerges, as in Fig. 1.13a). The transport gaps remaining above the critical field are typically smaller than in vanishing magnetic field, cf. Figs. 6.4a) and b), resulting in a weak spin-valve effect, as observed in Fig. 1.13b). Thus, the theoretical model explains the V_g dependence on the strength of the spin-valve effect which relies crucially on the incorporation of the effects of Coulomb blockade.

The value of conductance can be estimated in the case of a few open channels, $\mathcal{I} \sim 1$, which is realized for a small source-drain voltage $eV_{sd} \lesssim 0.3E_C$. For the conductance, we use Landauer formula as introduced in Sec. 2.3 with a transmission amplitude determined by the classical transmission in the limit of strong dephasing, cf. Sec. 5.2.1. Under the assumption that the transparency of the molecule $\mathcal{T}_M$ is much larger than the transparency of the barriers $\mathcal{T}_{L,R}$ (for energies not too close to the resonant energy, see Figure 5.2), the conductance of the system is given by

$$\frac{\mathcal{G}}{\mathcal{G}_0} \sim \frac{\mathcal{T}_L \mathcal{T}_R}{\mathcal{T}_L + \mathcal{T}_R}, \tag{6.23}$$

where the conductance is related to the quantum conductance $\mathcal{G}_0 = e^2/h$.

The conductance as a function of source-drain voltage is shown for a gate voltage of $U_g = 1.33$ in Fig. 6.6 with the red curve corresponding to $B = 0$, meaning anti-parallel molecular spins and the blue curve corresponding to magnetic field above the critical one B_c, meaning anti-parallel spins of SMMs. The clearly seen GMR in Fig. 6.6 is manifested by the opening of the transport gap at zero

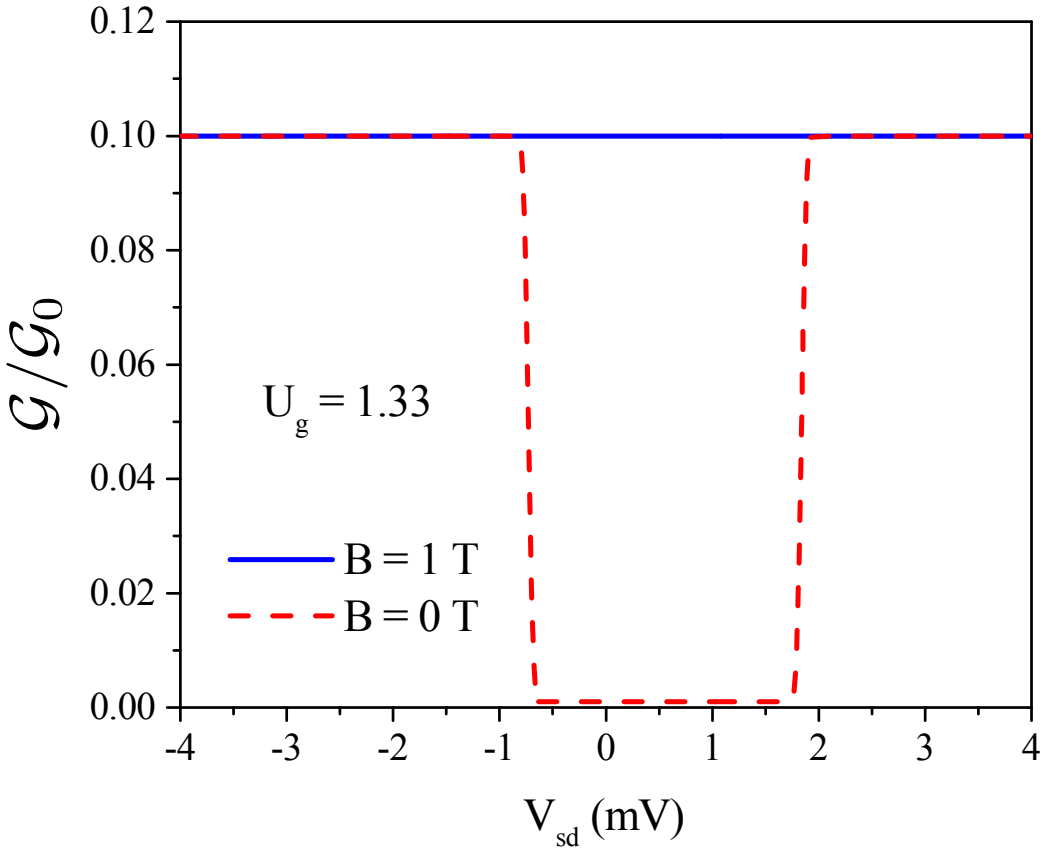

Figure 6.6: Linear conductance at zero T as a function of source-drain voltage at $U_g = 1.33$. The red dash curve corresponds to the absence of magnetic field (anti-parallel molecules spins), the blue curve is associated with a finite magnetic field above the critical one, B_c (parallel molecules spins). The molecules are located at $x_1 = 0.2$, $x_2 = 0.6$ and $\kappa = 25$.

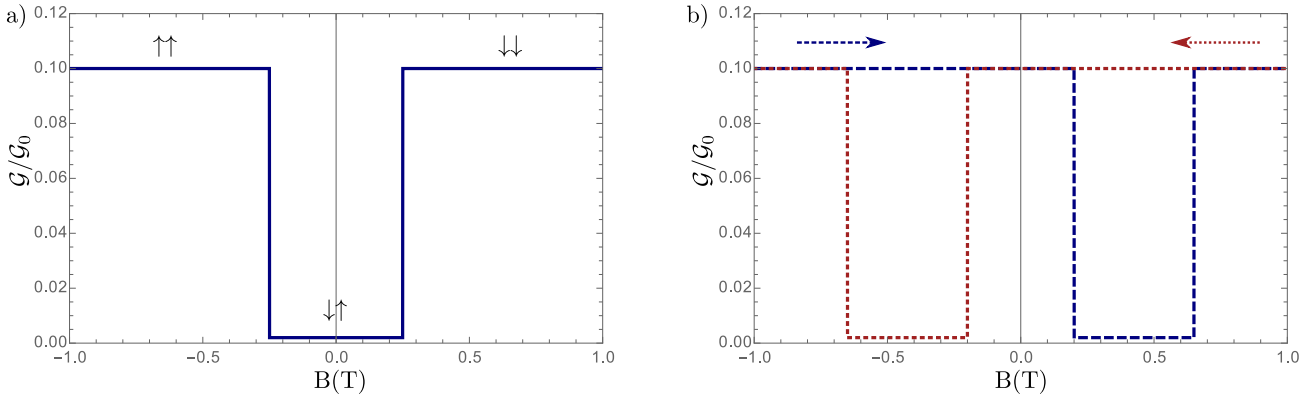

Figure 6.7: Schematic illustration of the conductance of a nanotube with two side-attached $TbPc_2$ SMMs in dependence of magnetic field for a negative interaction energy $E_{ss} < 0$ at zero magnetic field. Panel a) depicts the conductance in dependence of a static magnetic field showing the strongly reduced conductance for magnetic fields where the molecular spins are aligned anti-parallel. In panel b), effect of a dynamical sweep of the magnetic field is schematically shown. The retarded spin relaxation due to sufficiently fast sweeping is emphasized.

magnetic field, cf. Fig. 6.4a), caused by the anti-ferromagnetic arranged molecular spins. In both experiment and theoretical model the low-conductance window is asymmetric around $V_{sd} = 0$ and shifted to positive source-drain voltages by $0.5 \div 1$mV, cf. Figs. 1.13a) and 6.6, respectively.

A schematic illustration of the magnetoconductance is presented in Fig. 6.7a). It is shown that the conductance is strongly reduced in region of magnetic field, where the anti-parallel alignment of the molecular spins is energetically more favorable. In a dynamically swept magnetic field, the region of reduced conductance is dependent on the sweeping rate and direction of the magnetic field since the process of spin relaxation is retarded, cf. Fig. 6.7. This means that the spins need some time to "feel" the magnetic field as observed in experiment, Fig. 1.10.

6.5 Summary of Chapter 6

In conclusion, we have presented a theoretical model for the giant magnetoresistance effect (spin-valve effect) and Coulomb blockade in nanotubes with side-attached molecular magnets based on Ref. [94]. The proposed theoretical model explains qualitatively the giant magnetoresistance (cf. Fig. 1.13, 6.6, and 6.7) as well as the structure of Coulomb diamonds (cf. Fig. 1.11a),b) and 6.4a),b)) in the nonlinear transport in CNTs with side-attached SMMs [58, 77, 78].

The following aspects account particularly for the developed model. The model relies on the splitting of the spin-up and spin-down states for the transport of the carrier electrons and on the corresponding breaking of the nanotube into four quantum dots as we discussed in Ch. 5. As a remainder, the four quantum dots correspond either to a single quantum dot and three quantum dots for parallel aligned spins of the SMMs for spin-up and spin-down carrier electrons, or to two quantum dots for each spin species of electrons for anti-parallel molecular spins, cf. Fig. 5.6. The orientation of the molecular spin with respect to each other is determined by an effective magnetic interaction between the $TbPc_2$ spins caused by different energies of the spin configuration of the molecules, cf. Fig. 6.5.

The sign of this interaction may depend on the positions of SMMs and can be tuned by the gate voltage. In zero external magnetic fields, the most configurations and gate voltages provide an anti-ferromagnetic ordering of the spins providing a spin-valve effect. In this configuration, both spin-up and spin-down conduction electrons tunnel through a double quantum dot where the conductance is strongly suppressed by Coulomb blockade at zero source-drain voltage for all gate voltages, Fig. 6.4a). By applying an external magnetic field strong enough that the Zeeman energy overcomes the effective anti-ferromagnetic coupling, the spins of the molecules become parallel. Thus, electrons with the spin orientation of the molecules feel three quantum dots resulting in blocked transport. For electrons of opposite spin, the system acts as a single quantum dot and the transport gap closes at certain values of the gate voltage V_g, Fig. 6.4a). Thus, the parallel configuration of SMMs provides a higher conductance, Fig. 6.6), leading to the spin-valve effect. The strength of the spin-valve effect depends on and is controlled by the gate voltage due to the charging energy of the system and further depends on the positions of the molecules. Certain "resonant" values of the gate voltage provide a particularly strong the effect resulting in a giant magnetoresistance.

Importantly, the predicted existence of long-range interactions between SMMs mediated here by the charging effects in a CNT can be applied to generalize the description to the spin-valve effect in other nanostructures [79, 80]. We have shown that the sign and the magnitude of this effective spin-spin interaction depends on the gate voltage and positions of SMMs, cf. Figs. 6.5a) and b). Furthermore, due to the interaction of different spin channel of the conduction electrons in the CNT, the magnitude of the magnetoresistance also depends on the value of the gate voltage (cf. Fig. 1.13a) and b)), thus leading to a gate-controlled spin-valve effect. The explanation of this experimentally observed gate-controlled spin-valve effect marks an important aspect of this theoretical model implying that such supramolecular structures can be in general manipulated electrostatically by external gates. Thus, the nanostructures can be engineered by multiple gates which would mark a further step to establish SMMs for spintronic devices.

Chapter 7

Summary and conclusion

In this thesis, we outlined the properties of magnetotransport in novel Dirac systems on the examples of Weyl semimetals and carbon nanotubes with side-attached single-molecule magnets. This section presents a brief summary of the results and provides a perspective to further research projects in this context.

After reviewing the basic properties of the considered systems in Ch. 1 and the applied methods in Ch. 2, we turned to the study of disorder in Weyl semimetals in Ch. 3. In different analytical and numerical approaches, the appearance of a critical disorder strength was obtained [16–18, 22]. The analysis of pointlike impurities within the self-consistent Born approximation (SCBA) in the absence of magnetic field, as performed in Ch. 3, provides also a critical disorder strength, cf. Fig. 3.1. The SCBA analysis for pointlike impurities was already performed in Ref. [18] in weak and strong disorder. We go however beyond this limit and consider also the critical phase. As a result, we obtained a density of states in the regime of critical disorder behaving as $\varepsilon^{1/2}$, Eq. (3.17), consistent with the $1/N$ expansion [16, 17], in contrast to the linear behavior as obtained in the renormalization group analysis (RG) in $2-\epsilon$ dimensions [18, 19]. This indicates that the SCBA provides more accurate results than the RG which is applied far from the critical dimension for $\epsilon = -1$ in Weyl semimetals. The prove of this statement is a project delegated to future work. Furthermore, we showed that the SCBA analysis in strong disorder requires the incorporation of terms of the order of Γ/Λ for solving the self-consistent equation, cf. Eq. (3.19). This manifests itself in particular under the consideration of vertex corrections in the conductivity leading to a saturating conductivity in dependence of disorder in the strong disorder limit, Fig. 3.5. The saturating conductivity marks the suppression of backscattering in the strongly diffusive limit.

Performing the SCBA analysis in presence of a quantizing magnetic field for pointlike impurities, cf. Sec. 3.4, we find that the appearance of the critical disorder strength persists. However, due to broadening of Landau levels in the presence of disorder, all Landau levels overlap in the regime of strong disorder resulting in a density of states as in the absence of magnetic field. For weak disorder, the density of states consists of the zeroth Landau level, separated and overlapping Landau levels. The two most crucial results for the density of states in presence of magnetic field are: (i) there is a certain regime where Landau levels are still well quantized, but the background density of states is larger than contribution of the Landau level peaks, cf. Fig. 3.11; (ii) for increasing magnetic field, the Landau level broadening also increases in contrast to conventional semiconductors, cf. Fig. 3.12. However, with respect to disorder, we find that Landau level broadening increases with increasing disorder strength as expected.

One central aspect of this thesis concerns the evaluation of the transversal magnetoresistance (TMR) in Weyl semimetals. The analysis of the TMR in several regimes of magnetic field in relation to temperature and chemical potential was performed Ch. 4. A salient result of this calculation is that the TMR in the ultra quantum limit, where only the zeroth Landau level determines the TMR, strongly depends on the chosen model of disorder. We find that the linear TMR is determined by a model of screened Coulomb impurities as proposed in the seminal work of Ref. [82]. However, for pointlike disorder, the TMR vanishes as $1/H$ in the ultra quantum limit according to our theoretical model [83] which was recently confirmed by a numerical analysis [87]. Away from the quantum limit, the highly peculiar results are determined by an unusual broadening of Landau levels in presence of disorder which was discussed in Ch. 3. For finite temperatures, we find a non-analytic magnetoresistance in the low field limit proportional to $H^{1/3}$ for pointlike impurities while for Coulomb impurities, the TMR vanishes quadratically in the low field limit. The finite Hall conductivity for finite chemical potential leads to a competition between the conductivity and the Hall conductivity in the TMR. The particular large Hall conductivity leads to a vanishing magnetoresistance (except for the center of the Landau levels) up to the ultra quantum limit for zero temperature, cf. Fig. 4.8. Finite temperature smears the Landau levels and introduces a small correction to the vanishing TMR at zero temperature evolving linearly with magnetic field. As found in various experiments [5, 6], we considered a model of two pairs of Weyl nodes shifted in energy with respect to each other with the system being at complete charge neutrality, cf. Fig. 4.12. In this model, we find a huge magnetoresistance $\propto H^{2/3}$ superimposed by strong Shubnikov-de Haas oscillations. In the quantum limit of this model, the linear TMR for Coulomb impurities remains intact. We could further show in Fig. 4.14 that the slope of the obtained TMR is in agreement with the magnitude of the TMR obtained in experiment.

The huge TMR in Weyl semimetals offers new possible designs for magnetoresistance devices. Compared to conventional magnetoresistance devices, which are designed in complex structures, Weyl semimetals might lead to a significantly easier device fabrication. An even larger magnetoresistance was observed in type-II Weyl semimetals [48] where the Weyl nodes are tilted compared to type-I Weyl semimetals as considered in this thesis. The quadratic TMR in type-II Weyl semimetals still lacks a theoretical explanation. The design of a theoretical model for these material would be an interesting project for the future and would provide more insight in this class of materials. Moreover, the type-II material shows signatures of a hydrodynamic behavior [106]. The development of a full hydrodynamic description of both type-I and type-II Weyl semimetals would be a further step to uncover the interesting physics of Weyl semimetals.

Chapter 5 is devoted to another Dirac system showing a large magnetoresistance. We consider a carbon nanotube (CNT) with side-attached single-molecule magnets (SMM). To understand to physics of such a system which is tunnel-coupled to external leads, we first analyze the effect of Fano-resonances on transport within barriers. We analyzed the effect of a Fano state in a confined geometry in presence of strong dephasing and in a fully quantum mechanical description. Most importantly, we developed a Green's function formalism for a Fano state in a system of two barriers providing the transmission and reflection amplitudes in an elegant form allowing to directly read out the effect of the barriers on the Fano state. In future, this Green's function formalism can be developed further such that more complex structures can be included in an effective way. A well established Green's function formalism can provide a treatment of interaction effects of such complex scattering structures.

The transport properties result now in a theoretical model for a magnetoresistance and spin-valve effect of a carbon nanotube (CNT) tunnel-coupled to leads with side-attached single-molecule magnets (SMM) of $TbPc_2$ as experimentally realized in Ref. [58]. The model presented in Ch. 5 is based on the fact that the phthalocyanine ligands of $TbPc_2$ have a localized state near the Fermi surface coupling

to electronic states of the CNT. The localized states for spin-up and spin-down carriers are split by the exchange interaction between the localized electrons on the molecule and the $4f$ electrons of the terbium shell. The energy range of backscattering by the Fano-resonance introduced by the localized state is thus spin dependent. For a minimal model of two molecules, the backscattering on the Fano-resonances breaks the nanotube into four quantum dots. For anti-parallel aligned molecules, both spin channels for the carrier electrons are split into two dots while for parallel aligned molecules, a single quantum dot for one spin species of carrier electrons and a triple quantum dot for the other appears, cf. Fig. 5.6. The different scattering processes for parallel and anti-parallel aligned molecules account for a magnetoresistance since the conductance in the absence of magnetic field is reduced due to the possibility to have anti-parallel aligned SMMs, cf. Fig. 5.7a).

The obtained magnetoresistance and "spin-valve" effect of Ch. 5 are of a smaller magnitude than in experiment. In Ch. 6, we included Coulomb interaction which provides a more accurate explanation. An important feature of the Coulomb blockade map is that configurations of double or triple quantum dots result in a transport gap around zero source-drain voltage. However, due to the coupling of the single and triple quantum dot, the transport gap closes only at certain "resonant" values of gate voltage for parallel aligned molecules, cf. Fig. 6.4. The orientation of the molecules with respect to each other is mediated by an effective magnetic interaction dependent on gate voltage and positions of the molecules. For zero magnetic field, the most favorable orientation of the SMM spin is anti-parallel for most gate voltages and molecular positions, cf. Fig. 6.5. Above a certain magnetic field, the parallel configuration of molecular spin becomes favorable determining a giant magnetoresistance at the gate voltages where the transport gap closes for parallel aligned molecules, cf. Fig. 6.7. Thus, we modeled the origin of the gate-controlled spin-valve effect. Moreover, this effect is enhanced by the gate voltage and position dependence of the molecular spin orientation which further allows to manipulate nanostructures by multiple gates. To realize such multiple gate nanostructures with a controlled deposition of SMMs experimentally would be an important step in the direction of establishing molecular quantum spintronic devices in the community of nanoelectronics. A theoretical modeling of these nanostructures can supply a guideline for the fabrication and improvement of the devices such that in future supramolecular chemistry can provide powerful and affordable tools to tailor quite complex molecular devices.

In conclusion, this thesis covers the theoretical description of two systems hosting a giant magnetoresistance, Weyl semimetals and CNTs with side-attached single-molecule magnets. In Weyl semimetals, we discussed the effects of impurities on transport showing that in both in absence and in presence of a finite magnetic field impurities can strongly affect the transport properties. Moreover, we showed that the experimentally observed huge transversal magnetoresistance in Weyl semimetals can be explained by a model of shifted Weyl nodes in energy with respect to each other in presence of Coulomb impurities. Related to the CNT system, we provided a theoretical model to describe the gate-controlled spin-valve effect and giant magnetoresistance. The important ingredients of the model are Coulomb interaction and spin dependent resonant scattering on Fano resonances between barriers.

On a more general level, both considered systems offer a great potential in application for spintronic and magnetoresistance devices. While the Weyl semimetal promises to significantly simplify the devices fabrication, the carbon nanotube system has the potential to mark an important step in establishing molecular spintronic devices and in further device minimization. Finding such promising applications to an equation stated around 85 years earlier in a completely different context brings us back to the statement of Paul A. M. Dirac with which the thesis started. It is not only a peculiarity of Paul A. M. Dirac, but it is always worth to play with equations just looking for beautiful mathematical relations which might not have any physical meaning. Because sometimes they do.

List of publications

In the following, the list of publications of the author of this thesis is presented. The listed publications are also part of this thesis. The publications are:

- J. Klier, I. V. Gornyi, and A. D. Mirlin: *"Transversal magnetoresistance in Weyl semimetals"*, Phys. Rev. B **92**, 205113 (2015) (Editor's suggestion). Reference [83] in the bibliography.
- I. V. Krainov, J. Klier, A. P. Dmitriev, S. Klyatskaya, M. Ruben, W. Wernsdorfer, and I. V. Gornyi: *"Giant Magnetoresistance in Carbon Nanotubes with Single-Molecule Magnets $TbPc_2$"*, ACS Nano **11**, 6868-6880 (2017). Reference [94] in the bibliography.
- J. Klier, I. V. Gornyi, and A. D. Mirlin: *"Transversal magnetoresistance and Shubnikov-de Haas oscillations in Weyl semimetals"*, Phys. Rev. B **96**, 214209 (2017). Reference [84] in the bibliography.
- J. Klier, I. V. Gornyi, and A. D. Mirlin: *"Critical disorder in Weyl semimetals"*, to be submitted, (2018). Reference [141] in the bibliography.
- I. V. Krainov, J. Klier, A. P. Dmitriev, and I. V. Gornyi: *"Transport in Fano resonances"*, in preparation, (2018). Reference [162] in the bibliography.

Bibliography

[1] O. Vafek and A. Vishwanath, "Dirac Fermions in Solids: From High-Tc Cuprates and Graphene to Topological Insulators and Weyl Semimetals," *Annual Review of Condensed Matter Physics*, vol. 5, no. 1, pp. 83–112, 2014.
(Cited on pages v, vi, 2, and 5.)

[2] H. Weyl, "Elektron und Gravitation. I," *Zeitschrift für Physik*, vol. 56, no. 5-6, pp. 330–352, 1929.
(Cited on pages v and 2.)

[3] T. Liang, Q. Gibson, M. N. Ali, M. Liu, R. J. Cava, and N. P. Ong, "Ultrahigh mobility and giant magnetoresistance in the Dirac semimetal Cd3As2," *Nat Mater*, vol. 14, no. 3, pp. 280–284, 2015.
(Cited on pages v, 9, 12, and 59.)

[4] J. Feng, Y. Pang, D. Wu, Z. Wang, H. Weng, J. Li, X. Dai, Z. Fang, Y. Shi, and L. Lu, "Large linear magnetoresistance in Dirac semimetal Cd_3As_2 with Fermi surfaces close to the Dirac points," *Phys. Rev. B*, vol. 92, p. 081306, 2015.
(Not cited.)

[5] C. Shekhar, A. K. Nayak, Y. Sun, M. Schmidt, M. Nicklas, I. Leermakers, U. Zeitler, Y. Skourski, J. Wosnitza, Z. Liu, Y. Chen, W. Schnelle, H. Borrmann, Y. Grin, C. Felser, and B. Yan, "Extremely large magnetoresistance and ultrahigh mobility in the topological Weyl semimetal candidate NbP," *Nat Phys*, vol. advance online publication, 2015.
(Cited on pages v, vi, 1, 5, 6, 8, 9, 11, 91, 92, 95, 97, and 136.)

[6] A. C. Niemann, J. Gooth, S.-C. Wu, S. Bäßler, P. Sergelius, R. Hühne, B. Rellinghaus, C. Shekhar, V. Süß, M. Schmidt, C. Felser, B. Yan, and K. Nielsch, "Chiral magnetoresistance in the Weyl semimetal NbP," *Scientific Reports*, vol. 7, p. 43394, mar 2017.
(Cited on pages 92, 97, and 136.)

[7] M. Novak, S. Sasaki, K. Segawa, and Y. Ando, "Large linear magnetoresistance in the Dirac semimetal TlBiSSe," *Phys. Rev. B*, vol. 91, p. 041203, 2015.
(Not cited.)

[8] B. J. Ramshaw, K. A. Modic, A. Shekhter, Y. Zhang, E.-A. Kim, P. J. W. Moll, M. Bachmann, M. K. Chan, J. B. Betts, F. Balakirev, A. Migliori, N. J. Ghimire, E. D. Bauer, F. Ronning, and R. D. McDonald, "Unmasking Weyl Fermions using Extreme Magnetic Fields," *ArXiv e-prints*, Apr. 2017.
(Cited on page 85.)

[9] C.-L. Zhang, S.-Y. Xu, C. M. Wang, Z. Lin, Z. Z. Du, C. Guo, C.-C. Lee, H. Lu, Y. Feng, S.-M. Huang, G. Chang, C.-H. Hsu, H. Liu, H. Lin, L. Li, C. Zhang, J. Zhang, X.-C. Xie, T.

Neupert, M. Z. Hasan, H.-Z. Lu, J. Wang, and S. Jia, "Magnetic-tunnelling-induced Weyl node annihilation in TaP," *Nature Physics*, vol. 13, p. 979, 2017.
(Cited on pages v, 9, and 59.)

[10] M. Neupane, S.-Y. Xu, R. Sankar, N. Alidoust, G. Bian, C. Liu, I. Belopolski, T.-R. Chang, H.-T. Jeng, H. Lin, A. Bansil, F. Chou, and M. Z. Hasan, "Observation of a three-dimensional topological Dirac semimetal phase in high-mobility Cd_3As_2," *Nat Commun*, vol. 5, may 2014.
(Cited on pages v, 1, 5, and 9.)

[11] Z. K. Liu, B. Zhou, Y. Zhang, Z. J. Wang, H. M. Weng, D. Prabhakaran, S.-K. Mo, Z. X. Shen, Z. Fang, X. Dai, Z. Hussain, and Y. L. Chen, "Discovery of a Three-Dimensional Topological Dirac Semimetal, Na_3Bi," *Science*, vol. 343, no. 6173, pp. 864–867, 2014.
(Cited on pages vi, 1, and 5.)

[12] S.-Y. Xu, C. Liu, S. K. Kushwaha, R. Sankar, J. W. Krizan, I. Belopolski, M. Neupane, G. Bian, N. Alidoust, T.-R. Chang, H.-T. Jeng, C.-Y. Huang, W.-F. Tsai, H. Lin, P. P. Shibayev, F.-C. Chou, R. J. Cava, and M. Z. Hasan, "Observation of Fermi arc surface states in a topological metal," *Science*, vol. 347, no. 6219, pp. 294–298, 2015.
(Cited on pages vi, 1, and 5.)

[13] B. Q. Lv, H. M. Weng, B. B. Fu, X. P. Wang, H. Miao, J. Ma, P. Richard, X. C. Huang, L. X. Zhao, G. F. Chen, Z. Fang, X. Dai, T. Qian, and H. Ding, "Experimental Discovery of Weyl Semimetal TaAs," *Phys. Rev. X*, vol. 5, p. 031013, 2015.
(Cited on pages vi, 1, and 5.)

[14] S.-Y. Xu, N. Alidoust, I. Belopolski, Z. Yuan, G. Bian, T.-R. Chang, H. Zheng, V. N. Strocov, D. S. Sanchez, G. Chang, C. Zhang, D. Mou, Y. Wu, L. Huang, C.-C. Lee, S.-M. Huang, B. Wang, A. Bansil, H.-T. Jeng, T. Neupert, A. Kaminski, H. Lin, S. Jia, and M. Z. Hasan, "Discovery of a Weyl fermion state with Fermi arcs in niobium arsenide," *Nat Phys*, vol. 11, no. 9, pp. 748–754, 2015.
(Cited on pages vi, 1, and 5.)

[15] S.-Y. Xu, I. Belopolski, D. S. Sanchez, C. Zhang, G. Chang, C. Guo, G. Bian, Z. Yuan, H. Lu, T.-R. Chang, P. P. Shibayev, M. L. Prokopovych, N. Alidoust, H. Zheng, C.-C. Lee, S.-M. Huang, R. Sankar, F. Chou, C.-H. Hsu, H.-T. Jeng, A. Bansil, T. Neupert, V. N. Strocov, H. Lin, S. Jia, and M. Z. Hasan, "Experimental discovery of a topological weyl semimetal state in tap," *Science Advances*, vol. 1, no. 10, 2015.
(Cited on pages vi, 1, and 5.)

[16] E. Fradkin, "Critical behavior of disordered degenerate semiconductors. I. Models, symmetries, and formalism," *Phys. Rev. B*, vol. 33, pp. 3257–3262, 1986.
(Cited on pages vi, vii, 33, 36, 57, and 135.)

[17] E. Fradkin, "Critical behavior of disordered degenerate semiconductors. II. Spectrum and transport properties in mean-field theory," *Phys. Rev. B*, vol. 33, pp. 3263–3268, 1986.
(Cited on pages vi, vii, 33, 36, 57, and 135.)

[18] S. V. Syzranov, L. Radzihovsky, and V. Gurarie, "Critical Transport in Weakly Disordered Semiconductors and Semimetals," *Phys. Rev. Lett.*, vol. 114, p. 166601, 2015.
(Cited on pages vi, vii, 33, 52, 57, and 135.)

[19] S. V. Syzranov, P. M. Ostrovsky, V. Gurarie, and L. Radzihovsky, "Critical exponents at the unconventional disorder-driven transition in a Weyl semimetal," *Phys. Rev. B*, vol. 93, p. 155113, 2016.
(Cited on pages 33 and 135.)

[20] S. V. Syzranov, V. Gurarie, and L. Radzihovsky, "Unconventional localization transition in high dimensions," *Phys. Rev. B*, vol. 91, p. 035133, 2015.
(Cited on pages vi, vii, 36, 39, and 57.)

[21] A. Altland and D. Bagrets, "Effective Field Theory of the Disordered Weyl Semimetal," *Phys. Rev. Lett.*, vol. 114, p. 257201, 2015.
(Cited on pages vi and 52.)

[22] B. Sbierski, G. Pohl, E. J. Bergholtz, and P. W. Brouwer, "Quantum Transport of Disordered Weyl Semimetals at the Nodal Point," *Phys. Rev. Lett.*, vol. 113, p. 026602, 2014.
(Cited on pages vi, vii, 33, 52, and 135.)

[23] J. H. Pixley, D. A. Huse, and S. Das Sarma, "Rare-Region-Induced Avoided Quantum Criticality in Disordered Three-Dimensional Dirac and Weyl Semimetals," *Phys. Rev. X*, vol. 6, p. 021042, 2016.
(Cited on pages vi, 33, and 41.)

[24] J. H. Pixley, D. A. Huse, and S. Das Sarma, "Uncovering the hidden quantum critical point in disordered massless Dirac and Weyl semimetals," *Phys. Rev. B*, vol. 94, p. 121107, 2016.
(Not cited.)

[25] J. H. Pixley, Y.-Z. Chou, P. Goswami, D. A. Huse, R. Nandkishore, L. Radzihovsky, and S. Das Sarma, "Single-particle excitations in disordered Weyl fluids," *Phys. Rev. B*, vol. 95, p. 235101, 2017.
(Not cited.)

[26] B. Sbierski, K. A. Madsen, P. W. Brouwer, and C. Karrasch, "Quantitative analytical theory for disordered nodal points," *Phys. Rev. B*, vol. 96, p. 064203, 2017.
(Cited on pages vi and 33.)

[27] R. Nandkishore, D. A. Huse, and S. L. Sondhi, "Rare region effects dominate weakly disordered three-dimensional Dirac points," *Phys. Rev. B*, vol. 89, p. 245110, 2014.
(Cited on pages vi, 33, and 41.)

[28] T. Holder, C.-W. Huang, and P. M. Ostrovsky, "Electronic properties of disordered Weyl semimetals at charge neutrality," *Phys. Rev. B*, vol. 96, p. 174205, 2017.
(Cited on pages vi and 33.)

[29] M. Buchhold, S. Diehl, and A. Altland, "Vanishing density of states in weakly disordered Weyl semimetals," *ArXiv e-prints*, Apr. 2018.
(Cited on pages vi, 33, and 41.)

[30] P. Hosur, S. A. Parameswaran, and A. Vishwanath, "Charge Transport in Weyl Semimetals," *Phys. Rev. Lett.*, vol. 108, p. 046602, 2012.
(Cited on pages vi, 33, 57, 64, and 66.)

[31] A. A. Burkov, "Chiral anomaly and transport in Weyl metals," *Journal of Physics: Condensed Matter*, vol. 27, no. 11, p. 113201, 2015.
(Cited on page vi.)

[32] M. M. Vazifeh and M. Franz, "Electromagnetic Response of Weyl Semimetals," *Phys. Rev. Lett.*, vol. 111, p. 027201, 2013.
(Cited on page vi.)

[33] D. T. Son and B. Z. Spivak, "Chiral anomaly and classical negative magnetoresistance of Weyl metals," *Phys. Rev. B*, vol. 88, p. 104412, 2013.
(Cited on page vi.)

[34] E. V. Gorbar, V. A. Miransky, and I. A. Shovkovy, "Chiral anomaly, dimensional reduction, and magnetoresistivity of Weyl and Dirac semimetals," *Phys. Rev. B*, vol. 89, p. 085126, 2014.
(Not cited.)

[35] A. A. Burkov, "Chiral Anomaly and Diffusive Magnetotransport in Weyl Metals," *Phys. Rev. Lett.*, vol. 113, p. 247203, 2014.
(Not cited.)

[36] A. Lucas, A. Davison, and S. Sachdev, "Hydrodynamic theory of thermoelectric transport and negative magnetoresistance in weyl semimetals," *Proceedings of the National Academy of Sciences*, vol. 113, no. 34, pp. 9463–9468, 2016.
(Not cited.)

[37] A. A. Burkov, "Negative longitudinal magnetoresistance in dirac and weyl metals," *Phys. Rev. B*, vol. 91, p. 245157, 2015.
(Not cited.)

[38] P. Goswami, J. H. Pixley, and S. Das Sarma, "Axial anomaly and longitudinal magnetoresistance of a generic three-dimensional metal," *Phys. Rev. B*, vol. 92, p. 075205, 2015.
(Not cited.)

[39] N. J. Ghimire, Y. Luo, M. Neupane, D. J. Williams, E. D. Bauer, and F. Ronning, "Magnetotransport of single crystalline NbAs," *Journal of Physics: Condensed Matter*, vol. 27, no. 15, p. 152201, 2015.
(Not cited.)

[40] F. Arnold, C. Shekhar, S.-C. Wu, Y. Sun, R. D. dos Reis, N. Kumar, M. Naumann, M. O. Ajeesh, M. Schmidt, A. G. Grushin, J. H. Bardarson, M. Baenitz, D. Sokolov, H. Borrmann, M. Nicklas, C. Felser, E. Hassinger, and B. Yan, "Negative magnetoresistance without well-defined chirality in the Weyl semimetal TaP," *Nature Communications*, vol. 7, p. 11615, 2016.
(Cited on pages 8 and 96.)

[41] J. Behrends and J. H. Bardarson, "Strongly angle-dependent magnetoresistance in Weyl semimetals with long-range disorder," *Phys. Rev. B*, vol. 96, p. 060201, 2017.
(Cited on page vi.)

[42] J. Gooth, A. C. Niemann, T. Meng, A. G. Grushin, K. Landsteiner, B. Gotsmann, F. Menges, M. Schmidt, C. Shekhar, V. Süß, R. Hühne, B. Rellinghaus, C. Felser, B. Yan, and K. Nielsch,

"Experimental signatures of the mixed axial–gravitational anomaly in the Weyl semimetal NbP," *Nature*, vol. 547, no. 7663, pp. 324–327, 2017.
(Cited on page vi.)

[43] M. D. Bachmann, N. Nair, F. Flicker, R. Ilan, T. Meng, N. J. Ghimire, E. D. Bauer, F. Ronning, J. G. Analytis, and P. J. W. Moll, "Inducing superconductivity in Weyl semimetal microstructures by selective ion sputtering," *Science Advances*, vol. 3, no. 5, 2017.
(Cited on page vi.)

[44] K. A. Madsen, E. J. Bergholtz, and P. W. Brouwer, "Josephson effect in a Weyl SNS junction," *Phys. Rev. B*, vol. 95, p. 064511, 2017.
(Cited on page vi.)

[45] N. Bovenzi, M. Breitkreiz, P. Baireuther, T. E. O'Brien, J. Tworzydło, I. Adagideli, and C. W. J. Beenakker, "Chirality blockade of Andreev reflection in a magnetic Weyl semimetal," *Phys. Rev. B*, vol. 96, p. 035437, 2017.
(Not cited.)

[46] D. K. Mukherjee, S. Rao, and A. Kundu, "Transport through Andreev bound states in a Weyl semimetal quantum dot," *Phys. Rev. B*, vol. 96, p. 161408, 2017.
(Not cited.)

[47] S.-B. Zhang, F. Dolcini, D. Breunig, and B. Trauzettel, "Appearance of the universal value e^2/h of the zero-bias conductance in a Weyl semimetal-superconductor junction," *Phys. Rev. B*, vol. 97, p. 041116, 2018.
(Cited on page vi.)

[48] N. Kumar, Y. Sun, N. Xu, K. Manna, M. Yao, V. Süss, I. Leermakers, O. Young, T. Förster, M. Schmidt, H. Borrmann, B. Yan, U. Zeitler, M. Shi, C. Felser, and C. Shekhar, "Extremely high magnetoresistance and conductivity in the type-II Weyl semimetals WP_2 and MoP_2," *Nature Communications*, vol. 8, no. 1, p. 1642, 2017.
(Cited on pages vi, 4, and 136.)

[49] C. Jia and X. Guo, "Molecule-electrode interfaces in molecular electronic devices," *Chem. Soc. Rev.*, vol. 42, pp. 5642–5660, 2013.
(Cited on page vi.)

[50] D. Gatteschi, R. Sessoli, and J. Villain, *Molecular nanomagnets*. Mesoscopic physics and nanotechnology ; 5, Oxford [u.a.]: Oxford University Press, 2006.
(Cited on pages vi and 15.)

[51] A. R. Rocha, V. M. Garcia-Suarez, S. W. Bailey, C. J. Lambert, J. Ferrer, and S. Sanvito, "Towards molecular spintronics," *Nat Mater*, vol. 4, no. 4, pp. 335–339, 2005.
(Not cited.)

[52] L. Bogani and W. Wernsdorfer, "Molecular spintronics using single-molecule magnets," *Nat Mater*, vol. 7, no. 3, pp. 179–186, 2008.
(Cited on pages vii and 15.)

[53] S. Sanvito, "Molecular spintronics," *Chem. Soc. Rev.*, vol. 40, pp. 3336–3355, 2011.
(Not cited.)

[54] E. Moreno Pineda, T. Komeda, K. Katoh, M. Yamashita, and M. Ruben, "Surface confinement of TbPc2-SMMs: structural, electronic and magnetic properties ," *Dalton Trans.*, vol. 45, pp. 18417–18433, 2016.
(Cited on page vi.)

[55] J. Bartolomé, F. Luis, and J. F. Fernández, *Molecular Magnets: Physics and Applications*. NanoScience and Technology, Springer-Verlag Berlin Heidelberg, 2014.
(Cited on page vi.)

[56] L. E. Hueso, J. M. Pruneda, V. Ferrari, G. Burnell, J. P. Valdes-Herrera, B. D. Simons, P. B. Littlewood, E. Artacho, A. Fert, and N. D. Mathur, "Transformation of spin information into large electrical signals using carbon nanotubes," *Nature*, vol. 445, no. 7126, pp. 410–413, 2007.
(Cited on page vi.)

[57] T. Miyamachi, M. Gruber, V. Davesne, M. Bowen, S. Boukari, L. Joly, F. Scheurer, G. Rogez, T. K. Yamada, P. Ohresser, E. Beaurepaire, and W. Wulfhekel, "Robust spin crossover and memristance across a single molecule," *Nature Communications*, vol. 3, p. 938, 2012.
(Not cited.)

[58] M. Urdampilleta, S. Klyatskaya, J.-P. Cleuziou, M. Ruben, and W. Wernsdorfer, "Supramolecular spin valves," *Nature Materials*, vol. 10, pp. 502–506, 2011.
(Cited on pages vii, 15, 20, 21, 99, 119, 121, 133, and 136.)

[59] A. S. Zyazin, J. W. G. van den Berg, E. A. Osorio, H. S. J. van der Zant, N. P. Konstantinidis, M. Leijnse, M. R. Wegewijs, F. May, W. Hofstetter, C. Danieli, and A. Cornia, "Electric Field Controlled Magnetic Anisotropy in a Single Molecule," *Nano Letters*, vol. 10, no. 9, pp. 3307–3311, 2010.
(Not cited.)

[60] M. Galperin and A. Nitzan, "Molecular optoelectronics: the interaction of molecular conduction junctions with light," *Phys. Chem. Chem. Phys.*, vol. 14, pp. 9421–9438, 2012.
(Not cited.)

[61] K. Bairagi, O. Iasco, A. Bellec, A. Kartsev, D. Li, J. Lagoute, C. Chacon, Y. Girard, S. Rousset, F. Miserque, Y. J. Dappe, A. Smogunov, C. Barreteau, M.-L. Boillot, Mallah Talal, and V. Repain, "Molecular-scale dynamics of light-induced spin cross-over in a two-dimensional layer," *Nature Communications*, vol. 7, p. 12212, 2016.
(Not cited.)

[62] T. Komeda, H. Isshiki, J. Liu, Y.-F. Zhang, N. Lorente, K. Katoh, B. K. Breedlove, and M. Yamashita, "Observation and electric current control of a local spin in a single-molecule magnet," *Nature Communications*, vol. 2, p. 217, 2011.
(Cited on page 15.)

[63] V. Meded, A. Bagrets, K. Fink, R. Chandrasekar, M. Ruben, F. Evers, A. Bernand-Mantel, J. S. Seldenthuis, A. Beukman, and H. S. J. van der Zant, "Electrical control over the Fe(II) spin

crossover in a single molecule: Theory and experiment," *Phys. Rev. B*, vol. 83, p. 245415, 2011.
(Not cited.)

[64] C. Jia, A. Migliore, N. Xin, S. Huang, J. Wang, Q. Yang, S. Wang, H. Chen, D. Wang, B. Feng, Z. Liu, G. Zhang, D.-H. Qu, H. Tian, M. A. Ratner, H. Q. Xu, A. Nitzan, and X. Guo, "Covalently bonded single-molecule junctions with stable and reversible photoswitched conductivity," *Science*, vol. 352, no. 6292, pp. 1443–1445, 2016.
(Cited on page vi.)

[65] N. Ishikawa, M. Sugita, T. Okubo, N. Tanaka, T. Iino, and Y. Kaizu, "Determination of Ligand-Field Parameters and f-Electronic Structures of Double-Decker Bis(phthalocyaninato)lanthanide Complexes," *Inorganic Chemistry*, vol. 42, no. 7, pp. 2440–2446, 2003.
(Cited on page vi.)

[66] N. Ishikawa, M. Sugita, N. Tanaka, T. Ishikawa, S.-Y. Koshihara, and Y. Kaizu, "Upward Temperature Shift of the Intrinsic Phase Lag of the Magnetization of Bis(phthalocyaninato)terbium by Ligand Oxidation Creating an S = 1/2 Spin," *Inorganic Chemistry*, vol. 43, no. 18, pp. 5498–5500, 2004.
(Cited on pages vi and 15.)

[67] G. Christou, D. Gatteschi, D. N. Hendrickson, and R. Sessoli, "Single-Molecule Magnets," *MRS Bulletin*, vol. 25, no. 11, pp. 66–71, 2000.
(Cited on pages vi and 15.)

[68] A. Cornia, A. F. Costantino, L. Zobbi, A. Caneschi, D. Gatteschi, M. Mannini, and R. Sessoli, *Preparation of Novel Materials Using SMMs*, pp. 133–161. Berlin, Heidelberg: Springer Berlin Heidelberg, 2006.
(Cited on page 15.)

[69] K. Katoh, Y. Yoshida, M. Yamashita, H. Miyasaka, B. K. Breedlove, T. Kajiwara, S. Takaishi, N. Ishikawa, H. Isshiki, Y. F. Zhang, T. Komeda, M. Yamagishi, and J. Takeya, "Direct Observation of Lanthanide(III)-Phthalocyanine Molecules on Au(111) by Using Scanning Tunneling Microscopy and Scanning Tunneling Spectroscopy and Thin-Film Field-Effect Transistor Properties of Tb(III)- and Dy(III)-Phthalocyanine Molecules," *Journal of the American Chemical Society*, vol. 131, no. 29, pp. 9967–9976, 2009.
(Not cited.)

[70] B. Fleury, L. Catala, V. Huc, C. David, W. Zhao Zhong, P. Jegou, L. Baraton, S. Palacin, P.-A. Albouy, and T. Mallah, "A new approach to grafting a monolayer of oriented Mn12 nanomagnets on silicon," *Chem. Commun.*, pp. 2020–2022, 2005.
(Cited on page 15.)

[71] A. Naitabdi, J.-P. Bucher, P. Gerbier, P. Rabu, and M. Drillon, "Self-Assembly and Magnetism of Mn12 Nanomagnets on Native and Functionalized Gold Surfaces," *Advanced Materials*, vol. 17, no. 13, pp. 1612–1616, 2005.
(Not cited.)

[72] E. Coronado, A. Forment-Aliaga, A. Gaita-Arino, C. Gimenez-Saiz, F. M. Romero, and W. Wernsdorfer, "Polycationic Mn12 Single-Molecule Magnets as Electron Reservoirs with S¿10

Ground States," *Angewandte Chemie International Edition*, vol. 43, no. 45, pp. 6152–6156, 2004.
(Cited on pages vi and 15.)

[73] L. Bogani, L. Cavigli, M. Gurioli, R. Novak, M. Mannini, A. Caneschi, F. Pineider, R. Sessoli, M. Clemente-Leon, E. Coronado, A. Cornia, and D. Gatteschi, "Magneto-Optical Investigations of Nanostructured Materials Based on Single-Molecule Magnets Monitor Strong Environmental Effects," *Advanced Materials*, vol. 19, no. 22, pp. 3906–3911, 2007.
(Cited on pages vii and 15.)

[74] N. Ishikawa, M. Sugita, T. Ishikawa, S.-Y. Koshihara, and Y. Kaizu, "Mononuclear Lanthanide Complexes with a Long Magnetization Relaxation Time at High Temperatures: A New Category of Magnets at the Single-Molecular Level," *The Journal of Physical Chemistry B*, vol. 108, no. 31, pp. 11265–11271, 2004.
(Cited on page vii.)

[75] M. Mannini, F. Pineider, P. Sainctavit, C. Danieli, E. Otero, C. Sciancalepore, A. M. Talarico, M.-A. Arrio, A. Cornia, D. Gatteschi, and R. Sessoli, "Magnetic memory of a single-molecule quantum magnet wired to a gold surface," *Nature Materials*, vol. 8, pp. 194–197, 2009.
(Cited on page vii.)

[76] E. A. Laird, F. Kuemmeth, G. A. Steele, K. Grove-Rasmussen, J. Nygård, K. Flensberg, and L. P. Kouwenhoven, "Quantum transport in carbon nanotubes," *Rev. Mod. Phys.*, vol. 87, pp. 703–764, 2015.
(Cited on pages vii, 10, and 13.)

[77] M. Urdampilleta, S. Klyatskaya, M. Ruben, and W. Wernsdorfer, "Landau-Zener tunneling of a single Tb^{3+} magnetic moment allowing the electronic read-out of a nuclear spin," *Phys. Rev. B*, vol. 87, p. 195412, 2013.
(Cited on pages vii, 17, 99, and 133.)

[78] M. Urdampilleta, N.-V. Nguyen, J.-P. Cleuziou, S. Klyatskaya, M. Ruben, and W. Wernsdorfer, "Molecular Quantum Spintronics: Supramolecular Spin Valves Based on Single-Molecule Magnets and Carbon Nanotubes," *International Journal of Molecular Sciences*, vol. 12, no. 10, p. 6656, 2011.
(Cited on pages vii, 15, 99, and 133.)

[79] A. Candini, S. Klyatskaya, M. Ruben, W. Wernsdorfer, and M. Affronte, "Graphene spintronic devices with molecular nanomagnets," *Nano Lett.*, vol. 11 (7), p. 2634, 2011.
(Cited on pages vii, 99, and 134.)

[80] H. Aurich, A. Baumgartner, F. Freitag, A. Eichler, J. Trbovic, and C. Schönenberger, "Permalloy-based carbon nanotube spin-valve," *Applied Physics Letters*, vol. 97, no. 15, p. 153116, 2010.
(Cited on pages vii, 99, and 134.)

[81] R. R. Biswas and S. Ryu, "Diffusive transport in Weyl semimetals," *Phys. Rev. B*, vol. 89, p. 014205, 2014.
(Cited on pages viii, 28, 40, 57, 60, 177, 179, and 180.)

[82] A. A. Abrikosov, "Quantum magnetoresistance," *Phys. Rev. B*, vol. 58, pp. 2788–2794, 1998.
(Cited on pages viii, 10, 34, 55, 59, 77, 79, 89, 90, 136, and 180.)

[83] J. Klier, I. V. Gornyi, and A. D. Mirlin, "Transversal magnetoresistance in Weyl semimetals," *Phys. Rev. B*, vol. 92, p. 205113, 2015.
(Cited on pages viii, 34, 58, 59, 136, and 139.)

[84] J. Klier, I. V. Gornyi, and A. D. Mirlin, "Transversal magnetoresistance and Shubnikov-de Haas oscillations in Weyl semimetals," *Phys. Rev. B*, vol. 96, p. 214209, 2017.
(Cited on pages viii, 59, and 139.)

[85] D. A. Pesin, E. G. Mishchenko, and A. Levchenko, "Density of states and magnetotransport in Weyl semimetals with long-range disorder," *Phys. Rev. B*, vol. 92, p. 174202, 2015.
(Cited on pages viii and 59.)

[86] X. Xiao, K. T. Law, and P. A. Lee, "Magnetoconductivity in Weyl semimetals: Effect of chemical potential and temperature," *Phys. Rev. B*, vol. 96, p. 165101, 2017.
(Cited on pages viii, 59, 90, and 91.)

[87] J. Behrends, F. K. Kunst, and B. Sbierski, "Transversal magnetotransport in Weyl semimetals: Exact numerical approach," *Phys. Rev. B*, vol. 97, p. 064203, 2018.
(Cited on pages viii, 59, and 136.)

[88] J. C. W. Song, G. Refael, and P. A. Lee, "Linear magnetoresistance in metals: Guiding center diffusion in a smooth random potential," *Phys. Rev. B*, vol. 92, p. 180204, 2015.
(Cited on pages viii, 60, and 97.)

[89] H. Hammar and J. Fransson, "Time-dependent spin and transport properties of a single-molecule magnet in a tunnel junction," *Phys. Rev. B*, vol. 94, p. 054311, 2016.
(Cited on pages viii and 99.)

[90] A. A. Aligia, P. Roura-Bas, and S. Florens, "Impact of capacitance and tunneling asymmetries on Coulomb blockade edges and Kondo peaks in nonequilibrium transport through molecular quantum dots," *Phys. Rev. B*, vol. 92, p. 035404, 2015.
(Cited on pages viii and 99.)

[91] G. Luo and K. Park, "Magnetic-anisotropy-induced spin blockade in a single-molecule transistor," *Phys. Rev. B*, vol. 94, p. 174412, 2016.
(Cited on pages viii and 99.)

[92] K. Hong and W. Y. Kim, "FanoResonanceDriven SpinValve Effect Using SingleMolecule Magnets," *Angewandte Chemie International Edition*, vol. 52, no. 12, pp. 3389–3393, 2013.
(Cited on pages viii, 99, 113, and 116.)

[93] A. Płomińska and I. Weymann, "Nontrivial magnetoresistive behavior of a single-wall carbon nanotube with an attached molecular magnet," *Phys. Rev. B*, vol. 92, p. 205419, 2015.
(Cited on pages viii and 99.)

[94] I. V. Krainov, J. Klier, A. P. Dmitriev, S. Klyatskaya, M. Ruben, W. Wernsdorfer, and I. V. Gornyi, "Giant Magnetoresistance in Carbon Nanotubes with Single-Molecule Magnets TbPc2," *ACS Nano*, vol. 11, no. 7, pp. 6868–6880, 2017.
(Cited on pages viii, 17, 21, 99, 113, 121, 133, and 139.)

[95] K. S. Novoselov, A. K. Geim, S. V. Morozov, D. Jiang, Y. Zhang, S. V. Dubonos, I. V. Grigorieva, and A. A. Firsov, "Electric Field Effect in Atomically Thin Carbon Films," *Science*, vol. 306, no. 5696, pp. 666–669, 2004.
(Cited on pages 1 and 3.)

[96] K. S. Novoselov, Z. Jiang, Y. Zhang, S. V. Morozov, H. L. Stormer, U. Zeitler, J. C. Maan, G. S. Boebinger, P. Kim, and A. K. Geim, "Room-Temperature Quantum Hall Effect in Graphene," *Science*, vol. 315, no. 5817, pp. 1379–1379, 2007.
(Cited on page 1.)

[97] K. S.Novoselov, A. K. Geim, S. V. Morozov, D. Jiang, M. I. Katsnelson, I. V. Grigorieva, S. V. Dubonos, and A. A. Firsov, "Two-dimensional gas of massless Dirac fermions in graphene," *Nature*, vol. 438, p. 197, 2005.
(Cited on page 1.)

[98] Y. Zhang, Y.-W. Tan, H. L. Stormer, and P. Kim, "Experimental observation of the quantum Hall effect and Berry's phase in graphene," *Nature*, vol. 438, p. 201, 2005.
(Cited on page 1.)

[99] S. L. Adler, "Axial-Vector Vertex in Spinor Electrodynamics," *Phys. Rev.*, vol. 177, pp. 2426–2438, 1969.
(Cited on pages 1 and 8.)

[100] D. S. Bethune, C. H. Kiang, M. S. de Vries, G. Gorman, R. Savoy, J. Vazquez, and R. Beyers, "Cobalt-catalysed growth of carbon nanotubes with single-atomic-layer walls," *Nature*, vol. 363, p. 605, 1993.
(Cited on page 1.)

[101] S. Iijima and T. Ichihashi, "Single-shell carbon nanotubes of 1-nm diameter," *Nature*, vol. 363, p. 603, 1993.
(Cited on page 1.)

[102] P. R. Wallace, "The Band Theory of Graphite," *Phys. Rev.*, vol. 71, pp. 622–634, 1947.
(Cited on page 3.)

[103] A. H. Castro Neto, F. Guinea, N. M. R. Peres, K. S. Novoselov, and A. K. Geim, "The electronic properties of graphene," *Rev. Mod. Phys.*, vol. 81, pp. 109–162, 2009.
(Not cited.)

[104] M. Trescher, B. Sbierski, P. W. Brouwer, and E. J. Bergholtz, "Tilted disordered Weyl semimetals," *Phys. Rev. B*, vol. 95, p. 045139, 2017.
(Cited on page 4.)

[105] I. Belopolski, D. S. Sanchez, Y. Ishida, X. Pan, P. Yu, S.-Y. Xu, G. Chang, T.-R. Chang, H. Zheng, N. Alidoust, G. Bian, M. Neupane, S.-M. Huang, C.-C. Lee, Y. Song, H. Bu , G. Wang, S. Li, G. Eda, H.-T. Jeng, T. Kondo, H. Lin, Z. Liu, F. Song, S. Shin, and M. Z. Hasan, "Discovery of a new type of topological Weyl fermion semimetal state in $Mo_xW_{1-x}Te_2$," *Nature Communications*, vol. 7, p. 13643, 2016.
(Cited on page 4.)

[106] J. Gooth, F. Menges, C. Shekhar, V. Süß, N. Kumar, Y. Sun, U. Drechsler, R. Zierold, C. Felser, and B. Gotsmann, "Electrical and Thermal Transport at the Planckian Bound of Dissipation in the Hydrodynamic Electron Fluid of WP2," *ArXiv e-prints*, June 2017.
(Cited on pages 4 and 136.)

[107] J. M. Link, B. N. Narozhny, E. I. Kiselev, and J. Schmalian, "Out-of-bounds hydrodynamics in anisotropic dirac fluids," *Phys. Rev. Lett.*, vol. 120, p. 196801, 2018.
(Cited on page 4.)

[108] A. Kobayashi, Y. Suzumura, F. Piéchon, and G. Montambaux, "Emergence of dirac electron pair in the charge-ordered state of the organic conductor α-(bedt-ttf)$_2$i$_3$," *Phys. Rev. B*, vol. 84, p. 075450, 2011.
(Cited on page 4.)

[109] C. Herring, "Accidental Degeneracy in the Energy Bands of Crystals," *Phys. Rev.*, vol. 52, pp. 365–373, 1937.
(Cited on page 4.)

[110] J. von Neumann and E. Wigner, "Über das Verhalten von Eigenwerten bei adiabatischen Prozessen," in *The Collected Works of Eugene Paul Wigner* (A. Wightman, ed.), vol. A / 1 of *The Collected Works of Eugene Paul Wigner*, pp. 294–297, Springer Berlin Heidelberg, 1993.
(Cited on page 4.)

[111] S. Murakami, "Phase transition between the quantum spin hall and insulator phases in 3d: emergence of a topological gapless phase," *New Journal of Physics*, vol. 9, no. 9, p. 356, 2007.
(Cited on page 5.)

[112] X. Wan, A. M. Turner, A. Vishwanath, and S. Y. Savrasov, "Topological semimetal and Fermi-arc surface states in the electronic structure of pyrochlore iridates," *Phys. Rev. B*, vol. 83, p. 205101, 2011.
(Cited on pages 5 and 7.)

[113] K.-Y. Yang, Y.-M. Lu, and Y. Ran, "Quantum Hall effects in a Weyl semimetal: Possible application in pyrochlore iridates," *Phys. Rev. B*, vol. 84, p. 075129, 2011.
(Cited on page 5.)

[114] P. Delplace, J. Li, and D. Carpentier, "Topological Weyl semi-metal from a lattice model," *EPL (Europhysics Letters)*, vol. 97, no. 6, p. 67004, 2012.
(Cited on page 5.)

[115] H. Nielsen and M. Ninomiya, "The Adler-Bell-Jackiw anomaly and Weyl fermions in a crystal," *Physics Letters B*, vol. 130, no. 6, pp. 389 – 396, 1983.
(Cited on page 7.)

[116] J. S. Bell and R. Jackiw, "A PCAC puzzle: $\pi^0 \to \gamma\gamma$ in the σ-model," *Il Nuovo Cimento A (1965-1970)*, vol. 60, no. 1, pp. 47–61, 1969.
(Cited on page 8.)

[117] Y. Baum, E. Berg, S. A. Parameswaran, and A. Stern, "Current at a Distance and Resonant Transparency in Weyl Semimetals," *Phys. Rev. X*, vol. 5, p. 041046, 2015.
(Cited on page 8.)

[118] Z. Wang, H. Weng, Q. Wu, X. Dai, and Z. Fang, "Three-dimensional Dirac semimetal and quantum transport in Cd_3As_2," *Phys. Rev. B*, vol. 88, p. 125427, 2013.
(Cited on page 9.)

[119] Z. Wang, Y. Sun, X.-Q. Chen, C. Franchini, G. Xu, H. Weng, X. Dai, and Z. Fang, "Dirac semimetal and topological phase transitions in A_3bi (a = Na, k, rb)," *Phys. Rev. B*, vol. 85, p. 195320, 2012.
(Cited on page 9.)

[120] M. M. Parish and P. B. Littlewood, "Non-saturating magnetoresistance in heavily disordered semiconductors," *Nature*, vol. 426, p. 162, nov 2003.
(Cited on page 10.)

[121] R. Saito, G. Dresselhaus, and M. S. Dresselhaus, *Physical properties of carbon nanotubes*. London: Imperial College Press, 1998.
(Cited on page 10.)

[122] R. Saito, M. Fujita, G. Dresselhaus, and M. S. Dresselhaus, "Electronic structure of chiral graphene tubules," *Applied Physics Letters*, vol. 60, no. 18, pp. 2204–2206, 1992.
(Cited on page 10.)

[123] A. H. Jorio, ed., *Carbon nanotubes : advanced topics in the synthesis, structure, properties and applications*. Topics in applied physics ; 111, Berlin: Springer, 2008.
(Cited on page 13.)

[124] S. T. CARR, "STRONG CORRELATION EFFECTS IN SINGLE-WALL CARBON NANOTUBES," *International Journal of Modern Physics B*, vol. 22, no. 30, pp. 5235–5260, 2008.
(Cited on page 13.)

[125] S. Thiele, R. Vincent, M. Holzmann, S. Klyatskaya, M. Ruben, F. Balestro, and W. Wernsdorfer, "Electrical Readout of Individual Nuclear Spin Trajectories in a Single-Molecule Magnet Spin Transistor," *Phys. Rev. Lett.*, vol. 111, p. 037203, 2013.
(Cited on page 15.)

[126] R. Vincent, S. Klyatskaya, M. Ruben, W. Wernsdorfer, and F. Balestro, "Electronic read-out of a single nuclear spin using a molecular spin transistor," *Nature*, vol. 488, pp. 357–360, 2012.
(Cited on page 15.)

[127] S. Thiele, F. Balestro, R. Ballou, S. Klyatskaya, M. Ruben, and W. Wernsdorfer, "Electrically driven nuclear spin resonance in single-molecule magnets," *Science*, vol. 344, no. 6188, pp. 1135–1138, 2014.
(Cited on pages 15, 114, and 115.)

[128] M. Ganzhorn, S. Klyatskaya, M. Ruben, and W. Wernsdorfer, "Strong spin-phonon coupling between a single-molecule magnet and a carbon nanotube nanoelectromechanical system," *Nature Nanotechnology*, vol. 8, pp. 165–169, 2013.
(Cited on pages 15 and 17.)

[129] M. Ganzhorn, S. Klyatskaya, M. Ruben, and W. Wernsdorfer, "Quantum Einstein-de Haas effect," *Nature Communications*, vol. 7, p. 11443, 2016.
(Cited on page 15.)

[130] L. Vitali, S. Fabris, A. M. Conte, S. Brink, M. Ruben, S. Baroni, and K. Kern, "Electronic Structure of Surface-supported Bis(phthalocyaninato) terbium(III) Single Molecular Magnets," *Nano Lett.*, vol. 8 (10), p. 3364, 2008.
(Cited on pages 15, 113, and 115.)

[131] S. Klyatskaya, J. R. Galan Mascaros, L. Bogani, F. Hennrich, M. Kappes, W. Wernsdorfer, and M. Ruben, "Anchoring of rare-earth-based single-molecule magnets on single-walled carbon nanotubes," *Journal of the American Chemical Society*, vol. 131, no. 42, pp. 15143–15151, 2009.
(Cited on page 15.)

[132] M. Lopes, A. Candini, M. Urdampilleta, A. Reserbat-Plantey, V. Bellini, S. Klyatskaya, L. Marty, M. Ruben, M. Affronte, W. Wernsdorfer, and N. Bendiab, "Surface-Enhanced Raman Signal for Terbium Single-Molecule Magnets Grafted on Graphene," *ACS Nano*, vol. 4, no. 12, pp. 7531–7537, 2010.
(Cited on pages 15, 17, and 113.)

[133] W. Liang, Marc Bockrath, and H. Park, "TRANSPORT SPECTROSCOPY OF CHEMICAL NANOSTRUCTURES: The Case of Metallic Single-Walled Carbon Nanotubes," *Annual Review of Physical Chemistry*, vol. 56, no. 1, pp. 475–490, 2005.
(Cited on page 20.)

[134] C. W. J. Beenakker, "Theory of Coulomb-blockade oscillations in the conductance of a quantum dot," *Phys. Rev. B*, vol. 44, pp. 1646–1656, 1991.
(Cited on pages 20, 102, and 131.)

[135] J. Rammer, *Quantum transport theory.* Frontiers in physics ; 99, Reading, Mass.: Perseus Books, 1998. Includes bibliographical references (p. 501-505) and index.
(Cited on pages 24 and 27.)

[136] G. D. Mahan, *Many-particle physics.* Physics of solids and liquids, New York [u.a.]: Kluwer Academic, Plenum Publ., 3. ed. ed., 2000. Includes bibliographical references and index.
(Cited on page 27.)

[137] A. A. Abrikosov, L. P. Gorkov, and I. J. Daloinskij, *Quantum field theoretical methods in statistical physics.* International series of monographs in natural philosophy ; 4, Oxford [u.a.]: Pergamon Pr., 2. ed., rev. and enlarged ed., 1965.
(Cited on page 28.)

[138] P. Streda, "Theory of quantised Hall conductivity in two dimensions," *Journal of Physics C: Solid State Physics*, vol. 15, no. 22, p. L717, 1982.
(Cited on pages 28 and 68.)

[139] I. M. Lifshitz, "Structure of the Energy Spectrum of Impurity Bands in Disordered Solid Solutions," *Sov. Phys. JETP*, vol. 17, p. 1159, 1963.
(Cited on page 33.)

[140] V. Gurarie, "Theory of avoided criticality in quantum motion in a random potential in high dimensions," *Phys. Rev. B*, vol. 96, p. 014205, 2017.
(Cited on page 33.)

[141] J. Klier, I. V. Gornyi, and A. D. Mirlin, "Critical disorder in Weyl semimetals," *to be submitted*, 2018.
(Cited on pages 34, 57, and 139.)

[142] P. Ashby and J. Carbotte, "Theory of magnetic oscillations in Weyl semimetals," *The European Physical Journal B*, vol. 87, no. 4, 2014.
(Cited on page 46.)

[143] P. M. Ostrovsky, I. V. Gornyi, and A. D. Mirlin, "Theory of anomalous quantum Hall effects in graphene," *Phys. Rev. B*, vol. 77, p. 195430, 2008.
(Cited on page 49.)

[144] F. Wegner, "Exact density of states for lowest Landau level in white noise potential superfield representation for interacting systems," *Zeitschrift für Physik B Condensed Matter*, vol. 51, no. 4, pp. 279–285, 1983.
(Cited on page 49.)

[145] E. Brézin, D. J. Gross, and C. Itzykson, "Density of states in the presence of a strong magnetic field and random impurities," *Nuclear Physics B*, vol. 235, no. 1, pp. 24 – 44, 1984.
(Cited on page 49.)

[146] P. E. C. Ashby and J. P. Carbotte, "Magneto-optical conductivity of Weyl semimetals," *Phys. Rev. B*, vol. 87, p. 245131, 2013.
(Cited on page 52.)

[147] Y. Ominato and M. Koshino, "Quantum transport in a three-dimensional Weyl electron system," *Phys. Rev. B*, vol. 89, p. 054202, 2014.
(Cited on page 52.)

[148] K. Kobayashi, T. Ohtsuki, K.-I. Imura, and I. F. Herbut, "Density of states scaling at the semimetal to metal transition in three dimensional topological insulators," *Phys. Rev. Lett.*, vol. 112, p. 016402, 2014.
(Cited on page 52.)

[149] Y. Ominato and M. Koshino, "Quantum transport in three-dimensional Weyl electron system in the presence of charged impurity scattering," *Phys. Rev. B*, vol. 91, p. 035202, 2015.
(Cited on pages 56 and 78.)

[150] P. S. Alekseev, A. P. Dmitriev, I. V. Gornyi, and V. Y. Kachorovskii, "Strong magnetoresistance of disordered graphene," *Phys. Rev. B*, vol. 87, p. 165432, 2013.
(Cited on pages 63 and 76.)

[151] U. Briskot, I. A. Dmitriev, and A. D. Mirlin, "Quantum magneto-oscillations in the ac conductivity of disordered graphene," *Phys. Rev. B*, vol. 87, p. 195432, 2013.
(Cited on pages 63 and 67.)

[152] A. A. Burkov, M. D. Hook, and L. Balents, "Topological nodal semimetals," *Phys. Rev. B*, vol. 84, p. 235126, 2011.
(Cited on page 66.)

[153] I. A. Dmitriev, A. D. Mirlin, D. G. Polyakov, and M. A. Zudov, "Nonequilibrium phenomena in high Landau levels," *Rev. Mod. Phys.*, vol. 84, pp. 1709–1763, 2012.
(Cited on page 67.)

[154] F. T. Vasko and O. E. Raichev, *Quantum kinetic theory and applications : electrons, photons, phonons*. New York, NY: Springer, 2005. Erscheint: Januar 2006. - Gb. (Pr. in Vorb.).
(Cited on page 67.)

[155] J. F. Steiner, A. V. Andreev, and D. A. Pesin, "Anomalous Hall Effect in Type-I Weyl Metals," *Phys. Rev. Lett.*, vol. 119, p. 036601, 2017.
(Cited on page 73.)

[156] V. A. Zyuzin, "Magnetotransport of Weyl semimetals due to the chiral anomaly," *Phys. Rev. B*, vol. 95, p. 245128, 2017.
(Cited on page 76.)

[157] Y. I. Rodionov and S. V. Syzranov, "Conductivity of a Weyl semimetal with donor and acceptor impurities," *Phys. Rev. B*, vol. 91, p. 195107, 2015.
(Cited on page 78.)

[158] S. S. Murzin, "Electron transport in the extreme quantum limit in applied magnetic field," *Physics Uspekhi*, vol. 43, p. 349, 2000.
(Cited on page 97.)

[159] P. S. Alekseev, A. P. Dmitriev, I. V. Gornyi, V. Y. Kachorovskii, B. N. Narozhny, M. Schütt, and M. Titov, "Magnetoresistance in Two-Component Systems," *Phys. Rev. Lett.*, vol. 114, p. 156601, 2015.
(Cited on page 97.)

[160] U. Fano, "Effects of Configuration Interaction on Intensities and Phase Shifts," *Phys. Rev.*, vol. 124, pp. 1866–1878, 1961.
(Cited on pages 99, 100, and 113.)

[161] A. Miroshnichenko, S. Flach, and Y. Kivshar, "Fano resonances in nanoscale structures," *Rev. Mod. Phys.*, vol. 82, pp. 2257–2298, 2010.
(Cited on pages 99, 100, and 113.)

[162] I. V. Krainov, J. Klier, A. P. Dmitriev, and I. V. Gornyi, "Transport in Fano-resonances," *in preparation*, 2018.
(Cited on pages 100 and 139.)

[163] J. Bardeen, "Tunnelling from a Many-Particle Point of View," *Phys. Rev. Lett.*, vol. 6, pp. 57–59, 1961.
(Cited on page 100.)

[164] J. V. Nazarov and Y. M. Blanter, *Quantum transport: Introduction to nanoscience*. Cambridge [u.a.]: Cambridge Univ. Press, 1. publ. ed., 2009.
(Cited on pages 121, 122, 127, and 185.)

[165] S. Sapmaz, P. Jarillo-Herrero, J. Kong, C. Dekker, L. P. Kouwenhoven, and H. S. J. van der Zant, "Electronic excitation spectrum of metallic carbon nanotubes," *Phys. Rev. B*, vol. 71, p. 153402, 2005.
(Cited on page 122.)

[166] W. G. van der Wiel, S. De Franceschi, J. M. Elzerman, T. Fujisawa, S. Tarucha, and L. P. Kouwenhoven, "Electron transport through double quantum dots," *Rev. Mod. Phys.*, vol. 75, pp. 1–22, 2002.
(Cited on pages 122, 124, 127, and 185.)

[167] K. A. Matveev, L. I. Glazman, and H. U. Baranger, "Coulomb blockade of tunneling through a double quantum dot," *Phys. Rev. B*, vol. 54, pp. 5637–5646, 1996.
(Cited on pages 122, 124, and 131.)

List of Figures

Notations and Conventions

Here, we present a list of notations and conventions used throughout this thesis:

- Throughout the thesis, we set $\hbar = c = k_B = 1$, where $\hbar$ is the reduced Planck's constant, k_B the Boltzmann constant, and c the velocity of light.
- If not indicated differently, the trace includes the integral over the three dimensional momenta throughout the thesis:

$$\mathrm{Tr}[...] = \int \frac{d^3\mathbf{p}}{(2\pi)^3}\mathrm{Tr}[...]$$

- The Pauli matrices are defined as:

$$\sigma_x = \tau_x = \begin{pmatrix} 0 & 1 \\ 1 & 0 \end{pmatrix}, \qquad \sigma_y = \tau_y = \begin{pmatrix} 0 & -i \\ i & 0 \end{pmatrix}, \qquad \sigma_z = \tau_z = \begin{pmatrix} 1 & 0 \\ 0 & -1 \end{pmatrix},$$

  where the symbol σ refers to the pseudospin of the system (e.g. energyband for Weyl semimetals) and τ stands for the valley/Weyl node.
- Throughout this thesis, the term "magnetic field" is used for both the magnetic field $\mathbf{H}$ and the magnetic flux density $\mathbf{B}$. In vacuum, both quantities are proportional to each other related via the vacuum permeability μ_0, $\mathbf{B} = \mu_0\mathbf{H}$. To be consistent with the available experimental data, cf. Ch. 1, we use the notation $\mathbf{H}$ in context of Weyl semimetals for magnetic and $\mathbf{B}$ in context of the carbon nanotube with side-attached molecule magnets.
- The Fermi-Dirac distribution function is denote by

$$f_T(\varepsilon) = \frac{1}{1 + \exp\left(\frac{\varepsilon - \mu}{k_B T}\right)}$$

Next, we introduce the basic notations used throughout the thesis:

$\mathcal{H}$	Hamiltonian of the considered system
G	Green's function
Σ	self-energy
Γ	imaginary part of the retarded self-energy
e	elementary charge
v_F or v	Fermi velocity
μ	chemical potential
T	temperature
ω	external frequency

l	mean free path
l_H	magnetic length $l_H = (eH/c)^{-1/2}$
N	particle density
N_{imp}	impurity concentration
$\nu(\varepsilon)$	density of states
Ω	distance between zeroth and first Landau level in Weyl semimetals $\Omega = v\sqrt{2eH/c}$
Λ	ultraviolet cutoff for Weyl semimetals
$\omega_c(\varepsilon)$	cyclotron frequency of Weyl semimetals $\omega_c(\varepsilon) = \Omega^2/(2\varepsilon)$
σ_{xx}	conductivity
σ_{xy}	Hall conductivity
σ_{xy}^{I}	normal part of the Hall conductivity
$\sigma_{xy}^{\mathrm{II}}$	anomalous part of the Hall conductivity
Δ_ρ	magnetoresistivity
t	transmission coefficient
r	reflection coefficient
$\mathcal{T}$	transmission amplitude
$\mathcal{R}$	reflection amplitude
F	free energy
$\mathcal{G}$	conductance
$\mathcal{G}_0$	conductance quantum $\mathcal{G}_0 = e^2/h$
V_{sd}	source-drain voltage
V_g	gate voltage
E_C	charging energy
U_{sd}	dimensionless source-drain voltage $U_{sd} = eV_{sd}/E_C$
U_g	dimensionless source-drain voltage $U_g = eV_g/E_C$
Re	real part
Im	imaginary part
$\mathbb{1}$	unity matrix
P	principle value
$\delta(x)$	delta-function
$\theta(x)$	Heaviside theta-function

Acronyms

1D	one dimensional
2D	two dimensional
3D	three dimensional
SCBA	self-consistent Born approximation
RG	renormalization group
LL	Landau level
MR	magnetoresistance
TMR	transversal magnetoresistance
SdHO	Shubnikov-de Haas oscillations
GMR	giant magnetoresistance
CNT	carbon nanotube
SMM	single-molecule magnet
QD	quantum dot

Appendix A

A Disorder in Weyl semimetals

In this appendix, we present the details for the calculation of disorder in Weyl semimetals. Specifically, we present a detailed treatment of pointlike impurities in absence of magnetic field including higher order corrections. Moreover, we perform the evaluation of of the self-energy in a smooth disorder potential. In addition, we discuss the shape of the Landau level broadening due to disorder for separated Landau levels.

A.1 Detailed calculation of self-energy for pointlike impurities

To introduce disorder, we calculate the disorder dressed Green's function with the self-consistently obtained self-energy. The self-consistent equation for the self-energy for arbitrary energy, ε, as obtained under momentum integration as performed in the main text, Eq. (3.11), reads

$$\Sigma^R(\varepsilon) = \beta(\varepsilon - \Sigma^R)\left[-1 + \frac{(\varepsilon - \Sigma^R)}{2\Lambda}\ln\left(\frac{\varepsilon - \Sigma^R + \Lambda}{\varepsilon - \Sigma^R - \Lambda}\right)\right]. \tag{A.1}$$

We split the self-consistent equation in real and imaginary part which leads to

$$\begin{aligned}\mathrm{Re}\Sigma^R = &-\beta(\varepsilon - \mathrm{Re}\Sigma^R) + \beta\frac{(\varepsilon - \mathrm{Re}\Sigma^R)^2 - \Gamma^2}{2\Lambda}\ln\left(\frac{\sqrt{((\varepsilon - \mathrm{Re}\Sigma^R)^2 - \Lambda^2 + \Gamma^2)^2 + (2\Gamma\Lambda)^2}}{(\varepsilon - \mathrm{Re}\Sigma^R - \Lambda)^2 + \Gamma^2}\right)\\ &+ \beta\frac{2\Gamma(\varepsilon - \mathrm{Re}\Sigma^R)}{2\Lambda}\left[\arctan\left(\frac{2\Gamma\Lambda}{(\varepsilon - \mathrm{Re}\Sigma^R)^2 - \Lambda^2 + \Gamma^2}\right) + \pi\right],\end{aligned} \tag{A.2}$$

$$\begin{aligned}\Gamma = &\beta\Gamma - \beta\frac{2\Gamma(\varepsilon - \mathrm{Re}\Sigma^R))}{2\Lambda}\ln\left(\frac{\sqrt{((\varepsilon - \mathrm{Re}\Sigma^R)^2 - \Lambda^2 + \Gamma^2)^2 + (2\Gamma\Lambda)^2}}{(\varepsilon - \mathrm{Re}\Sigma^R - \Lambda)^2 + \Gamma^2}\right)\\ &+ \beta\frac{(\varepsilon - \mathrm{Re}\Sigma^R))^2 - \Gamma^2}{2\Lambda}\left[\arctan\left(\frac{2\Gamma\Lambda}{(\varepsilon - \mathrm{Re}\Sigma^R)^2 - \Lambda^2 + \Gamma^2}\right) + \pi\right],\end{aligned} \tag{A.3}$$

where the solutions with $+\pi$ correspond to $(\varepsilon - \mathrm{Re}\Sigma^R)^2 - \Lambda^2 + \Gamma^2 < 0$ while in the opposite limit $(\varepsilon - \mathrm{Re}\Sigma^R)^2 - \Lambda^2 + \Gamma^2 > 0$ the equation is valid without any further terms. We expand the equations

now up to quadratic order in $\varepsilon - \mathrm{Re}\Sigma^R$ (under the assumption $(\varepsilon - \mathrm{Re}\Sigma)/|\Gamma^2 - \Lambda^2| < 1$) to solve the self-consistent equations. The expansion of the logarithm is

$$\ln\left(\frac{\sqrt{((\varepsilon - \mathrm{Re}\Sigma^R)^2 - \Lambda^2 + \Gamma^2)^2 + (2\Gamma\Lambda)^2}}{(\varepsilon - \mathrm{Re}\Sigma^R - \Lambda)^2 + \Gamma^2}\right) \approx \frac{2\Lambda(\varepsilon - \mathrm{Re}\Sigma^R)}{\Lambda^2 + \Gamma^2} - \frac{(5\Lambda^2 - \Gamma^2)(\varepsilon - \mathrm{Re}\Sigma^R)^2}{(\Lambda^2 + \Gamma^2)^2} \tag{A.4}$$

The expansion of the arctan leads to

$$\arctan\left(\frac{2\Gamma\Lambda}{(\varepsilon - \mathrm{Re}\Sigma^R)^2 - \Lambda^2 + \Gamma^2}\right) + \pi \approx 2\arctan\left(\frac{\Lambda}{\Gamma}\right) - \frac{2\Lambda\Gamma(\varepsilon - \mathrm{Re}\Sigma^R)^2}{(\Gamma^2 + \Lambda^2)^2}, \tag{A.5}$$

where two branches of the arctan finite $\varepsilon - \mathrm{Re}\Sigma^R$ is fully incorporated in the limit $\varepsilon - \mathrm{Re}\Sigma^R = 0$. Therefore, the expansion of the arctan holds for both cases $(\varepsilon - \mathrm{Re}\Sigma^R)^2 - \Lambda^2 + \Gamma^2 > 0$ and $(\varepsilon - \mathrm{Re}\Sigma^R)^2 - \Lambda^2 + \Gamma^2 < 0$.

The Eqs. (A.2) and (A.3) up to second order in $\varepsilon - \mathrm{Re}\Sigma^R$ read

$$\begin{aligned}\mathrm{Re}\Sigma^R = &-\beta(\varepsilon - \mathrm{Re}\Sigma^R) - \beta\frac{\Gamma^2}{\Lambda^2 + \Gamma^2}(\varepsilon - \mathrm{Re}\Sigma^R) + \beta\frac{2\Gamma}{\Lambda}\arctan(\Lambda/\Gamma)(\varepsilon - \mathrm{Re}\Sigma^R) \\ &- \beta\frac{\Gamma^2(\Gamma^2 - 5\Lambda^2)}{(\Lambda^2 + \Gamma^2)^2}(\varepsilon - \mathrm{Re}\Sigma^R)^2 \end{aligned} \tag{A.6}$$

$$\begin{aligned}\Gamma = &\beta\Gamma - \beta\frac{2(\varepsilon - \mathrm{Re}\Sigma^R)^2\Gamma}{\Lambda^2 + \Gamma^2} + \beta\frac{(\varepsilon - \mathrm{Re}\Sigma^R)^2}{\Lambda}\arctan(\Lambda/\Gamma) - \beta\frac{\Gamma^2}{\Lambda}\arctan(\Lambda/\Gamma) \\ &+ \beta\frac{\Gamma^2}{2\Lambda}\frac{2\Gamma\Lambda(\varepsilon - \mathrm{Re}\Sigma^R)^2}{(\Gamma^2 + \Lambda^2)^2}. \end{aligned} \tag{A.7}$$

The results of the numerical evaluation of these equations for $(\varepsilon - \mathrm{Re}\Sigma^R)/\Lambda < 1$ were shown in Fig. 3.1 of the main text for the imaginary part. We find that the imaginary part does not substantially dependent on the quadratic corrections in energy away from the critical regime. The critical regime is present in the region $-\sqrt{2\pi\varepsilon/\Lambda} < \beta < \sqrt{2\pi\varepsilon/\Lambda}$ nicely matching with the deviation of energy in the Fig. 3.1. Therefore, we neglect the energy dependence in the considered case of strong disorder and solve Eq. (A.2) with neglecting the energy dependence of Γ, yielding

$$\mathrm{Re}\Sigma = \varepsilon\left(1 - \frac{1}{|\bar{\beta} - 1|}\right) \tag{A.8}$$

with the renormalization of the dimensionless disorder strength according to

$$\bar{\beta} = \beta\left(1 - \frac{2\Gamma}{\Lambda}\arctan\left(\frac{\Lambda}{\Gamma}\right) + \frac{\Gamma^2}{\Lambda^2 + \Gamma^2}\right) = \beta\left(\frac{2}{\beta} - \frac{1}{1 + \Gamma^2/\Lambda^2}\right). \tag{A.9}$$

These results are used in the main text to analyze the density of states and the conductivity.

A.2 Evaluation of the self-energy for smooth disorder

With the definition of the impurity correlator for smooth disorder Eq. (3.29), we self-energy is defined as

$$\Sigma(p, \varepsilon) = \gamma\int\frac{d^3q}{(2\pi)^3}\frac{\theta(1 - b|\mathbf{p} - \mathbf{q}|)(\varepsilon - \Sigma(q, \varepsilon))}{(\varepsilon - \Sigma(q, \varepsilon))^2 - v^2q^2}. \tag{A.10}$$

The momentum integration of the angular momenta is performed by the integral

$$\Sigma(p,\varepsilon) = \gamma \int \frac{dq}{(2\pi)^2} q^2 \int_{b|p-q|}^{b\sqrt{p^2+q^2}} dy \theta(1-y) \frac{y}{b^2 pq} \frac{(\varepsilon - \Sigma(q,\varepsilon))}{(\varepsilon - \Sigma(q,\varepsilon))^2 - v^2 q^2}. \tag{A.11}$$

The restrictions of the momenta due to the θ-function lead to the following result of the integral

$$\begin{aligned}
\Sigma(p,\varepsilon) = {} & \gamma\theta(1-bp) \int_0^{1/b} \frac{dq}{(2\pi)^2} q^2 \frac{(\varepsilon - \Sigma(q,\varepsilon))}{(\varepsilon - \Sigma(q,\varepsilon))^2 - v^2 q^2} \\
& + \gamma\theta(1-bp) \int_{\sqrt{1/b^2-p^2}}^{1/b} \frac{1-b^2(p^2+q^2)}{2b^2 p} \frac{dq}{(2\pi)^2} q^2 \frac{(\varepsilon - \Sigma(q,\varepsilon))}{(\varepsilon - \Sigma(q,\varepsilon))^2 - v^2 q^2} \\
& + \gamma\theta(bp-1) \int_{p-1/b}^{p+1/b} \frac{1-b^2(p-q)^2}{2b^2 p} \frac{dq}{(2\pi)^2} q^2 \frac{(\varepsilon - \Sigma(q,\varepsilon))}{(\varepsilon - \Sigma(q,\varepsilon))^2 - v^2 q^2}
\end{aligned} \tag{A.12}$$

We separate now the terms for small and large momenta

$$\Sigma(p,\varepsilon) = \Sigma_1(p,\varepsilon)\theta(1-bp) + \Sigma_2(p,\varepsilon)\theta(bp-1) \tag{A.13}$$

The terms for small momenta $bp \ll 1$, Σ_1, is given by

$$\begin{aligned}
\Sigma_1(p,\varepsilon) = {} & \gamma \int_0^{1/b} \frac{dq}{(2\pi)^2} q^2 \frac{(\varepsilon - \Sigma_1(q,\varepsilon))}{(\varepsilon - \Sigma_1(q,\varepsilon))^2 - v^2 q^2} \\
& + \gamma \int_{\sqrt{1/b^2-p^2}}^{1/b} \frac{1-b^2(p^2+q^2)}{2b^2 p} \frac{dq}{(2\pi)^2} q^2 \frac{(\varepsilon - \Sigma_1(q,\varepsilon))}{(\varepsilon - \Sigma_1(q,\varepsilon))^2 - v^2 q^2} \\
& + \gamma \int_{1/b}^{1/b+p} \frac{1-b^2(p-q)^2}{2b^2 p} \frac{dq}{(2\pi)^2} q^2 \frac{(\varepsilon - \Sigma_2(q,\varepsilon))}{(\varepsilon - \Sigma_2(q,\varepsilon))^2 - v^2 q^2},
\end{aligned} \tag{A.14}$$

and correspondingly for large momenta $bp \gg 1$, Σ_2 reads

$$\Sigma_2(p,\varepsilon) = \gamma \int_{p-1/b}^{p+1/b} \frac{1-b^2(p-q)^2}{2b^2 p} \frac{dq}{(2\pi)^2} q^2 \frac{(\varepsilon - \Sigma_2(q,\varepsilon))}{(\varepsilon - \Sigma_2(q,\varepsilon))^2 - v^2 q^2}. \tag{A.15}$$

We first solve the equation of Σ_2 and use the result to obtain Σ_1. In the limit $bp \ll 1$ and for $\varepsilon = 0$, we approximate the integral for $\mathrm{Im}\Sigma_2 = -\Gamma_2$ as

$$\begin{aligned}
\Gamma_2 &= \frac{\gamma}{2b^2} \int_{-1/b}^{1/b} \frac{dk}{(2\pi)^2} (1 - b^2 k^2) \frac{\Gamma_2}{\Gamma_2^2 + v^2 p^2} \\
&= \frac{2}{3} \beta_b \Lambda_b \frac{\Gamma_2}{\Gamma_2^2 + v^2 p^2},
\end{aligned} \tag{A.16}$$

where

$$\beta_b = \frac{\gamma}{2\pi^2 b v^2}, \qquad \Lambda_b = \frac{v}{b}. \tag{A.17}$$

Solving the self-consistent equation leads to

$$\Gamma_2(p) = \theta\left(\frac{2}{3}\beta_b \Lambda_b^2 - v^2 p^2\right) \sqrt{\frac{2}{3}\beta_b \Lambda_b^2 - v^2 p^2}. \tag{A.18}$$

Applying this result to Eq. (A.14) provides

$$\Gamma_1(p) = \gamma \int_0^{1/b} \frac{dq}{(2\pi)^2} \frac{2\Gamma_1}{\Gamma_1^2 + v^2 q^2} + \frac{3b^3}{2} \int_{1/b}^{1/b+p} dqq \frac{1 - b^2(p-q)^2}{2b^2 p} \Gamma_2(\Lambda_b)$$
$$= \beta_b \Gamma_1 \left[1 - \frac{\Gamma_1}{\Lambda_b} \arctan\left(\frac{\Lambda_b}{\Gamma_1}\right) \right] + \frac{3}{4} bp\Lambda_b \sqrt{\frac{2}{3}\beta_b - 1}\theta\left(2\beta_b - 3\right), \tag{A.19}$$

with $\Sigma_1 = -\Gamma_1$.

A.3 Shape of the disorder broadening of separated Landau levels

In this part of the appendix we analyze the shape of the LL broadening at $\varepsilon < \varepsilon_* = \Omega(\Omega/A)^{1/5}$ (when LL are well separated). The maximum of $\Gamma(\varepsilon)$ around $\varepsilon \sim W_{n_0}$ is located at $\varepsilon \simeq W_{n_0} + \Gamma(W_{n_0})/2^{2/3}$ and is given by $\Gamma_{\text{top}} = \Gamma(W_{n_0})3^{1/2}/2^{2/3}$, where $\Gamma(W_{n_0}) = (A/2)^{2/3} W_N^{1/3}$. For brevity, we use the abbreviation $\Gamma_{n_0} = \Gamma(W_{n_0})$.

For $\varepsilon > W_{n_0} + \Gamma_{n_0}$, the peak in $\Gamma(\varepsilon)$ decreases as

$$\Gamma(\varepsilon) \simeq \Gamma_{n_0} \sqrt{\frac{2\Gamma_{n_0}}{\varepsilon - W_{n_0}}} = \frac{A}{\sqrt{2}} \sqrt{\frac{W_{n_0}}{\varepsilon - W_{n_0}}}, \tag{A.20}$$

and reaches the value of the background at $\varepsilon \sim W_{n_0} + \Omega(\Omega/\varepsilon)^3$. This value is always smaller than $W_{n_0+1} \simeq W_{n_0} + \Omega^2/(2\varepsilon)$. Thus, in the range $W_{n_0} + \Omega(\Omega/\varepsilon)^3 < \varepsilon < W_{n_0+1} - \Gamma(W_{n_0+1})$, the Landau level broadening is of the order of $A(\varepsilon/\Omega)^2$ (zero-H result).

On the left side of the peak, for $\varepsilon < W_{n_0} - \Gamma_{n_0}$, the solution of the self-consistency equation (3.70) yields

$$\Gamma(\varepsilon) \simeq 2A\frac{\varepsilon^2}{\Omega^2} \left[1 + \frac{A\sqrt{W_{n_0}}}{[2(W_{n_0} - \varepsilon)]^{3/2} - A\sqrt{W_{n_0}}} \right]. \tag{A.21}$$

which matches Γ_{n_0} at $\varepsilon \sim W_{n_0} - \Gamma_{n_0} - A\varepsilon^2/\Omega^2$. The decrease of left side of the peak from $\Gamma(\varepsilon) \sim \Gamma_{n_0}$ to $\Gamma(\varepsilon) \sim A\varepsilon^2/\Omega^2$ is thus very sharp. The Landau-level broadening for the case of well separated levels is shown schematically in Fig. A.1.

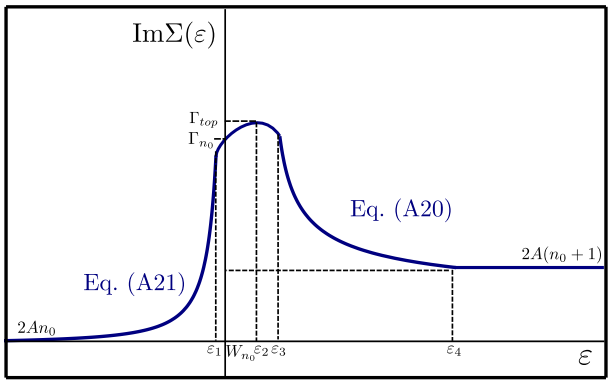

[Reprinted figure with permission from J. Klier, I. V. Gornyi, A. D. Mirlin, Physical Review B, **92**, 205113 (2015) Copyright 2015 by the American Physical Society. http://dx.doi.org/10.1103/PhysRevB.92.205113]

Figure A.1: Schematic illustration of the Landau-level broadening. At energies $\varepsilon < \varepsilon_1$, such that $|\varepsilon_1 - W_{n_0}| \sim \Gamma_{n_0}$, the broadening is given by Eq. (A.21). The maximum of $\mathrm{Im}\Sigma$ is $\Gamma_{\mathrm{top}} \simeq \Gamma_{n_0} 3^{1/2}/2^{2/3} \simeq 1.1\Gamma_{n_0}$ and is achieved at $\varepsilon_2 = W_{n_0} + \Gamma_{n_0}/2^{2/3} \simeq W_{n_0} + 0.63\Gamma_{n_0}$. At $\varepsilon_3 \sim W_{n_0} + \Gamma_{n_0}$ the tail (A.20) develops. At $\varepsilon_4 \sim W_{n_0} + \Omega(\Omega/\varepsilon)^3$ this tail reaches the background $2A(n_0 + 1)$.

B Appendix B

Transport properties in Weyl semimetals

In this appendix, we show some details of the calculation of the transport properties in Weyl semimetals. This includes the calculation of the conductivity and the normal part of the Hall conductivity away from the zeroth Landau level as well as the anomalous part of the Hall conductivity without disorder.

B.1 Conductivity for high temperatures

Here, we present details of the evaluation of the conductivity in the regime of high temperatures when many Landau levels contribute to the result. We first calculate the conductivity without current-vertex corrections and include the vertex corrections in the end of the calculation. Using the Kubo formula (4.1), the dc conductivity reads

$$\sigma_{xx}^{(0)} = \frac{e^2\Omega^2}{2\pi^2 v}\int_{-\infty}^{\infty}\frac{d\varepsilon}{4T\cosh^2\left(\frac{\varepsilon}{2T}\right)}\sum_{n=0}Q_n(\varepsilon), \tag{B.1}$$

$$Q_n(\varepsilon) = \int_{-\infty}^{\infty}\frac{dz}{2\pi}\,\mathrm{Im}G_{11}^R(\varepsilon,n,p_z)\mathrm{Im}G_{22}^R(\varepsilon,n,p_z). \tag{B.2}$$

With the Green's functions $\mathrm{Im}G_{11}^R$ and $\mathrm{Im}G_{22}^R$, Eqs. (4.10) and (4.11), respectively, Eq. (B.2) results in

$$\begin{aligned} Q_n(\varepsilon) &= \Gamma^2\int_{-\infty}^{\infty}\frac{dz}{2\pi}\,\frac{(\varepsilon^2+z^2+\Omega^2n+\Gamma^2+2\varepsilon z)(\varepsilon^2+z^2+\Omega^2(n+1)+\Gamma^2+2\varepsilon z)-4\varepsilon^2z^2}{[(\varepsilon^2-z^2-\Omega^2n-\Gamma^2)^2+4\varepsilon^2\Gamma^2][(\varepsilon^2-z^2-\Omega^2(n+1)-\Gamma^2)^2+4\varepsilon^2\Gamma^2]} \\ &= Q_n^{(\mathrm{I})}+Q_n^{(\mathrm{II})}, \end{aligned} \tag{B.3}$$

where (with $W_n^2 = \Omega^2 n + \Gamma^2$)

$$Q_n^{(\mathrm{I})} = \Gamma \frac{2\Gamma^2[\Omega^2 - 4\varepsilon^2(2n+1)] + [4\Gamma^2 + \Omega^2(2n+1)]\left[\varepsilon^2 - W_n^2 + \sqrt{(\varepsilon^2 - W_n^2)^2 + 4\varepsilon^2\Gamma^2}\right]}{2[(4\varepsilon\Gamma)^2 + \Omega^4]\sqrt{(\varepsilon^2 - W_n^2)^2 + 4\varepsilon^2\Gamma^2}\sqrt{\varepsilon^2 - W_n^2 + \sqrt{(\varepsilon^2 - W_n^2)^2 + 4\varepsilon^2\Gamma^2}}}, \quad \text{(B.4)}$$

$$Q_n^{(\mathrm{II})} = \Gamma \frac{-2\Gamma^2[\Omega^2 - 4\varepsilon^2(2n+1)] + [4\Gamma^2 + \Omega^2(2n+1)]\left[\varepsilon^2 - W_{n+1}^2 + \sqrt{(\varepsilon^2 - W_{n+1}^2)^2 + 4\varepsilon^2\Gamma^2}\right]}{2[(4\varepsilon\Gamma)^2 + \Omega^4]\sqrt{(\varepsilon^2 - W_{n+1}^2)^2 + 4\varepsilon^2\Gamma^2}\sqrt{\varepsilon^2 - W_{n+1}^2 + \sqrt{(\varepsilon^2 - W_{n+1}^2)^2 + 4\varepsilon^2\Gamma^2}}}. \quad \text{(B.5)}$$

Since the term $Q_n^{(\mathrm{II})}$ is dominated by $\varepsilon \sim W_{n+1}$, it is convenient to shift the summation over n for this term. For definiteness, we use the hard cut-off for the summation over Landau levels, such that the highest Landau level involved in the summation is $(N_{\max} - 1) + 1 = N_{\max}$ from $Q^{(\mathrm{II})}$:

$$\sum_{n=0}^{N_{\max}-1} Q_n = Q_0^{(\mathrm{I})} + \sum_{n=1}^{N_{\max}-1}\left[Q_n^{(\mathrm{I})} + Q_{n-1}^{(\mathrm{II})}\right] + Q_{N_{\max}-1}^{(\mathrm{II})}, \quad \text{(B.6)}$$

where

$$Q_0^{(\mathrm{I})} = \frac{\Gamma\Omega^2}{2[(4\varepsilon\Gamma)^2 + \Omega^4]}, \quad \text{(B.7)}$$

$$Q_{N_{\max}-1}^{(\mathrm{II})} \simeq \frac{4\varepsilon^2\Gamma^2\sqrt{N_{\max}}}{\Omega[(4\varepsilon\Gamma)^2 + \Omega^4]}, \quad \text{(B.8)}$$

and we write

$$Q_n^{(\mathrm{I})} + Q_{n-1}^{(\mathrm{II})} = \frac{\sqrt{2}\Gamma\varepsilon}{(4\varepsilon\Gamma)^2 + \Omega^4}\, q_n, \quad \text{(B.9)}$$

$$q_n = q_{n,1} - q_{n,2}. \quad \text{(B.10)}$$

Here we have split q_n into two parts related to the asymmetry of each Landau level:

$$q_{n,1} = \Omega^2 n \frac{\sqrt{\varepsilon^2 - W_n^2 + \sqrt{(\varepsilon^2 - W_n^2)^2 + 4\varepsilon^2\Gamma^2}}}{\sqrt{(\varepsilon^2 - W_n^2)^2 + 4\varepsilon^2\Gamma^2}}, \quad \text{(B.11)}$$

$$q_{n,2} = \frac{\Gamma}{\varepsilon}\left[\varepsilon^2 + W_n^2 - \sqrt{(\varepsilon^2 - W_n^2)^2 + 4\varepsilon^2\Gamma^2}\right]\frac{\sqrt{W_n^2 - \varepsilon^2 + \sqrt{(\varepsilon^2 - W_n^2)^2 + 4\varepsilon^2\Gamma^2}}}{\sqrt{(\varepsilon^2 - W_n^2)^2 + 4\varepsilon^2\Gamma^2}}. \quad \text{(B.12)}$$

For weak disorder, $\Gamma(\varepsilon) \ll \varepsilon$, and $q_{n,1} \gg q_{n,2}$. We note that these functions have resonant structure and take their maximal values when

$$\varepsilon^2 \simeq \Omega^2 n + \frac{2}{\sqrt{3}}\Gamma\Omega\sqrt{n}. \quad \text{(B.13)}$$

Comparing Eqs. (B.11) and (B.12) at resonances, we see that the maximal value of q_n is dominated by $q_{n,1}$:

$$q_{n,1} \simeq \frac{\varepsilon^{3/2}}{\sqrt{2}\Gamma^{1/2}}, \qquad q_{n,2} \simeq \sqrt{2}\Gamma^{1/2}\varepsilon^{1/2} \ll q_{n,1}. \quad \text{(B.14)}$$

One can check that $q_{n,1} \gg q_{n,2}$ in the whole range of energies $W_n < \varepsilon < W_{n+1}$. Therefore, in what follows we will disregard the contribution of $q_{n,2}$, using $q_n \simeq q_{n,1}$. Comparing Eq. (B.11) and (3.63), we find [see also Eq. (3.70)]:

$$q_n \simeq \Omega^2 n \frac{\sqrt{2}\Gamma^{(n)}(\varepsilon)}{A\varepsilon} = \Omega^2 n\sqrt{2}\left(\frac{\Gamma}{A\varepsilon} - \frac{2\varepsilon}{\Omega^2}\right) \tag{B.15}$$

Let us now consider energy ε located between the Landau levels n_0 and n_0+1. We split the sum over Landau levels in Eq. (B.6) as follows:

$$\begin{aligned}\sum_{n=1}^{N_{\max}-1}\left[Q_n^{(\mathrm{I})} + Q_{n-1}^{(\mathrm{II})}\right] &= \frac{\sqrt{2}\Gamma\varepsilon}{(4\varepsilon\Gamma)^2+\Omega^4}\sum_{n=1}^{N_{\max}-1} q_n \\ &= \frac{\sqrt{2}\Gamma\varepsilon}{(4\varepsilon\Gamma)^2+\Omega^4}\left\{\sum_{n=1}^{n_0-1} q_n + q_{n_0} + q_{n_0+1} + \sum_{n=n_0+2}^{N_{\max}-1} q_n\right\}. \end{aligned} \tag{B.16}$$

When the Landau-level broadening is smaller than the distance between the neighboring levels, $W_{n_0} - W_{n_0+1} \sim \Omega^2/\varepsilon \gg \Gamma(\varepsilon)$, i.e., $\varepsilon \ll \varepsilon_{**} = \Omega(\Omega/A)^{1/3}$, we can neglect Γ in the contributions of all Landau levels with $n < n_0$. Replacing the sums by integrals, we find

$$\sum_{n=1}^{n_0-1} q_n \simeq \sum_{n=1}^{n_0-1}\frac{\sqrt{2}\Omega^2 n}{\sqrt{\varepsilon^2-\Omega^2 n}} \simeq \frac{4\sqrt{2}}{3}\frac{\varepsilon^3}{\Omega^2}. \tag{B.17}$$

This contribution to Eq. (B.6) is by a factor ε^4/Ω^4 larger than the $n=0$ term, Eq. (B.7), so the latter can be neglected. For $n > n_0+1$ we expand q_n in Γ and get

$$\begin{aligned}\sum_{n=n_0+2}^{N_{\max}-1} q_n &\simeq \sum_{n=n_0+2}^{N_{\max}-1}\frac{\sqrt{2}\Gamma(2\varepsilon^2-\Omega^2 n)}{(\Omega^2 n-\varepsilon^2)^{3/2}} \\ &\simeq -\frac{2\sqrt{2}\varepsilon\Gamma}{\Omega}\sqrt{N_{\max}} + \frac{2\sqrt{2}\varepsilon^3\Gamma}{\Omega^2\sqrt{\Omega^2(n_0+2)-\varepsilon^2}}. \end{aligned} \tag{B.18}$$

The term proportional to $\sqrt{N_{\max}}$ exactly cancels the contribution of Eq. (B.8) in the sum over n, Eq. (B.6). The second term here is of the order of Γ/Ω [remember that $\Omega^2 n_0 < \varepsilon^2 < \Omega^2(n_0+1)$] and can be neglected for $\varepsilon < \Omega(\Omega/A)^{1/2}$ compared to the contribution of $n < n_0$. Then Eq. (B.6) takes the form

$$\sum_{n=0} Q_n \simeq \frac{2\Gamma\varepsilon^4}{\Omega^2[(4\varepsilon\Gamma)^2+\Omega^4]}\left[\frac{4}{3} + \frac{\Omega^2}{\sqrt{2}\varepsilon^3}\left(q_{n_0}+q_{n_0+1}\right)\right]. \tag{B.19}$$

According to Eq. (B.15), the second term in Eq. (B.19) is given by

$$\frac{\Omega^2}{\sqrt{2}\varepsilon^3}\left(q_{n_0}+q_{n_0+1}\right) \sim \frac{\Omega^2}{\varepsilon}\left(\frac{\Gamma(\varepsilon)}{A\varepsilon} - \frac{2\varepsilon}{\Omega^2}\right). \tag{B.20}$$

This term may dominate the sum in Eq. (B.19) only for $\varepsilon < \varepsilon_* \sim \Omega(\Omega/A)^{1/5}$ and when ε is located close to a Landau level center. We will return to this case later and first analyze the opposite (simpler) regime of $\varepsilon > \varepsilon_*$.

For $\varepsilon > \varepsilon_{**} = \Omega(\Omega/A)^{1/3}$, the level broadening in q_n is larger than the distance $|\varepsilon - W_n|$ for Landau levels sufficiently close to n_0:

$$\begin{aligned} &\Gamma_{n_0} > |\varepsilon - W_n| \sim |W_{n_0} - W_n| \\ &\Rightarrow \quad |n_0 - n| < n_{0\Gamma} \equiv \frac{\sqrt{n_0}\Gamma_{n_0}}{\Omega} \sim \frac{A}{\Omega}\left(\frac{\varepsilon}{\Omega}\right)^3. \end{aligned} \tag{B.21}$$

For such values of n we can neglect $\varepsilon^2 - W_n^2$ as compared to $\varepsilon\Gamma$ in Eq. (B.11):

$$q_n = \frac{\Omega^2 n}{\sqrt{2\varepsilon\Gamma}}. \tag{B.22}$$

In this case, the sum over n in Eq. (B.16) is written as

$$\sum_{n=1}^{N_{\max}-1} q_n = \left\{ \sum_{n=1}^{N-n_{0\Gamma}-1} + \sum_{n=n_0-n_{0\Gamma}}^{n_0+n_{0\Gamma}} + \sum_{n=n_0+n_{0\Gamma}+1}^{N_{\max}-1} \right\} q_n,$$

$$\sum_{n=1}^{n_0-n_{0\Gamma}-1} q_n \simeq \frac{4\sqrt{2}}{3}\frac{\varepsilon^3}{\Omega^2}\left[1 - \frac{3}{2}\sqrt{\frac{n_{0\Gamma}}{n_0}}\right], \tag{B.23}$$

$$\sum_{n=n_0-n_{0\Gamma}}^{n_0+n_{0\Gamma}} q_n \simeq n_{0\Gamma}^2 \frac{\Omega^2}{\sqrt{2\varepsilon\Gamma}} = \frac{\varepsilon^{3/2}\Gamma^{3/2}}{\Omega^2}, \tag{B.24}$$

$$\sum_{n=n_0+n_{0\Gamma}+1}^{N_{\max}-1} q_n \simeq -\frac{2\sqrt{2}\varepsilon\Gamma}{\Omega}\sqrt{N_{\max}} + \frac{2\sqrt{2}\varepsilon^2\Gamma}{\Omega^2}. \tag{B.25}$$

We see that for $\varepsilon > \varepsilon_{**}$ again the first term ($n < n_0 - n_{0\Gamma}$) dominates, yielding the same result as for $\varepsilon < \varepsilon_{**}$ (clearly, $n_{0\Gamma} \ll n_0$, in view of $\Gamma(\varepsilon) \ll \varepsilon$). Including the vertex correction calculated in Appendix C.2, we arrive at Eqs. (4.12) and (4.17) of the main text.

Let us now return to the case of lower temperatures, $\Omega < T < \varepsilon_* \sim \Omega(\Omega/A)^{1/5}$. In this case, the contribution of the Landau level n_0 closest to the energy ε in the sum in Eq. (B.19) should be analyzed. In order to estimate this contribution, we replace the integral over energy in Eq. (B.1) by a sum over regions of width Γ_{n_0} around Landau levels, use Eq. (B.15), replace ε by W_{n_0}, and replace $\Gamma^{(n_0)}(\varepsilon)$ there by its maximal value $\Gamma^{(n_0)}(W_{n_0}) \equiv \Gamma_{n_0} \sim A^{2/3}\Omega^{1/3}n_0^{1/6}$. As a result, we get

$$\sigma_{xx}^{(n_0)} \sim \frac{e^2\Omega^2}{ATv} \sum_{n_0 < (T/\Omega)^2} \Gamma_{n_0} \frac{\Gamma_{n_0}^2 W_{n_0}^2}{(4W_{n_0}\Gamma_{n_0})^2 + \Omega^4} \tag{B.26}$$

$$\sim \frac{e^2\gamma T^4}{\Omega^2 v^4} \propto \frac{\gamma T^4}{H} \tag{B.27}$$

In addition to this contribution, there is a contribution of the tail at $\Gamma_{n_0} < \varepsilon - W_{n_0} < \Omega(\Omega/W_{n_0})^3$, see Fig. A.1 and Eq. (A.20). The integral over $|\varepsilon - W_{n_0}|$ is logarithmic since $\Gamma^2(\varepsilon)$ decays as $(\varepsilon - W_{n_0})^{-1}$ in this range and thus enhances the result (B.27) by a logarithmic factor. We see that the contribution to the conductivity of the Landau level n_0 is smaller than the semiclassical contribution, Eq. (4.18), by factor $\Omega^2/T^2 \ll 1$ (up to the logarithm) and can be neglected.

B.2 Normal part of the Hall conductivity for large chemical potential

In this part of the appendix, we present the details for the calculation of the normal contribution to the Hall conductivity σ_{xy}^{I} for large chemical potential, $\mu \gg \Omega$. Starting from Eq. (4.35), we use the Green's functions for LLs with $n > 0$. The resulting formula is

$$\sigma_{xy}^{\mathrm{I}} = -\frac{2e^2\Omega^2}{(2\pi)^2 v}\int d\varepsilon \frac{df_T(\varepsilon)}{d\varepsilon}\int \frac{dz}{2\pi}\sum_n \frac{\varepsilon\Gamma\Omega^2}{(\varepsilon^2 - z^2 - \Omega^2 n - \Gamma^2)^2 + 4\varepsilon^2\Gamma^2} \times \frac{z^2 - \Gamma^2 - \varepsilon^2}{(\varepsilon^2 - z^2 - \Omega^2(n+1) - \Gamma^2)^2 + 4\varepsilon^2\Gamma^2} \tag{B.28}$$

The evaluation of the integral over $z = vp_z$ leads to

$$\sigma_{xy}^{\mathrm{I}} = -\frac{2e^2\Omega^2}{(2\pi)^2 v}\int d\varepsilon \frac{df_T(\varepsilon)}{d\varepsilon}\sum_n \mathrm{Re}\left\{\frac{1}{\Omega^2 + 4i\varepsilon\Gamma}\left[\frac{-\Omega^2 n - 2\Gamma^2 + 2i\varepsilon\Gamma}{\sqrt{\varepsilon^2 - \Omega^2 n - \Gamma^2 + 2i\varepsilon\Gamma}} + \frac{-\Omega^2(n+1) - 2\Gamma^2 + 2i\varepsilon\Gamma}{\sqrt{\varepsilon^2 - \Omega^2(n+1) - \Gamma^2 + 2i\varepsilon\Gamma}}\right]\right\}. \tag{B.29}$$

To simplify the equation, we can shift the sum over n for the terms containing $n+1$ by -1 and evaluate the real part of the equation. The Hall conductivity σ_{xy}^{I} can be then written as

$$\sigma_{xy}^{\mathrm{I}} = -\frac{2e^2\Omega^2}{(2\pi)^2 v}\int d\varepsilon \frac{df_T(\varepsilon)}{d\varepsilon}\left[\frac{-(2\Omega^2\Gamma^2 - 8\varepsilon^2\Gamma^2)}{\Omega^4(+4\varepsilon\Gamma)^2}\frac{\varepsilon - \Gamma}{\varepsilon^2 + \Gamma^2} - \sum_{n=1}^{N_{\max}-1}\frac{\Omega^4 n + 2\Omega^2\Gamma^2}{\Omega^4 + (4\varepsilon\Gamma)^2}\frac{\sqrt{\varepsilon^2 - \Omega^2 n - \Gamma^2 + \sqrt{(\varepsilon^2 - \Omega^2 - \Gamma^2)^2 + 4\varepsilon^2\Gamma^2}}}{\sqrt{2}\sqrt{(\varepsilon^2 - \Omega^2 n - \Gamma^2)^2 + 4\varepsilon^2\Gamma^2}} + \frac{4\varepsilon\Gamma\Omega\sqrt{N_{\max}}}{\Omega^4 + (4\varepsilon\Gamma)^2}\right]. \tag{B.30}$$

We can split the sum over n in three parts: $n < n_0$, n_0, n_0+1 and $n > n_0+1$, where n_0 is the resonant energy. For the part of $n < n_0$, we can neglect Γ and for $n > n_0 + 1$ we can expand in Γ. After some algebra, the Hall conductivity reads

$$\sigma_{xy}^{\mathrm{I}} = \frac{2e^2\Omega^2}{(2\pi)^2 v}\int d\varepsilon \frac{df_T(\varepsilon)}{d\varepsilon}\left[\frac{(2\Omega^2\Gamma^2 - 8\varepsilon^2\Gamma^2)}{\Omega^4(+4\varepsilon\Gamma)^2}\frac{\varepsilon - \Gamma}{\varepsilon^2 + \Gamma^2} + \frac{2}{\Omega^4 + (4\varepsilon\Gamma)^2}\sum_{n=1}^{n_0-1}\frac{n}{\sqrt{\varepsilon^2 - \Omega^2 n}} + \frac{2\Omega^4 n_0}{\Omega^4 + (4\varepsilon\Gamma)^2}\frac{\Gamma^{(n_0)}}{A\varepsilon} + \frac{2\Omega^4(n_0+1)}{\Omega^4 + (4\varepsilon\Gamma)^2}\frac{\Gamma^{(n_0+1)}}{A\varepsilon} + \sum_{n=n_0+2}^{N_{\max}-1}\frac{2\Omega^4 n}{\Omega^4 + (4\varepsilon\Gamma)^2}\frac{2\varepsilon\Gamma}{\sqrt{\Omega^2 n - \varepsilon^2}^3} - \frac{4\varepsilon\Gamma\Omega\sqrt{N_{\max}}}{\Omega^4 + (4\varepsilon\Gamma)^2}\right]. \tag{B.31}$$

Here $\Gamma^{(n_0)}$ and $\Gamma^{(n_0+1)}$ are defined via the self-consistent equation $\Gamma = \sum_n \Gamma^n$. By evaluating the second sum, we see that term of the upper limit $N_{\max} - 1$ cancels with the last term of Eq.(B.31). Furthermore, the contribution of the lower limit $n_0 + 2$ of this sum and the term from the $n = 0$ are

parametrically small and can be neglected. The normal contribution to the Hall conductivity then reads

$$\sigma_{xy}^{\mathrm{I}} = \frac{2e^2\Omega^2}{(2\pi)^2 v}\int d\varepsilon \frac{df(\varepsilon)}{d\varepsilon}\left[\frac{4}{3}\frac{\varepsilon^3}{\Omega^4+(4\varepsilon\Gamma)^2}+\frac{\Omega^2\varepsilon^2}{\Omega^4+(4\varepsilon\Gamma)^2}\left(\frac{\Gamma}{A\varepsilon}-\frac{2\varepsilon}{\Omega^2}\right)\right]. \tag{B.32}$$

This expression is further evaluated in the main text, where we consider the different regimes of LL broadening.

B.3 Anomalous part of the Hall conductivity

To evaluate the anomalous part of Hall conductivity, we calculate the particle density by integrating the density of states up to the ultraviolet cutoff:

$$N(\mu,H) = \frac{\Omega^2}{8\pi^2 v^3}\int_0^{\Lambda} d\varepsilon \left[f_T(\varepsilon-\mu)-f_T(\varepsilon+\mu)+1\right]\left(1+2\sum_{n=1}^{\varepsilon^2/\Omega^2}\frac{\varepsilon}{\sqrt{\varepsilon^2-\Omega^2 n}}\right), \tag{B.33}$$

where $f_T(\varepsilon\pm\mu) = (\exp((\varepsilon\pm\mu)/2T)+1)^{-1}$ denotes the Fermi-Dirac distribution function. Taking the derivative with respect to H leads to the following anomalous Hall conductivity:

$$\begin{aligned}\sigma_{xy}^{\mathrm{II}} =& \frac{e^2}{4\pi^2 v}\left\{\int_0^{\infty} d\varepsilon \left[f_T(\varepsilon-\mu)-f_T(\varepsilon+\mu)+1\right]\left(1+2\sum_{n=1}^{\varepsilon^2/\Omega^2}\frac{\varepsilon}{\sqrt{\varepsilon^2-\Omega^2 n}}\right)\right.\\ &\left.+2\sum_{n=1}^{\Lambda^2/\Omega^2}\frac{\Omega^2 n}{\sqrt{\Lambda^2-\Omega^2 n}}-2\int_0^{\infty}d\varepsilon\left[\frac{df_T(\varepsilon-\mu)}{d\varepsilon}-\frac{df_T(\varepsilon+\mu)}{d\varepsilon}\right]\sum_{n=1}^{\varepsilon^2/\Omega^2}\frac{\Omega^2 n}{\sqrt{\varepsilon^2-\Omega^2 n}}\right\}.\end{aligned} \tag{B.34}$$

The last term of Eq. (B.34) differs from the normal Hall conductivity Eq. (4.40) only by the sign. The anomalous Hall conductivity reads

$$\sigma_{xy}^{\mathrm{II}} = \frac{e^2}{4\pi^2 v}\left\{\mu+2\sum_{n=1}^{\mu^2/\Omega^2}\sqrt{\mu^2-\Omega^2 n}+\Lambda+2\sum_{n=1}^{\Lambda^2/\Omega^2}\sqrt{\Lambda^2-\Omega^2 n}+2\sum_{n=1}^{\Lambda^2/\Omega^2}\frac{\Omega^2 n}{\sqrt{\Lambda^2-\Omega^2 n}}\right\}-\sigma_{xy}^{\mathrm{I}}. \tag{B.35}$$

Employing the Euler Maclaurin formula to Eq. (B.35) leads to a cancellation of the terms that depend on the ultraviolet cutoff Λ. The remaining terms are

$$\sigma_{xy}^{\mathrm{II}} = \frac{e^2}{4\pi^2 v}\left\{\mu+2\sum_{n=1}^{\mu^2/\Omega^2}\sqrt{\mu^2-\Omega^2 n}\right\}-\sigma_{xy}^{\mathrm{I}}, \tag{B.36}$$

which corresponds to Eq. (4.42).

Appendix C

Vertex corrections to the conductivity in Weyl semimetals

This appendix is devoted to the calculation of the vertex corrections to the conductivity in Weyl semimetals. The following diagram describes the dressing of a current vertex by disorder lines and is mathematically expressed for pointlike impurities as:

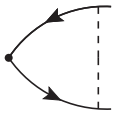

$$= ev\gamma \int \frac{dp_x}{2\pi} \int \frac{dp_y}{2\pi} \int \frac{dp_z}{2\pi} \hat{G}^A(\varepsilon+\omega; p_x, p_y, p_z)\sigma_x \hat{G}^R(\varepsilon; p_x, p_y, p_z). \tag{C.1}$$

This appendix is devoted to both the absence and the presence of a magnetic field. In absence of magnetic field, we calculate the vertex corrections arbitrary disorder and for finite external frequency in contrast to Ref. [81]. In the presence of magnetic field, we distinguish between the zeroth Landau level and higher Landau levels in the limit of zero external frequency.

C.1 Vertex corrections in absence of magnetic field

In the absence of magnetic field, there exists in general also a contribution of the two retarded Green's functions in the conductivity and thus the corresponding vertex correction is required. Using the Green's function in absence of magnetic field, Eq. (3.8), the retarded-retarded correction to the velocity for a single impurity line is given by

$$\begin{aligned} v_x^{\mathrm{RR}}(\varepsilon,\omega) &= v\gamma \int \frac{d^3p}{(2\pi)^3} G^R(\varepsilon+\omega,\mathbf{p}) G^R(\varepsilon,\mathbf{p}) \\ &= v\gamma \int \frac{d^3p}{(2\pi)^3} \frac{\varepsilon+\omega-\Sigma^R(\varepsilon+\omega)}{(\varepsilon+\omega-\Sigma^R(\varepsilon+\omega))^2+v^2p^2} \frac{\varepsilon-\Sigma^R(\varepsilon)}{(\varepsilon-\Sigma^R(\varepsilon))^2+v^2p^2}. \end{aligned} \tag{C.2}$$

Solving the integral, the retarded-retarded vertex correction can be expressed as

$$v_x^{\mathrm{RR}} = v\left[\frac{\Big(\varepsilon+\omega-\Sigma^R(\varepsilon+\omega)\Big)\Big(\varepsilon-\Sigma^R(\varepsilon)\Big)}{\Big(\varepsilon-\Sigma^R(\varepsilon)\Big)^2-\Big(\varepsilon+\omega-\Sigma^R(\varepsilon+\omega)\Big)^2}\left(\frac{\Sigma^R(\varepsilon+\omega)}{\varepsilon+\omega-\Sigma^R(\varepsilon+\omega)}-\frac{\Sigma^R(\varepsilon)}{\varepsilon-\Sigma^R(\varepsilon)}\right)\right.$$
$$+\frac{1}{6}\left(\frac{\Sigma^R(\varepsilon+\omega)}{\varepsilon+\omega-\Sigma^R(\varepsilon+\omega)}+\frac{\Sigma^R(\varepsilon)}{\varepsilon-\Sigma^R(\varepsilon)}\right)$$
$$\left.-\frac{1}{6}\frac{\Big(\varepsilon+\omega-\Sigma^R(\varepsilon+\omega)\Big)^2+\Big(\varepsilon-\Sigma^R(\varepsilon)\Big)^2}{\Big(\varepsilon-\Sigma^R(\varepsilon)\Big)^2-\Big(\varepsilon+\omega-\Sigma^R(\varepsilon+\omega)\Big)^2}\left(\frac{\Sigma^R(\varepsilon+\omega)}{\varepsilon+\omega-\Sigma^R(\varepsilon+\omega)}-\frac{\Sigma^R(\varepsilon)}{\varepsilon-\Sigma^R(\varepsilon)}\right)\right]. \tag{C.3}$$

The retarded-advanced correction to the velocity for a single impurity line is given by the following integral:

$$\begin{aligned} v_x^{\mathrm{RA}}(\varepsilon,\omega) &= v\gamma\int\frac{d^3p}{(2\pi)^3}G^R(\varepsilon+\omega,\mathbf{p})G^A(\varepsilon,\mathbf{p}) \\ &= v\gamma\int\frac{d^3p}{(2\pi)^3}\frac{\varepsilon+\omega-\Sigma^R(\varepsilon+\omega)}{(\varepsilon+\omega-\Sigma^R(\varepsilon+\omega))^2+v^2p^2}\frac{\varepsilon-\Sigma^A(\varepsilon)}{(\varepsilon-\Sigma^A(\varepsilon))^2+v^2p^2}. \end{aligned} \tag{C.4}$$

In full analogy to the retarded-retarded correction, we obtain the retarded-advanced correction, reading

$$v_x^{\mathrm{RA}} = v\left[\frac{\Big(\varepsilon+\omega-\Sigma^R(\varepsilon+\omega)\Big)\Big(\varepsilon-\Sigma^A(\varepsilon)\Big)}{\Big(\varepsilon-\Sigma^A(\varepsilon)\Big)^2-\Big(\varepsilon+\omega-\Sigma^R(\varepsilon+\omega)\Big)^2}\left(\frac{\Sigma^R(\varepsilon+\omega)}{\varepsilon+\omega-\Sigma^R(\varepsilon+\omega)}-\frac{\Sigma^A(\varepsilon)}{\varepsilon-\Sigma^A(\varepsilon)}\right)\right.$$
$$+\frac{1}{6}\left(\frac{\Sigma^R(\varepsilon+\omega)}{\varepsilon+\omega-\Sigma^R(\varepsilon+\omega)}+\frac{\Sigma^A(\varepsilon)}{\varepsilon-\Sigma^A(\varepsilon)}\right)$$
$$\left.-\frac{1}{6}\frac{\Big(\varepsilon+\omega-\Sigma^R(\varepsilon+\omega)\Big)^2+\Big(\varepsilon-\Sigma^A(\varepsilon)\Big)^2}{\Big(\varepsilon-\Sigma^A(\varepsilon)\Big)^2-\Big(\varepsilon+\omega-\Sigma^R(\varepsilon+\omega)\Big)^2}\left(\frac{\Sigma^R(\varepsilon+\omega)}{\varepsilon+\omega-\Sigma^R(\varepsilon+\omega)}-\frac{\Sigma^A(\varepsilon)}{\varepsilon-\Sigma^A(\varepsilon)}\right)\right] \tag{C.5}$$

After some algebra the vertex corrections can be expressed as

$$v_x^{\mathrm{RR}}(\varepsilon,\omega) = v\frac{\Sigma^R_{\varepsilon+\omega}(\varepsilon-\Sigma^R_\varepsilon)-\Sigma^R_\varepsilon(\varepsilon+\omega-\Sigma^R_{\varepsilon+\omega})+\frac{1}{3}\left[(\varepsilon-\Sigma^R_\varepsilon)\Sigma^R_\varepsilon-(\varepsilon+\omega-\Sigma^R_{\varepsilon+\omega})\Sigma^R_{\varepsilon+\omega}\right]}{(\varepsilon-\Sigma^R_\varepsilon)^2-(\varepsilon+\omega-\Sigma^R_{\varepsilon+\omega})^2}, \tag{C.6}$$

$$v_x^{\mathrm{RA}}(\varepsilon,\omega) = v\frac{\Sigma^R_{\varepsilon+\omega}(\varepsilon-\Sigma^A_\varepsilon)-\Sigma^A_\varepsilon(\varepsilon+\omega-\Sigma^R_{\varepsilon+\omega})+\frac{1}{3}\left[(\varepsilon-\Sigma^A_\varepsilon)\Sigma^A_\varepsilon-(\varepsilon+\omega-\Sigma^R_{\varepsilon+\omega})\Sigma^R_{\varepsilon+\omega}\right]}{(\varepsilon-\Sigma^A_\varepsilon)^2-(\varepsilon+\omega-\Sigma^R_{\varepsilon+\omega})^2}, \tag{C.7}$$

where the subscript marks the dependence of external frequency and energy of the self-energy. In the main text, we use these corrections to calculate the conductivity via the summation over the ladder of

impurity lines

$$V_0^{\rm tr}(\varepsilon)\left[1-\frac{v_x^{\rm RR/RA}}{v}\right]^{-1}. \tag{C.8}$$

We can show that the above calculated vertex corrections are in full agreement with the vertex corrections in the dc limit for weak disorder in Ref. [81]. For weak disorder, we use Eq. (3.16) for the self-energy. In the dc limit, we obtain

$$v_x^{\rm RR}=-\frac{v\beta}{3}, \tag{C.9}$$

$$v_x^{\rm RA}=\frac{v(1-2\beta)}{3}. \tag{C.10}$$

This corresponds to the result $v_x^{\rm RR}=0$ and $v_x^{\rm RA}=v/3$ of Ref. [81], where the limit $\beta\to 0$ was discussed.

C.2 Vertex corrections in presence of magnetic field

In presence of a finite magnetic field, the diagonal elements for the resulting matrix of retarded and advanced Green's functions vanish after the integration over x, x' and p_y because of the orthogonality of the Hermite functions. The off-diagonal elements $v_{x,12}$ are equal. They read

$$v_x^{\rm RA}=v\gamma\int\frac{dp_y}{2\pi}\int\frac{dp_z}{2\pi}\int dx\int dx'\delta(x-x')\hat{G}^A(\varepsilon,p_y,p_z,x,x')\sigma_x\hat{G}^R(\varepsilon,p_y,p_z,x',x) \tag{C.11}$$

$$\begin{aligned}&=ev\int\frac{dp_z}{2\pi}\frac{\gamma eH}{2\pi c}\sum_{n=0}^{N_{\rm max}}\frac{\varepsilon-\Sigma_2^R+vp_z}{(\varepsilon-\Sigma_1^R-vp_z)(\varepsilon-\Sigma_2^R+vp_z)+\Omega^2 n}\\&\quad\times\frac{\varepsilon-\Sigma_1^A-vp_z}{(\varepsilon-\Sigma_1^A-vp_z)(\varepsilon-\Sigma_2^A+vp_z)+\Omega^2(n+1)}.\end{aligned} \tag{C.12}$$

For energies away from the Weyl point, the difference between the two self-energies, Σ_1 and Σ_2, can be neglected. Furthermore, for high Landau levels we can express the Landau level index n in terms of the momenta in p_x and p_y direction. The correction to the current vertex then simplifies as follows

$$v_x^{\rm RA}=v\gamma\int\frac{dp^3}{(2\pi)^3}\frac{(\varepsilon-\Sigma^A)(\varepsilon-\Sigma^R)-v^2p_z^2}{((\varepsilon-\Sigma^A)^2-v^2p^2)((\varepsilon-\Sigma^R)^2-v^2p^2-\Omega^2)}, \tag{C.13}$$

which can be cast in the form:

$$\begin{aligned}v_x^{\rm RA}=&\frac{v\gamma}{\pi}\frac{(\varepsilon-\Sigma^A)(\varepsilon-\Sigma^R)}{(\varepsilon-\Sigma^R)^2-(\varepsilon-\Sigma^A)^2+\Omega^2}\int\frac{dp}{2\pi}p^2\left[\frac{1}{(\varepsilon-\Sigma^A)^2-v^2p^2-\Omega^2}-\frac{1}{(\varepsilon-\Sigma^R)^2-v^2p^2}\right]\\&-\frac{ev\gamma}{6\pi}\frac{(\varepsilon-\Sigma^A)^2+(\varepsilon-\Sigma^R)^2-\Omega^2}{(\varepsilon-\Sigma^R)^2-(\varepsilon-\Sigma^A)^2+\Omega^2}\int\frac{dp}{2\pi}p^2\left[\frac{1}{(\varepsilon-\Sigma^A)^2-v^2p^2-\Omega^2}-\frac{1}{(\varepsilon-\Sigma^R)^2-v^2p^2}\right]\\&+\frac{v\gamma}{6\pi}\int\frac{dp}{2\pi}p^2\left[\frac{1}{(\varepsilon-\Sigma^A)^2-v^2p^2-\Omega^2}+\frac{1}{(\varepsilon-\Sigma^R)^2-v^2p^2}\right].\end{aligned} \tag{C.14}$$

The integrals over momenta here can be identified with those for the self-energy. The shift in the denominator by Ω^2 of the integrands is unimportant (similarly to the difference between Σ_1 and Σ_2) and can be neglected; it is then sufficient to keep Ω^2 in the prefactors of the integrals. The corrections to the current in x-direction then reads

$$v_x^{\mathrm{RA}} = v\left(\frac{(\varepsilon-\Sigma^A)(\varepsilon-\Sigma^R)}{(\varepsilon-\Sigma^R)^2-(\varepsilon-\Sigma^A)^2+\Omega^2}\left[\frac{\Sigma^A}{\varepsilon-\Sigma^A}-\frac{\Sigma^R}{\varepsilon-\Sigma^R}\right]+\frac{1}{6}\left[\frac{\Sigma^A}{\varepsilon-\Sigma^A}+\frac{\Sigma^R}{\varepsilon-\Sigma^R}\right]\right.$$
$$\left.-\frac{1}{6}\frac{(\varepsilon-\Sigma^A)^2+(\varepsilon-\Sigma^R)^2-\Omega^2}{(\varepsilon-\Sigma^R)^2-(\varepsilon-\Sigma^A)^2+\Omega^2}\left[\frac{\Sigma^A}{\varepsilon-\Sigma^A}-\frac{\Sigma^R}{\varepsilon-\Sigma^R}\right]\right). \tag{C.15}$$

For weak disorder, using $\Sigma^{R,A} \ll \varepsilon$, after some algebra we arrive at:

$$v_x^{\mathrm{RA}} = \frac{v}{3}\frac{4i\varepsilon\Gamma}{4i\varepsilon\Gamma+\Omega^2}. \tag{C.16}$$

This result matches to the result in Ref. [81] for the case $H = 0$. The summation over the ladder of impurity lines yields

$$V^{\mathrm{tr}}(\varepsilon) = \left[1-\frac{1}{3}\frac{4i\varepsilon\Gamma(\varepsilon)}{4i\varepsilon\Gamma(\varepsilon)+\Omega^2}\right]^{-1}, \tag{C.17}$$

leading to Eq. (4.2) and hence

$$\tau^{\mathrm{tr}}(\varepsilon) = \frac{3}{2}\tau^q(\varepsilon) \tag{C.18}$$

in the Drude formula for the conductivity (4.13) and for the Hall conductivity (4.49).

This result is not applicable at the Weyl point, where $\Sigma_1 \neq \Sigma_2$. To simplify Eq. (C.11), we can use $\Sigma_2 = 0$ which is justified for weak disorder. Equation (C.11) simplifies then as follows

$$v_x^{\mathrm{RA}} = \frac{\gamma eHv}{2\pi c}\int\frac{dp_z}{2\pi}\sum_{n=0}^{N_{\max}}\frac{\varepsilon+vp_z}{(\varepsilon-\Sigma_1^R-vp_z)(\varepsilon+vp_z)+\Omega^2 n}$$
$$\times\frac{\varepsilon-\Sigma_1^A-vp_z}{(\varepsilon-\Sigma_1^A-vp_z)(\varepsilon+vp_z)+\Omega^2(n+1)}. \tag{C.19}$$

We find that this integral is proportional to A/Ω and hence the vertex corrections are small. This is in agreement with the neglect of vertex corrections in the calculation of the strong-H conductivity dominated by the lowest Landau level in Ref. [82].

D Appendix D

Fano-resonances in a double barrier system

In this appendix, we present the details of the developed Green's function approach for a double barrier structure with a Fano state between the barriers. In order to do this, we use now the Green's function (5.33)-(5.36) obtained in Sec. 5.2.2 where we treated the Fano state as a perturbation of the clean system consisting in this case of the two barriers. The Green's functions provide then the transmission and reflection coefficient.

We use the Green's functions of the double barrier system obtained in Sec. 5.2.2 and apply them to obtain the Green's of the double barrier structure with a molecule between the barriers. The Green's functions are given by Eqs. (5.40)-(5.45). For clarity, we provide these Green's functions again, reading

$$G^{\text{trans}}_{0,\text{RR}}(x',x) = \frac{2\pi i m}{k}\left(t_{BB}(k)e^{ik(x-x')} + t_{BB}(k)r^*_{BB}(k)e^{ik(x+x')}\right) \tag{D.1}$$

$$G^{\text{trans}}_{0,\text{LL}}(x',x) = \frac{2\pi i m}{k}\left(t^*_{BB}(k)e^{-ik(x-x')} + t^*_{BB}(k)r_{BB}(k)e^{-ik(x+x')}\right) \tag{D.2}$$

$$G^{\text{trans}}_{0,\text{RR}}(0,x) = \frac{2\pi i m}{k}(a^*_+(k)\cos(ka) + a^*_-(k)\sin(ka))t_{BB}(k)e^{ikx} \tag{D.3}$$

$$G^{\text{trans}}_{0,\text{RR}}(x',0) = \frac{2\pi i m}{k}(a_+(k)\cos(ka) + a_-(k)\sin(ka))\left(e^{-ikx'} + r^*_{BB}(k)e^{ikx'}\right) \tag{D.4}$$

$$G^{\text{trans}}_{0,\text{LL}}(0,x) = \frac{2\pi i m}{k}(a^*_+(k)\cos(ka) - a^*_-(k)\sin(ka))\left(e^{-ikx} + r_{BB}(k)e^{ikx}\right) \tag{D.5}$$

$$G^{\text{trans}}_{0,\text{LL}}(x',0) = \frac{2\pi i m}{k}(a_+(k)\cos(ka) - a_-(k)\sin(ka))t^*_{BB}(k)e^{ikx'}. \tag{D.6}$$

The full Green's functions with the Fano state located at position a thus read

$$G^{\text{trans}}_{\text{RR}}(x',x) = \frac{E_k - E'_0 - \frac{4\pi i m}{k}|V|^2\text{Re}(a_+(k)a_-(k))\cos(ka)\sin(ka))}{E_k - E'_0 - \frac{2\pi i m}{k}|V|^2(|a_+(k)|^2\cos^2(ka) + |a_-(k)|^2\sin^2(ka))} \cdot \frac{2\pi i m}{k}\left(t_{BB}(k)e^{ik(x-x')} + t_{BB}(k)r^*_{BB}(k)e^{ik(x+x')}\right), \tag{D.7}$$

$$G^{\text{trans}}_{\text{RL}}(x',x) = \frac{\frac{2\pi i m}{k}|V|^2(|a_+(k)|^2\cos^2(ka) + |a_-(k)|^2\sin^2(ka) - 2\text{Im}(a_+(k)a_-(k))\cos(ka)\sin(ka))}{E_k - E'_0 - \frac{2\pi i m}{k}|V|^2|a_+(k)|^2} \cdot \frac{2\pi i m}{k}\left(|r_{BB}(k)|^2e^{ik(x+x')} + e^{-ik(x+x')} + r^*_{BB}(k)e^{-ik(x-x')} + r_{BB}(k)e^{ik(x-x')}\right), \tag{D.8}$$

$$G_{\mathrm{LL}}^{\mathrm{trans}}(x',x) = \frac{E_k - E_0' - \frac{4\pi i m}{k}|V|^2 \mathrm{Re}(a_+(k)a_-(k))\cos(ka)\sin(ka))}{E_k - E_0' - \frac{2\pi i m}{k}|V|^2(|a_+(k)|^2\cos^2(ka) + |a_-(k)|^2\sin^2(ka))} \cdot \frac{2\pi i m}{k}\frac{2\pi i m}{k}\left(t_{BB}^*(k)e^{-ik(x-x')} + t_{BB}^*(k)r_{BB}(k)e^{ik(x+x')}\right), \tag{D.9}$$

$$G_{\mathrm{LR}}^{\mathrm{trans}}(x',x) = \frac{\frac{2\pi i m}{k}|V|^2(|a_+(k)|^2\cos^2(ka) + |a_-(k)|^2\sin^2(ka) - 2\mathrm{Im}(a_+(k)a_-(k))\cos(ka)\sin(ka))}{E_k - E_0' - \frac{2\pi i m}{k}|V|^2|a_+(k)|^2} \cdot \frac{2\pi i m}{k}\left(|t_{BB}(k)|^2\frac{2\pi i m}{k}e^{ik(x+x')}\right). \tag{D.10}$$

The local Green's function at the position of the Fano state has a non-negligible real part, which is absorbed into the energy renormalization of the Fano state, reading

$$E_0' = E_0 + P\int_0^\infty \frac{|V|^2(|a_+(k')|^2\cos^2(ka) + |a_-(k)|^2\sin^2(ka))}{E_k - E_{k'}}dk'. \tag{D.11}$$

To obtain from these Green's functions now the transmission coefficient, we need to take into account all terms proportional to $e^{ik(x-x')}$. This results in the transmission coefficient for the double barrier structure with a molecule at position a of

$$t_{BMB}(k) = \frac{E_k - E_0' - \frac{4i|V|^2\pi m}{k}\mathrm{Re}(a_+a_-^*)\cos(ka)\sin(ka)}{E_k - E_0' - \frac{2i|V|^2\pi m}{k}(|a_+|^2\cos^2(ka) + |a_-|^2\sin^2(ka))}t_{BB} - \frac{\frac{2i|V|^2\pi m}{k}(|a_+|^2\cos^2(ka) - |a_-|^2\sin^2(ka) - 2\mathrm{Im}(a_+a_-^*)\cos(ka)\sin(ka))}{E_k - E_0' - \frac{2i|V|^2\pi m}{k}(|a_+|^2\cos^2(ka) + |a_-|^2\sin^2(ka))}r_{BB}. \tag{D.12}$$

For the reflection, we use the clean Green's functions (5.46)-(5.51), reading for clarity

$$G_{0,\mathrm{RR}}^{\mathrm{ref}}(x',x) = \frac{2\pi i m}{k}\left(e^{ik(x-x')} + |r_{BB}|^2e^{-ik(x-x')} + r_{BB}^*(k)e^{ik(x+x')} + r_{BB}e^{-ik(x+x')}\right), \tag{D.13}$$

$$G_{0,\mathrm{LL}}^{\mathrm{ref}}(x',x) = \frac{2\pi i m}{k}|t_{BB}(k)|^2e^{-ik(x-x')}, \tag{D.14}$$

$$G_{0,\mathrm{RR}}^{\mathrm{ref}}(0,x) = \frac{2\pi i m}{k}(a_+^*(k)\cos(ka) - a_-^*(k)\sin(ka))\left(e^{ikx} + r_{BB}(k)e^{-ikx}\right), \tag{D.15}$$

$$G_{0,\mathrm{RR}}^{\mathrm{ref}}(x',0) = \frac{2\pi i m}{k}(a_+(k)\cos(ka) + a_-(k)\sin(ka))\left(e^{-ikx'} + r_{BB}^*(k)e^{ikx'}\right), \tag{D.16}$$

$$G_{0,\mathrm{LL}}^{\mathrm{ref}}(0,x) = \frac{2\pi i m}{k}(a_+^*(k)\cos(ka) - a_-^*(k)\sin(ka))t_{BB}(k)e^{-ikx}, \tag{D.17}$$

$$G_{0,\mathrm{LL}}^{\mathrm{ref}}(x',0) = \frac{2\pi i m}{k}(a_+(k)\cos(ka) + a_-(k)\sin(ka))t_{BB}^*(k)e^{ikx'}. \tag{D.18}$$

With the definitions of the full Green's function within the develop perturbative method (5.33)-(5.36), we find the following full Green's functions for the double barrier structure with one molecule relevant

for the reflection coefficient

$$G^{\mathrm{ref}}_{\mathrm{RR}}(x',x) = \frac{E_k - E_0' - \frac{4\pi i m}{k}|V|^2 \mathrm{Re}(a_+(k)a_-(k))\cos(ka)\sin(ka))}{E_k - E_0' - \frac{2\pi i m}{k}|V|^2(|a_+(k)|^2\cos^2(ka) + |a_-(k)|^2\sin^2(ka))}$$
$$\cdot \frac{2\pi i m}{k}\left(e^{ik(x-x')} + |r_{BB}|^2 e^{-ik(x-x')} + r^*_{BB}(k)e^{ik(x+x')} + r_{BB}e^{-ik(x+x')}\right) \tag{D.19}$$

$$G^{\mathrm{ref}}_{\mathrm{RL}}(x',x) = \frac{\frac{2\pi i m}{k}|V|^2(|a_+(k)|^2\cos^2(ka) + |a_-(k)|^2\sin^2(ka) - 2\mathrm{Im}(a_+(k)a_-(k))\cos(ka)\sin(ka))}{E_k - E_0' - \frac{2\pi i m}{k}|V|^2|a_+(k)|^2}$$
$$\cdot \frac{2\pi i m}{k}\left(e^{-ik(x+x')} + r^*_{BB}e^{-ik(x-x')}\right) \tag{D.20}$$

$$G^{\mathrm{ref}}_{\mathrm{LL}}(x',x) = \frac{E_k - E_0' - \frac{4\pi i m}{k}|V|^2 \mathrm{Re}(a_+(k)a_-(k))\cos(ka)\sin(ka))}{E_k - E_0' - \frac{2\pi i m}{k}|V|^2(|a_+(k)|^2\cos^2(ka) + |a_-(k)|^2\sin^2(ka))}$$
$$\cdot \frac{2\pi i m}{k}|t_{BB}(k)|^2 e^{-ik(x-x')} \tag{D.21}$$

$$G^{\mathrm{ref}}_{\mathrm{LR}}(x',x) = \frac{\frac{2\pi i m}{k}|V|^2(|a_+(k)|^2\cos^2(ka) + |a_-(k)|^2\sin^2(ka) - 2\mathrm{Im}(a_+(k)a_-(k))\cos(ka)\sin(ka))}{E_k - E_0' - \frac{2\pi i m}{k}|V|^2|a_+(k)|^2}$$
$$\cdot t^*_{BB}\frac{2\pi i m}{k}\left(e^{ik(x+x')} + r_{BB}e^{ik(x-x')}\right) \tag{D.22}$$

Similar to the transmission coefficient, we can now determine the reflection coefficient which is given by the terms proportional to $e^{-ik(x+x')}$. The reflection coefficient reads

$$r_{BMB}(k) = \frac{E_k - E_0' - \frac{4i|V|^2\pi m}{k}\mathrm{Re}(a_+a_-^*)\cos(ka)\sin(ka)}{E_k - E_0' - \frac{2i|V|^2\pi m}{k}(|a_+|^2\cos^2(ka) + |a_-|^2\sin^2(ka))}r_{BB}$$
$$- \frac{\frac{2i|V|^2\pi m}{k}(|a_+|^2\cos^2(ka) - |a_-|^2\sin^2(ka) - 2\mathrm{Im}(a_+a_-^*)\cos(ka)\sin(ka))}{E_k - E_0' - \frac{2i|V|^2\pi m}{k}(|a_+|^2\cos^2(ka) + |a_-|^2\sin^2(ka))}t_{BB}. \tag{D.23}$$

For the transmission and reflection coefficient of the full system with the Fano state written in terms of the system with the two barriers, it is straightforward to show that the equations fulfill the conditions $|t_{BMB}|^2 + |r_{BMB}|^2 = 1$ and $t_{BMB}r^*_{BMB} + t^*_{BMB}r_{BMB} = 0$.

Appendix E

Coulomb blockade in a nanotube with two SMMs

In this appendix, we employ the formalism of transport in a multi-quantum dot system introduced in Sec. 6.1 to the setup with four quantum dots in a CNT with SMMs, cf. Fig. 5.6. To calculate the free energy, we represent our system by means of equivalent schemes [164, 166] for different spin orientations of the molecules, see Figs. E.1 and E.2. We write the electrostatic energy in terms of a dimensionless function $\phi_{\alpha\beta}$, where α and β denote the spin projections of the two molecules.

The electrostatic energy for parallel molecular spin orientation (Fig. E.1) is given by

$$\phi_{\uparrow\uparrow}(N_i, U_g, U_{sd}) = \frac{1}{2}\mathbf{Q}'^{T}_{\uparrow\uparrow}\left(\hat{C}^{-1}_{\uparrow\uparrow}\right)^{T}\mathbf{Q}'_{\uparrow\uparrow}, \qquad \mathbf{Q}'_{\uparrow\uparrow} = \begin{pmatrix} N_1 + C_{1g}U_g + C_{1L}U_L \\ N_2 + C_{2g}U_g \\ N_3 + C_{3g}U_g + C_{3R}U_R \\ N_4 + C_{4g}U_g + C_{4L}U_L + C_{4R}U_R \end{pmatrix}, \tag{E.1}$$

where the capacitance matrix is expressed as

$$\hat{C}_{\uparrow\uparrow} = \begin{pmatrix} C_{1g}+C_{1L}+C_{14}+C_{12} & -C_{12} & 0 & -C_{14} \\ -C_{12} & C_{2g}+C_{12}+C_{24}+C_{23} & -C_{23} & -C_{24} \\ 0 & -C_{23} & C_{3g}+C_{23}+C_{34}+C_{3R} & -C_{34} \\ -C_{14} & -C_{24} & -C_{34} & C_{4g}+C_{4L}+C_{4R}+C_{14}+C_{24}+C_{34} \end{pmatrix}. \tag{E.2}$$

The matrix elements are obtained by the capacitance of the different capacitors in the equivalent scheme. They are obtained as discussed in Sec. 6.2 and are given by

$$\begin{gathered} C_{1g} = x_1, \quad C_{2g} = x_2 - x_1, \quad C_{3g} = 1 - x_2, \quad C_{4g} = 1, \\ C_{14} = x_1, \quad C_{24} = x_2 - x_1, \quad C_{34} = 1 - x_2, \\ C_{12} = \kappa\frac{x_1(x_2 - x_1)}{x_2}, \quad C_{23} = \kappa\frac{(x_2 - x_1)(1 - x_2)}{1 - x_1}, \quad C_{1L} = C_{3R} = C_{4L} = C_{4R} = l_{LR}. \end{gathered} \tag{E.3}$$

We assume that the source-drain voltage drops like $V_L = -V_{sd}$, $V_R = 0$, i.e., the voltage is applied to the left lead.

For the anti-parallel molecular spin (Fig. E.2), the electrostatic energy reads

$$\phi_{\uparrow\downarrow}(N_i, U_g, U_{sd}) = \frac{1}{2}\mathbf{Q}'^{T}_{\uparrow\downarrow}\left(\hat{C}^{-1}_{\uparrow\downarrow}\right)^{T}\mathbf{Q}'_{\uparrow\downarrow}, \qquad \mathbf{Q}'_{\uparrow\downarrow} = \begin{pmatrix} N_1 + C_{1g}U_g + C_{1L}U_L \\ N_2 + C_{2g}U_g + C_{2R}U_R \\ N_3 + C_{3g}U_g + C_{3L}U_L \\ N_4 + C_{4g}U_g + C_{4R}U_R \end{pmatrix}, \tag{E.4}$$

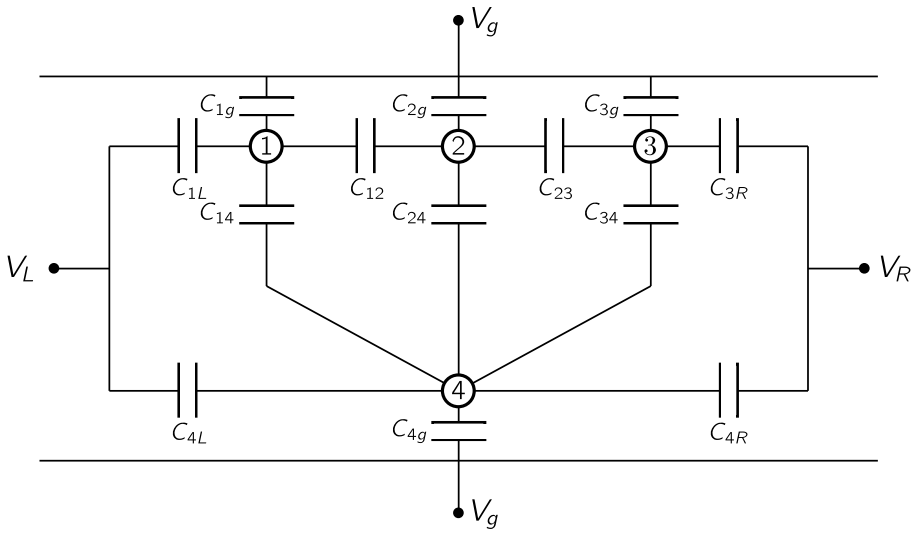

[Reprinted figure with permission from I. V. Krainov, J. Klier, A. P. Dmitriev, S. Klyatskaya, M. Ruben, W. Wernsdorfer, and I. V. Gornyi, ACS Nano, 2017 **11** (7), 6868-6880. Copyright 2017 by the American Chemical Society. DOI: 10.1021/acsnano.7b02014]

Figure E.1: Equivalent scheme for carriers for the case of parallel molecular spins. The channels 4 and 1-2-3 are associated with different spin orientation of the carriers.

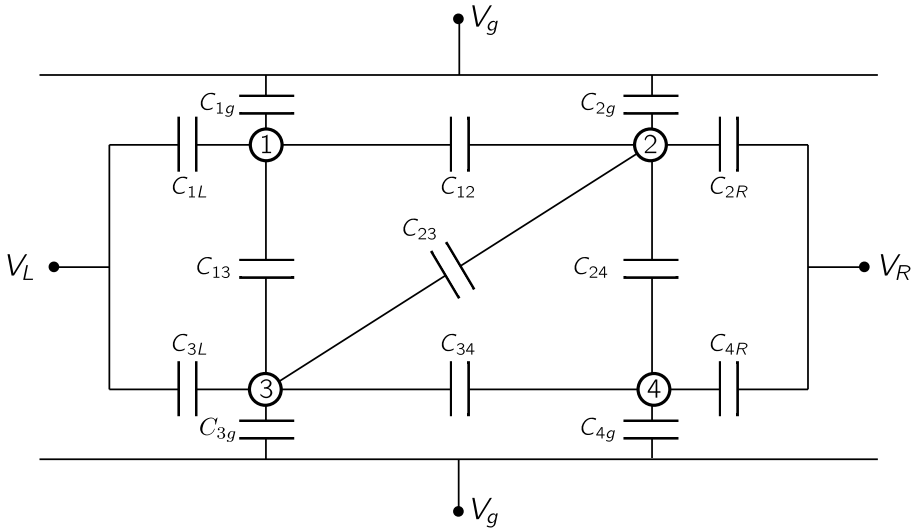

[Reprinted figure with permission from I. V. Krainov, J. Klier, A. P. Dmitriev, S. Klyatskaya, M. Ruben, W. Wernsdorfer, and I. V. Gornyi, ACS Nano, 2017 **11** (7), 6868-6880. Copyright 2017 by the American Chemical Society. DOI: 10.1021/acsnano.7b02014]

Figure E.2: Equivalent scheme for carriers for the case of anti-parallel molecular spins. The channels 1-2 and 3-4 are associated with different spin orientation of the carriers.

The capacitance matrix now is written as:

$$\hat{C}_{\uparrow\downarrow} = \begin{pmatrix} C_{1g}+C_{1L}+C_{12}+C_{13} & -C_{12} & -C_{13} & 0 \\ -C_{12} & C_{2g}+C_{2R}+C_{24}+C_{12}+C_{23} & -C_{23} & -C_{24} \\ -C_{13} & -C_{23} & C_{3g}+C_{3L}+C_{34}+C_{23}+C_{13} & -C_{34} \\ 0 & -C_{24} & -C_{34} & C_{4g}+C_{4R}+C_{24}+C_{34} \end{pmatrix}, \tag{E.5}$$

with the matrix elements obtained similar as of the parallel aligned molecules. The capacitance is given by

$$\begin{gathered} C_{1g} = x_1, \quad C_{2g} = 1 - x_1, \quad C_{3g} = x_2, \quad C_{4g} = 1 - x_2, \\ C_{13} = x_1, \quad C_{23} = x_2 - x_1, \quad C_{24} = 1 - x_2, \\ C_{12} = \kappa x_1(1 - x_1), \quad C_{34} = \kappa x_2(1 - x_2), \quad C_{1L} = C_{3L} = C_{2R} = C_{4R} = l_{LR}. \end{gathered} \tag{E.6}$$

As explained in Sec. 6.1, we can write the current in terms of open channels. For the parallel molecular spin configuration, equations for the currents in all channels with the set $\{N\}_i$ of electrons are

$$\begin{aligned} J^{(4)}_{L\to R}(\{N\}_i) &= \Theta\big(\Delta\mathcal{E}_{L\to 4}\big)\,\Theta\big(\Delta\mathcal{E}_{4\to R}\big)\,, \\ J^{(1-2-3)}_{L\to R}(\{N\}_i) &= \Theta\big(\Delta\mathcal{E}_{L\to 1}\big)\,\Theta\big(\Delta\mathcal{E}_{1\to 2}\big)\,\Theta\big(\Delta\mathcal{E}_{2\to 3}\big)\,\Theta\big(\Delta\mathcal{E}_{3\to R}\big)\,, \end{aligned} \tag{E.7}$$

where the upper index denotes the QDs acting in channel and $\Delta\mathcal{E}$ is the dimensionless energy difference given by $\Delta E_{j\to k}$ in units E_C. For electrons moving in the opposite direction $R \to L$, the currents can be obtained in the same manner. The equation for the total current then reads:

$$\begin{aligned} \mathcal{I}_{\uparrow\uparrow}(U_g, U_{sd}) = \sum_i P^{0(\uparrow\uparrow)}_{\{N\}}(i) \Big[& J^{(4)}_{L\to R}(\{N\}_i) + J^{(1-2-3)}_{L\to R}(\{N\}_i) \\ & + J^{(4)}_{R\to L}(\{N\}_i) + J^{(1-2-3)}_{R\to L}(\{N\}_i) \Big]. \end{aligned} \tag{E.8}$$

For the anti-parallel molecular spin configuration, the equations for currents for electrons moving from the left to the right lead $L \to R$ are

$$J^{(1-2)}_{L\to R}(\{N\}_i) = \Theta\big(\Delta\mathcal{E}_{L\to 1}\big)\,\Theta\big(\Delta\mathcal{E}_{1\to 2}\big)\,\Theta\big(\Delta\mathcal{E}_{2\to R}\big)\,, \tag{E.9}$$

$$J^{(3-4)}_{L\to R}(\{N\}_i) = \Theta\big(\Delta\mathcal{E}_{L\to 3}\big)\,\Theta\big(\Delta\mathcal{E}_{3\to 4}\big)\,\Theta\big(\Delta\mathcal{E}_{4\to R}\big)\,. \tag{E.10}$$

The equation for the total current is:

$$\mathcal{I}_{\uparrow\downarrow}(U_g, U_{sd}) = \sum_i P^{0(\uparrow\downarrow)}_{\{N\}}(i) \Big[J^{(1-2)}_{L\to R}(\{N\}_i) + J^{(3-4)}_{L\to R}(\{N\}_i) + J^{(1-2)}_{R\to L}(\{N\}_i) + J^{(3-4)}_{R\to L}(\{N\}_i) \Big].$$

The two equations for the total current are now used to calculate the Coulomb map for the parallel and anti-parallel molecular spin orientation.